DISTRIBUTION STATEMENT A
Approved for public release
Distribution Unlimited

FAILURE CHARACTERISTICS OF SANDWICH PLATES UNDER STATIC AND DYNAMIC LOADING

Technical Report

A.N. Palazotto, Professor, Principal Investigator
L.N.B. Gummadi, Research Associate

AFIT/ENY/TR-97-03

DEPARTMENT OF THE AIR FORCE
AIR UNIVERSITY
AIR FORCE INSTITUTE OF TECHNOLOGY

Wright-Patterson Air Force Base, Ohio

DTIC QUALITY INSPECTED 3

AFIT/ENY/TR-97-03

FAILURE CHARACTERISTICS OF SANDWICH PLATES UNDER STATIC AND DYNAMIC LOADING

Technical Report

A.N. Palazotto, Professor, Principal Investigator
L.N.B. Gummadi, Research Associate

AFIT/ENY/TR-97-03

DTIC QUALITY INSPECTED 3

Approved for public release; distribution unlimited

19980227 013

AFIT/ENY/TR-97-03

FAILURE CHARACTERISTICS OF SANDWICH PLATES UNDER STATIC AND DYNAMIC LOADING

Prepared by

A.N. Palazotto, Professor, Principal Investigator
L.N.B. Gummadi, Research Associate

Approved for public release; distribution unlimited

October, 1997
Department of Aeronautics and Astronautics
Air Force Institute of Technology
WPAFB, OH-45433

The views expressed in this report are those of the authors and do not reflect the official policy or position of the Department of Defense or the U.S. Government

ABSTRACT

Laminated sandwich plate constructions are extensively used in various aerospace and industrial applications. These plates offer advantages when compared with plates made of conventional materials due to their high specific modulus and high specific strength. Also, sandwich plates can be tailored to the designer's requirements. However, these plates are prone to many defects. Specifically, their resistance to impact is a major concern. Impact can significantly reduce the strength and stiffness of the structure. Studying various aspects that can be used to improve the resistance to impact of sandwich plates is the objective of this project. Two different sandwich models are studied. First, the sandwich plate is made of conventional honeycomb construction, while the second plate is made of z-pins. Experiments are conducted and, based on the experimental observations, a phenomenological analytical approach is developed. Issues studied include the determination of impact induced damage initiation, types of damage modes, propagation of damage modes, and the effect of damage on the overall performance of the sandwich plates.

ACKNOWLEDGMENTS

This work is performed as a part of the project WAL 53025. The authors thank Mr. William Baron and Mr. Thomas Holcomb of the Air Force Flight Dynamics Directorate for sponsoring this work.

Table of Contents

Abstract

Acknowledgments

Chapter I : Introduction I

Chapter II: Experimentation III

Attachment I: Low Velocity Impact Damage Initiation in Graphite-Epoxy/ Nomex Honeycomb Sandwich Plates VI

Attachment II: Low Velocity Impact Damage Characteristics of Z-fiber Reinforced Sandwich Panels - An Experimental Study VII

Attachment III: Low Velocity Impact Response and Nondestructive Evaluation of Sandwich Composite Structures VIII

Chapter III: Finite Element Model IX

Attachment IV: Elasticity Solutions for Hertzian Loaded Composite Sandwich Plates XIII

Attachment V: Finite Element Analysis of Low Velocity Impact on Composite Sandwich Plates XIV

Attachment VI: Analytical Modeling of Sandwich Plate Dynamics under Low Velocity Impact XV

Attachment VII: Finite element Analysis of Sandwich Composite Plates Under Low Velocity Impact XVI

Attachment VIII: Finite Element Analysis of Z-Pin Sandwich Panels and Comparison to Failure Modes Found in the Experimental Phase XVII

Attachment IX: Optimization of Z-Pin Composite Sandwich Plates XVIII

I. INTRODUCTION

Composite sandwich constructions are being increasingly used in various aerospace applications because of their high specific strength and specific modulus. Typically, a sandwich construction consists of stiff face sheets to carry the axial loads and a core for bearing the shear and compressive loads. In general, material used for the core is light of weight and not so strong in flexural stiffness but provides a significant shear stiffness. The core also serves the purpose of keeping the face sheets away from the bending neutral axis of the structure, there by improving the bending resistance of the face sheets. Different material and geometric configurations can be used for the core. In this project, two different core materials were used. In the first sandwich construction, a core made of Nomax honey comb was used while in the second sandwich construction, a z-pin sandwich construction was incorporated.

These sandwich constructions are prone to many defects such as delaminations, core crushing etc. Causes for such defects are numerous. Defects or damage caused by the low velocity impact is one of the most commonly encountered practical problem as related to aerospace applications. Thus, the present report is focused on studying the effects of impact induced damages on sandwich panels. Both experimental and analytical investigations are carried out in a phenomenological way. Due to the availability of the material, Nomax honeycomb sandwich panels are extensively tested and the lessons learned while testing are extended to the testing of z-pin sandwich panels. The phenomena that are observed in the experimentation are modeled adequately using 'in-house' developed analytical tools in addition to commercial software tools.

Many people contributed in this work at various stages along with the main authors of this report. Dr. Victor Birman, a Professor at University of Missouri was involved in the initial 'back of the envelop calculations' (this work was published as a technical report AFIT/ENY/TR-95-04). Major Eric Herup participated (as a part of his Ph.D. dissertation) in the testing and analysis of Nomax honeycomb sandwich panels. Dr. William Baker, Associate Professor in the Mathematics Department of AFIT is a co-author in the development of simple dynamic analytical models. Mr. Victor Perel, as a graduate student, helped in modeling the z-pin sandwich panels using I-DEAS. Mr. Galen Deeds, a Wright State University student, worked on the analysis of z-pin sandwich panels and compared these results with the experimentation results considering static loading conditions. Dr. Uday Vaidya, Associate Professor of Mechanical Engineering at Tuskegee University was involved in the experimentation of z-pin sandwich panels and carried out further post impact NDE studies. Dr. Lloyd Eldred, a NRC fellow helped in the optimization of sandwich panels using ASTROS. All these people's contribution is appreciated and resulted in various publications. The work performed under this project is divided into two major sections- Experimentation and Finite Element Model.

CHAPTER II: EXPERIMENTATION

In this chapter, experimental work carried out as part of this project is described. Two different sandwich constructions are considered and work carried out for each of the sandwich constructions is described in three technical papers. The first technical paper was accepted for publication in the Journal of Composite Science and Technology. The second paper was published in the proceedings of the 38 th AIAA/ASME/ASCE/AHS Structural Dynamics and Materials conference, 1997 held at Orlando, Florida. The third technical paper is to be published in the proceedings of the ASME winter annual meeting, held at Dallas, TX. All the three papers are enclosed in the report as attachments. A brief description related to the content of each paper is provided. Details of this description can be obtained by following the papers.

The title of the first paper is " Low Velocity Impact Damage Initiation in Graphite Epoxy/Nomex Honeycomb Sandwich Plates". The contributing authors for this paper include Major Eric J. Herup and Professor A.N. Palazotto. As the title indicates, this paper is about conventional Nomex sandwich plates. Face plates used for the sandwich plate are made up of graphite epoxy. Five different thicknesses of face plates are considered. The thickness variation is achieved by changing the number of layers used for the face plate. All the plates considered have [0/90]s layer combinations. Static and low velocity impact tests were carried out to characterize the damage initiation as a function of face plate thickness and loading rate. Two different test systems were used to provide the impact energy. In the first test system, a drop weight initiated the impact induced damage. As a second system, a pendulum test was used. In both test systems, force versus time histories were measured. It can be observed that damage within the plate changes the plate stiffness and hence its response to a load. A correlation is observed between the load history and the damage initiation. Based on this measured data, energy - time history is determined and damage initiation as a function of impact energy, is determined. Some of the problems characterized by the use of drop weight test system and solutions to these problems are discussed. For example, the mass used for the tup should be significantly less when compared with the overall mass of the plate in order to minimize the influence of the impactor dynamics on the test results. Thus, the manufacturer supplied tup of 151 gm mass is replaced by a manufactured tup of 8 gms and is used for testing the sandwich plates. The effect of the influence of the larger tup mass is discussed. By plotting impact energy as a function of absorbed energy, the energy level at which the damage initiates is determined.

Based on the experience of using both the test systems (drop weight and pendulum), it was concluded that the pendulum test system has some advantages over the drop weight. Static indentation tests were performed and force versus displacement data is collected from these test. These force displacement histories were compared for both low velocity tests and the static indentation tests. Based on the comparison, it was concluded that when the thickness of the face sheet is small, low velocity impact test results closely match those of static indentation test results, and hence an assumption that the low velocity impact system can be considered as quasi-static is valid. However, for thicker face plates, these two phenomena differ. It was observed that damage initiation occurs at lower load levels in static tests when compared with low velocity impact tests. All these specimens are C-scanned before and after the impact event to study the size of the damage due to the impact. The type of damage seems to be the same in both the static indentation tests and low velocity impact tests. Detailed description about each of these observations can be found in Attachment I.

Based on the experience gained on the low velocity impact studies on the Nomex sandwich panels, experiments were designed to study the low velocity impact characteristics of Z pin sandwich panels. For these experiments, only the pendulum test system was used. Two different pin orientations were considered (10 degrees and 20 degrees). Again, force versus time histories were measured and based on this data, energy versus time histories were determined. Damage initiation was obtained from the plot of impact energy versus the absorbed energy. The impact energy level at which there was a significant absorbed energy was defined as the damage initiation energy. Results were again compared with static indentation tests. As before, it was observed that the damage initiates at a lower level in static tests when compared with the low velocity impact tests. Due to the unavailability of specimens, only one face plate thickness was considered in all the experimentation. Results are discussed in Attachment II.

In the third technical paper, post impact studies were carried out. The authors for the third paper include Dr. U.V. Vaidya, Dr. A.N. Palazotto and Dr. L.N.B. Gummadi. In this work, nondestructive evaluation (NDE) tests were carried out for the z-pin sandwiches after the low velocity impact testing. These tests include Ultrasonic C-scan testing, Compression After

Impact testing, Acoustic emission testing and vibration testing. C-scan tests indicated that a series of pins are undergoing a push through phenomena accompanied by coalescence of delaminations between the adjacent pins. The compression after impact tests indicated that for the specimens with multi impacts, the final failure load is decreased. For example, for a 10 degree oriented pin, the failure load after the first impact is 3949 kgm while the failure load after the four repeated impact events reduced the failure strength to 3291 kgm, a drop of 16.6 percent in the failure strength. In the Acoustic emission testing, energy, amplitude and the event duration of the Acoustic emission events are monitored during the compression after impact testing. Results indicated that matrix microcracking and localized debonding of the pin from the face sheet with accompanying ply delamination may be the first failure phenomena. It should be remembered that this failure phenomena does not result in a drop in the load deflection characteristics. First major failure phenomena that reduces the strength seems to be the pin push through. Also, all these specimens are vibration tested (tested for natural frequencies). From these tests, it can be observed that the impact event associated with a major failure (such as pin push through) is associated with a reduction in natural frequencies and an increase in the damping. Details of all these tests and results are provided in Attachment III.

ATTACHMENT I

LOW VELOCITY IMPACT DAMAGE INITIATION IN GRAPHITE-EPOXY/NOMEX HONEYCOMB SANDWICH PLATES

LOW-VELOCITY IMPACT DAMAGE INITIATION IN GRAPHITE-EPOXY/NOMEX HONEYCOMB SANDWICH PLATES

Eric J. Herup & Anthony N. Palazotto

Department of Aeronautics and Astronautics, Air Force Institute of Technology,

Wright-Patterson AFB, OH 45433, USA

Abstract

Low-velocity impact and static indentation tests on sandwich plates composed of 4- to 48-ply graphite-epoxy cross-ply laminate facesheets and Nomex honeycomb cores are performed to characterize damage initiation as a function of facesheet thickness and loading rate. Force histories during low-velocity impact are measured using an instrumented impactor and integrated to produce energy histories. Energy histories are shown to reveal damage initiation. Static indentation tests show damages that are similar to those produced by low-velocity impact. The force at which damage initiates is shown to be lower for static tests than for low-velocity impact tests, and differences between equilibrium curves for the two types of loading are discussed. The difference between static and low-velocity impact tests is greater for plates with thicker facesheets. This may indicate a limitation of the applicability of the common assumption that low-velocity impact is a quasi-steady process.

Keywords: low-velocity impact:B, delamination, instrumented impactor, honeycomb, composite sandwich plate:C.

1. INTRODUCTION

Experimental studies of the impact force history resulting from low-velocity impact on composite plates have revealed that the impact force is not a smooth function of time.[1-4] A significant amount of research has been performed in this area, and several survey papers[5-8] summarize the previous work. Load drops on the impact force versus time plot are often taken to be indicative of strain energy release due to damage propagation within the plate. An objective of this investigation is to relate force history to damage. To do this, the temporal fidelity of the measured impact force must be sufficient to resolve individual load drops associated with damage growth. Since impact force may be influenced by impactor dynamics, characterization of the instrumented impactor test system is first addressed (Section 2.1). When an instrumented impactor system is used for impacts at energy levels low enough to avoid significant damage to the plate, calculated absorbed energies indicative of damage have still been observed.[1,4] A correction for this is discussed in Section 2.2. An experimental investigation of low-velocity impact to laminated composite sandwich plates is discussed in Section 3. Square, flat, sandwich panels of uniform in-plane size and honeycomb core thickness and varying facesheet thickness were subjected to a transverse load applied at their center by a steel spherical indentor (tup). Both quasi-static indentation and dynamic impact were considered and compared. Contact force was monitored throughout the event through the use of an instrumented impactor.

1.1 Objectives

1.1.1 Understand damage initiation and progress.

The experimental parameter space was designed to reveal the course of events which transpire when a composite sandwich plate is subjected to low-velocity impact. Loads applied, measurements taken, calculations made, and both non-destructive and destructive inspections after impact were all tailored to maximize the insights available into these events. These insights, in turn, can be used in an attempt to identify general trends and, ultimately, guide subsequent research aimed at controlling and reducing the degradation of residual properties of impacted composite sandwich structures.

1.1.2 Relate damage to load history.

Instrumented impactor tests are attractive because of the simplicity of the procedure and the relative swiftness with which a large number of impact events can be performed. The principal measurement in instrumented impactor tests is load as a function of time. This load history is used to integrate the tup equations of motion to infer the displacement and absorbed energy of the plate. To measure damage within the plate, more time- and labor-intensive procedures such as C-scan, radiography, and photomicrography are generally employed. It is desirable to reduce or eliminate these procedures if the needed information available by them can be obtained by other means.

Damage within the plate changes the plate stiffness and hence its response to load. In this way damage can be expected to show up as an equilibrium change which may be observable in the load history. One objective of the experimental portion of the current work was to correlate the observed load history to the internal damage. This correlation has the potential to greatly reduce the cost of testing these structures and/or increase the number of impact events (hence increase the resolution or parameter envelope) any given test program can provide to the existing database.

1.1.3 Validate quasi-static assumption.

An important simplification very common to low-velocity impact testing and modeling is that the damage depends not upon the impact energy per se, but upon the peak load reached in the process of transferring that energy. If this is the case, static tests and static analyses can be expected to adequately simulate the impact event. The objective here was to validate this simplification and (within the context of the parameters varied) define the boundaries of the usefulness of quasi-static assumptions.

1.2 Approach

1.2.1 Multiple facesheet lay-ups.

One of the very obvious decisions required of a designer of a composite sandwich plate structure is how thick to make the facesheets. Bending stiffness will be a principal consideration here. Damage resistance will be another important and potentially constraining consideration. For this reason, a range of facesheet thicknesses were tested, providing impact resistance data as a function of facesheet thickness. In an effort to limit the number of parameters being varied, the core thickness was held constant for all tests.

1.2.2 Static and dynamic testing.

Although load histories for the "static" and dynamic events are on time scales several orders of magnitude different, load versus displacement (equilibrium) curves for the two types of events can be compared directly. Differences between these curves provide insight into the dynamics of the impact event and the errors likely to be present in static analyses or simulations. Both static and dynamic tests were performed in an effort to mark off that portion of the parameter space in which time-dependence of the process of damage should not be ignored. The principal tool used to make this judgment is the load versus displacement curve. If the process were indeed quasi-static, one would expect the load versus displacement curve to be independent of the speed at which the load was applied. Where inertial stiffening is significant, the dynamic equilibrium curve should have a greater slope than the static. Where dynamic effects are not important to the damage process, such characteristics as peak load before damage, the magnitude of the load drop associated with a particular damage, stiffness after damage, and energy absorbed by the damage process should all be independent of the loading rate. Thus, static and dynamic test data are compared and implications for analyses based upon quasi-static assumptions are discussed.

1.2.3 Instrumented impactor.

A load cell mounted within the impactor/indentor provided load histories for all of the events. As discussed in Section 2, a reduced-mass tup tip effectively removed tup dynamics from the measurements providing excellent temporal fidelity in the load history (and hence velocity, energy, and displacement histories).

1.2.4 Post-impact C-scan and photomicrographs.

After the load was removed, damage present in the specimens was observed through the use of ultrasonic time-of-flight C-scans. Focused pressure waves were directed transverse to the top facesheet and echoes were timed and recorded as the focal point was traversed over the surface of the specimen. The first reflection (from the plate surface) was used to set the observation window (in time) so that the time of any subsequent returns was indicative of their depth relative to the first surface. By this process, delaminations are observed as returns and are recorded on a two-dimensional color map indicating, for each point, the depth of the delamination nearest the top surface of the specimen. On the C-scans, the color at any point represents the time of the first observed reflection after the reflection from the top surface. This reflection corresponds to the shallowest (i.e. nearest the top surface) delamination present at the given point. Thus, only the uppermost delamination was recorded at any given point. If, for example, at some point within the specimen there were three delaminations located at ply interfaces 1, 3, and 5 (numbering interfaces sequentially from the top of the plate), then the C-scan would show a color at that point representing the depth of interface 1. The existence of the other two delaminations would not be observable at that point in the C-scan. Neither fiber failure, matrix cracking, nor core crushing were observable by C-scans. To see these modes of damage, several specimens were sliced through their thickness in several equally spaced planes perpendicular to the fiber direction. The exposed surfaces were stabilized with an epoxy potting compound, polished, and viewed under visible reflected light at various magnifications. This process allowed the viewer to record (photographically and by sketch) the damage present in any of the slice planes. The majority of the cross-section data used in this research was observed by Harrington.[1] Damage observed was in the forms of matrix cracks, delaminations, and crushed core walls.

2. INSTRUMENTED IMPACTOR SYSTEM CHARACTERIZATION

2.1 Force Temporal Fidelity

The fundamental characteristic of an instrumented impactor impact test system is that the contact force between the impactor and the target is measured by means of a load cell built into the impactor. The load cell actually measures the force between two portions of the impactor, the main mass, m_1 and the tip mass, m_2. Typically, the main mass is much greater than the tip mass, and the load cell is very stiff compared to the target, so the dynamics of the impactor (vibration of the tip mass against the load cell stiffness) are neglected. Neglecting impactor dynamics has been shown to lead to significant force and energy history errors for some choices of system parameters.[4] In particular, the tup mass ratio, $(m_1+m_2)/m_1$, must be near unity to avoid significant errors. In order to make the tup mass ratio near unity, the main mass must be much larger than the tip mass. Since the main mass is effectively sized by the chosen test system and the impact energies required, the tip mass must be as small as practical in order to minimize the influence of impactor dynamics on the test results. This idea is illustrated graphically in figure 1 which shows the response of an instrumented impactor load cell (load range 0-15 kN) when subjected to an axial impulse load from a hammer strike. With the manufacturer-supplied 151.4 gm tup tip, a large portion of the impact energy is evidently transferred to the first axial vibration mode of the tup and slowly dissipated by light damping. Thus the tup "rings" as seen in the lowest curve. Though it was not measured, one must conclude that a significant portion of the impact energy was not returned to the hammer which lost contact with the tup after the first half-cycle. In contrast, the center curve shows the impulse response with the tup tip removed. The much higher fidelity impulse response indicates that very little energy is absorbed by tup vibrations. The upper most curve in figure 1 shows the response with a much lighter tup tip fabricated for the current work. It is evident that the new tup tip approximates the response of no tup tip.

The effect of the reduced-mass tup tip on the fidelity of the force history in an actual composite sandwich plate impact event is illustrated in figure 2. In that figure the large amplitude oscillations present in the 151.4 gm tup tip data are not actually loads seen by the plate, but are load cell loads induced by the dynamics of the tup. The two different 8.2 gm tests (#1 and #2) are shown to indicate the variation of response from one event to another.

As seen in figure 2, reducing the tup tip mass by changing from the manufacturer-supplied 151.4 gm tip to the 8.2 gm tip significantly enhances the temporal fidelity of the load histories available from instrumented impactor tests. The improvement is most valuable for more flexible (low range) load cells and manifests itself most strongly following a load drop like those often seen in composite impact tests. The lesson here is that the force oscillations following a load drop in an instrumented impactor test can be significantly influenced by instrumentation dynamic response and should not be blindly attributed to the dynamics of the specimen. For the load cell used for the impact portion of this work (15kN), a relatively low-frequency, relatively high-force axial vibration mode exists when the manufacturer-supplied tup tip is used. This mode contributes significant error to the observed load history. Reducing the tup tip mass presumably increases the frequency of the error but reduces its magnitude to the point that it can not be observed in the impulse response of the system. Without this improvement the tup tip dynamics can effectively mask the high frequency response of the plate (figure 2). With this minor system improvement there is hope of being able to correlate load history with damage. Without it, after the first load drop the noise overwhelms the signal and it appears very unlikely that such a correlation can be made. It should be emphasized that, for a given load cell, it is the tup mass ratio, and not the tup tip mass per se, that dictates the strength of the tup dynamics (force noise). With the 15 kN load cell and the 3.5 kg main mass, m_1, used in this work, the 151.4 gm tup tip provided a tup mass ratio of 1.043 while the 8.2 gm tup tip reduced the ratio to 1.002. The stiffness of the load cell must also be considered. Higher stiffness is better from the point of view of temporal resolution, but a tradeoff is made here in that the higher the stiffness, the poorer the load resolution due to the fact that the force is measured by internal strain gages and strain is inversely proportional to stiffness. When load resolution requirements dictate a low stiffness load cell be used, minimizing the tup mass ratio is shown to significantly improve the temporal fidelity of the load data produced by an instrumented impactor test system.

2.2 Energy Calculations

In instrumented impactor tests, impact energy and specimen absorbed energy are often used to characterize the event. Impact energy is the kinetic energy of the impactor (tup) at the instant that it strikes the specimen. Impact energy is usually controlled by varying the mass of the tup, m_{tup}, and the height from which it is dropped (or swung in the case of a pendulum impactor). Thus the potential energy of the tup before release is an upper bound for its kinetic energy at the time of impact. Energy losses during the acceleration of the tup (sliding friction at the guide rails, air resistance, etc.) are typically accounted for by measuring the velocity of the tup just prior to impact, $V_{tup}(0)$. Impact energy is then calculated by the relation,

$$\text{Impact energy} = \frac{m_{tup}}{2} V_{tup}(0)^2 \tag{1}$$

The impact event transfers energy between the initially moving tup and the initially stationary specimen. Specimen absorbed energy (usually called "absorbed energy") is that net portion of the impact energy at any given time, which has been transferred to the specimen. It includes the strain energy of the specimen, the kinetic energy of the specimen, the total strain energy released from the specimen up to that time through damage progression, and frictional losses in the contact area and at the boundaries of the plate. Frictional losses at guide rails and air resistance during the impact event are usually assumed small, but they are actually implicitly included in the absorbed energy. The absorbed energy is calculated by the kinetic energy loss of the tup in which the tup velocity, $V_{tup}(t)$, is integrated from the contact force, $F(t)$, by Newton's second law, that is,

$$V_{tup}(t) = V_{tup}(0) - \frac{1}{m_{tup}} \int_0^t F(\tau) \mathrm{d}\tau \qquad (2)$$

and the kinetic energy loss of the tup, called the "absorbed energy" or often just "energy" and labeled $E(t)$, is then

$$E(t) = \frac{m_{tup}}{2} \left(V_{tup}(0)^2 - V_{tup}(t)^2 \right) \qquad (3)$$

Thus, absorbed energy is a calculated, not directly measured, quantity. Its accuracy depends on the accuracy of the measured velocity $V_{tup}(0)$, the measured contact force $F(t)$, the measured mass m_{tup}, and the neglected frictional losses during the impact event. Figure 3 is a typical load and absorbed energy history from a low-velocity impact event in which the specimen was a composite sandwich plate and the force was measured using an instrumented impactor (in this case drop weight) with a tup mass ratio of 1.043. After the event of figure 3, no damage was detected in the specimen.

In figure 3 the absorbed energy for an impact event which produced no damage (as detected by C-scan[1]) indicates that a significant amount of energy is not returned to the tup (absorbed energy does not return to zero when force does). The calculated residual energy for this test was a large portion (more than 60 percent) of the impact energy (the maximum on the energy plot). That is, if the absorbed energy in the plate is correct, the undetectable damage and other losses absorb the majority of the impact energy. It has been demonstrated[4] that this is not the case. The force shown in figure 3 is in error due to the large tup tip mass. A correction for the tup tip mass was developed (reference 4). This correction is applied to an analytical model of the impact event of figure 3 with the result shown in figure 4. It is obviously desireable to eliminate the error, rather than correct for it. This was accomplished for the current work by reducing the tup tip mass ratio from 1.043 to 1.002 by fabricating a lightweight tup tip. With the lightweight tup tip, the correction was no longer needed.

3. EXPERIMENTAL INVESTIGATION

3.1 Parameters

The panels consisted of AS4/3501-6 graphite-epoxy face sheets secondarily bonded to 1.27 cm thick HRH-10-1/8-9.0 Nomex honeycomb core using two layers of FM300-2 film adhesive. Typical honeycomb core material and a completed sandwich structure are shown in figure 5. The face sheets had the following stacking sequences: $[0/90]_S$, $[0/90]_{2S}$, $[0/90]_{4S}$, $[0/90]_{8S}$, and $[0/90]_{12S}$. In the following, sandwich structures made from these facesheets are referred to as 4-, 8-, 16-, 32-, and 48-ply, respectively. Each of the panels from which the individual specimens were cut were C-scanned to ensure no significant flaws were present before impact. The specimen size was 17.8 cm by 17.8 cm and they were restrained in a steel fixture simulating simple supports[1] having dimensions of 12.7cm by 12.7 cm. The same restraint fixture was used for both static and dynamic tests. All tests were performed at room temperature. The impactor/indentor radius was 1.27 cm and constant for all tests. For pendulum tests the tup mass was 3.48 kg while that for drop weight tests was 3.49 kg. Tup tip mass for the drop weight tests was 8.2 gm while that for the pendulum tests was 12.3 gm. Drop height (or pendulum swing) was varied to provide impact energies between 0.06 and 25 joules. For each facesheet thickness the impact energies were chosen to span the damage initiation energy (threshold) and extend for at least a factor of two above it. The entire impact test matrix is given in figure 6.

3.2 Static Indentation Test System

A 9 kN load cell was used to measure load for the 4-, 8-, 16-, and 32-ply specimens and a 90 kN load cell was used for the 48-ply specimens. A displacement transducer (LVDT) was used to measure the displacement of the lower surface of the plate. The static test system is shown schematically in figure 7. The principal features are: 1) a stiff crosshead driven down by precisely controlled screws; 2) a stiff load cell mounted under the crosshead which measures the force between the crosshead and the specimen; 3) a 12.7 mm radius hardened steel ball bearing between the load cell and the specimen; 4) a stiff restraint fixture to hold the specimen; 5) an LVDT mounted under the specimen; 6) a control system; 7) signal conditioners; and 8) a digital data acquisition system.

3.3 Dynamic Impact Test Systems

Force and energy histories are part of the reduced data generally available from instrumented impactor impact test systems. To facilitate comparisons with static test data as well as static analysis data, force versus tup displacement plots were also generated. Integration of the tup equations of motion produced the tup displacement.

In the early portion of the testing, a commercially available drop weight impact testing system was used to impact 8- and 16-ply sandwich specimens. The minimum energy for which data could be obtained with this system was ~0.5 J. This minimum was found to be unacceptable because the initiation of damage in the 8-ply specimens occurred at less than this value. In order to obtain data for lower energies, the remainder of the test matrix was filled using the same load cell, but mounting it in a pendulum impact test system. The minimum energy at which the pendulum system could be used (without reducing tup mass) was found to be less than 0.05 J and this was low enough to resolve the initiation of damage in the 8-ply as well as the 4-ply specimens.

3.3.1 Drop weight test system.

The drop weight test system used for all of the 16-ply and part of the 8-ply portion of the test matrix is shown schematically in figure 8. Its principal features are: 1) a stiff, guided, near-free-falling mass; 2) a stiff load cell mounted under the falling mass which measures the force between the mass and the specimen; 3) a spherical 12.7 mm radius hardened steel tup tip between the load cell and the specimen; 4) a light gate to measure tup velocity just prior to impact; 5) a stiff restraint fixture to hold the specimen; 6) a control system including brakes to prevent multiple hits; and 7) a digital data acquisition system.

3.3.2 Pendulum test system.

The pendulum impact test system had several advantages over the drop weight test system. Not only could it reliably take data at an order of magnitude smaller impact energy for the same tup mass, but also it had the singular advantage of measuring both impact velocity and rebound velocity. Thus absorbed energy was effectively measured, providing a check for the integrations of the tup equation of motion. In addition, the fact that these velocity measurements were taken at the bottom of the pendulum swing (when the tup acceleration is near zero) provided a greater degree of consistency in the impact velocity measurements than was available from the drop weight system. The handicap that the drop weight system had in this regard was that the acceleration of the tup at the time that impact velocity was measured was not zero, in fact the acceleration was constant during the whole drop. Thus, any small variability in the location of the velocity measurement light gate with respect to the specimen had a significantly greater effect on the drop weight impact velocity calculation than it would have had on the pendulum impact velocity calculation. In short, the pendulum was a more forgiving system.

The pendulum impact test system was used for all of the 4-, 32-, and 48-ply tests and the low-energy part of the 8-ply tests. The system is shown schematically in figure 9. Its principal features are: 1) four 3.6 m kevlar strings positioned so as to provide a 3.37 m effective pendulum arm with a stable planar swing and a consistent impact point; 2) a stiff suspended mass; 3) a stiff load cell mounted on the swinging mass which measures the force between the mass and the specimen; 4) a spherical 12.7 mm radius hardened steel tup tip between the load cell and the specimen; 5) a light gate to measure tup velocity just prior to and just after impact; 6) a stiff restraint fixture to hold the specimen; and 7) a digital data acquisition system.

3.3.3 Impact test calculations.

Other differences aside, the calculations required for the pendulum and drop weight data were nearly identical. The fact that the pendulum is horizontal and the drop weight system was vertical did not influence the calculations. In the first place, the deflections were small, so the change in tup potential energy while in contact with the plate was neglected. In the second place, the acceleration due to gravity was assumed to be small compared to the acceleration produced by the impact force. Both of these higher order effects would have had a much greater influence on the drop weight calculations than on the pendulum. The important calculations for the dynamic impact tests are equations 1 through 3 and the displacement. Determining displacement as a function of time required an additional time integration of the tup equation of motion. The coordinate system is chosen such that the initial tup displacement, $\delta(0)$, is zero. Displacement calculation is important because load versus displacement is used to compare static and dynamic test data in order to judge the applicability of the quasi-static assumption. The tup displacement, $\delta(t)$, is integrated from the tup velocity, $V_{tup}(t)$, by the relation,

$$\delta(t) = \int_0^t V_{tup}(\tau)d\tau + \delta(0) \tag{4}$$

For impact tests then, $F(t)$ is measured and absorbed energy ($E(t)$) and displacement ($\delta(t)$) are calculated while for "static" tests $F(t)$ and $\delta(t)$ are both measured and $E(t)$ is simply the product of the two.

3.4 Test Results

As indicated by the impact test matrix given in figure 6, two parameters were varied for the dynamic portion of this research. These are, facesheet thickness (or number of plies) and impact energy. For each event, a number of measures can provide insight into the physics. The measures found most prominently in the literature are force history, absorbed energy history, and C-scans. In addition to these, other measures were found to be quite useful in the present research. These include absorbed energy at the end of the event, photomicrographs, and most significantly load-displacement curves. In discussing the results of a test matrix varying facesheet thickness and impact energy, one could choose to take one facesheet thickness at a time and show the effect of different energies on each measure, or one energy at a time and discuss the effect of facesheet thickness on each measure. In contrast to these admittedly logical presentation orders, the organization of the following was chosen because it enhances the communication of the key ideas gleaned from these data while minimizing the repetition of words. For this presentation, the measures (not the experimental parameters) provide the top level discussion points and the effects of first facesheet thickness and then impact energy are discussed in relation to each measure.

3.4.1 Absorbed energy.

In figures 10 through 14 absorbed energy has been nondimensionalized by impact energy and plotted versus impact energy. Several important trends are observable in figures 10 through 14. First, for all of the pendulum data (figures 10, 11, 13, and 14) at least 15 percent of the impact energy was not returned to the tup. This was the case even for impact energies low enough to produce no detectable damage. The second trend that should be observed is that in each figure a threshold impact energy is evident below which the absorbed energy is relatively small and above which a significantly larger portion of the impact energy is absorbed. This threshold impact energy corresponds precisely with the damage initiation impact energy determined by post-impact inspections of the specimens. That is, no damage was detected in any specimens impacted with less than the threshold impact energy, and damage was detected in every specimen impacted with more than the threshold impact energy. Absorbed energy appears to be a reliable indicator of damage. This is to be expected since the strain energy release associated with damage progression is an energy loss to the system. What is interesting is how sharply the threshold can be seen as each plot approximates a step function. The third important trend is that, after the damage initiates, the absorbed energy increases linearly with impact energy. This trend can be seen in figures 10 through 14 by observing that for impact energies above the threshold impact energy the absorbed energy/impact energy ratio is independent of impact energy. This constant ratio implies, for example, that doubling the impact energy will simply double the absorbed energy. A fourth trend is that the absorbed energy/impact energy ratio for damaged specimens seems to increase with facesheet thickness. That is, as facesheet thickness increases, the energy absorbed in the process of damage also increases. An interpretation of this may be, damage is delayed (i.e. threshold impact energy is increased) by increasing facesheet thickness but at the cost of making the damage more severe when threshold is breached.

3.4.2 Force history.

Force histories for several impact energies near the threshold impact energy for each facesheet thickness are shown in figures 15 through 19. In each of those figures the facesheet thickness is held constant and the impact energy is varied. Some general trends which can be seen in these data are:

1. At impact energies below the threshold impact energy, the loading and unloading is relatively smooth and not unlike a half sine wave with a superposed smaller-amplitude higher-frequency secondary sine wave. Increasing the facesheet thickness increases the prominence of the secondary sine wave. These observations support the conjecture that the secondary sine wave may be attributable to specimen dynamics. The specimen mass, and therefore the maximum specimen kinetic energy,

increases with facesheet thickness. Thus, the prominence of the force oscillations brought about by the vibrations of the specimen can be expected to increase with facesheet thickness.

2. For any given facesheet thickness, as impact energy increases, eventually a point is reached where the load history is no longer smooth, instead, a major load drop occurs and is followed by multiple cycles of loading and partial unloading. It is of interest to identify the damage or damages that give rise to the major load drop. The damage that is responsible is a major energy absorbing process. Force history alone can not reveal the damage that produces this load drop, but the current work does eventually identify the damage associated with the major load drop.

3. For any given facesheet thickness, the load at which the major load drop occurs is independent of impact energy. This is the fact often observed in the literature which motivates the idea that damage from low-velocity impact is controlled by the maximum load reached and not by the energy of the impact. From this, the assumption that quasi-static analyses and static indentation tests can be used to model and simulate impact tests was born. The range of validity of this assumption is of concern in this work and will be investigated by comparing load displacement curves and C-scans from statically and dynamically loaded specimens.

4. Increasing the facesheet thickness increases the load at which the major load drop occurs. This idea is intuitive, a thick facesheet is more damage resistant than a thin one.

5. Increasing the facesheet thickness increases the magnitude of the major load drop. This idea agrees with the absorbed energy data which found that the thicker facesheet specimens absorbed a greater proportion of the impact energy when they did receive damage.

6. The initial loading rate (slope of the load history at the beginning of the event) and final unloading rate (slope of the load history at the end of the event) are of the same magnitude for those events not showing a major load drop, while the final unloading rate drops off for those events showing a major load drop. This can be observed in figures 15 through 19 as a slight "tail" at the end of the impact events

showing a major load drop, or more prominently in figures 21 through 25 as the difference between the loading and unloading slopes near zero load. The major load drop has been attributed to damage. The damage can be considered a loss of stiffness. The reduction in the final unloading rate (without noticeable reduction unloading rate immediately after the damage) may indicate that the damage present induces a nonlinearity in the stiffness. The effect of the nonlinearity is to locally soften the structure for small displacements (or loads) but for large displacements (or loads) the global stiffness of the structure dominates and the structure stiffens.

7. The major load drop is followed by a response that appears to have a superposed secondary sine wave of nearly the same frequency as was seen before damage but with much greater amplitude. One could think of this as follows. The major load drop appears to the undamaged portion of the plate to be a negative step function in load. It is to be expected that such an abrupt change in load will excite a broad range of natural frequencies of the plate. The most prominent of these frequencies is the same as that seen before damage, indicating that the global stiffness of the specimen has not changed significantly. This point argues for a localized damage.

3.4.3 Transverse strain.

In considering the static indentation data, the average (through the thickness) transverse strain immediately under the indentor gives additional insight into the damage processes. Knowing the displacement of both surfaces δ_{Top} and δ_{Bottom} as well as the original sandwich thickness, average transverse strain is defined as

$$\text{average transverse strain} = \frac{\delta_{Top} - \delta_{Bottom}}{\text{thickness}} \qquad (5)$$

This quantity is plotted against tup displacement for specimens of each facesheet thickness in figure 20.

The value of the transverse strain measure outlined above is that it highlights the points in the loading sequence when the top surface and the bottom surface moved toward each other abruptly. That is, the top surface moved down slowly with the crosshead and the bottom surface followed except for certain times when the bottom surface moved rapidly back up. These rapid movements of the bottom surface coincided with load drops. A drop in load for a given top surface displacement indicates strain energy release, or damage progression. The question is, what form or forms of damage are producing these load drops? Undamaged core between the facesheets resists transverse strain. By Hooks law, an abrupt increase in transverse strain indicates either an abrupt increase in transverse stress or and abrupt decrease in transverse stiffness. Since the load, and hence the transverse stress, is dropping (or at least not increasing) these jumps in transverse strain must indicate a drop in transverse stiffness. Of the two possible contributors to this stiffness drop, facesheet and core, core has by far the greater potential for causing such a large strain jump. If the top facesheet failed by delamination or matrix cracking without core failure, the transverse facesheet strain jumps implied by the observed average transverse strain jumps are unreasonably high (e.g. ~8 percent for the 16 ply case). Therefore, the observed average transverse strain jumps are assumed to indicate abrupt core failure. If the core had no attached facesheets and were under compression from the indentor directly, only that portion in contact with the indentor would fail. The facesheet effectively spreads the transverse stress out over the core. The thicker the facesheet, the greater the core area over which the transverse stress is spread. Thus, sandwiches with thicker facesheets should be expected to take a higher load before the core fails. In addition, when they fail, a larger portion of the core should be expected to fail so that the strain energy released should be expected to be greater.

3.4.4 Dynamic and static compared.

A major question addressed by this research is the range of validity of the assumption that low-velocity impact to composite sandwich plates is a quasi-static process. By comparing static and dynamic equilibrium and delamination patterns, a look at the importance of dynamics on the processes of damage initiation and progression in composite sandwich structures is available. Two metrics will be used to compare static and dynamic data, the load versus tup displacement curve (equilibrium) and C-scan (delamination pattern).

3.4.4.1 *Load-displacement curves.* For a static or quasi-static loading, a load versus displacement curve is essentially a record of the equilibrium states before, during, and after damage. The difference between a truly static load versus displacement curve and that of a time-dependent process is the inertial loading present in the dynamic process and absent from the static. Comparison of load versus displacement curves then, will allow the analyst to judge the magnitude of the inertial forces relative to the static forces. In addition, since the strain energy release associated with damage manifests itself as a drop in load, the first failure loads, displacements, and load drops can also be compared. Similar damages will presumably have similar effects on the load versus displacement curve.

Figures 21 through 25 show load versus displacement curves under static loading as well as several impact loadings with and without damage. By these figures the reader is intended to observe both the similarities and differences between static indentation and dynamic impact for the several facesheet thicknesses tested. The load histories for the impact events in figures 21 through 25 were previously given in figures 15 through 19. In all but the 4-ply case (figure 21), the static displacement was increased until the first major load drop, then it was decreased. For the 4-ply case, the first "major" load drop was a more subjective judgment (load drops occurred at 270 N, 330 N and 530 N as well as the easily seen drop at 690 N) so data for the full range of static displacement is shown in figure 21.

The first major load drop was difficult to distinguish in the 4-ply impact data shown in figure 21. Damage is apparent in the 0.34 J event and in the 0.094 J event (see figure 15) but not in the 0.11 J and 0.22 J events. It is thought that for this very thin facesheet the contact pressure is transferred almost directly to the core. That is, the facesheets have very little bending stiffness and hence do a poor job of spreading out the contact stress. As a result, a very small area of the core sees all of the transverse load. This small portion of the core may be a single cell or just part of a cell. The loaded portion of the core begins to fail very early but since it is so small the strain energy released by the failure is also small. Thus the almost imperceptible load drop at 325 N in the static case may in fact be the first core failure. Another drop at 510 N in the static case is more readily discerned and may represent the failure of adjoining cell walls. The next few drops near 700 N in the static case are easy to see and are more like those seen on the thicker facesheet specimens, perhaps indicating that the contact is fully established and core failure and facesheet delamination are happening together. If this explanation is correct, then turning to the dynamic data, the anomaly of damage in the 0.34 J event and in the 0.094 J event but not in the 0.11 J and 0.22 J events could be simply the result of minor differences of the impact point with respect to the honeycomb cells. Suppose the 0.094 J event had the impact point directly over a cell wall while the 0.11 J and 0.22 J events had the impact point near the center of a cell. In this case, the 0.094 J case might be expected to fail at a lower load because a fewer cell walls were available to react the load. For impact energies above 0.3 J, the 4-ply data are consistent in showing a first major load drop near 600 N.

The 8-ply data in figure 22 show loading and unloading for the 0.19 J and 0.28 J events to be almost perfectly following the same path. This fact is thought to indicate that no damage is taking place and that the energy absorbed by the dynamics of the system is small. Interestingly, the 0.28 J event reaches a load which is equal to the load for the first major load drop in the higher energy events and is more than 15 percent greater than that which caused the first major load drop in the static indentation data. In figure 22 it can be seen that the static test shows the first major load drop near 830 N while the impact tests show it near 1100 N. The tendency for the static loading to bring about the first major load drop at a lower applied load than the dynamic loading was consistent among all facesheets tested. The slopes of the curves here represent the local stiffness of the plate. In the dynamic tests, the applied force can be thought of as having two components. The first is the product of the static stiffness and the displacement, and the second is the product of the plate effective mass and acceleration (Newton's second law). For the purposes of the following discussion, the second term will be referred to as the "inertial stiffening force." In the 8-ply data the inertial stiffening effect is more pronounced than in the 4-ply data as can be seen by the "waviness" of the slope in the impact curves before the first load drop. This is believed to be an effect brought about by the increased inertia related to the larger mass of the thicker specimens.

Similar to the 8-ply data, the 16-ply data in figure 23 show loading and unloading for the 0.47 J and 0.88 J events to be nearly following the same path. Much more dramatic than the 8-ply data, however, is the magnitude of the first major load drop. Since the magnitude of the load drop reflects the strain energy released, these data indicate that much more energy is absorbed by the damage causing first failure in the 16-ply specimens than in the 8- and 4-ply specimens. In these data it can be seen that the static test shows the first major load drop near 2300 N while the impact tests show it near 2800 N. Also, the magnitude of the load drop is roughly 600 N for the static test while it ranges from 800 N to 1100 N for the impact tests. In the 16-ply data the inertial stiffening effect is even more pronounced than in the 8-ply data as can be seen by the greater initial slope of the load versus displacement curve for the impact events. This is believed to be an effect brought about by the increased mass of the specimen.

Unlike the 8- and 16-ply data, the 32-ply data in figure 24 show loading and unloading for events not exhibiting a major load drop (3.49 J, 3.90 J and 4.40 J) do not follow the same path. There are evidently more energy losses before damage in these tests than in the thinner facesheet tests. This is confirmed by figures 12 and 13 in which the below-threshold 16-ply specimens absorbed less than 10% of the impact energy while the below-threshold 32-ply specimens absorbed more than 30% of impact energy. The dramatic load drop of the 16-ply data continues in the thicker 32-ply data. The static test shows the first major load drop near 5800 N while the impact tests show it near 8000 N. Also, the magnitude of the load drop is roughly a factor of 2.0 lower for the static test than it was for the impact tests. The inertial stiffening effect continues to become yet more pronounced than in the thinner facesheets.

All the trends observed in the 32-ply data continue in the 48-ply data (figure 25). The static test shows the first major load drop near 10500 N while the impact tests show it greater than 13000 N. The magnitude of the load drop is roughly a factor of 1.5 lower for the static test than it is for the impact tests.

A general statement about the influence of facesheet thickness on the dynamics of the impact event can now be made. The load versus displacement curves of the static and dynamic tests compare better for thin facesheets than for thick ones. Thus, increasing the facesheet thickness makes the dynamics of impact more important. This is expected because the additional mass of the thicker facesheets increases the inertia of the specimens.

3.4.4.2 *C-scans*. No information about the physical effect of the damage processes is available from a load versus displacement curve. In order to obtain such information, after impact or static indentation, all specimens were ultrasonically inspected for damage using the time-of-flight C-scan technique. The images thus produced show delamination patterns and can be used to qualitatively compare damages from different events. Figure 26 shows a direct comparison of C-scans for static and impact events. The events were chosen for that comparison based upon a similarity in the load histories. In particular, the impact events were performed first and the lowest energy event that showed a major load drop was chosen. For these events the load histories are identified as 0.34 J, 0.47 J, 1.35 J, 5.24 J, and 10.08 J respectively in figures 10 through 14. The static events were created specifically for this comparison based on a similar criteria, that is, the crosshead displacement was slowly increased until the first major drop in load was observed and then the crosshead displacement was slowly decreased. The comparison of static and dynamic impact damages shown in figure 26 then, is not based on equivalent peak loads. The conventional wisdom that, "equivalent peak loads produce equivalent damage," was not validated by this research. The equivalence found in this research is based on load drops rather than peak loads, so the static and dynamic data associated with the first major load drop are compared in figure 26.

The shades in the C-scans of figure 26 indicate the depths (distance from the top surface) of the delaminations present in the specimens after impact. The scales relating shade to delamination depth are different for each scan, so shades should not be compared between scans. The shades are shown to give the overall perspective that delaminations are occurring at different depths and that the delaminations become larger in the deeper interfaces. The shades also allow a better view of the in-plane shapes of the delaminations. The C-scans in figure 26 show some similarity between the damage associated with the first major load drop in a static test and the damage associated with the first major load drop in a dynamic test. This similarity can be seen in figure 26 by comparing the overall sizes and shapes of the delaminations. The similarity is present for all facesheet thicknesses tested. In particular, the overall size of the deepest and shallowest delaminations, the number of interfaces (different colors) found to have delaminations, and the general shape of the delamination pattern all compare well between static and dynamic data.

If a comparison were made of C-scans of statically and dynamically loaded plates with similar peak loads, a very different story would be obtained. The essence of the difference is that the dynamically loaded plates reached a higher peak load before failure. Thus, dynamic events reaching the same peak loads as the static events of figure 26, show no delaminations in the C-scans. Alternatively, however, static events reaching the same peak loads as the dynamic events of figure 26, show delaminations similar to those of figure 26. Peak load, then, is not an appropriate equivalence between the static indentation and dynamic impact events for composite sandwich plates since two specimens loaded to the same peak load (one impact, the other static) may or may not show similar damages. This indicates that quasi-static analysis and testing in which peak load is compared with the peak load from a dynamic event, may indicate failure at a lower peak load than an actual impact event would find.

Comparison of the C-scans in figure 26 might lead one to conclude that there are both similarities and differences between the static and dynamic delamination fields. A word of caution is appropriate here. At best, the general shapes (hour glass and crossed hour glasses) and gross size of the delamination patterns of the 4- and 8-ply data are repeatable. There is also a good deal of randomness in the patterns observed. This randomness can be seen in figure 26 when one considers the fact that all loads, material properties, and boundary conditions possessed bilateral symmetry while the delamination patterns deviate from this symmetry somewhat. Less can be said for the thicker facesheet specimens. For the thicker facesheet specimens, the gross size may be repeatable and the general feature of delaminations becoming wider as the depth increases is characteristic of all of the data, but to try to compare shade by shade and shape by shape is asking too much of these data. The purpose of figure 26 is to show overall similarity of delamination patterns and sizes for static indentation and dynamic impact loaded composite sandwich plates. Meaningful comparisons stop there.

3.4.4.3 *Photomicrographs*. Neither core failure nor matrix cracking are generally observable by C-scan. In order to observe these damage mechanisms a representative portion of the specimens were sectioned, and observed under an optical microscope. A typical photomicrograph is shown in figure 27. Crushing of three of the five honeycomb core cell walls is evident as are multiple delaminations and transverse matrix cracks. As observed elsewhere[1], the termination of transverse matrix cracks at the interfaces between plies of differing orientations appears to be associated with delaminations at those interfaces.

4. CONCLUSIONS

Minimizing the tup mass ratio is shown to significantly improve the temporal fidelity of the load data produced by an instrumented impactor test system. Corrected absorbed energy seems to indicate damage. Figures 10 through 14 demonstrate a jump in absorbed energy at the impact energy that initiates damage. It is possible to confirm that there is failure within a composite sandwich plate subjected to low-velocity impact by an instrumented impactor without relying on post-impact inspection of the specimen. Thick and damaged sandwiches are not quasi-static. The assumption that low-velocity impact damage within a composite sandwich plate is independent of the loading rate does not appear to be valid in these cases. The static and dynamic events differ significantly in the load at which the first major load drop occurs and the energy that is absorbed in the damage process associated with the first major load drop. Important damage information may be obtained from force history. For the range of parameters in this study, the first major load drop observed in the load history is associated with core failure.

ACKNOWLEDGEMENT

This work was sposored by Willian Baron of the Flight Dynamics Directorate of Wright Laboratories.

REFERENCES

1. Harrington, T. M., *An Experimental Investigation of Sandwich Panels Under Low Velocity Impact*, MS thesis, AFIT/GAE/ENY/94D-22. School of Engineering, Air Force Institute of Technology (AU), Wright-Patterson AFB OH, (1994)

2. Choi, I. H., & Hong, C. S., New Approach for Simple Prediction of Impact Force History on Composite Laminates, *AIAA J.* **32** (1994) 2067-72.

3. Schoeppner, G. A., *Damage in Graphite/Epoxy Plates Subjected to Low Velocity Impact, 1988 USAF-UES Summer Faculty Research Program / Graduate Student Summer Support Program - Final Report.* (1988)

4. Herup, E. J., *Low-Velocity Impact on Composite Sandwich Plates*, Ph.D. dissertation, AFIT/DS/ENY/96-11. School of Engineering, Air Force Institute of Technology (AU), Wright-Patterson AFB OH, (1996)

5. Abrate, S., Impact On Laminated Composite Materials, *Applied Mechanics Reviews*, Vol. 44, No. 4 (1991) 155-190.

6. Zhong, Z.-H., and Mackerle, J., Contact-Impact Problems: A Review With Bibliography, *Applied Mechanics Reviews*, Vol. 47, No. 2 (1994) 55-76.

7. Cantwell, W.J., and Morton, J., The Impact Resistance Of Composite Materials - A Review, *Composites*, Vol. 22 (1991) 347-362.

8. Nahas, M.N. Survey Of Failure And Post-Failure Theories Of Laminated Fiber-Reinforced Composites, *Journal of Composites Technology & Research*, Vol. 8, No. 4 (1986) 138-153.

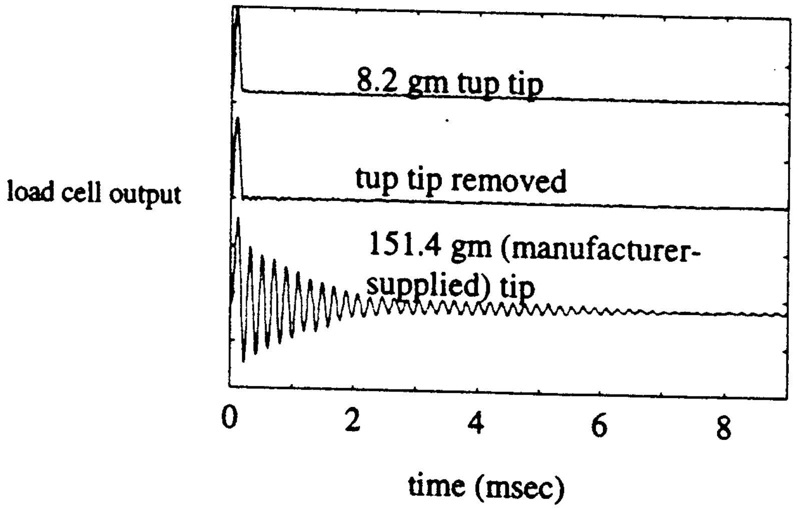

Fig. 1. Impulse response of instrumented impactor showing effect of tup tip mass.

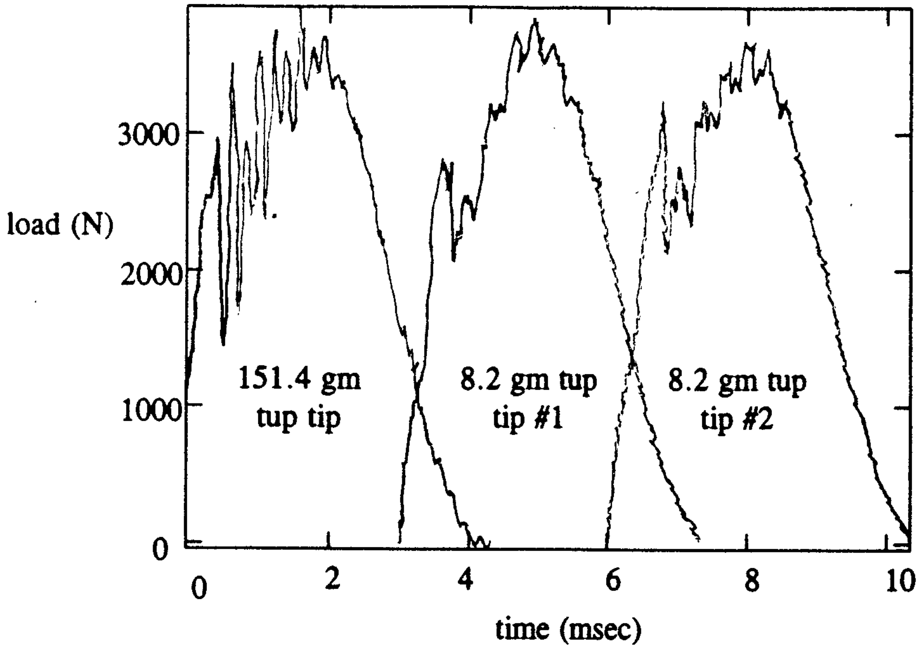

Fig. 2. Typical load histories showing effect of tup tip mass.

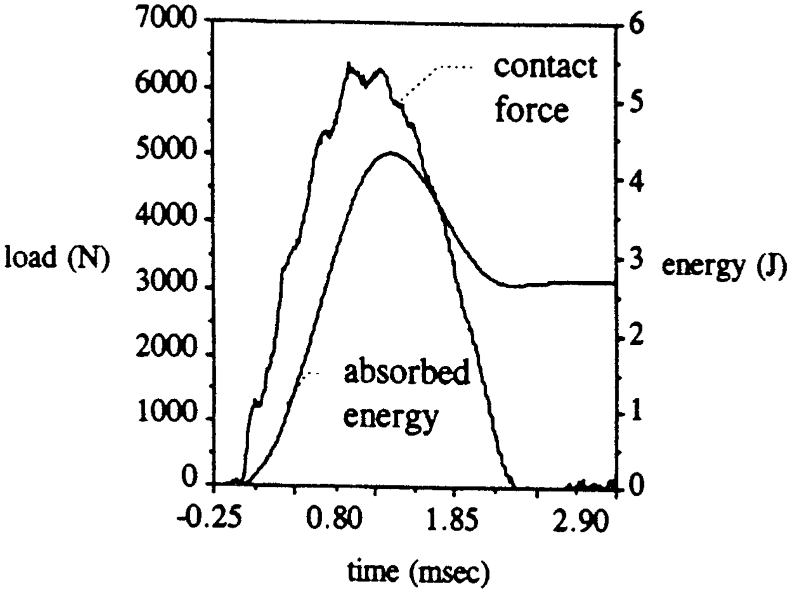

Fig. 3. Typical force and energy histories for an event without damage.[1]

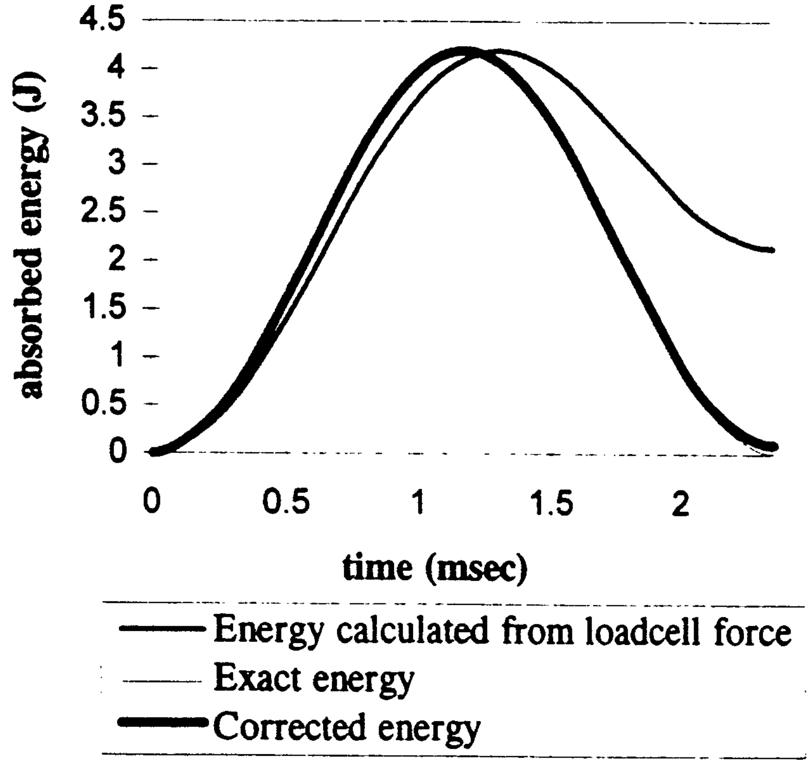

Fig. 4. Instrumented impactor model calculated and corrected energy histories.

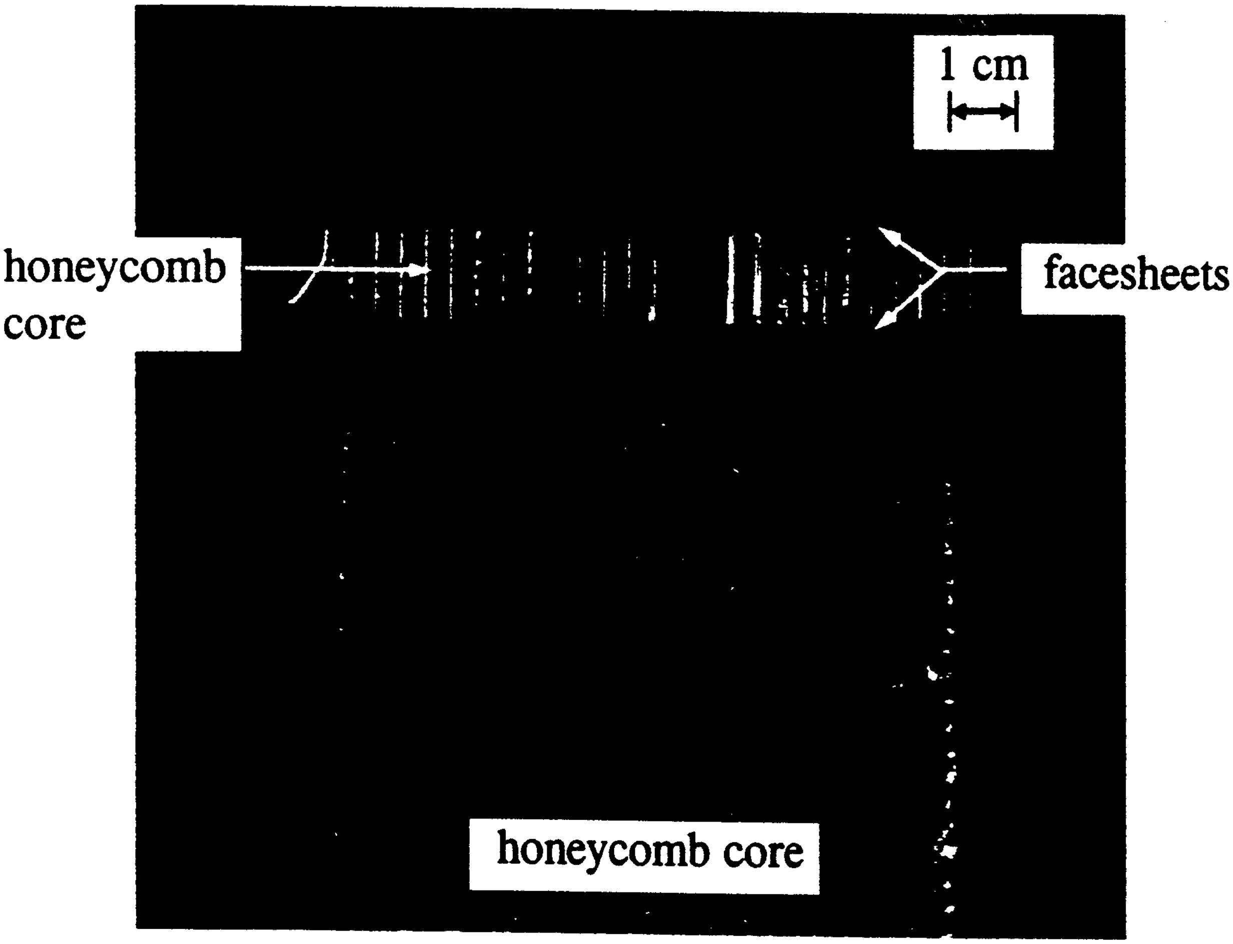
1 cm
honeycomb core
facesheets
honeycomb core

Fig. 5. 16-ply composite sandwich plate and Nomex honeycomb core.

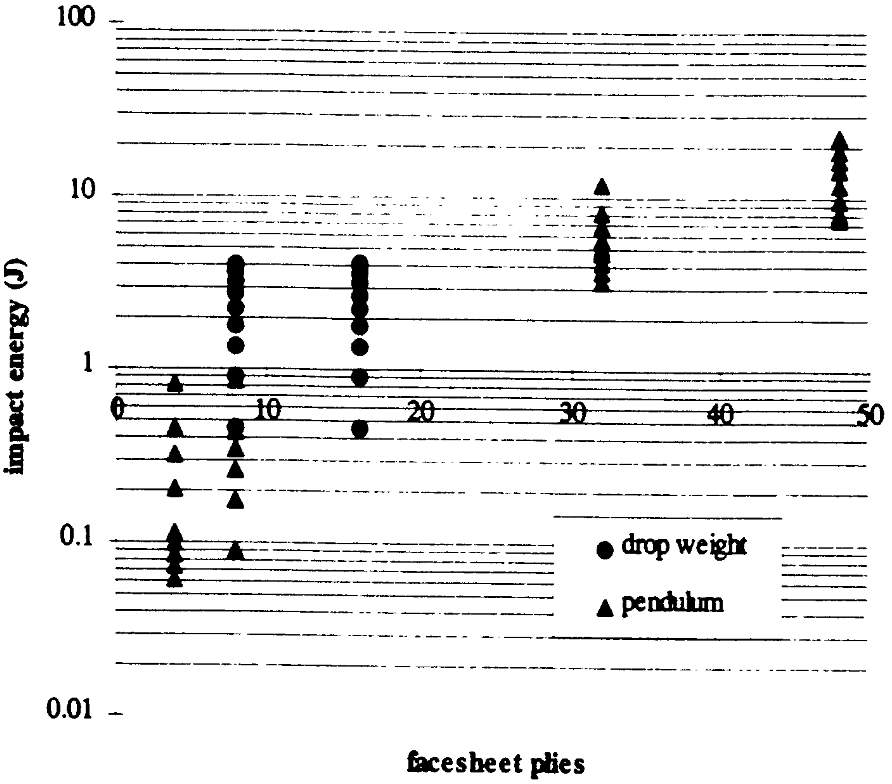

Fig. 6. Impact test matrix.

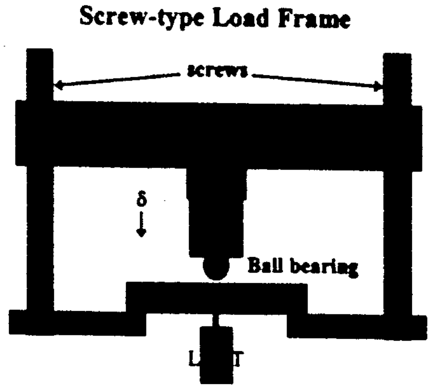
Screw-type Load Frame
screws
δ
Ball bearing
LVDT

Fig. 7. Schematic of static indentation test system. (The direction of the applied displacement is shown by δ).

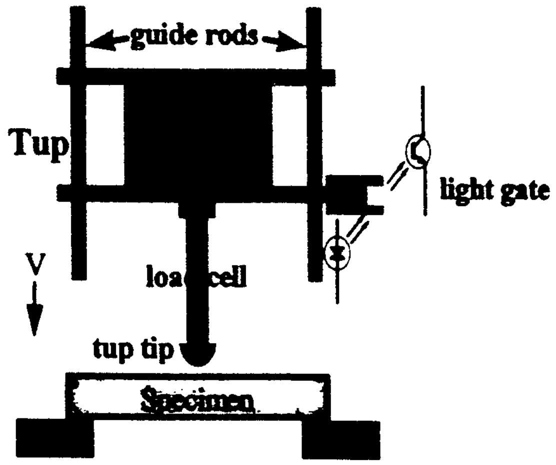
guide rods
Tup
light gate
V
load cell
tup tip
Specimen

Fig. 8. Schematic of commercial drop weight impact test system.

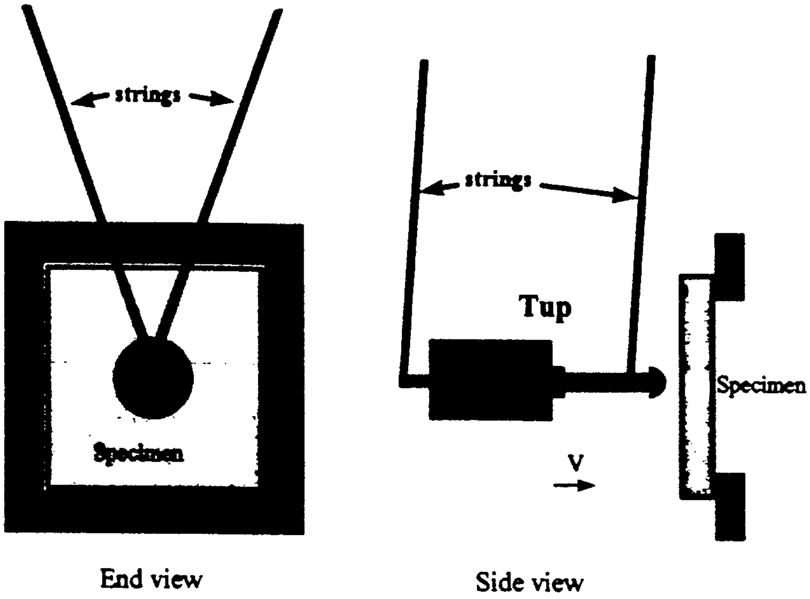
strings
Specimen
End view
strings
Tup
Specimen
V
Side view

Fig. 9. Schematic of pendulum impact test system.

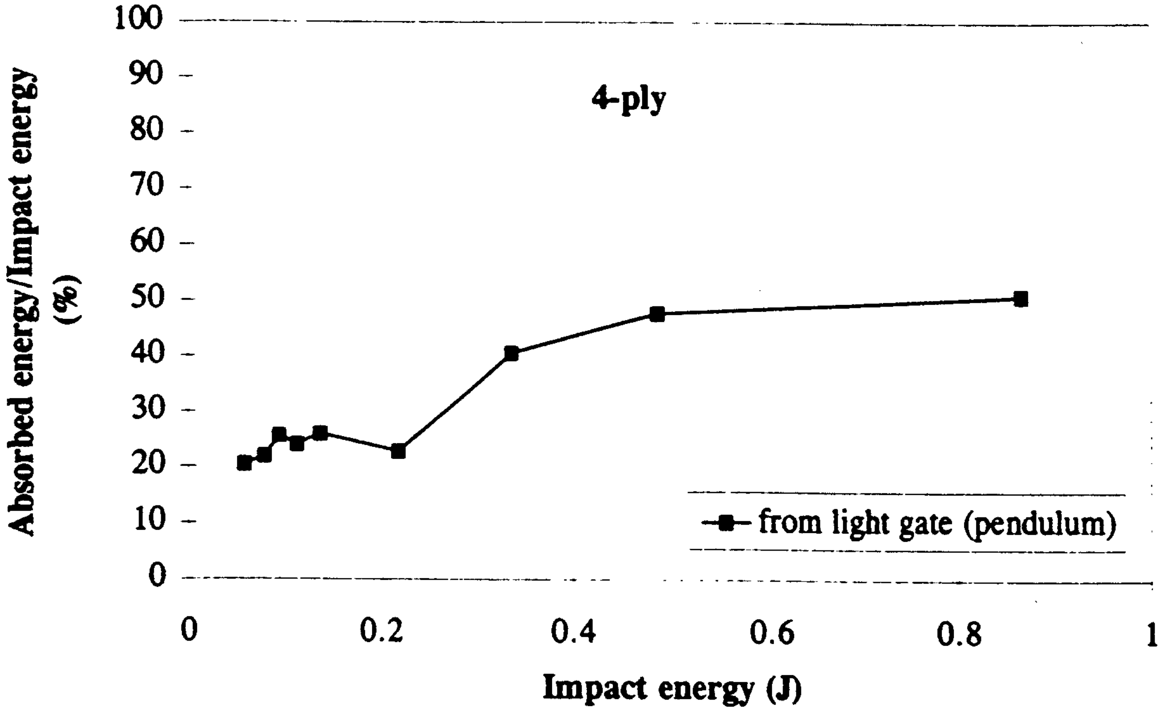

Fig. 10. 4-ply Absorbed energy versus impact energy showing threshold near 0.3 J. Pendulum data only.

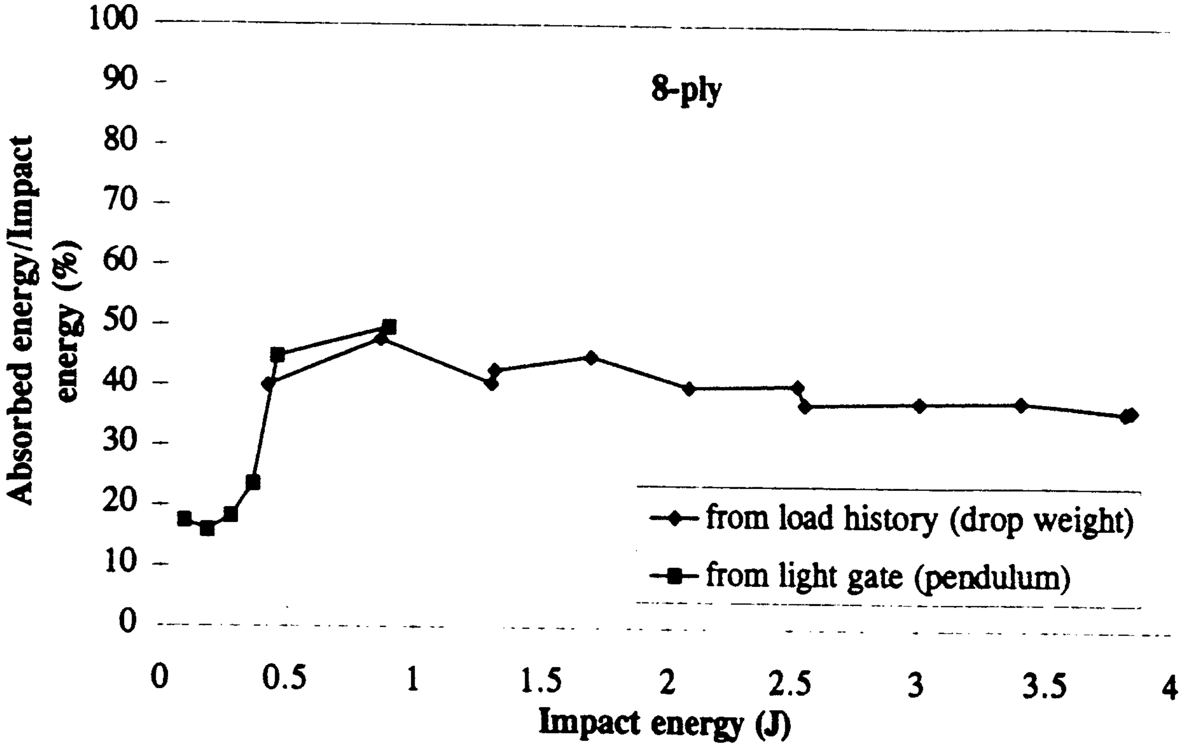

Fig. 11. 8-ply Absorbed energy versus impact energy showing threshold near 0.45 J. Pendulum and drop weight data.

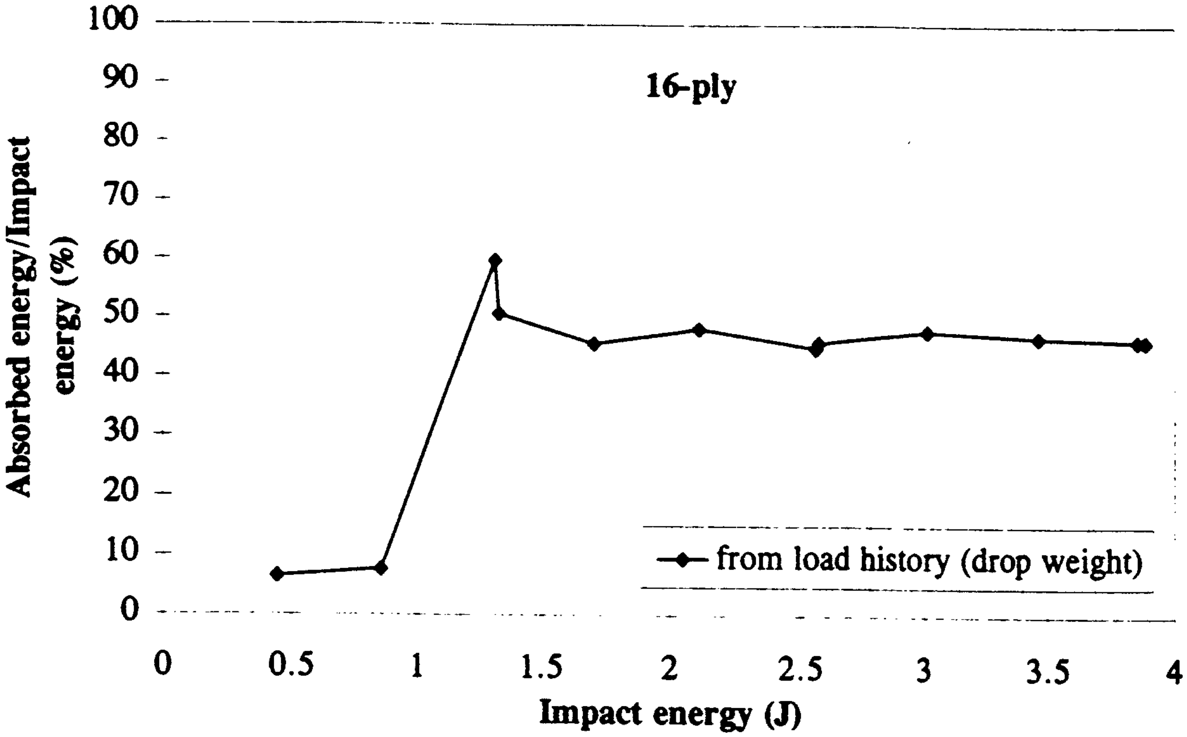

Fig. 12. 16-ply Absorbed energy versus impact energy showing threshold near 1.0 J. Drop weight data only.

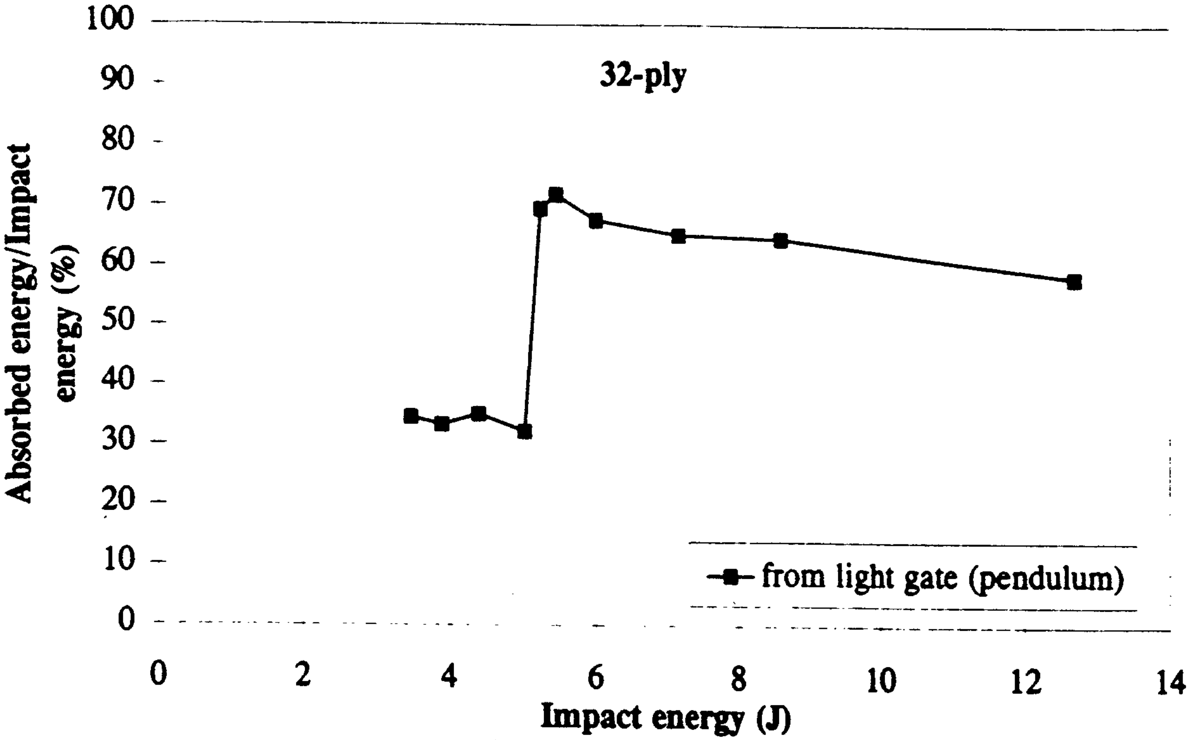

Fig. 13. 32-ply Absorbed energy versus impact energy showing threshold near 5.1 J. Pendulum data only.

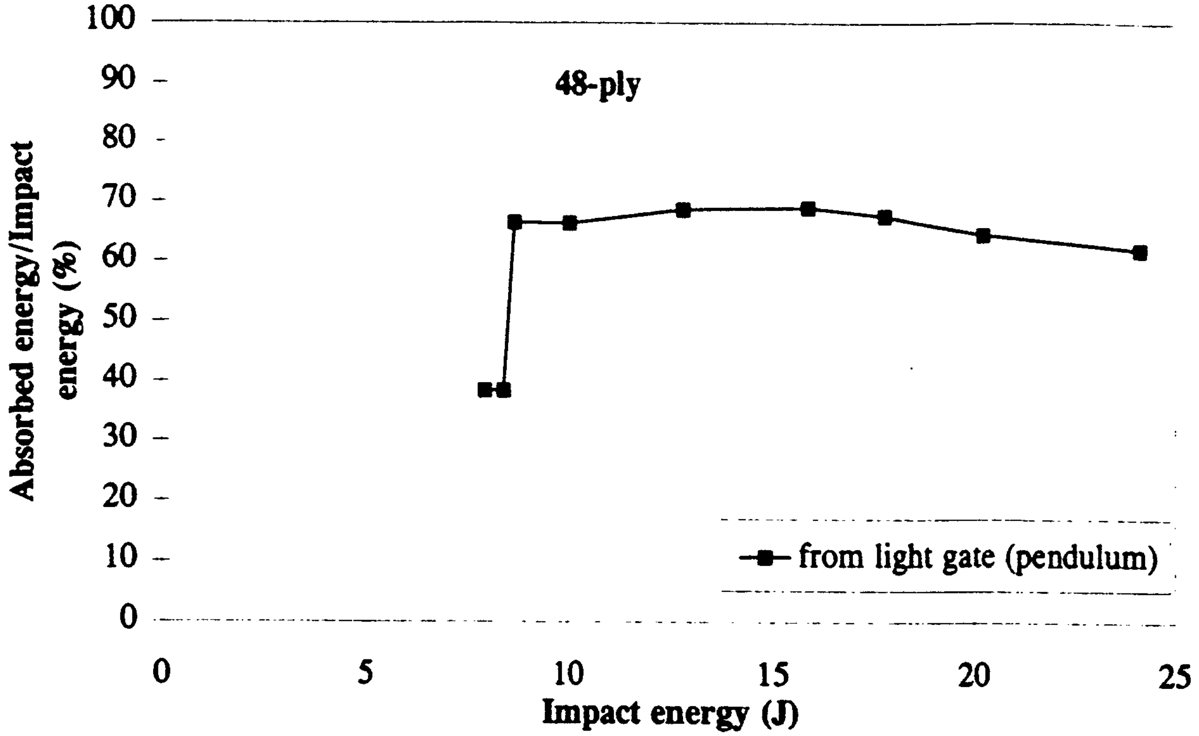

Fig. 14. 48-ply Absorbed energy versus impact energy showing threshold near 8.5 J. Pendulum data only.

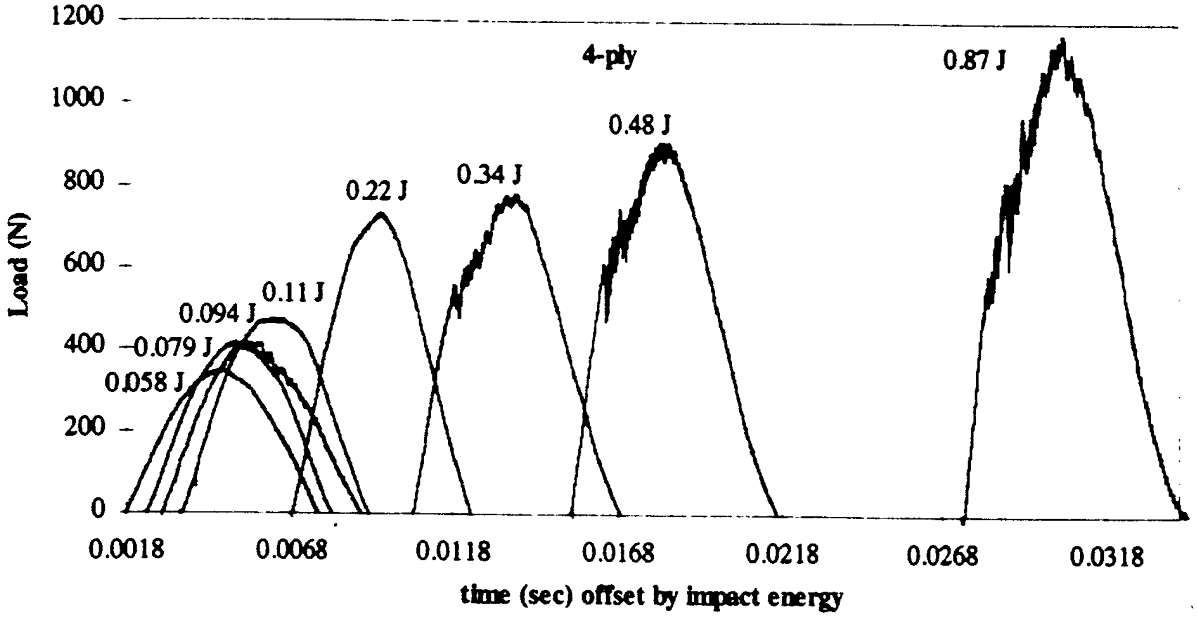

Fig. 15. 4-ply force histories offset by impact energy showing possible damage initiation near 400 N in the 0.094 J event while first major load drop does not occur until near 550 N in the > 0.3 J events. Pendulum data only.

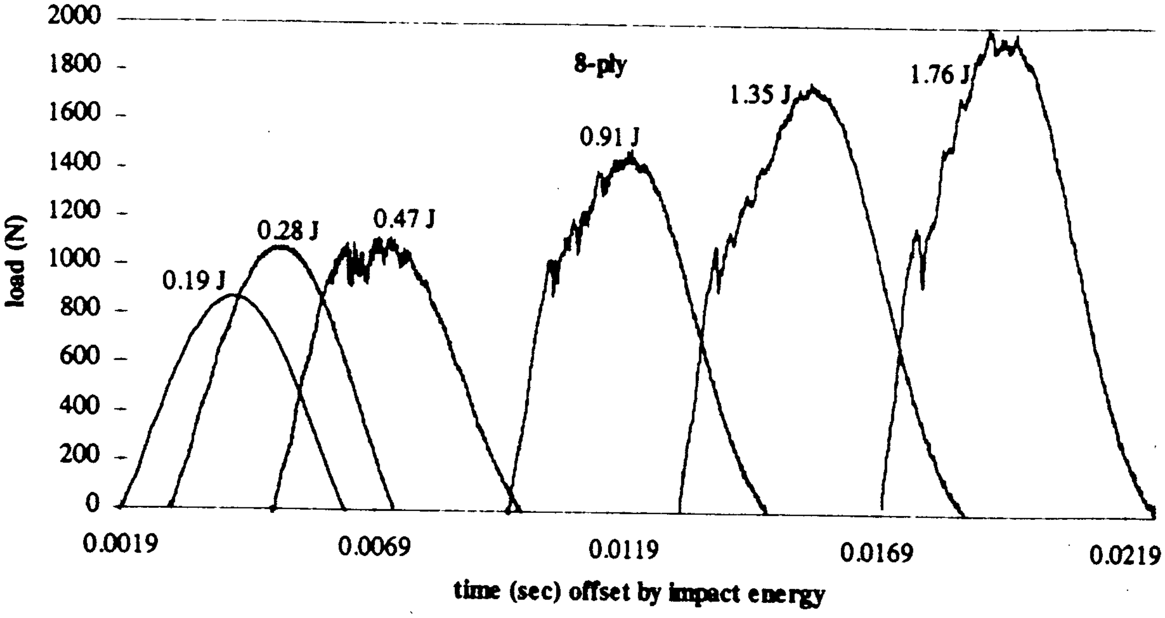

Fig. 16. 8-ply force histories offset by impact energy showing possible damage initiation near 1000 N in the 0.47 J event while first major load drop does not occur until near 1100 N in the > 0.4 J events. Pendulum (<1 J) and drop weight (> 1 J) data.

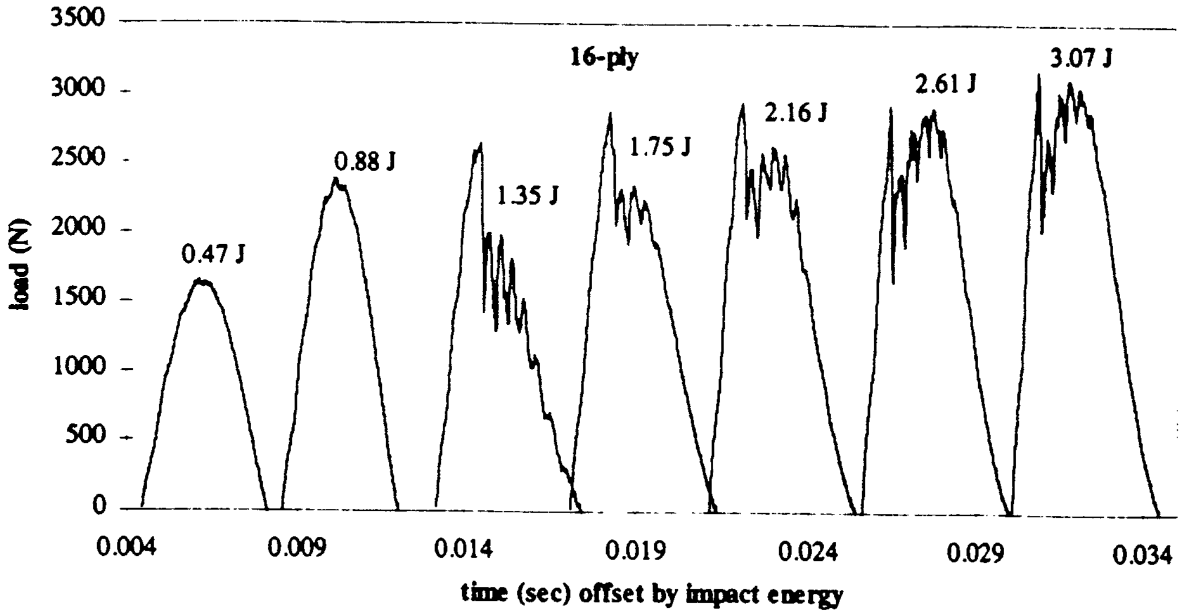

Fig. 17. 16-ply force histories offset by impact energy showing damage initiation near 2700 N in the impact energy > 1.3 J events. Drop weight data.

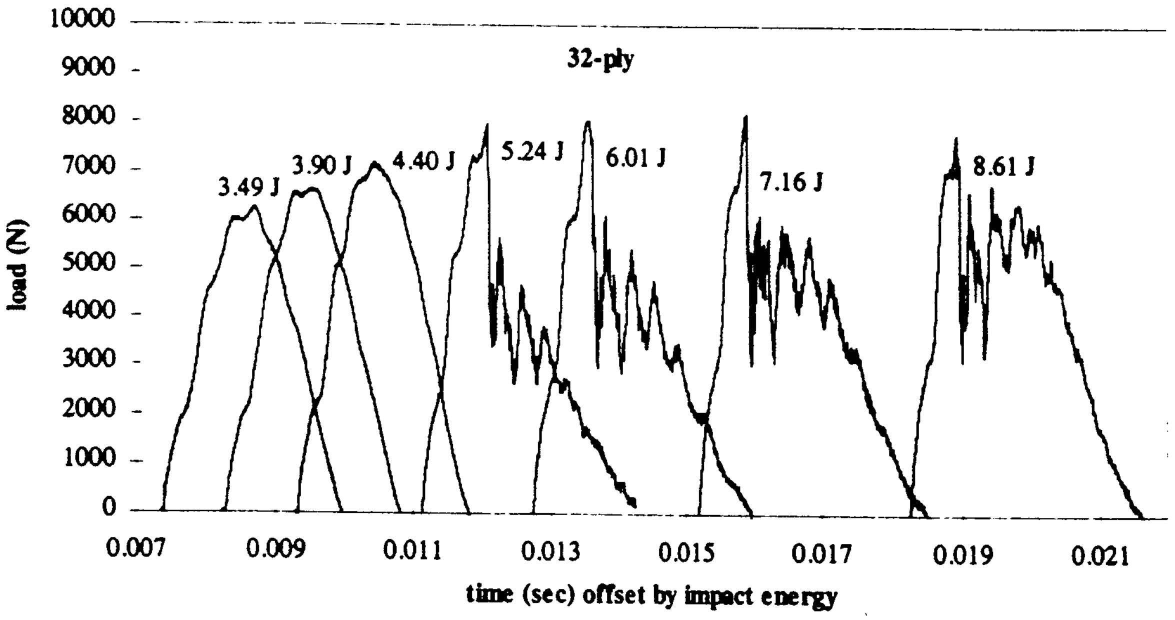

Fig. 18. 32-ply force histories offset by impact energy showing damage initiation near 8000 N in the impact energy > 5.2 J events. Pendulum data.

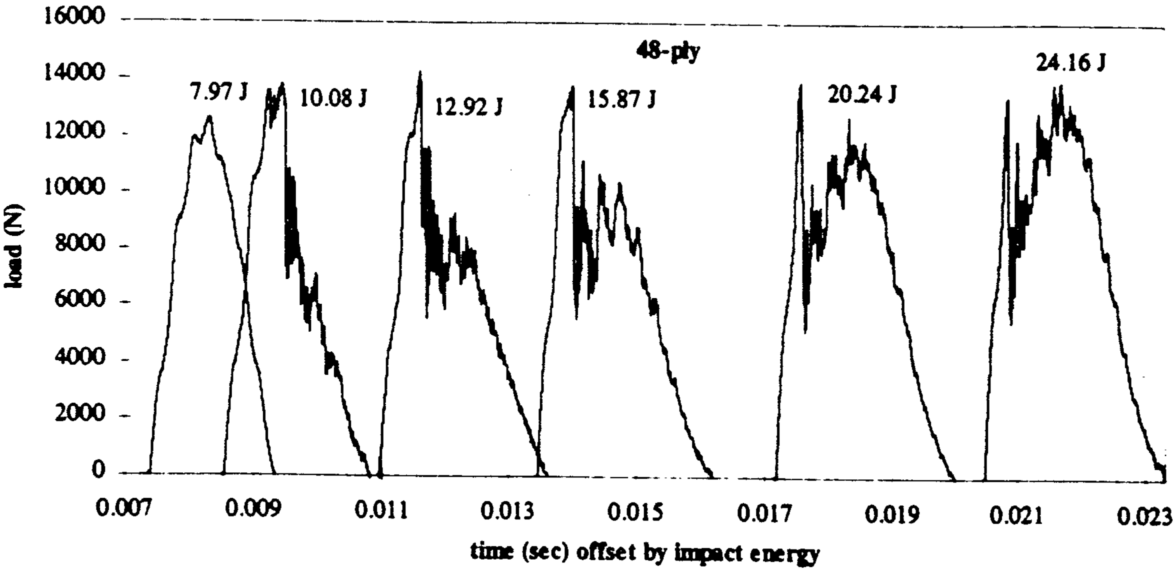

Fig. 19. 48-ply force histories offset by impact energy showing damage initiation near 14000 N in the impact energy > 10.0 J events. Pendulum data.

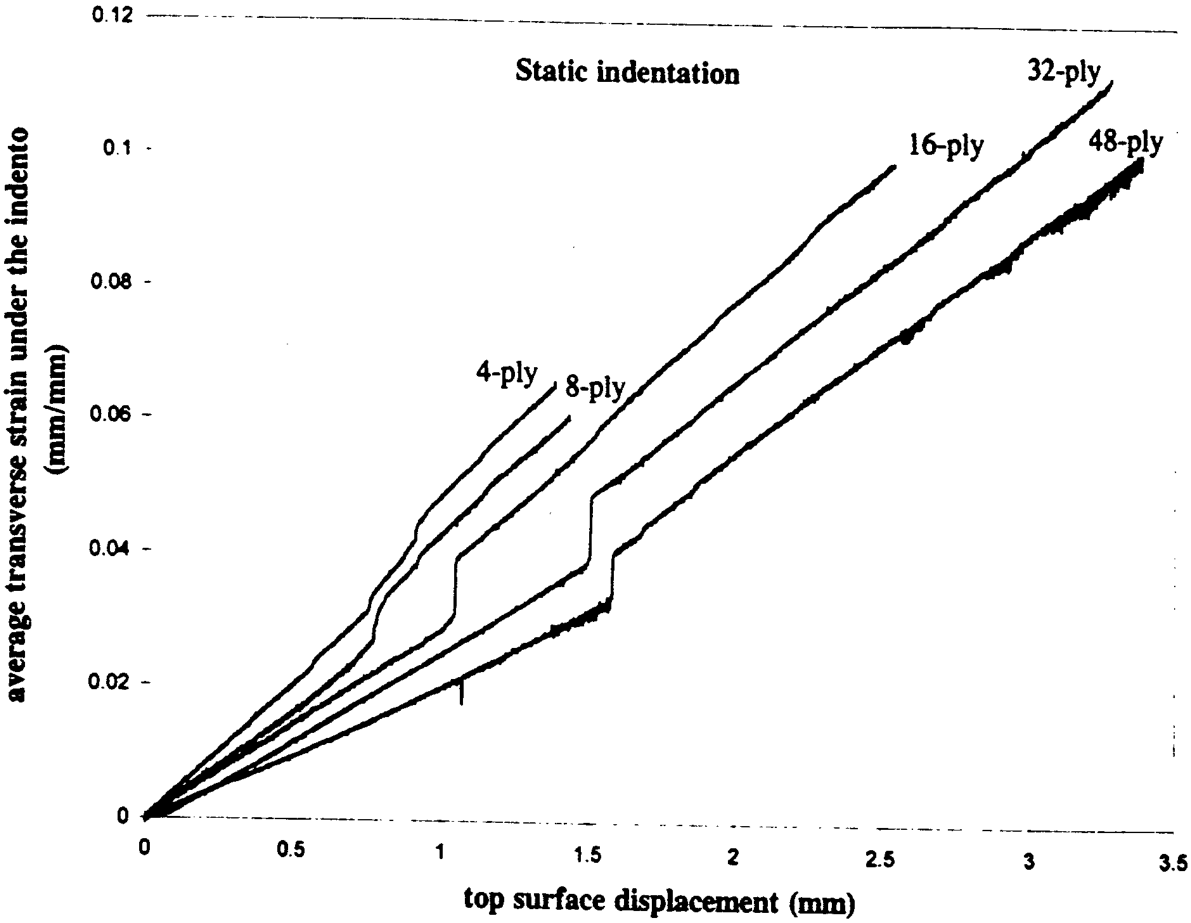

Fig. 20. Transverse strain verses displacement for static indentation showing strain jumps presumed to be indicative of multiple cell core failure.

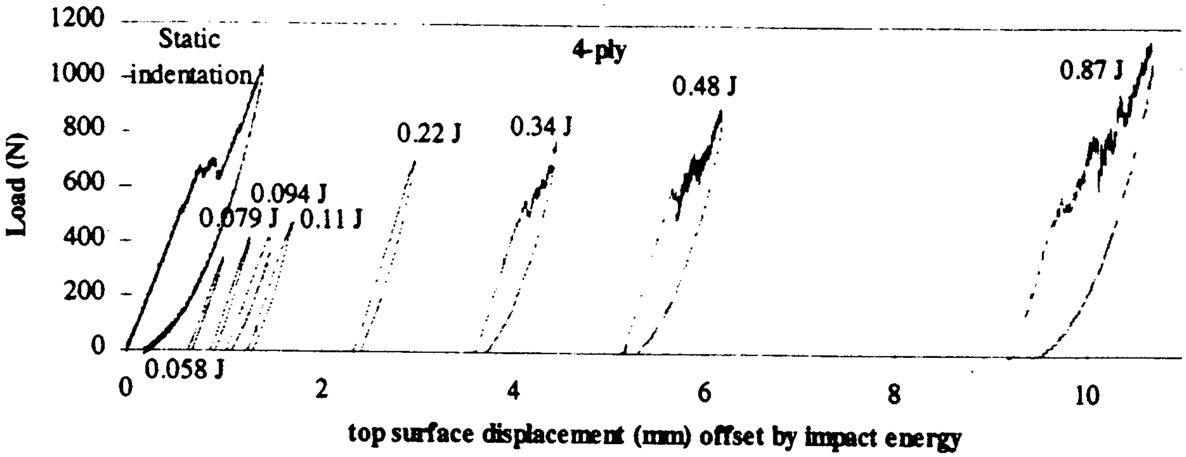

Fig. 21. 4-ply static and dynamic force verses displacement showing the effects of damage.

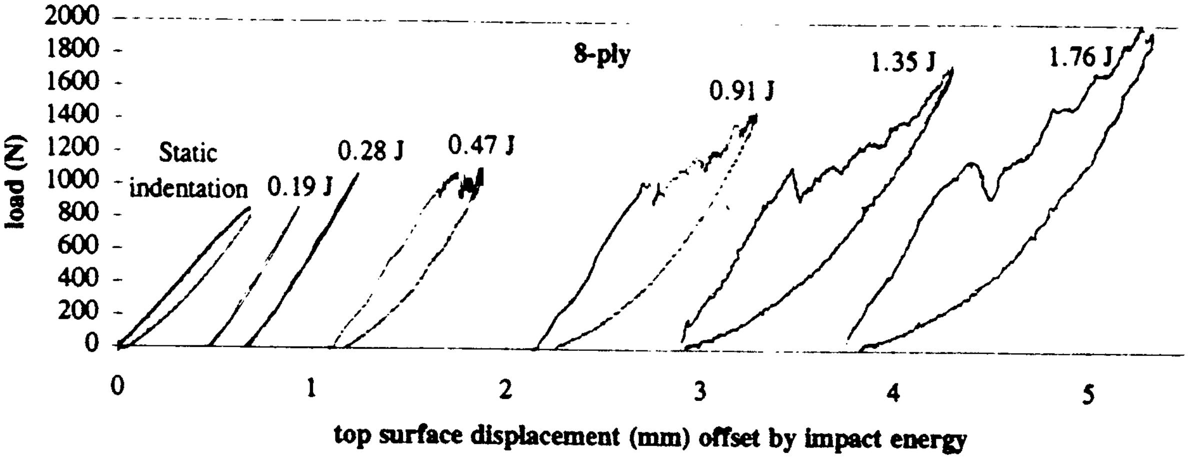

Fig. 22. 8-ply static and dynamic force verses displacement showing the effects of damage.

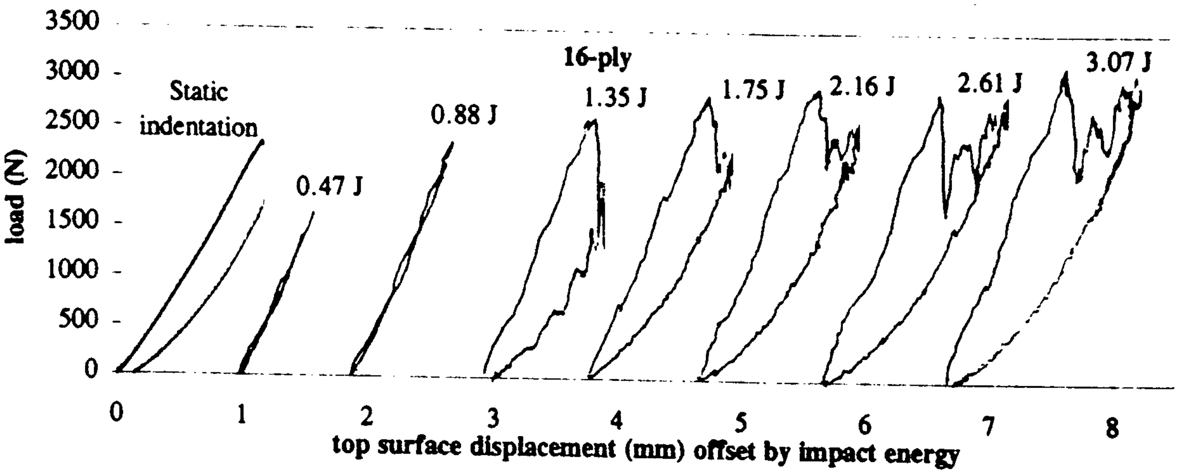

Fig. 23. 16-ply static and dynamic force verses displacement showing the effects of damage.

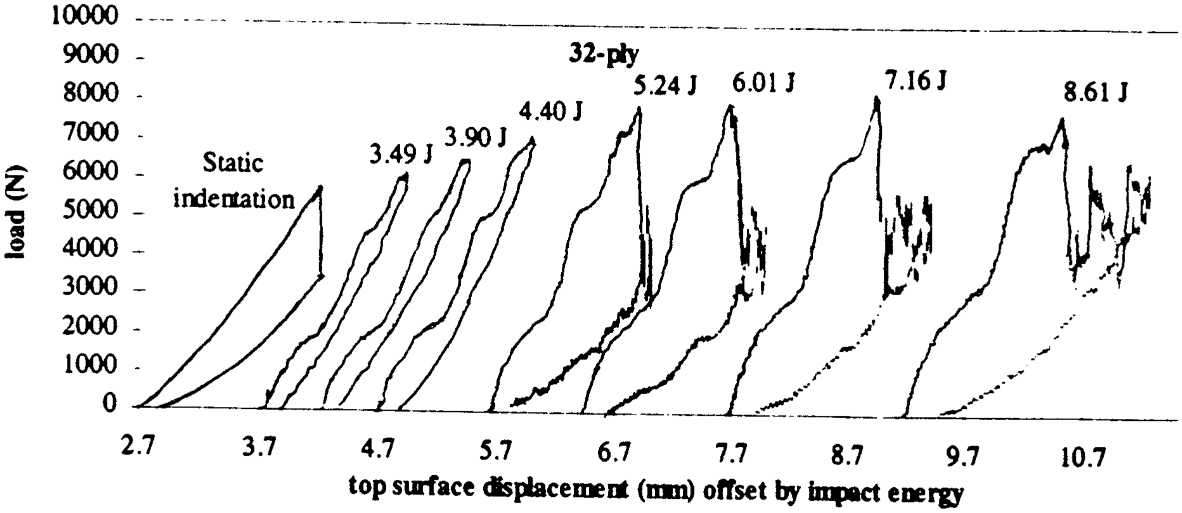

Fig. 24. 32-ply static and dynamic force verses displacement showing the effects of damage.

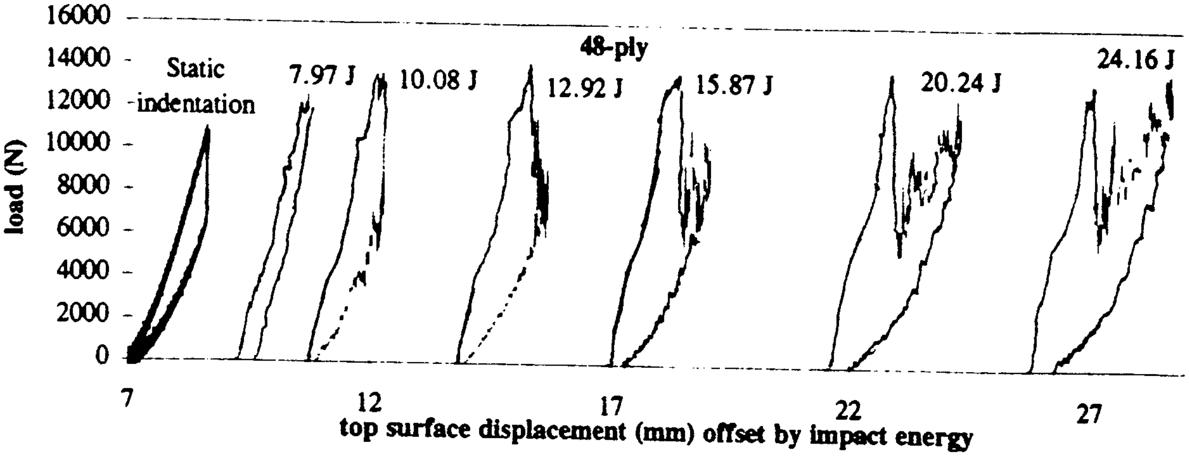

Fig. 25. 48-ply static and dynamic force verses displacement showing the effects of damage.

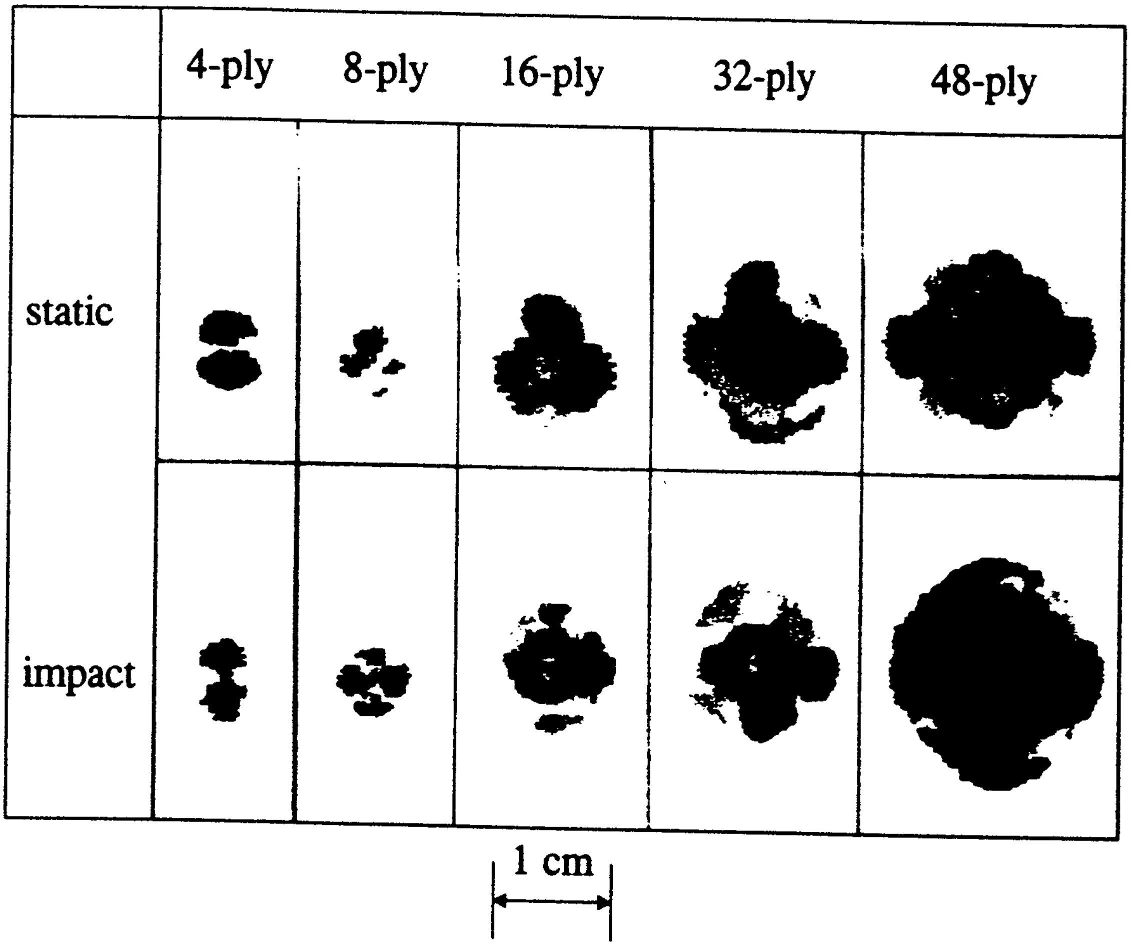
4-ply
8-ply
16-ply
32-ply
48-ply
static
impact
1 cm

Fig. 26. C-scans for static and dynamic events found to exhibit the first major load drop.

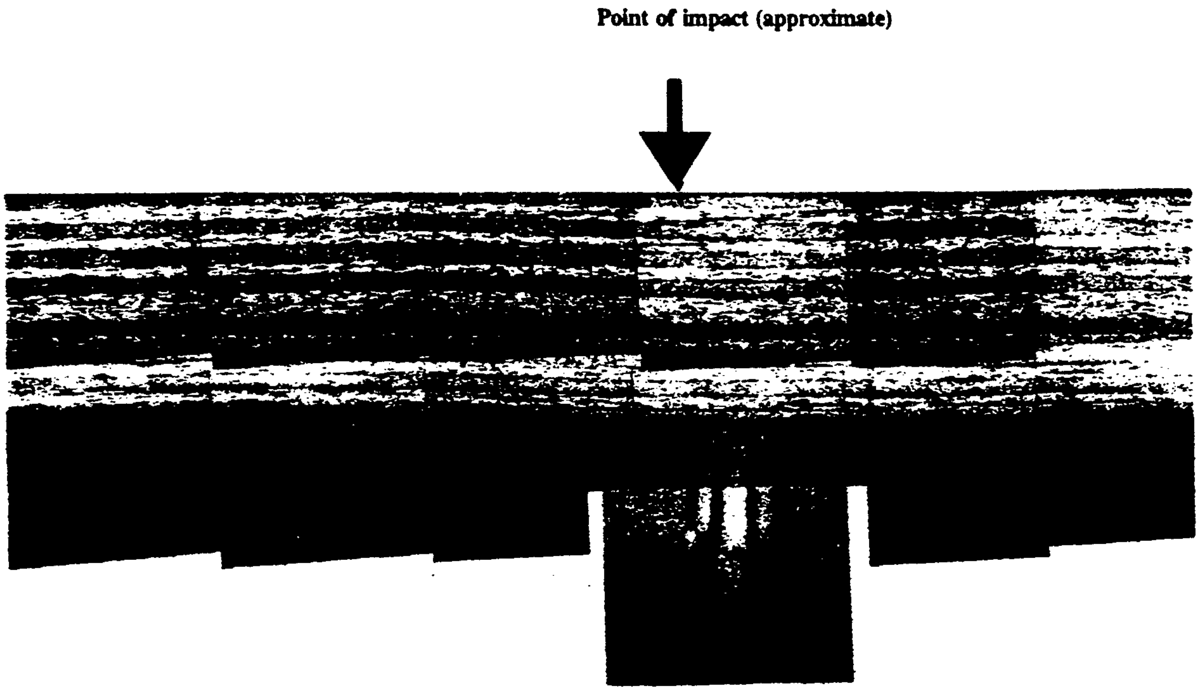
Point of impact (approximate)

Fig. 27. Photomicrograph of the top facesheet of a 16-ply specimen after 1.35 joule impact. The plane of the paper is perpendicular to the laminate 0° axis.

ATTACHMENT II

LOW VELOCITY IMPACT DAMAGE CHARACTERISTICS OF Z-FIBER REINFORCED SANDWICH PANELS - AN EXPERIMENTAL STUDY

LOW VELOCITY IMPACT DAMAGE CHARACTERISTICS OF Z - FIBER REINFORCED SANDWICH PANELS - AN EXPERIMENTAL STUDY

A.N. Palazotto [*] L.N.B. Gummadi [†] U.K. Vaidya [‡] and E.J. Herup [§]
Department of Aeronautics and Astronautics
Air Force Institute of Technology
WPAFB, OH-45433

Abstract

Experimental results related to the initiation of damage in Z - fiber truss reinforced sandwich panels are presented. Two different orientations of pin angles are considered. A pendulum type impactor is used to impart very low levels of impact energy. Threshold energy levels at which the observable damage initiation occurs are determined. Nondestructive evaluation studies conducted prior to the impact are compared with the post impact status of the panels for assessing the type and magnitude of the damage. Effects specific to the impact phenomena are studied by comparing the load displacement characteristics.

Introduction

Composite materials made of sandwich construction are being increasingly used in various aerospace applications. Some of the advantages of using sandwich materials when compared to the conventional materials include high specific modulus, high specific strength and the ability to tailor to the requirements. Typically, a composite sandwich material consist of stiff face sheets, primarily for resisting flexural bending and a core for transferring the shear and transverse compression loads. In general, the material used for the core is light of weight and weak in flexural stiffness, but provides significant shear stiffness. Conventional materials used for the core include honeycomb and foam and each has been investigated extensively.

A newly developed concept of a truss reinforced core [1-2] has entered the market place in the recent years. This concept involves the replacement of a conventional foam core with either a truss reinforced core or truss reinforced hollow core. Details of the construction of the core can be found in Ref. 1. The general idea is based on inserting high strength and stiffness pins into a sandwich panel, either to replace the existing core or to supplement the core. These pins act as trusses transmitting forces through out the sandwich and provide the required structural integrity. If the space between the pins is filled with foam or honeycomb, the filler material will provide a higher pin stability. On the other hand, leaving the core space between the pins empty can provide space for fuel storage, among other things. Both types of sandwich constructions offers better delamination growth control when compared with other sandwich type constructions[1].

These materials are prone to many types of damages, such as pin compression failure, pin buckling, pin pull out from the face sheet etc(pin related failure modes), delaminations, debonding etc (face sheet related failure modes). All or some of these damage modes can be severe under low velocity conditions, which is a most common occurrence in the life span

---

[*] Professor, Associate Fellow AIAA, Fellow ASCE

[†] Research Associate, Member, AIAA

[‡] Assistant Professor, Tuskegee University, Member ASME

[§] Ph.D. Candidate, Student Member AIAA

This paper is a declared work of the U.S. Government and is not subject to copyright protection in the United States.

of the material. Experimental study of the various damage modes due to low velocity impact events. and the energy required for the initiation of these damage modes is the main focus of this paper.

In this experimental study, sandwich plates are composed of graphite epoxy face sheets and steel fiber pins for the core. Two orientations of pin angle (10 and 20 degrees) are considered in which the volume of the pins per unit plate area is kept constant. Face plates consist of 16 layers of symmetric orientation. The sandwich plates are impacted by pendulum type impactors with a hemispherical nose (tup). Contact force is monitored through out the impact event using an instrumented impactor. Before the impact event, a sampling of the specimens were evaluated using ultrasonic c-scan in order to check for various defects. After impact loading, the specimens are inspected nondestructively for the presence of various damage modes and their extent. Impact energy associated with damage modes is discussed.

Specimen and Method

Specimens used in this experimental investigation consisted of two face sheets each of orientation $[0/45/90/\text{-}45]_{2S}$ made up of graphite epoxy material. The pins used as core are made of steel and are of 0.508 mm in diameter. Foster Miller Inc provided three plates of 10 degree pin orientation and three plates of 20 degree pin orientation, each of size 254 mm X 254 mm. Orientation of the pin angle is measured from the vertical axis (as shown in Figs 1-3).Each plate is cut into 4 specimens of 10.16 mm X 10.16 mm dimension. The remaining plate material is used to gain initial insight into the types of damage modes and the energy levels associated. All these specimens are restrained in a 20.32 mm X 20.32 mm fixture providing near simple support on all edges of the 7.62 mm X 7.62 mm effective specimen size.

An instrumented pendulum testing system is used for all the experimentation. Past experience[3-6] with various impact testing systems resulted in the selection of this testing system as it is possible to impart very low impact energies. Impact energies of less than 0.5 Joule are expected to initiate the damage in the considered specimens. A picture of the pendulum set up used is shown in Figure 4 and a a schematic of

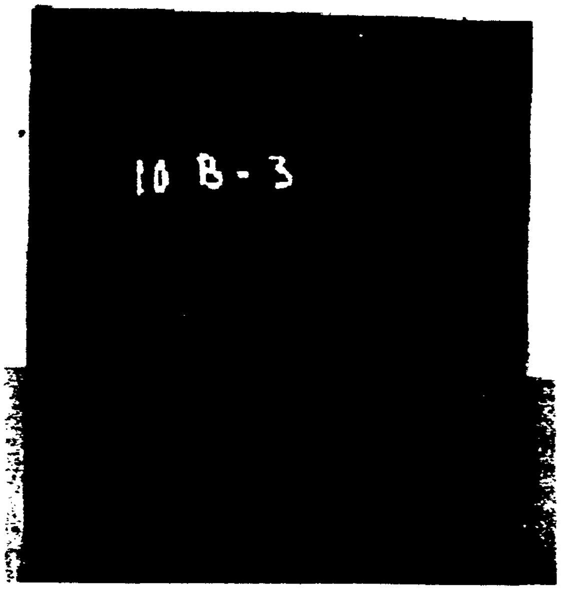

Figure 1: Top view for the z-pin sandwich construction

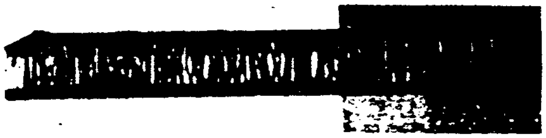

Figure 2: Side view for the z-pin sandwich construction

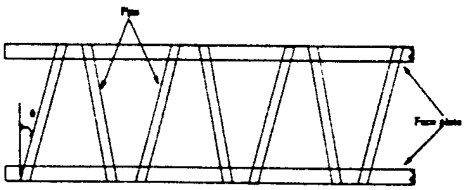

Figure 3: Schematic of Side view for the z-pin sandwich construction

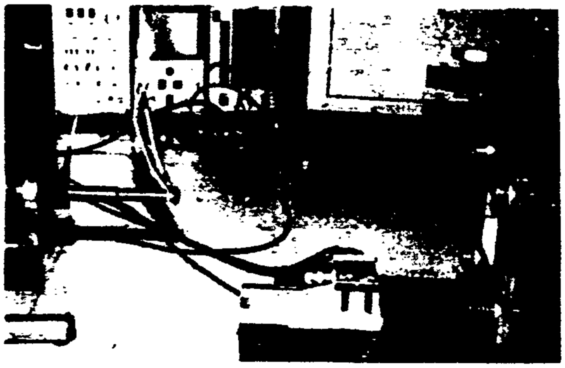

Figure 4: A Pendulum test set up

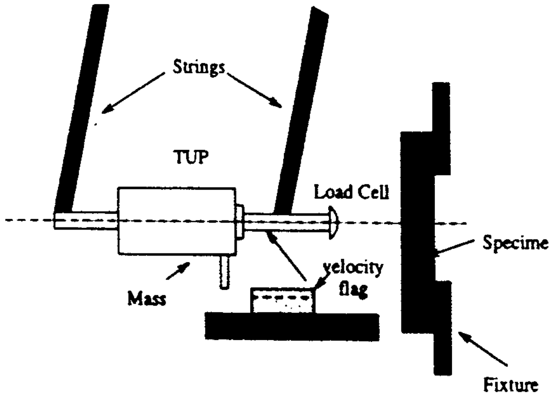

Figure 5: Schematic for the pendulum test set up

the system is shown in Fig 5. The pendulum consist of 15 KN load cell with a 1.27 cm radius nose. Impact energy is regulated by means of the swing of the pendulum and resolved by measuring the mass of the pendulum and its velocity just prior to impact. A digital oscilloscope is used to record the force data from the experiment at 5 μsec intervals. Mass of the pendulum used in the experiments is 3.48 kg. No specimens are impacted more than once. All the specimens are visually and ultrasonically inspected after impact to determine the existence of the damage in the form of crushing failure at the surface under the tup, interply delamination in the top face sheet, buckling or compression failure of the pins, pull out or push up of the pins from the facesheet. Several specimens were sectioned and photomicrographed after C-scanning to reveal the through the thickness distribution of delaminations and matrix cracking.

Results and Discussions

Results obtained from these experimental studies are discussed in two parts. In the first part, results obtained from the low velocity impact experiment, in the form of load deflection curves etc are discussed. The energy levels, at which the damage initiates, are determined. In the second part of this section, specimens are analyzed using nondestructive evaluation techniques.

The Force - Time histories of load levels are shown in Figure 6 for 10 degree pin orientation and in Fig 7 for 20 degree orientation. Newton's second law related to impulse and momentum for the tup is integrated to calculate velocity as a function of time. The tup velocity, $V(t)$ is determined from the contact force as

$$V(t) = V(0) - \frac{1}{m}\int_0^t F(\tau)d\tau \qquad (1)$$

Here $V(0)$ is the initial impact velocity of the tup which is a measured quantity and m is the mass of the tup. Based on the velocity calculation, displacement is determined by again numerically integrating with respect to time. The displacement as a function of time $\delta(t)$ can be written as

$$\delta(t) = \int_0^t V(\tau)d\tau + \delta(0) \qquad (2)$$

Here $\delta(0)$ is the initial displacement which is taken equal to zero. Load - displacement curves for the individual orientations are shown in Figure 8 and Figure 9. In Figs. 6 and 7, it can be observed that some of the load time curves associated with lower energy levels are smooth curves while some of the load curves associated with higher load levels have high frequency variations in the load time histories. Load displacement curves corresponding to these load time histories also indicate a similar phenomena. An interesting phenomena which can be observed is that the load creating the onset of high frequency variations occurs at a relatively constant value for all the specimens tested (it is 1400 N for 10 degree orientation pin and 1000 N for 20 degree orientation pin). If the applied

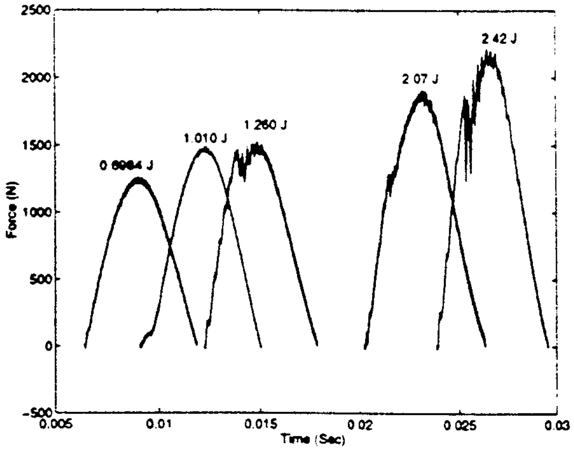

Figure 6: Load Time curves for 10 degree orientation

load is less than this threshold level, there is no indication of significant damage. This corresponds to an energy level of 1.26 Joules for 10 degree orientation and 0.7168 J in 20 degree orientation. If the applied load is much higher than this load level, there is the onset of high frequency variation followed by a relatively smooth load time history. This phenomena indicates the load and the impact energy level at which the first major failure occurs. C -Scan results indicated the first major failure phenomena to be face sheet related, primarily characterized by pin push - through. Visual inspection indicated the possibility of some pin buckling and face sheet delaminations at a lower load level which was not visible in the load time curve but appeared as a residual displacement in the load displacement curves.

Absorbed energy as a percentage of impact energy is shown in Figure 10 and 11 (for 10 and 20 degree angle orientations). First major increase in the absorbed energy level can be estimated to be the threshold energy level at which the damage occurs. It is obvious that this energy is a function of pin orientation, being lower at the higher angle. It should be noted that local pin failures did not reflect in the increased energy absorption levels.

Post-Failure Analysis of Truss Core Panels

The damage developed in the top and bottom facesheets was not visible on visual inspection. Post - failure analysis of few of the samples was conducted using optical microscopy. The samples were potted in

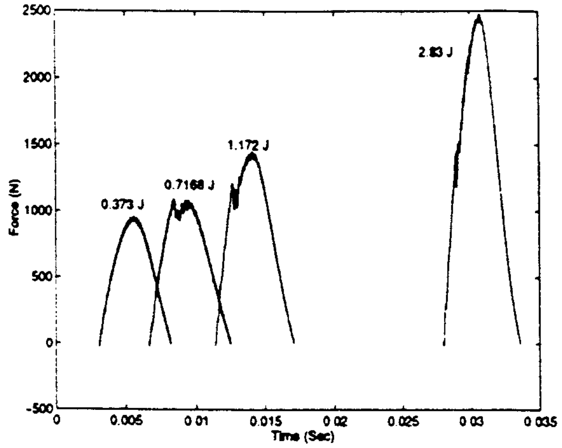

Figure 7: Load Time curves for 20 degree orientation

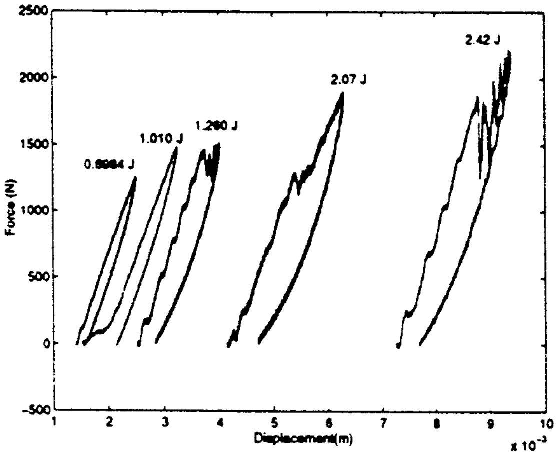

Figure 8: Load Displacement curves for 10 degree orientation

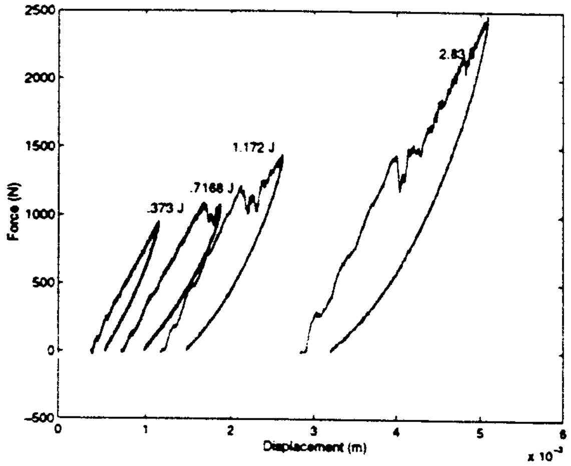

Figure 9: Load Displacement curves for 20 degree orientation

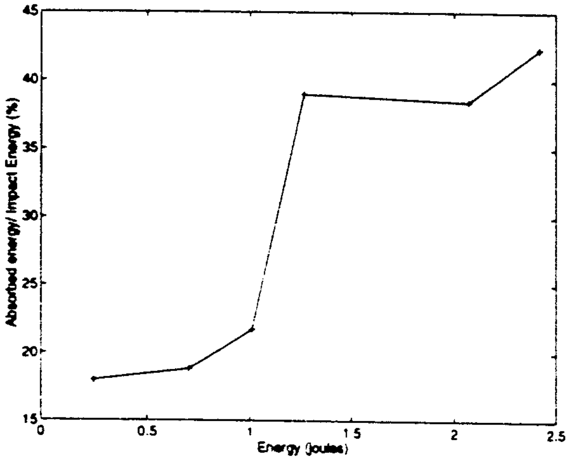

Figure 10: Nondimensionalized Energy plot for 10 degree orientation

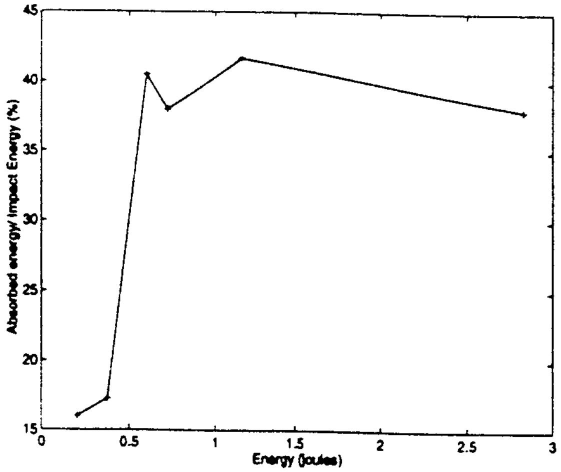

Figure 11: Nondimensionalized Energy plot for 20 degree orientation

a room temperature cure epoxy resin and sectioned carefully along the impact location. The cut sections were polished and observed on an optical microscope to reveal the through-the-thickness distribution of damage. Representative failure modes at the threshold load in the top and bottom facesheets, shown in Fig. 12 -14, were found to be a combination of pin-push out (pin piercing) from the facesheet, deformation of the facesheet in the direction of pin push out, delamination progression arising from pin locations and the coalescence of delaminations between adjacent pins along the interfaces. The core damage was restricted to local pins in the vicinity of the impact location. Although the energy levels for damage initiation for the 10 and 20 degree orientation specimens was different, their failure modes did not change significantly.

Conclusions

The force - time histories can be used as a measure to determine the energy levels where the significant damage occurs in sandwich panels. 10 degree orientation pins seem to be more resistant to impact induced damage when compared to 20 degree orientation pin angles in the core region. In both the orientations, face sheet damage seems to be the first significant failure mode.

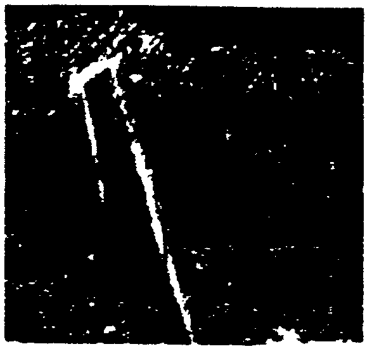

Figure 12: Pin push through

Figure 13: Delaminations

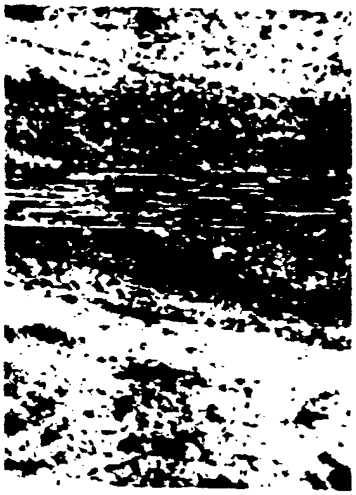

Figure 14: Shear cracks

Acknowledgements

The authors would like to thank Mr. William Baron, WL/FIBA for the financial support provided under the contract F33601-95. Foster - Miller Inc, of Waltham, MA, provided the specimens.

References

1. Freitas, G., Magee, C., Dardzinski, P and Fusco, T., " Fiber Insertion Process for Improved Damage Tolerance in Aircraft Laminates", Journal of Advanced Materials, Vol. 25, No. 4, pp. 36-43 (1994).

2. Barrett, D.J., " A Micromechanical Model For the Analysis of Z- Fiber Reinforcement", 37 th AIAA /ASCE/ ASME/ AHS SDM Conference, pp. 62-67 (1996).

3. Harrington, T.M., "An Experimental Investigation of Sandwich Panels Under Low Velocity Impact ", A MS thesis submitted to Air Force Institute of Technology, AFIT/GAE/ENY/94D-22 (1994)

4. Herup, E,J and Palazotto, A.N., " Low Velocity Impact Damage Initiation in Graphite-Epoxy/Nomex Honeycomb Sandwich Plates", 37 th AIAA/ ASCE/ ASME/ AHS SDM conference, pp. 1765-1773 (1996)

5. Palazotto, A.N, Herup, E.J and Harrington, T., " An Experimental Investigation of Sandwich Panels

Under Low Velocity Impact", ASCE 11 th Engineering Mechanics Conference, Vol. 1, pp. 402-407 (1996).

6. Herup, E.J., " Low Velocity Impact on Composite Sandwich Plates" A Ph.D Dissertation submitted to Air Force Institute of Technology, (1996).

ATTACHMENT III

LOW VELOCITY IMPACT RESPONSE AND NONDESTRUCTIVE EVALUATION OF SANDWICH COMPOSITE STRUCTURES

LOW VELOCITY IMPACT RESPONSE AND NONDESTRUCTIVE EVALUATION OF SANDWICH COMPOSITE STRUCTURES

Uday K.Vaidya
Center of Excellence for Advanced Materials (T-CAM)
Tuskegee University
Tuskegee, AL 36088

Anthony N. Palazatto and L.N.B.Gummadi
Department of Aeronautics and Astronautics
Air Force Institute of Technology (AFIT)
WPAFB, OH 45433

ABSTRACT

Composite sandwich constructions offer light weight and high bending stiffness advantages for aerospace and automotive applications among other structures. The use of a hollow truss core or z-fiber pin core is a new concept in sandwich composites, where the core is hollow and accessible, thereby providing space advantages for fuel cells and/or electronic assemblies besides from possessing high shear and axial stiffness. The z-fiber pins are oriented at predetermined geometry's and penetrate into the laminated facesheets making-up the sandwich composite. In the reference (Palazatto et. al, 1997), the low velocity response of hollow truss core composites with z-fiber pins oriented at 10 degree and 20 degree angles with respect to the facesheets were investigated by us. The current paper presents the post-impact microstructure, ultrasonic and vibration based nondestructive evaluation (NDE) studies and compression-after-impact response accompanied by acoustic emission (AE) testing of these composites.

BACKGROUND

A number of composite marine vessels, transportation body frames, structural parts in aircraft and helicopter blade components utilize advanced sandwich composite constructions because of their design flexibility and lightweight characteristics. Typically, a sandwich composite is comprised of a low density core sandwiched between a top and bottom face sheet made of fiber reinforcement that provides high bending strength/stiffness. There is considerable interest in developing innovative sandwich composites that offer space advantages in addition to high bending and axial stiffness for aerospace applications (Freitas et al., 1994; Herup and Palazatto, 1996; Herup, 1996). Truss core or Z-fiber pin core (Freitas et al., 1994, Palazatto et al., 1997) composites provide an alternative sandwich construction, where the core is hollow and comprises a system of z-fiber pins that penetrate into the facesheets according to predetermined geometry and configuration as shown in Fig. 1. This innovative concept makes the composite suitable for a variety of processing alternatives including, autoclave bag molding and vacuum assisted resin transfer molding. The z-fiber pins making up the core are of extremely fine diameter (0.508 mm - 0.889 mm). In the current study the z-fiber pins were oriented at 10 degree and 20 degree orientation with respect to graphite/ epoxy facesheets. The general arrangement of the z-fiber pins is described in (Palazatto et al., 1997). The facesheets are made of 16 layers of graphite/epoxy arranged in a quasi-isotropic stacking sequence.

The experimental details of the swing pendulum type low velocity test are similar to those used in (Herup and Palazatto, 1996; Herup, 1996). In the previous part of this work (Palazatto, 1997), the low velocity impact characteristics of the sandwich composites with 10 degree and 20 degree oriented z-fiber pins were investigated. The energy thresholds for impact were presented and it was found that the energy required to cause damage initiation in the 10 degree oriented samples was 1.26 J, while for the 20 degree z-fiber pin orientation, it was 0.72 J. Furthermore, the load at which the initiation of damage occurred was independent of the impact energy. For the 10 degree z-fiber pin oriented samples, the load was 1400 N, while for the 20 degree z-fiber pin oriented samples, it was 1200 N. The current paper presents the results on the low velocity impact related failure modes, the post-impact nondestructive evaluation (NDE) studies and compression-after-impact (CAI) testing conducted on the truss core specimens. The NDE studies included ultrasonic and vibration testing of the specimens and acoustic emission testing (AE) accompanying the CAI tests.

ULTRASONIC C-SCAN TESTING

The specimens were subjected to ultrasonic C-scan using a Testech immersion type pulse-echo system with a Krautkramer USP-12 ultrasonic pulser-receiver and a 5 MHz transducer. The specimens were tested for back and front facesheets separately, first prior to testing and subsequently after the impact tests. The C-scans obtained were satisfactory in terms of resolving individual z-fiber pins and mapping the z-fiber pin clusters accurately. Figures 2a and 2b show typical C-scans for "before testing" of a specimen with 10 degree and 20 degree z-fiber pin orientations. Figures 3a and 3b show typical C-scans of a specimen subjected to low velocity impact loading. The damage caused by the indentor is clearly observed from Fig. 3a on the top facesheet. In addition, at several locations on the top as well as bottom (Fig. 3b) facesheets, a coalescence of dark lines and enlargement of dark spots indicate locations where pin push-through accompanied by coalescence of delamination between adjacent pins occurs. These observations are in agreement with microstructural studies performed by sectioning the samples at regions of C-scan indications. These damage conditions are seen to spread out over a large portion of the top and bottom facesheets, and are not localized around the loading region.

FAILURE ANALYSIS OF Z-FIBER PIN COMPOSITES

The schematic of failure as observed across the top and bottom facesheet is illustrated in Fig. 4 and details around a single z-fiber pin is shown in Fig. 5. Typically failure initiation at low impact energies occurred by matrix cracking and microdelaminations in the vicinity of the locations where the z-fiber pins entered the facesheet. Also, initiation of debond at pin - facesheet is seen at low impact energies. Both these phenomena are illustrated in Fig. 6. Prior to the pin push-out that occurs at threshold energy, the facesheet plies around the pin exhibit a tendency to displace along with the pin for the top and bottom facesheets. With further displacement, the plies undergo shear cracking and delamination, first at individual pin locations and subsequently coalescence of delaminations that extend between a system of pins. A typical pin-facesheet debond, and delamination extending outwards from the pins are shown in Fig. 7. The failure is distributed over a system of pins and not limited to a single pin cluster. The pin push-through that occurs at threshold energy is shown in Fig. 8. In addition, to the above phenomena, the global bending of the facesheets was observed at higher impact energies and quasi-static loads.

COMPRESSION AFTER IMPACT (CAI) TESTING

Four of the samples representative of various impact conditions and pin orientations were subjected to compression-after-impact testing using a SACMA recommended plate compression fixture. A 150 kHz acoustic emission (AE) sensor was attached to the specimen's geometric center using a viscous couplant and an electrical tape. A two channel LOCAN-AT Physical Acoustics system was used for AE monitoring. The specimens were loaded at a constant crosshead speed of 0.254 mm / min until significant load drop was observed in the load-displacement curve. Figure 9 represents load-displacement curves for three of the four specimens tested for the CAI tests. Table 1. summarizes the results from the CAI tests. At several locations along the load-displacements local variations in the load corresponded to audible clicking of the pins, as they tended to debond from the facesheet. Towards failure, this phenomenon occurred with more frequency, and a facesheet delamination which was audible, was evident at failure. The failure loads were representative of the impact event that they underwent: the 10 degree z-fiber pin oriented specimen subjected to repeated impact loading failed at 3291 kgs, the 10 degree z-fiber pin oriented specimen subjected to single impact at failure load, failed at 3949 kgs, the specimen with 10 degree z-fiber pin orientation below failure initiation load exhibited a highest value of 3745 kgs and the 20 degree z-fiber pin orientation under failure load exhibited 3222 kgs, the lowest of all. Ultrasonic C-scans of the failed specimens are shown in Figs. 10 and 11. The coalescence of delaminations across a system of pins is evident for all the specimens tested. The damage area around the impact location is not influenced by the compression loading as seen in Figs. 10. The failure is initiated primarily by the localized failure of a system of pins. The 20 degree z-fiber pin orientation specimens show a greater damage state than the 10 degree z-fiber pin orientation specimen as seen in Fig. 11.

ACOUSTIC EMISSION TESTING

Energy, amplitude and event durations of AE events were monitored during the CAI tests. AE activity was seen to be continuous throughout the loading history of the specimens. Figure 12 represents the parametric distributions of amplitude and duration with respect to test time, while Fig. 13 represents the same information using amplitude and energy with respect to test time. The distribution of AE events shown in Fig. 12 broadly lies in three groups; first a low duration <500 ms, low amplitude 40-55 dB, second, a medium duration 500-2000 ms, medium amplitude 55-70 dB and third, a high duration >2000 ms, high amplitude events. The energy based grouping of these events as shown in Fig. 13 show a small energy <100 for a majority of type one and type two events described above. Only a few events, are seen to exhibit high amplitude, high energy >750, corresponding to dominant occurrence of pin pull-out and facesheet delamination. The first set of events occur from the early stage of loading and last till failure and are primarily attributed to matrix microcracking and events corresponding to initiation of localized debond pin-facesheet. The second set of events are primarily due to pins separating and/or sliding against the facesheet plies creating microdelaminations and further debonds. These events also corresponded to audible clicking of the pins, indicating that some pins undergo a pin pull-out phenomenon.

VIBRATION TESTING

The specimens were tested to investigate the global stiffness changes using a vibration based nondestructive evaluation (NDE) testing following impact and/or static loading. The specimen was mounted in a near free-free boundary condition using bees wax at its geometric center on an impedance head connected to a electrodynamic shaker Bruel & Kjaer 4810 excited using random noise excitation. The input force and output acceleration signals from the impedance head were fed to a dual channel frequency analyzer B&K 2032. The frequency response function (FRF) of the specimen under predominantly bending vibrations were recorded. Figure 14 compares the FRF of 10 degree z-fiber pin orientation specimens subjected to a single impact vs that subjected to a repeated impact. The first three modes are seen to be unaffected by the impact event related condition of the specimens, however, at the higher modes between 5500 Hz - 12,500 Hz within the measurement range, it is seen that the specimen subjected to repeated impact loading exhibits 15-20 % reduction in frequency as compared to the specimen subjected to a single impact at failure load. For example, the 6450 Hz frequency is seen to reduce to 6320 Hz for the specimen subjected to repeated loading. Figure 15 compares the FRF's for an impact loaded specimen at failure load and statically loaded specimen under failure load, with 10 degree z-fiber pin orientation. In this case, the first two modes and higher modes for the statically loaded specimens showed lower frequency values as compared with the impact loaded specimens. This indicates that the stiffness loss for the statically loaded specimen is greater, and hence, the delaminations and pin push-through is more extensive as compared with the impact loaded specimens. Furthermore, based on the vibration tests, it is noticed that not all the modes are sensitive to the presence of damage, or variations in localized stiffness conditions, however, only some of the modes within the FRF are seen to be sensitive to the specimen condition. This suggests that depending upon the location and proximity of the damage state (which is not uniform for unit area of the facesheet) for a system of pins, the vibration response of that mode is accounted. No correlation has been attempted in this article to investigate the influence of damage position with respect to a mode number. Figure 16 compares the FRF for the 10 degree z-fiber pin oriented composite to the 20 degree z-fiber pin oriented composite. The 20 degree z-fiber pin oriented specimen exhibits slightly lower stiffness as compared to the 10 degree z-fiber pin oriented composite.

The damping ratio of the specimens has been measured by performing zoom transform on the peak of the FRF using the half-power points method. The range of damping exhibited for the specimens for the modes measured was in the range of 0.0015-0.009. The highest damping ratio was exhibited by the specimen subjected to repeated impact loading (0.009) which was attributed to the large frictional energy dissipated at the larger damage zone.

CONCLUSIONS

Failure characteristic appears to be pin push-through at threshold energy level for the z-fiber pin reinforced sandwich composite plates. The area surrounding the pins shows features of delamination and debonding between pins. The 10 degree oriented z-fiber pins caused threshold energy at a higher level than the 20 degree oriented z-fiber pins. Damage is significant at 1.26J for 10 degree z-fiber pin orientation, and 0.72J for the 20 degree z-fiber pin orientation. The C-scans verify the phenomenon of delamination after pin push-through. The compressive failure of the 10 degree and 20 degree z-fiber pin oriented sandwich composites is governed by the threshold impact event. It was observed that compressive failure was characterized by pin debond and formation of delaminations. Compressive failure becomes a localized event predicated by local pin debond characterized by the CAI curves. Acoustic emission curves indicate the dominant failure modes of matrix cracking, pin debonding and delamination. The natural frequency and damping ratio are sensitive to the static vs dynamic impact loading, however are unaffected by the local damage states.

REFERENCES

Freitas, G., Magee, C., Dardzinski, P and Fusco, T, 1994. "Fiber Insertion Process for Improved Damage Tolerance in Aircraft Laminates," Journal of Advanced Materials, Vol.25, No.4, pp.36-43.

Herup, E.J and Palazatto, A.N, 1996, "Low Velocity Impact Damage Initiation in Graphite/Epoxy Nomex Honeycomb Sandwich Plates," 37th AIAA/ASCE/ASME/ AHS SDM Conference, pp.1765-1773.

Herup, E.J, 1996, "Low Velocity Impact on Composite Sandwich Plates," Ph.D Dissertation, Air Force Institute of Technology, Dayton, Ohio.

Palazatto, A.N., Gummadi, L.N.B., Vaidya, U.K., and Herup, E.J, 1997, "Low Velocity Impact Damage Characteristics of Z-Fiber Reinforced Sandwich Panels - An Experimental Study," 38th AIAA/ASME/ASCE/AHS SDM, Kissimmee, FL, April.

ACKNOWLEDGMENTS

The authors would like to thank Mr.William Baron, WL/FIBA for the financial support provided under the contract F33601-95. Foster Miller-Inc, of Waltham, MA, provided the specimens.

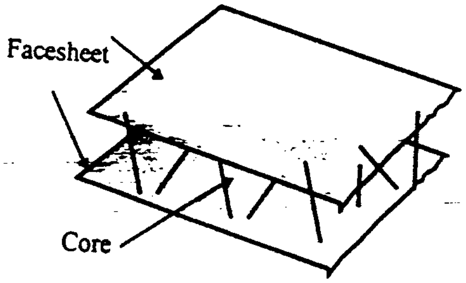

Figure 1. Typical Truss Core Sandwich Composite

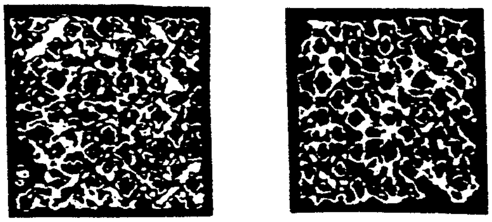

10 degree

20 degree

Figure 2. Ultrasonic C-scans of Truss Core Composites "before" impact testing a. *10 degree z-fiber pin orientation b. 20 degree z-fiber pin orientation*

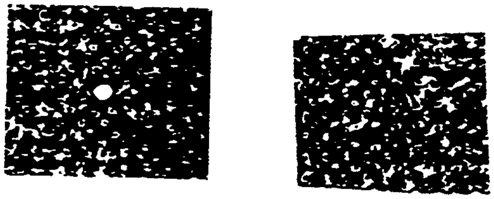

Loading Side Facesheet

Back Facesheet

Figure 3. Ultrasonic C-scans of Truss Core Composites "after" low velocity impact testing *for a 10 degree z-fiber pin orientation a. Impact Side Facesheet and b. Backside Facesheet*

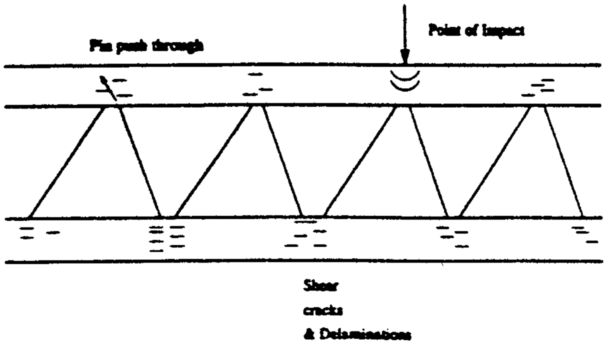
Pin push through
Point of Impact
Shear
cracks
& Delaminations

Figure 4. Schematic of Failure Initiation and Progression

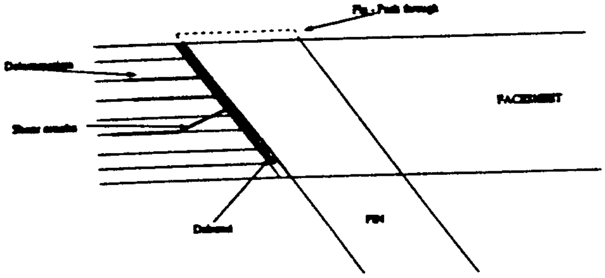
Pin Push through
Delamination
Shear cracks
FACESHEET
Debond
PIN

Figure 5. Details of Failure around in the vicinity of single pin-facesheet

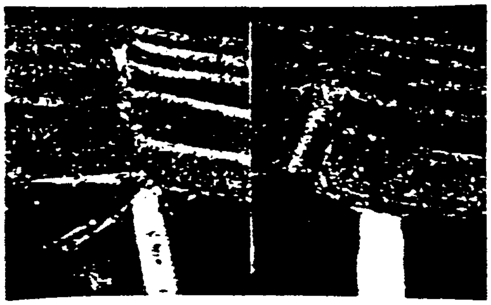

Figure 7. Debond Development at Pin-Facesheet Interface and Propagation of Delamination to Adjacent Pin

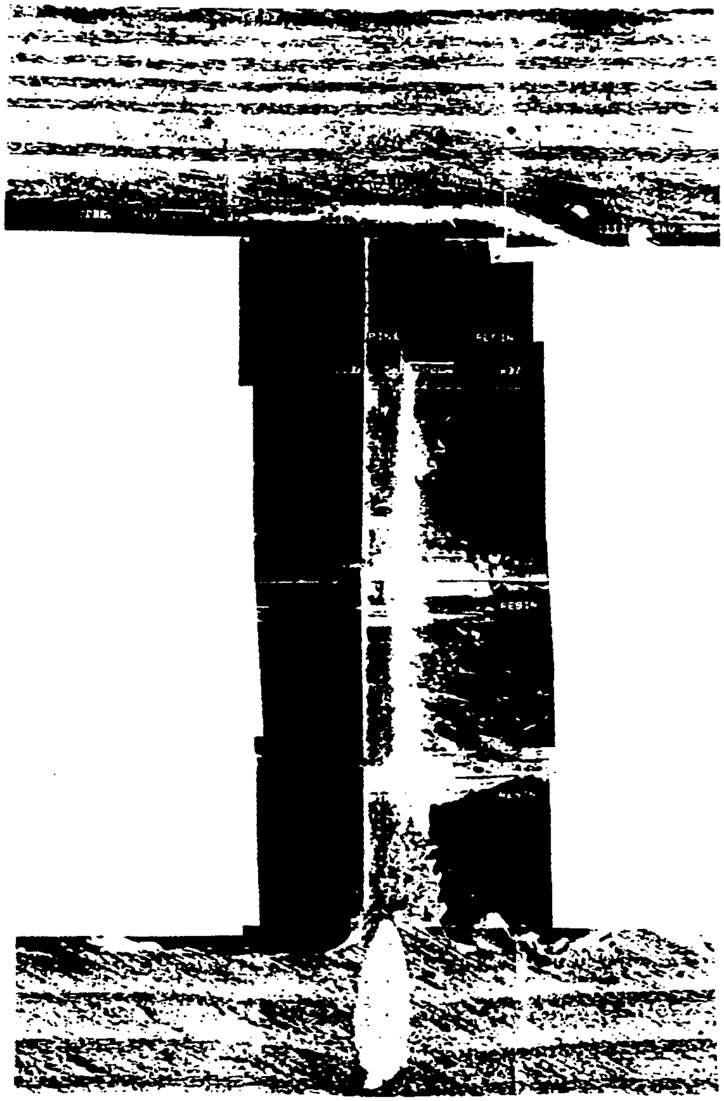

Figure 6. Damage Initiation at very low impact energies <1 J

Figure 8. Pin Push-Through

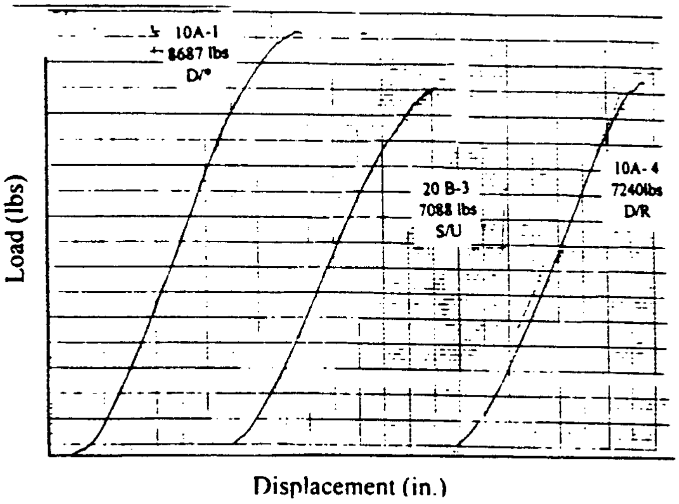

Figure 9. CAI load - displacement curves for 10 and 20 degree z-fiber pin oriented samples

Table 1 : Summary of Compression-After-Impact Tests

Specimen	Orientation	Failure Load (kgs)
D/*	10 degree	3949
D/R	10 degree	3291
S/U	10 degree	3745
S/U	20 degree	3222

Note: Samples were subjected to following static and/or low velocity impact conditions:
D/* : Low Velocity Impact; Failure Initiation Energy
D/R : Low Velocity, Four Repeated Impact Events
S/U : Static Loading, Under Failure Load

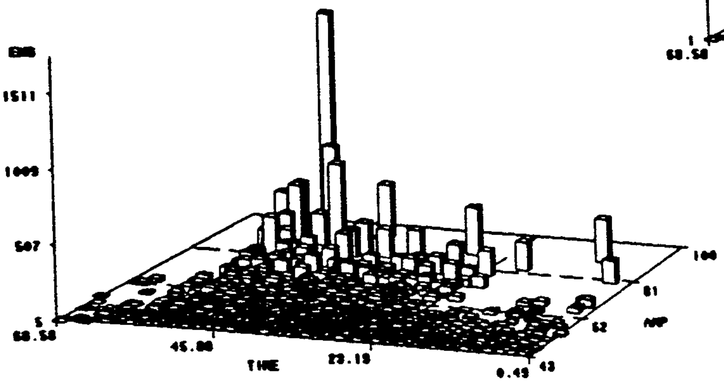

Figure 13. AE parametric distribution for the same specimen of Fig.12 represented in terms of Amplitude and Energy of AE Hits

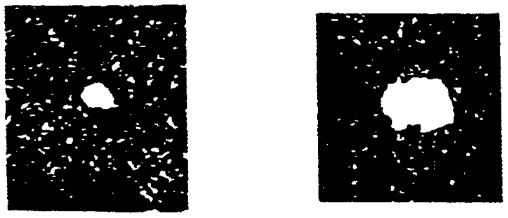

Single Impact **Repeated Impact**

Figure 10. Ultrasonic C-scan for a 10 degree z-fiber pin oriented specimen subjected to a) single impact event (energy 1.26 J) b) four repeated impact events. *Note: The scans are taken after CAI testing*

Loading Side Facesheet **Back Facesheet**

Figure 11. Ultrasonic C-scan after CAI test for a 20 degree z-fiber pin oriented specimen subjected to 1.17 J impact energy

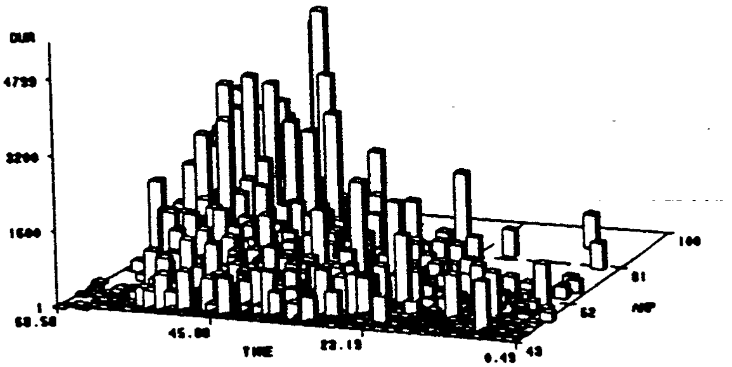

Figure 12. AE parametric distribution for a CAI loading of a 10 degree z-fiber pin oriented specimen (AE Parameters : Amplitude and Duration of AE Hits)

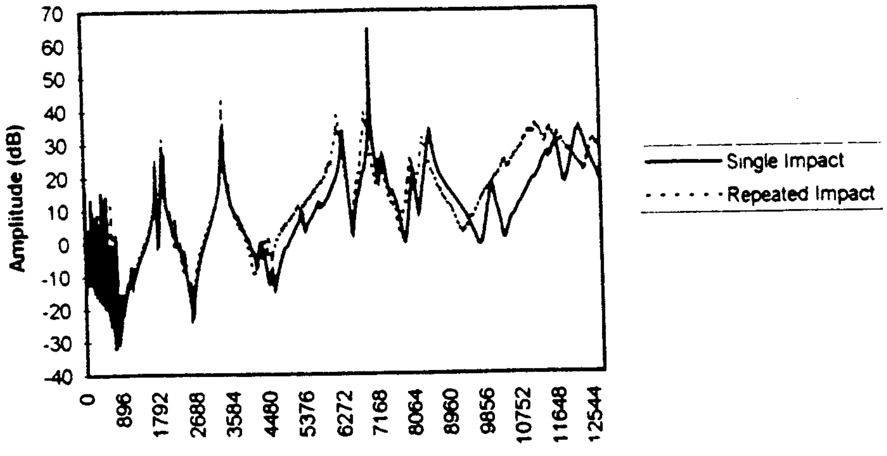

Figure 14. FRF comparing vibrational response of a specimen subjected to single impact vs repeated impact

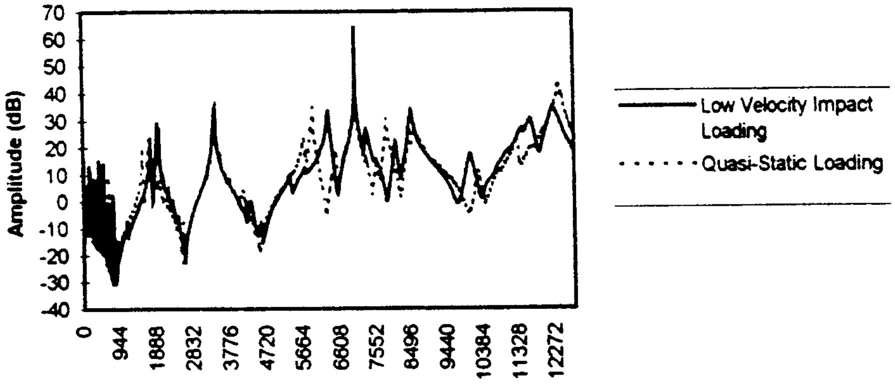

Figure 15. FRF comparing vibrational response of a specimen subjected to quasi-static loading vs low velocity impact loading

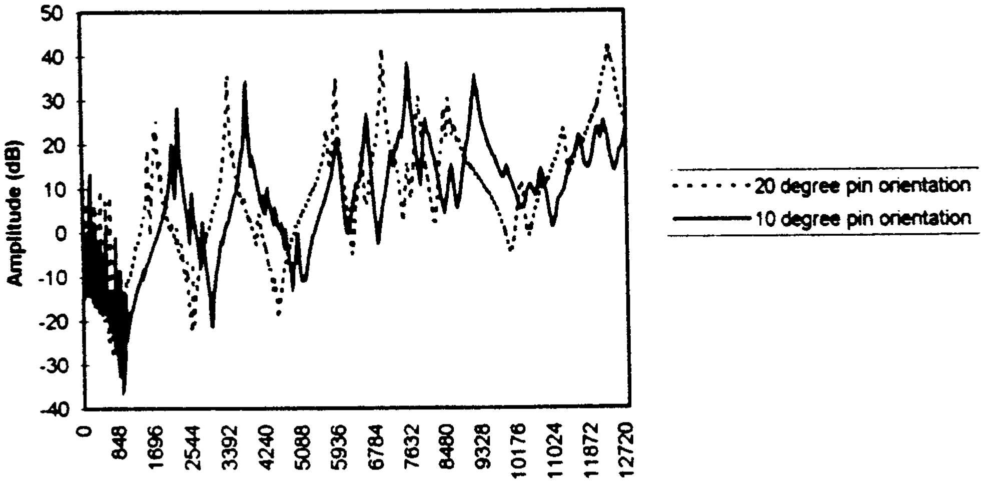

Figure 16. FRF comparing vibrational response of a 10 degree vs 20 degree oriented z-fiber pin composite

CHAPTER III: FINITE ELEMENT MODELING

In this chapter, our efforts in the modeling of the sandwich panels is discussed. It included both analytical modeling using closed form solutions and numerical modeling using various commercially available finite element software such as NASTRAN, ASTROS etc. Efforts were also made to develop "in-house" finite element software to model the sandwich panels. All the modeling efforts carried out in the report can be described as " Phenomenological". That is, what ever results observed in the laboratory while carrying out the experiment, were simulated using the numerical modeling techniques. Parts of the work carried out were published in refereed journals. Instead of repeating the research work presented in specific journal articles, only the salient results are discussed, and the copies of the papers are provided as attachment.

The work carried out in this chapter can be divided into six sub sections. In the first sub section, elasticity solutions for honeycomb sandwich panels under Hertizian loading (which closely resembles the low velocity impact) is discussed. This work was carried out by Major Herup and Dr. A.N. Palazotto and was published by the Journal of Aerospace Engineering. It is provided as attachment IV. In this paper, Pagano's original solutions for the bending of composite plates was extended for sandwich panels under Hertizian loading. The main purpose of this research was to gain insight into the interpretation of the experimental data and to judge the performance of the 'in-house' developed finite element software. In this work, two different solutions are obtained, one corresponding to the cylindrical bending of rectangular plate while the other pertains to the three dimensional bending of a rectangular plate. Contact stresses representing the impact loading are obtained in the form of truncated Fourier series. The elasticity solution pertaining to the cylindrical bending of the plate has shown the similar trend as was observed in the experimentation regarding the face sheet thickness. That is, the elasticity solution is indicating that when the face sheet thickness is small, static modeling can be used to describe the phenomena of low velocity impact while for thicker face sheets, both phenomena seem to differ significantly.

The next section is about the development of an 'in-house' finite element code used to model the phenomena of low velocity impact of honey comb sandwich panels. The work that is carried out in this section is under preparation for a possible journal publication(Attachment V).

A detailed description of this work can be seen in the Ph.D. Dissertation of Major Herup (Submitted to Air Force Institute of Technology, 1996). A detailed description about the finite element theory for the sandwich panels, development of a contact algorithm, and comparison with the experimental results are presented. A global finite element model was proposed for load deflection characteristics which interacts with a local finite element model. The local finite element model was used to determine the load distribution due to the contact. For a global model, a 56 degree of freedom model was developed. For the local model, an iterative scheme was developed. Load deflection curves matched very well with those of experiment. Also, damage patterns created by the impact loading matched with those of experiments. However, as the analytical model described in attachment IV suggests, as the thickness of the face plate of the sandwich plate increased, the phenomena of the low velocity impact tends to be a dynamic instead of quasi static (as treated in the finite element model and the analytical model). Towards this end, it was proposed to carry out simple analytical investigations to model the dynamic aspects of the low velocity impact. Work carried out in this aspect is described as an attachment (attachment VI).

The dynamics of a sandwich plate under low velocity impact is analytically modeled using simple spring -beams models by Dr. William Baker and Dr. Anthony Palazotto. Work carried out in this aspect is inconclusive. Preliminary results seem to indicate certain experimental results observed in the laboratory are due to the dynamics of the sandwich plate. One of the most important observation concluded that the commonly used Hertizian contact power law that is originally developed for isotropic materials may not be applicable to composite materials (in the literature it seems to be the practice).

As a next attachment (attachment VII) modeling efforts towards the analysis of z-pins under low velocity impact loading was provided. Four different software packages were used , I-DEAS, NASTRAN, ASTROS and ABAQUS. The work on I-DEAS was carried out by Mr. V. Perel while similar work was carried out by Dr. Gummadi using ASTROS, NASTRAN and ABAQUS. In all the cases, similar results are obtained. In the report, results obtained graphically using the I-DEAS software only are provided. Three different models are discussed. These are: a two dimensional local model (model 1), a three dimensional global model with rod and plate elements (model 2), and finally, a three dimensional global model with brick elements (model

3). In all the cases, a number of mesh sizes were used and the final mesh size was arrived at after convergence. The objective of the first local model was to understand the load bearing characteristics of the pins. From this model, it was observed that there was very little bending occurring within the pins and the major loading resistance within the pins was axial loading. However, when it comes to local failure of the pins through buckling, the moments (even though they are small) were taken into consideration. But there was very little difference in terms of load deflection characteristics when the pin was modeled using a bar (that can also have bending loads) or pin. Thus, for subsequent optimization studies, it was decided that a global plate -rod model could be used. In both these models (model 1 and 2), the composite face plate was modeled as an orthotropic plate with equivalent properties. Also, it was observed that the two dimensional finite element models that are used for honeycomb sandwich plates can not be used for modeling z-pin sandwiches since there is a significant through the thickness strain. Next, a three dimensional brick element model was developed for the sandwich plate. Refinement of the mesh was restricted by the memory of the computer. The primary objective of this study was to observe the trends of stress within the face plate across the thickness. To validate the mesh refinement, an analytical study was carried out for an isotropic material and the results matched exactly with that of the finite element model. Then the finite element model was modified to account for the lay up configuration of the face plate. Stress contour patterns across the thickness of the face plate were determined. This information was then used for the determination of the pin push out failure across the face plate.

The converged finite element model was used to determine the load deflection characteristics of the sandwich plate under static loading considering the phenomena of failure. Two different failure modes were considered. The first failure mode considered is the buckling of the pins. Moments at the ends of the pins are taken into consideration while determining the buckling load of the pins. As a second failure mode, pin push through was considered. However, pin push through is a phenomena associated with the stress pattern in the face plate. Consequently, a correlation between the pin load and the face sheet maximum stress (based on the 3D brick finite element model discussed in attachment VIII) was characterized and used as the criteria for determining this failure. A quasi-nonlinear finite element model was developed. A number of NASTRAN runs were used to arrive at the result. The results matched very closely with those of experiments.

As the last section of this report, studies carried out in optimizing the pin orientation are presented (Attachment IX). The Wright Lab developed ASTROS (a weight optimization software) was used to determine the best orientation of the pin that can have maximum buckling strength, maximum pull out strength and maximum compressive strength but least weight. A number of ASTROS runs are carried out with different pin orientation angles and at each orientation, an optimized sandwich plate, with the above mentioned constraints (buckling strength, pull out strength and compressive strength) was obtained. The angle at which the plate satisfies all the constraints but with the lowest weight was considered the best optimized pin orientation. From the analysis, it was concluded that between 20^0 and 35^0 angles, the pin orientation is almost the same in terms of the above constraints and can be used as the optimum pin angle.

ATTACHMENT IV

ELASTICITY SOLUTIONS FOR HERTZIAN LOADED COMPOSITE SANDWICH PLATES

ELASTICITY SOLUTIONS FOR HERTZIAN LOADED COMPOSITE SANDWICH PLATES

By Eric J. Herup[1] and Anthony N. Palazotto,[2] Fellow, ASCE

ABSTRACT: The elasticity solutions for composite laminates in bending originally developed by Pagano are extended for Hertzian contact-type loading in this paper. Two solutions are obtained, corresponding to cylindrical bending and three-dimensional bending of a rectangular plate. Loads simulating contact with a spherical indentor are obtained by superposition of the elasticity solutions for individual terms of truncated Fourier sine series representations of Hertzian contact stresses. In this way, a benchmark for models of impact loaded plates is provided in which the loading is more representative of contact than the solutions often used for that purpose. The solutions provide insight into the interpretation of experimental data from low-velocity impact tests and are used to judge the performance of finite-element–based low-velocity impact algorithms in predicting stress under the impactor.

INTRODUCTION

The need for strong, stiff, lightweight structures in bending-loaded applications for aerospace vehicle components has motivated the design and analysis of sandwich structures using composite materials. These hybrid constructions consist of two relatively dense and stiff outer facesheets that are bonded to either side of a low-density core. The facesheets carry bending-induced axial loads and the core sustains shear stresses as well as compressive stresses normal to the panel and resists wrinkling or buckling of the facesheets under axial compressive loading (Hackman 1965). The core usually has little inplane and flexural stiffness, compared to the facesheets, but it can have significant transverse stiffness and adequate shear stiffness. The presence of the core places the facesheets away from the plate bending neutral axis, enhancing the bending resistance provided by the facesheets. The result is a thicker plate or shell with a much higher bending stiffness-to-weight ratio than the facesheets alone.

A principal drawback of laminated composite panels in general and composite sandwiches in particular is their susceptibility to low-velocity impact damage such as that brought about by dropped tools and runway/taxiway debris. In particular, significant loss of compressive strength has been found to occur without any visible sign of damage (Rhodes 1975; 1978; Schoeppner 1994). This is a major concern for both manufacturers and end users who need to locate damages and define criteria for acceptance and/or repair of structural members. There remains much room for improvement of composite sandwich damage resistance. Increasing the damage resistance of a structure requires understanding of its response to mechanical loads. In particular, the response of composite sandwich structures to low-velocity impact loading is of significant interest. Perhaps the most popular among the approaches for predicting the response of composite sandwich structures to low-velocity impact loading is finite-element analysis. Often-used benchmarks for finite-element codes used for such analyses are the elasticity solutions of Pagano (1969), which provide exact solutions for composite laminates in cylindrical bending and rectangular composite laminates in three-dimensional bending (Pagano 1970), each with simple supports and sine-wave transverse pressure profiles over the entire upper surface. In contrast, for low-velocity impact problems, the loading is typically distributed over a relatively small portion of the structure (the contact footprint, Fig. 1). The loading in Pagano (1969) is a half sine wave in the span direction while that of Pagano (1970) is sinusoidal in both in-plane directions. This loading was found to be quite benign from a three-dimensional point of view (i.e., stress gradients were small) when compared to a Hertzian contact load representing a spherical impactor. As discussed by Greszczuk (1982), when the contact duration between the impactor and the plate is long compared to the natural vibration periods, system vibrations can be neglected and a Hertz law relationship between applied force and indentation can be assumed. This relationship is often assumed in low-velocity impact analyses. The assumed Hertzian distribution of applied pressure on the top surface is

$$q\left(x, y, \frac{h}{2}\right) = \begin{cases} 0, & x^2 + y^2 > R_{\text{contact}}^2 \\ q_0 \sqrt{1 - \dfrac{x^2 + y^2}{R_{\text{contact}}^2}}, & x^2 + y^2 \le R_{\text{contact}}^2 \end{cases} \tag{1}$$

where R_{contact} = radius of the circular contact footprint. In the cylindrical bending case, the contact footprint is one-dimensional and R_{contact} is the contact half-width.

An algorithm that can accurately reproduce the stresses of

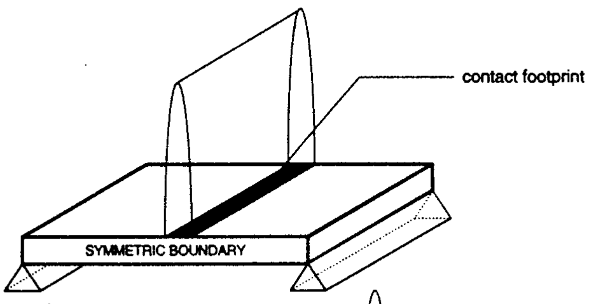

(a) Cylindrical bending

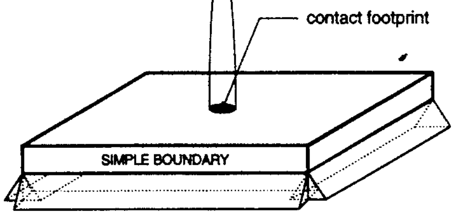

(b) Three-dimensional bending

FIG. 1. Cylindrical Bending and Three-Dimensional Plate Loading and Boundaries

---

[1] PhD Candidate, Dept. of Aeronautics and Astronautics, Air Force Inst. of Technol., Wright-Patterson AFB, OH 45433.

[2] Prof., Dept. of Aeronautics and Astronautics, Air Force Inst. of Technol., Wright-Patterson AFB, OH.

Note. Discussion open until June 1, 1997. To extend the closing date one month, a written request must be filed with the ASCE Manager of Journals. The manuscript for this paper was submitted for review and possible publication on October 14, 1996. This paper is part of the ***Journal of Aerospace Engineering***, Vol. 10, No. 1, January, 1997. ©ASCE, ISSN 0893-1321/97/0001-0027–0037/$4.00 + $.50 per page. Paper No. 14243.

an exact elasticity solution for a simple sinusoidal load may still fall far short when a Hertzian contact load is applied. Thus, the elasticity solutions of Pagano do not provide an appropriate benchmark for contact-type loading and a finite-element code that compares well with Pagano's solutions for sine-wave loading is not assured of being correct for contact-type loading. Therefore, the elasticity solutions of Pagano (1969, 1970) are extended to Hertzian contact loading in the present research. The contact pressure profile (Hertzian) is approximated by a truncated Fourier sine series. The solution is obtained by the principle of superposition; the solution for each term of the series is calculated and the stresses and displacements are summed. Clearly, for the principle of superposition to hold, linear elasticity must be assumed. To assure linearity, the total load applied is kept small (here 1 N). In this way, a linear-elastic benchmark for models of impact loaded plates is provided.

CYLINDRICAL BENDING SOLUTION

A first step toward understanding the response of composite sandwich plates to impact loads can be made by solving a simpler problem having many similar features to the problem of interest. It is evident that the low-velocity impact of a flat plate by a spherical indentor is a three-dimensional problem. Considering a slice through the thickness at the center of impact, a two-dimensional cylindrical bending analysis of that slice may reveal some of the important transverse effects. An elasticity solution that includes transverse stresses was found in the literature and applied here. Pagano (1969) presented an elasticity solution for bidirectional (0–90°) layered composite laminates in cylindrical bending. The solution is briefly described in the following paragraphs.

In Fig. 2, a laminate composed of m orthotropic layers, such that the axes of material symmetry are aligned with the plate axes x, y, z, is considered. The body is in a state of plane strain with respect to the xz-plane and is simply supported on the ends $x = 0$ and $x = L$. A normal traction $q(x)$ is applied to the upper surface $z = h/2$.

For each layer, the orthotropic constitutive relations for plane strain are given by Pagano (1969)

$$\varepsilon_x = R_{11}\sigma_x + R_{13}\sigma_z; \quad \varepsilon_z = R_{13}\sigma_x + R_{33}\sigma_z \qquad (2a,b)$$

$$\gamma_{xz} = R_{55}\tau_{xz}; \quad R_{ij} = S_{ij} - \frac{S_{13}S_{j3}}{S_{33}}, \quad (i, j = 1, 3, 5) \qquad (2c,d)$$

In which R_{ij} = reduced compliance coefficients for plane strain; and S_{ij} = compliances with respect to the axes of material symmetry. The equations of equilibrium for plane strain in the xz-plane are

$$\sigma_{x,x} + \tau_{xz,z} = 0; \quad \sigma_{z,z} + \tau_{xz,x} = 0 \qquad (3a,b)$$

and the linear strain-displacement relations are

$$\varepsilon_x = u_{,x}; \quad \varepsilon_z = w_{,z}; \quad \gamma_{xz} = u_{,z} + w_{,x} \qquad (4a-c)$$

These complete the governing equations for the problem, and it should be observed that all stress, strain, and displacement components are independent of the y-coordinate. The stress boundary conditions on the upper and lower surfaces are given by

$$\sigma_z\left(x, \frac{h}{2}\right) = -q(x); \quad \sigma_z\left(x, -\frac{h}{2}\right) = \tau_{xz}\left(x, \pm\frac{h}{2}\right) = 0 \qquad (5a,b)$$

and the simple support conditions are

$$\sigma_x(0, z) = \sigma_x(L, z) = 0; \quad w(0, z) = w(L, z) = 0 \qquad (6a,b)$$

Next, we introduce the index i to identify the lamina such that the top lamina corresponds to $i = 1$ and the bottom lamina corresponds to $i = m$. Construct a local coordinate system (x_i, z_i) parallel to the global coordinate system (x, z) on the center of the ith lamina such that at the left end, $x = x_i = 0$. Further, define h_i to be the thickness of the ith lamina. Stress and displacement continuity between lamina can be expressed as

$$\sigma_z^{(i)}\left(x, \frac{-h_i}{2}\right) = \sigma_z^{(i+1)}\left(x, \frac{h_{i+1}}{2}\right), \quad (i = 1, 2, \ldots, m - 1) \qquad (7a)$$

$$\tau_{xz}^{(i)}\left(x, \frac{-h_i}{2}\right) = \tau_{xz}^{(i+1)}\left(x, \frac{-h_{i+1}}{2}\right), \quad (i = 1, 2, \ldots, m - 1) \qquad (7b)$$

$$u^{(i)}\left(x, \frac{-h_i}{2}\right) = u^{(i+1)}\left(x, \frac{-h_{i+1}}{2}\right), \quad (i = 1, 2, \ldots, m - 1) \qquad (7c)$$

$$w^{(i)}\left(x, \frac{-h_i}{2}\right) = w^{(i+1)}\left(x, \frac{-h_{i+1}}{2}\right), \quad (i = 1, 2, \ldots, m - 1) \qquad (7d)$$

Taking now a particular form for $q(x)$, namely

$$q(x) = q_0 \sin(px); \quad q_0 = \text{constant}; \quad p = \frac{\pi}{L} \qquad (8a-c)$$

Pagano (1969) shows that the solution of the boundary value problem described by (2)–(8) can be found by putting

$$\sigma_x^{(i)} = f_i(z)\sin(px); \quad \sigma_z^{(i)} = -p^2 f_i(z)\sin(px); \quad \tau_{xz}^{(i)} = -pf_i'(z)\cos(px) \qquad (9a-c)$$

in which the functions $f_i(z)$ are expressed by

$$f_i(z) = \sum_{j=1}^{4} A_{ji}e^{m_{ji}z_i}, \quad (i = 1, 2, \ldots, m) \qquad (10a)$$

$$m_{ji} = -(-1)^j p \sqrt{\frac{a_i - (-1)^j b_i}{c_i}} \qquad (10b)$$

$$a_i = R_{55}^{(i)} + 2R_{13}^{(i)}; \quad b_i = \sqrt{a_i^2 - 4R_{11}^{(i)}R_{33}^{(i)}}; \quad c_i = 2R_{11}^{(i)} \qquad (10c-e)$$

where A_{ji} = constants. The stresses then can be expressed as

$$\sigma_x^{(i)} = \sin(px) \sum_{j=1}^{4} A_{ji}m_{ji}^2 e^{m_{ji}z_i} \qquad (11a)$$

$$\sigma_z^{(i)} = -p^2 \sin(px) \sum_{j=1}^{4} A_{ji}e^{m_{ji}z_i} \qquad (11b)$$

$$\tau_{xz}^{(i)} = -p \cos(px) \sum_{j=1}^{4} A_{ji}m_{ji}e^{m_{ji}z_i} \qquad (11c)$$

and the displacements can then be expressed as

$$u_i = \frac{\cos(px)}{p} \sum_{j=1}^{4} A_{ji}(R_{13}^{(i)}p^2 - R_{11}^{(i)}m_{ji}^2)e^{m_{ji}z_i} \qquad (12a)$$

$$w_i = \sin(px) \sum_{j=1}^{4} A_{ji}\left(R_{13}^{(i)}m_{ji} - \frac{R_{33}^{(i)}}{m_{ji}}p^2\right)e^{m_{ji}z_i} \qquad (12b)$$

which satisfy the simple support boundary conditions [(6)] identically. Satisfaction of the remaining boundary conditions,

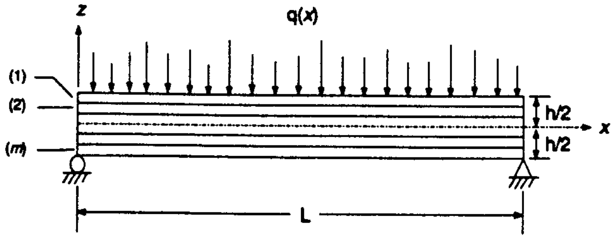

FIG. 2. Cylindrical Bending Plate Notation

(5) and (7), leads to a system of 4m unknowns A_{ji}. This system is set up for the present research by placing the A_{ji} in a 4m × 1 vector, **AA**

$$\mathbf{AA}_{j+4(i-1)} = A_{ji} \tag{13}$$

and defining a 4m × 4m matrix **B**, which, on premultiplying **AA** produces a 4m × 1 vector, **BC**, of the boundary conditions

$$\mathbf{BC}_1 = q_0 \tag{14a}$$

$$\mathbf{BC}_{j+4(i-1)} = 0, \quad (j = 1, 2, 3, 4;\ i = 1, 2, \ldots, m;\ ij \neq 1) \tag{14b}$$

$$\underset{(4m\times 4m)}{\mathbf{B}} \ \underset{(4m\times 1)}{\mathbf{AA}} = \underset{(4m\times 1)}{\mathbf{BC}} \tag{14c}$$

For example, σ_z on the top and bottom surfaces [the left-hand side (LHS) of (5)] was placed into (14) by setting

$$\mathbf{B}_{1,j} = -p^2 e^{(1/2)m_{j1}h}; \quad \mathbf{B}_{1,j+4(m-1)} = -p^2 e^{-(1/2)m_{jm}h} \tag{15a,b}$$

The contributions to **B** from the other boundary conditions and interface continuity conditions are given in Herup [(1996), Appendix A]. The solution, **AA**, is then obtained by inverting **B**

$$\mathbf{AA} = \mathbf{B}^{-1}\mathbf{BC} \tag{16}$$

The stresses and displacements are then obtained by (11)–(13) with **AA** from (16). A personal computer, running the numerical manipulation tool Mathcad, was found to be adequate to set up and solve the matrix algebra described [see Herup (1996), Appendix A].

Material Properties

Material properties for the specimens used by Herup (1996) are obtained from the manufacturer's test data or chosen to be consistent with that data. These properties are chosen to allow comparison with the experimental and finite-element data from that work. The properties used in the elasticity solution calculations that follow are summarized in Table 1. In Table 1, the numerical subscripts for the facesheet properties (1, 2, 3) refer to the longitudinal, lateral, and transverse lamina directions while for the core properties they refer to the ribbon, lateral, and transverse directions. **X**, **Y**, and **Z** are the strengths in the longitudinal, lateral, and transverse lamina directions; subscripts t and c refer to tension and compression; and S_{ij} are the shear strengths. Five cases in which facesheet layups incorporating four, eight, 16, 32, and 48 plies per facesheet are considered. The stacking sequences for these facesheets are $(0/90)_{nS}$, with $n = 1, 2, 4, 8$, and 12, respectively. In each case, the core thickness, h_{core}, is 12.7 mm and the plate width, L, is 127 mm.

TABLE 1. Material Properties

Variables (1)	Facesheet (AS4/3501-6) (2)	Core (nomex HRH10-1/8-4.0) (3)
E_1	144.8 GPa	80.4 MPa
E_2	9.7 GPa	80.4 MPa
E_3	9.7 GPa	1.005 GPa
G_{23}	3.6 GPa	75.8 GPa
G_{13}	6.0 GPa	120.6 MPa
G_{12}	6.0 GPa	32.2 MPa
ν_{23}	0.34	0.02
ν_{13}	0.3	0.02
ν_{12}	0.3	0.25
X_t	2.17 GPa	N/A
X_c	−1.72 GPa	N/A
Y_t	53.8 MPa	N/A
Y_c	−205.5 MPa	N/A
Z_c	−205.5 MPa	3.83 MPa
S_{23}	89.3 MPa	142.3 MPa
S_{13}	120.7 MPa	177.9 MPa
S_{12}	120.7 MPa	N/A

Note: N/A stands for not available.

Sinusoidal Load, Same Material and Geometry as Test Specimens

As a first step, Pagano's solution algorithm described earlier is used with the original sinusoidal loading [(8)] but modified to permit the solution for a composite sandwich plate to be obtained. The loading in this solution is transverse pressure distributed as a half sine wave over the top surface of the plate and the supports are simple. The geometry is shown in Fig. 3. The solution of this problem is exact, within the assumptions of elasticity. Though the in-plane stress, σ_x, and displacement, u, of the finite-element methodology of Herup (1996) do not precisely follow the exact solution due to the assumed kinematics, the transverse shear and direct stresses from the finite-element solution (with equilibrium postprocessing) are within a few percent of the exact solution throughout the computational domain. If this solution were the only available benchmark for the finite-element code, the analyst would be tempted to think the finite-element solution was doing great and to trust it for the contact loading problem. Such a conclusion may prove unfounded when Hertzian contact loading is considered.

Extension for Indentation Problem

The sinusoidal load of the previous solution is distributed over the entire plate top surface, whereas the load for the impact problem is concentrated over the small portion of the top surface that is in contact with the impactor. To more accurately model the load profile of an impact problem, a truncated Fourier sine series approximation of a Hertzian contact load distribution is applied to the elasticity solution algorithm. In this case, however, a FORTRAN program is used in place of the Mathcad template because the computational effort required does not lend itself to solution within Mathcad's interactive environment. The increased computational intensity results from the fact that the problem has to be solved for each term in the odd (i.e., sine since all cosine terms vanish) Fourier series and the solutions superposed. For small contact radii, the number of Fourier terms required to accurately represent a Hertzian load can be more than one hundred. Fig. 4 shows a Hertzian load with a small contact radius (1.59 mm) and the equivalent Fourier series truncated to 50, 150, 250, and 350 terms. It should be observed in Fig. 4 that to show the differences, only the portion of the load near and to the right of center (63.5 mm < x < 67 mm) is plotted; the entire plate is 127-mm wide. The 1.59-mm contact radius is chosen for this illustration because it is typical of those measured for eight-16-, and 32-ply specimens before damage in the static indentation tests discussed in Herup [(1996), Chapter 4]. The small improvement in fidelity obtained by increasing the number of odd Fourier terms above 150 for this contact radius is not judged to be worth the significant additional computational expense. A FORTRAN program ETPSFL (elasticity theory,

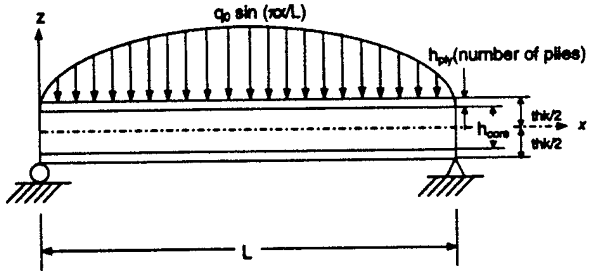

FIG. 3. Geometry for Sinusoidally Loaded Sandwich Plate in Cylindrical Bending

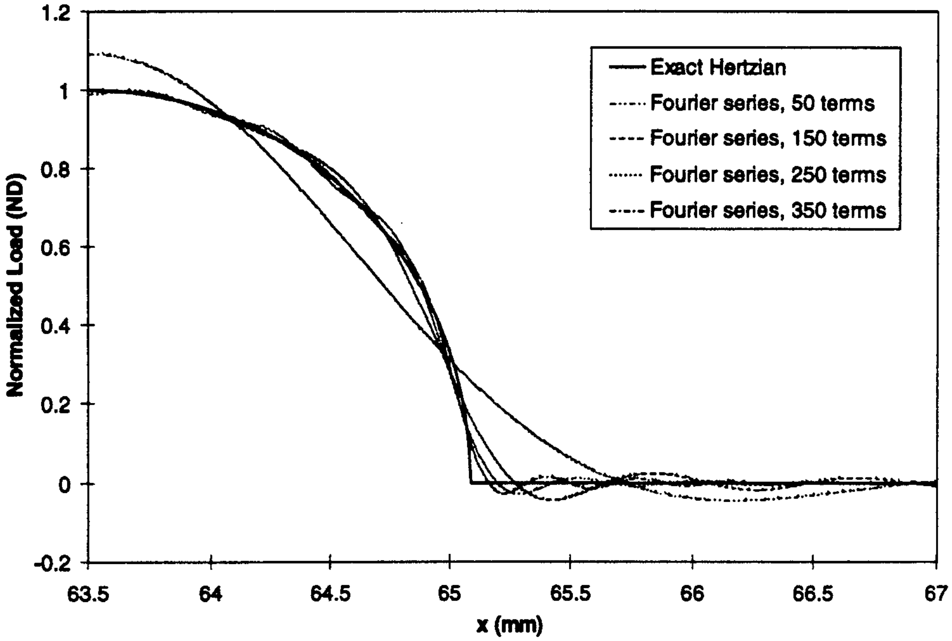

FIG. 4. Hertzian Load Approximation by Truncated Fourier Series for 1.59-mm Contact Radius Case

plane strain, Fourier load) was developed for this solution [Herup (1996), Appendix A]. As with the previous sinusoidal load, the solution of this problem is exact, within the assumptions of elasticity and for the approximated load distribution, and thus serves as a more appropriate benchmark for the computational algorithms simulating static indentation or low-velocity impact. It is compared to that obtained from the finite-element analysis of a plate strip loaded with the same truncated Fourier series load in Herup [(1996), Chapter 7].

Cylindrical Bending Solution to Hertzian Loaded Sandwich Plate

This cylindrical bending solution to a simply supported, Hertzian loaded, sandwich plate strip provides both a benchmark for the finite-element analysis before damage and a tool to judge the appropriateness of the various failure theories in the context of impact to composite sandwich structures. The cylindrical bending solution requires only a one-dimensional Fourier series for the loading, and thus hundreds of terms can be used to represent a contact-type load over a very small contact area without encountering solution matrix singularity problems associated with a two-dimensional Fourier series. Cylindrical bending elasticity solution stress data for two cross sections of the specimens (the planes defined by the 0- and 90°-ply orientation directions) will now be studied to develop a general understanding of how a contact pressure is distributed into a sandwich plate and the role that facesheet thickness plays in the process. This solution is found to be so valuable for this purpose that it suggests an entirely new study beyond the scope of this paper in which parameters such as core thickness, core stiffness, impactor radius, and facesheet material properties can all be varied and their influences presented in a usable form for designers of these structures. It is possible that rules of thumb to aid the designers in the many trade-off decisions inherent in any structural application of composite sandwich plates could result from such a study.

Fig. 5 shows the geometry of the problem and Fig. 6 shows the variation of transverse direct stress σ_z through the thickness predicted by cylindrical bending elasticity theory for the various specimens tested in the experimental portion of Herup (1996). The intuitive idea that the thicker facesheets distribute the load over a greater portion of the core and thus reduce the peak core compressive stress is both verified and quantified by these data. The top surface of the core in the four-ply specimens apparently experiences 56% of the peak applied stress, q_0, which was unity. The thicker facesheets lower the peak stress at the top of the core to such an extent that the top surface of the core in the 48-ply specimens apparently experiences only 8% of the peak applied stress.

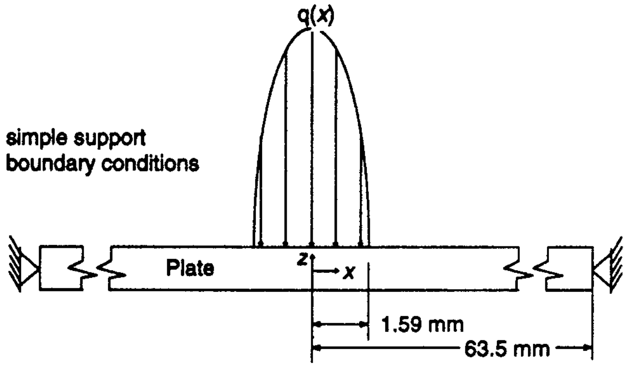

FIG. 5. Geometry for Cylindrical Bending Solution

One advantage of sandwiches with the thicker facesheets (which can be seen in Fig. 6) is that they will achieve a higher peak load before core failure occurs. This advantage is, of course, tempered by the fact that for a given impact energy, plates with the thicker facesheets experience greater loads. This is because the thicker plates are stiffer, leading to shorter contact durations and higher impactor accelerations (hence greater force, by Newton's second law). To account for this, stress data similar to Fig. 6 are scaled by the forces from low-velocity impact experimental data [Herup (1996), Chapter 4]. The experimental data provides the load and contact radius at failure (the first major load drop). In each case, an axisymmetric Hertzian distribution of the load is assumed, leading to peak stress as a function of load and contact radius. Table 2 shows the failure loads, contact radii, and peak stresses for each case. The cylindrical bending elasticity solution is obtained using the particular contact radius and peak stress from the experiment for each facesheet thickness. The transverse stress profile from this solution is an estimate of the transverse stress profile present at the first major load drop. This load drop is shown to correspond to core failure in Herup (1996). The elasticity result is plotted for each facesheet thickness in

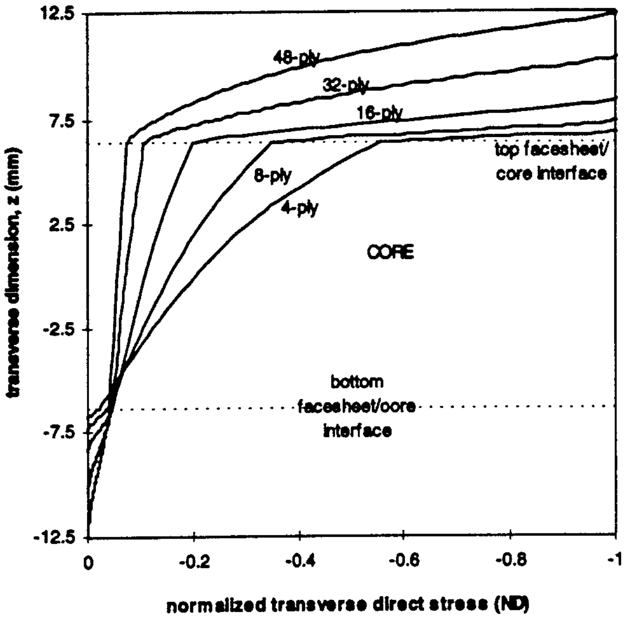

FIG. 6. Normalized Transverse Direct Stress under Center of a Hertzian Load Showing How Thicker Facesheets Serve to Reduce Compressive Stress Seen by the Core, thus Delaying Core Failure (Contact Half-Width was 1.59 mm and Normalization Is by Peak Applied Stress)

TABLE 2. Experimental Data at Failure and Hertzian Peak Stresses

Facesheet thickness (1)	Energy (J) (2)	Contact radius (mm) (3)	Failure load (N) (4)	Peak stress (MPa) (5)
Four-ply	0.30	0.96	550	285
Eight-ply	0.47	1.18	1,100	378
16-ply	1.35	1.70	2,700	446
32-ply	5.24	3.08	8,000	404
48-ply	10.08	4.51	13,500	318

Fig. 7. In this way Fig. 7 gives the elasticity solution for the transverse direct stress profile under the impactor at the instant of the first major load drop found in the experiments. The elasticity solution, when used in conjunction with the experimental data, allows the analyst to estimate the stress present in each specimen when the failure occurs.

The scaling of Fig. 7 allows another point to be observed. The only compression strength data available for the core is from uniaxial compression and shear tests (Bitzer 1983). Uniaxial compression strength is shown as the vertical line in Fig. 7. In the experiments [Herup (1996), Chapter 4], core failure always occurs near the interface between the core and the top facesheet. As facesheet thickness increases, Fig. 7 clearly indicates that the transverse compressive stress associated with the first major load drop decreases at the interface between the core and the top facesheet. None of the specimens, however, apparently experience core failure until this stress was well above the uniaxial core strength. This suggests that a maximum stress failure criterion incorporating uniaxial core strength is highly conservative for predicting core failure. The error decreases with increasing facesheet thickness, but is significant for all facesheet thicknesses tested. Other criteria incorporating shear are not expected to significantly improve upon maximum stress either, since both transverse and in-plane shear are zero at the center. This presents a potentially critical problem to any analysis intending to predict core failure based upon stress using a uniaxial strength as the criterion for failure. A semiempirical maximum stress failure criterion

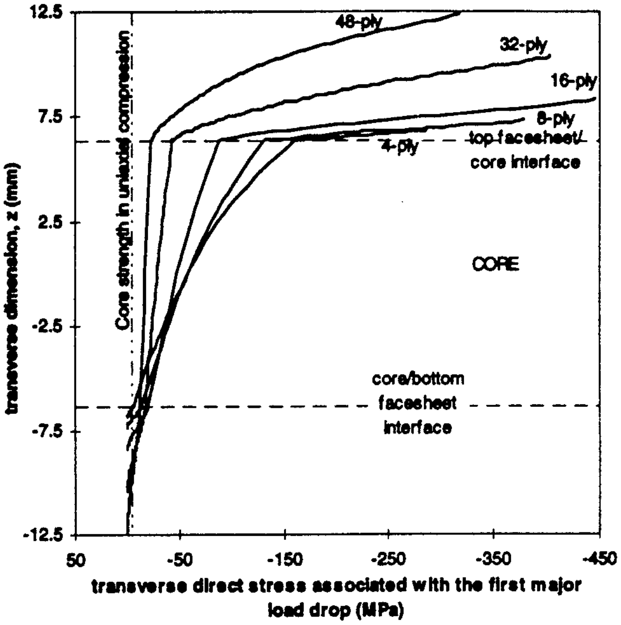

FIG. 7. Transverse Direct Stress under Center of a Hertzian Load Scaled to Match Peak Stress and Contact Radius for First Major Load Drop Seen in Experiments (for Comparison, Uniaxial Core Strength Is also Plotted Indicating the Core Achieves a Stress Higher Than Its Uniaxial Compression Strength before Failure)

incorporating a facesheet-thickness-dependent core strength is given in the following:

$$\text{apparent core strength} = \bar{\sigma}_z \frac{3}{2\pi} \frac{F_{\text{fail}}}{R^2_{\text{contact}}} \tag{17a}$$

$\bar{\sigma}_z$ = transverse direct stress at top of core normalized by peak applied stress (from elasticity solution) (17*b*)

F_{fail} = load at first major load drop (empirical) (17*c*)

R_{contact} = contact radius at first major load drop (empirical) (17*d*)

$\frac{3}{2\pi R^2_{\text{contact}}}$ = load to peak stress conversion factor for Hertzian contact (17*e*)

The semiempirical maximum stress failure criterion given in (17) allows the analyst to predict core failure from the stress at the top surface of the core. By providing the through-the-thickness transverse direct stress profile, the cylindrical bending elasticity solution bridges the gap between the experimental data and the needed core strengths. Fig. 8 shows the

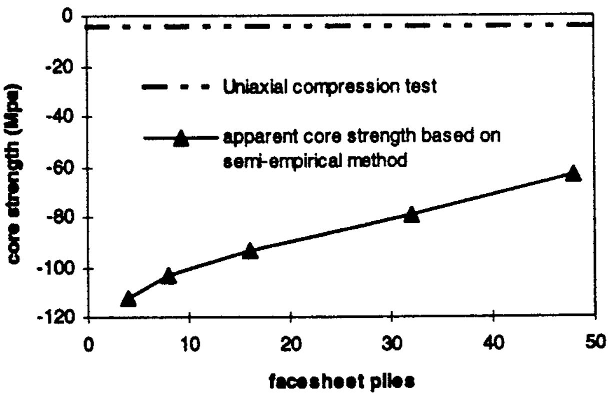

FIG. 8. Apparent Core Strength as Calculated by Eq. (17)

semiempirical apparent core strength as a function of facesheet thickness for the current structure.

Fig. 9 shows the in-plane stress, σ_x, normalized by the peak applied stress for the cylindrical bending elasticity solution. The first and most obvious bit of information to gain from this scaling is that thicker facesheets lead to lower in-plane loads for static indentation problems. This comes as no surprise since thicker facesheets imply that the same load can be spread out over more plies, reducing the average stress in each ply. More interesting in Fig. 9 is the insight that can be gained about the relative importance of local (top facesheet) and global (entire sandwich) bending. Pure local bending is characterized by the linear variation of σ_x through the top facesheet thickness and would show a neutral axis at the midplane of the top facesheet. On the other hand, pure global bending is characterized by a linear variation of σ_x through the entire sandwich and would show a neutral axis in the middle of the core. An effect of adding global bending σ_x to a local bending σ_x profile would be to move the neutral axis down. The position of the apparent neutral axis (z-coordinate at which σ_x passes through zero) in the top facesheet is thus an indicator of the relative magnitudes of the local and global stresses. When the apparent neutral axis is at the midplane of the top facesheet, global stresses are not important. As the apparent neutral axis shifts down, global stresses become more important. When the apparent neutral axis is at the bottom of the top facesheet, global and local stresses are contributing approximately equal amounts to the overall stress profile. Considering first the four-ply data of Fig. 9, one can see that the apparent neutral axis is near the bottom of the top facesheet. Thus global plate bending is important to the four-ply in-plane stress σ_x. Increasing facesheet thickness shifts the apparent neutral axis up (note that it is at the midplane of the top facesheet in the 48-ply data). This is because increasing facesheet thickness increases the global bending stiffness much faster than it does the local facesheet bending stiffness because of the proportionalities shown in the following equation. This explains the fact that the data in Fig. 9 show progressively more local bending stress and relatively less global bending stress as the facesheet thickness increases

$$\Delta \text{ local (facesheet) bending stiffness} \propto \left(\frac{\Delta \text{ facesheet thickness}}{2}\right)^3 \tag{18a}$$

while, Δ global (plate) bending stiffness

$$\propto \left(\frac{h}{2} + \Delta \text{ facesheet thickness}\right)^3 \tag{18b}$$

$$\text{where, typically, } \frac{h}{2} >> \Delta \text{ facesheet thickness} \tag{18c}$$

The last observation from Fig. 9 is that the top facesheet does have more local bending than the bottom facesheet for all of the facesheet thicknesses. This is the expected result because the core serves to relax the coupling between the bottom and top facesheet motions so the radius of curvature of the bottom facesheet is greater than that of the top.

Since σ_x is the principal contributor to fiber failure and has little contribution to the other failure mechanisms, the preceding comments apply almost directly to the influence of facesheet thickness on fiber failure. Fig. 10 scales the data of Fig. 9 to show estimates for the fiber stresses at the applied load that produced the first major load drop. This alarming plot indicates that sandwich plates of all the facesheet thicknesses should have shown fiber failure prior to the major load drop, whereas fiber failure was not observed in the specimens when they were sectioned, polished, and viewed under magnification (Harrington 1994). Also, the peak compressive fiber stress occurs at the top surface of the plate and the significant fiber failure indicated by Fig. 10 should be observable on the surface even without sectioning the specimen. No such failure

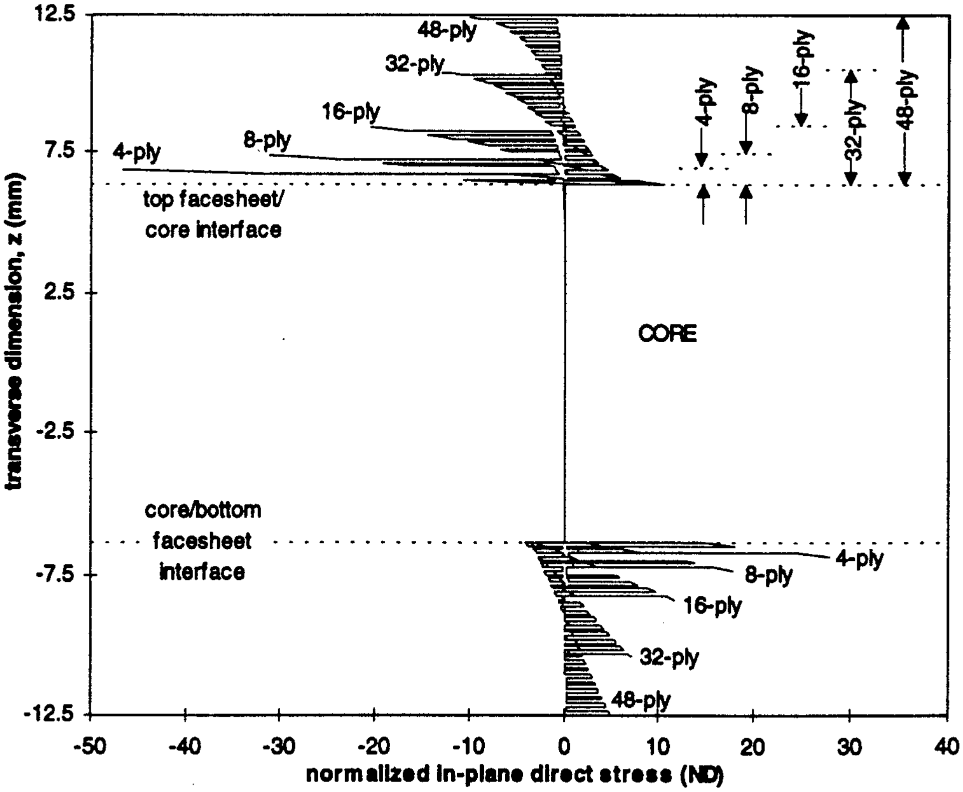

FIG. 9. In-Plane Direct Stress under Center of a Hertzian Load Normalized by Peak Applied (Transverse) Stress Showing Reduction in In-Plane Stress Brought about by Thicker Facesheets (Contact Half-Width was 1.59 mm and Normalization is by Peak Applied Stress)

was observed in Herup (1996) or Harrington (1994). These data indicate that maximum stress may be an overly conservative criterion for fiber failure, but since no fiber failure has been observed in the experiments, ignoring this potential failure mechanism may be justifiable on that basis.

Transverse shear stress is the dominant driver for matrix cracking and delamination. Unlike fiber failure, these damage mechanisms have been observed extensively in all the damaged specimens. Unlike transverse or in-plane direct stress, shear does not have a peak in the center of the plate. To locate the x-dimension of the peak of transverse shear, as well as to show the x-dependence of transverse shear, the shear at the midplane of the top facesheet is plotted against the x-dimension in Fig. 11.

Fig. 11 shows that increasing the thickness of the facesheets has at least three important effects on transverse shear and, therefore, on both delamination and transverse matrix cracking. The first, and most dramatic, is the reduction in the peak value that will serve to delay initiation of damage. The second is that it moves the peak value away from the plate center so the damages will be initiating from a location further from the point of application of the load. The third is that the peaks are broadened and flattened so that damage will not be as well defined and repeatable. These conjectures are based on the assumptions that shear dominates the initiation of damage and that damage can occur when shear is within some range and not only at a specific value. Thus a broad, flat peak puts a relatively large portion of the facesheet within the critical stress range and matrix cracking and delamination initiation may start from anywhere within that range. Once started, strain energy released in the process of damage, load redistribution, and stress singularities at the crack tips will bias the progression of the damage in a way that is dependent on the initiation point. Though simplistic, these ideas do explain why the C-scans show damage in thin facesheet specimens, impacted at the same energies that are more consistent than those of thick facesheet specimens [Herup (1996), Chapter 4]. C-scans from thin facesheet specimens also show more bidirectional symmetry in the delamination patterns, which is consistent with these ideas.

Normalized transverse shear stress at the x-location of the peaks in Fig. 11 is plotted through the thickness in Fig. 12. This figure shows very clearly why delaminations and matrix cracks are found in the top facesheets but not in the bottom facesheets. These data are scaled to the first major load drop values in Fig. 13. This figure indicates that for the thin facesheet specimens facesheet damage in the form of matrix cracking and/or delaminations should precede core failure if indeed the major load drop is an indicator of core failure as found in Herup [(1996), Chapter 4].

THREE-DIMENSIONAL SOLUTION TO HERTZIAN LOADED PLATE

The difficulties found in relating a cylindrical bending solution to a truly three-dimensional problem could have been avoided if a true three-dimensional elasticity solution was available. Such a solution for a rectangular sandwich plate under a sinusoidal loading does indeed exist (Pagano 1970). This solution is a valuable tool for benchmarking finite-element or other approximate analyses. A Mathcad template was written to carry out the very burdensome manipulations and is included in Appendix A of Herup (1996). The low-velocity impact problem differs from the sinusoidally loaded plate chiefly in the relative area over which the load is applied. The Fourier series representation of the Hertzian contact load used in the cylindrical bending solution suggests the possibility of applying a double Fourier series to the three-dimensional plate

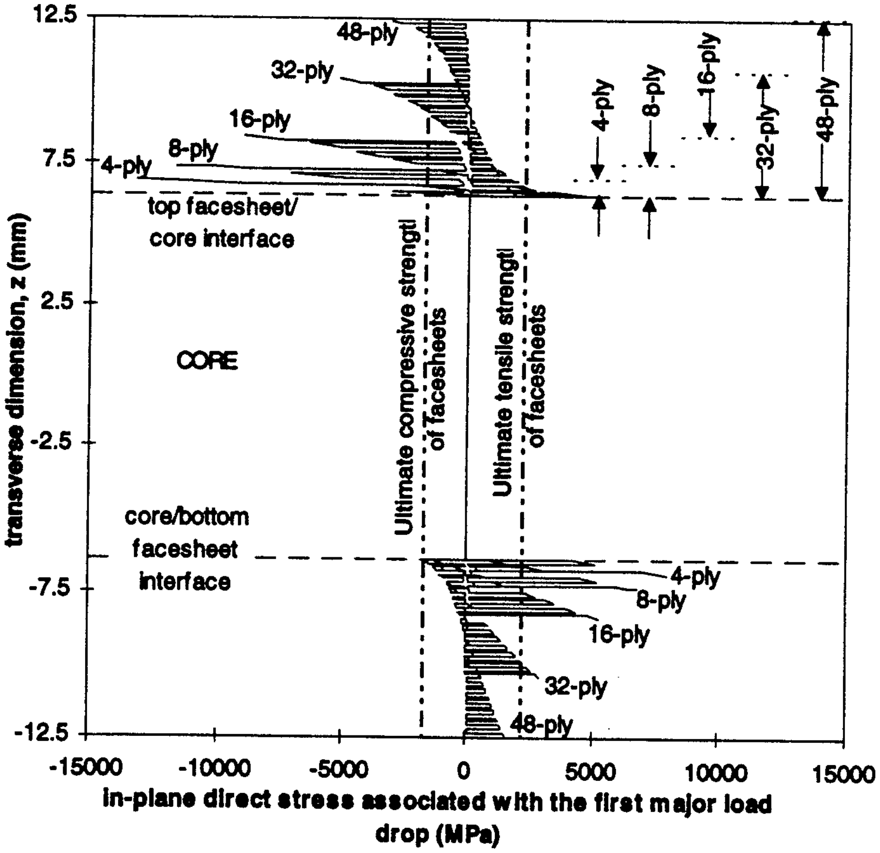

FIG. 10. In-Plane Direct Stress under Center of a Hertzian Load Scaled to Show Values for First Major Load Drop Seen in Experiments (for Comparison, Ultimate Tensile and Compressive Strengths of Facesheets are also Plotted Indicating the Facesheets Achieve a Stress Higher than Ultimate Strength before First Major Load Drop)

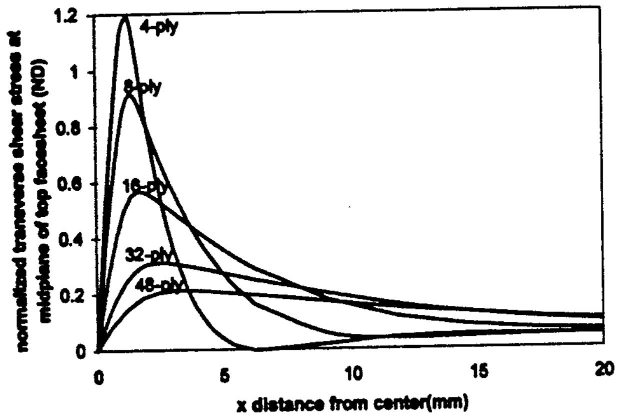

FIG. 11. Normalized Transverse Shear Stress in Midplane of Top Facesheet Showing How Thicker Facesheets Serve to Reduce Peak Transverse Shear Stress and Move Its Location Away From Center of the Plate (Contact Half-Width was 1.59 mm and Normalization Is by Peak Applied Stress)

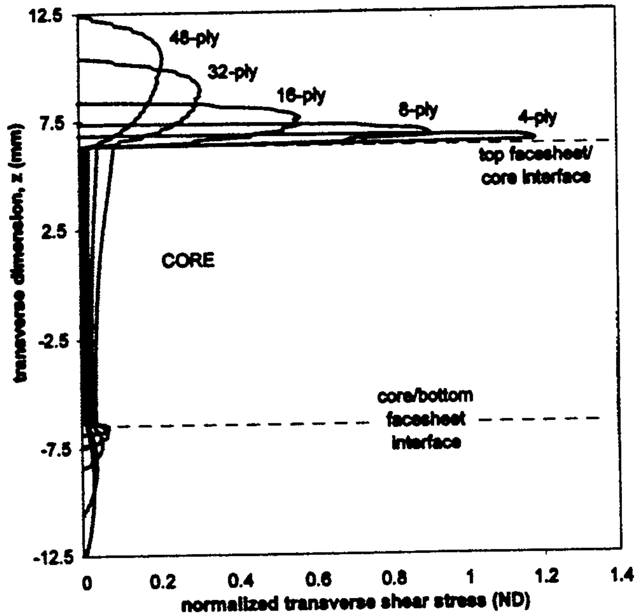

FIG. 12. Transverse Shear Stress at Location of Peaks Found in Fig. 11, Normalized by Peak Applied (Transverse) Stress, showing Reduction in Transverse Shear Stress Brought about by Thicker Facesheets (Contact Half-Width was 1.59 mm)

to approximate the contact load. This is nothing more than extending the cylindrical previously described bending solution to a third dimension. Yet, there are some difficulties. The coding of the solution is an extension of the program ETPSFL written for the cylindrical bending solution. A FORTRAN program called PAG3D (Pagano's three-dimensional) was written using, as much as possible, various names that suggest what they represent in Pagano (1970). PAG3D is included in Appendix B of Herup (1996), and its output is compared to the finite-element solution of Herup. A severe limitation to the usefulness of the three-dimensional solution for low-velocity impact problems should be pointed out first; when the large number of odd Fourier terms needed to accurately represent an axisymmetric Hertzian contact load is used, the matrix solver fails because the coefficient matrix becomes numerically singular. As applied to the three-dimensional problem, the solution procedure outlined effectively limits the number of odd Fourier terms that can be used to represent the Hertzian load to eight in each in-plane direction or 64 total terms. It is possible that a modified procedure in which the direct matrix inversion of (15) is avoided could relieve this limitation, but such a procedure is not attempted for this research. The actual maximum number of odd Fourier terms is larger (11 × 11) for thin facesheet sandwiches and even larger (25 × 25) for thin monolithic laminates representative of the facesheets alone, but is considered inadequate to represent the load that was applied experimentally. The loads are shown in Fig. 14.

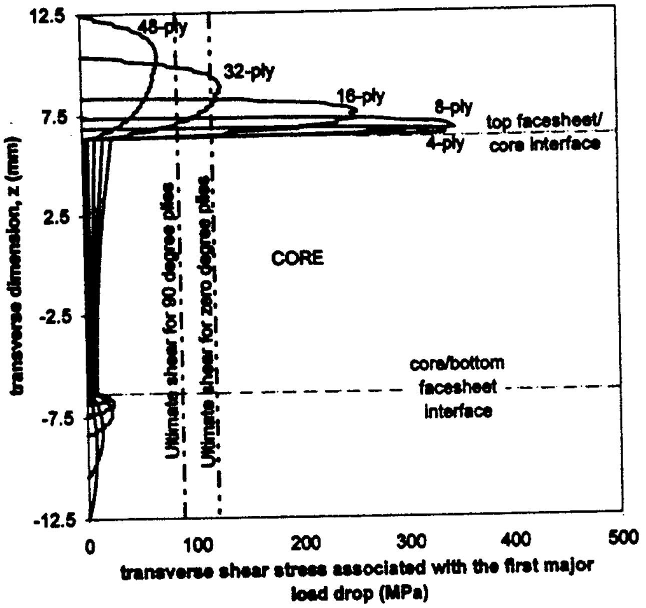

FIG. 13. Transverse Shear Stress at Location of Peaks Found in Fig. 11, Scaled to Show Values for First Major Load Drop Seen in Experiments (for Comparison, Ultimate Shear Strengths of the 0 and 90° Plies of the Facesheets are also Plotted Indicating that for Most Facesheet Thicknesses a Maximum Stress Criteria Would Indicate Matrix Cracking before First Major Load Drop)

A Hertzian load that can be marginally well represented by a double Fourier series truncated to a few terms is shown in Fig. 15. The contact radius of this load is 12.7 mm as compared to the more representative 1.59-mm contact radius of Fig. 14. This large contact radius implies an unrealistic tup radius (many meters) rather than the 12.7-mm experimental tup radius. In short, the three-dimensional elasticity solution cannot be used to interpret experimental data as the cylindrical bending elasticity solution can, because the contact radius of the two cannot be matched. Without matching contact radii, the applied pressure (and hence σ_z) for any given applied load are very different. Thus, any comparison between the experiment and the analysis would be meaningless. Even so, the three-dimensional elasticity solution with this large contact radius does provide a benchmark for approximate solutions such as the finite-element code of Herup (1996) because the loading on the finite-element model can be matched to the truncated Fourier series for which the three-dimensional elasticity problem can be solved. That is, though a low-velocity impact experiment cannot be modeled by the three-dimensional elasticity solution, it is nevertheless useful as a benchmarking tool for approximate solutions that are intended to model the experiment. This application is illustrated in the following.

COMPARISON OF FINITE-ELEMENT AND THREE-DIMENSIONAL ELASTICITY SOLUTIONS

The purpose of this section is to compare the results of the finite-element analysis described in Herup [(1996), Chapter 6] to the elasticity theory results obtained from the modified Pagano solution described earlier. In particular, the stress available from local (facesheet on an elastic foundation) and global (sandwich) models are compared to the elasticity solution. One facesheet thickness (16-ply) is chosen for comparison here.

The test case shown here is for the three-dimensional bend-

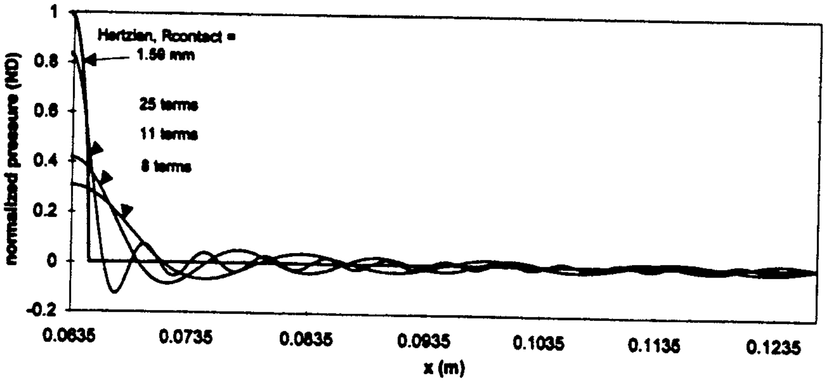

FIG. 14. Truncated Fourier Sine Series Representations of Hertzian Contact with 1.59-mm Contact Radius Showing Poor Representation of Loading with the Number of Terms for Which a Three-Dimensional Solution was Available [Maximum Number of Terms for a Sandwich was 11 (Four-ply)]

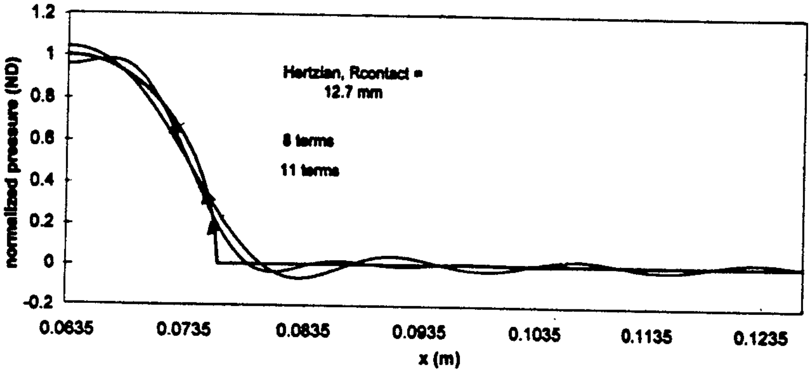

FIG. 15. Truncated Fourier Sine Series Representations of Hertzian Contact with 12.7-mm Contact Radius Showing Marginal Representation of Loading with the Number of Terms for Which a Three-Dimensional Solution was Available

ing of a square plate. The load is located in the center of the plate and is Hertzian in its distribution (as approximated by a Fourier sine series), simulating contact with a spherical indentor (or impactor) located at the center of the plate and moved transverse to the plane of the plate. The applied stress is axisymmetric about the z-axis (Fig. 1). In the finite-element–based analysis methodology, a sandwich plate is modeled using plate bending elements loaded with a Hertzian contact load. Two different models are actually studied, a local model and a global model. In the local model, the top facesheet is modeled with monolithic plate elements on an elastic-plastic foundation (simulating the core). In the global model, both facesheets and the core are modeled by a sandwich element having stiffness contributions from each.

To benchmark the finite-element analysis with a three-dimensional elasticity test case, the 8 × 8-term double Fourier sine series representation of the 12.7-mm radius Hertzian contact load illustrated in Fig. 15 is used. To be sure the problem remains in the elastic regime, the total force applied is 1.0 N. The finite-element model is loaded with a Hertzian contact load having a 12.7-mm radius and the same total force. In Figs. 16–18, the 16-ply results are shown for both the global (sandwich) and the local (plate on elastic foundation) models. The displacements for the global and local finite-element models are not comparable because of the very different nature of the restraints (simple supports versus simple supports plus elastic foundation). Nevertheless, the top facesheet stresses are comparable. The top facesheet stresses are shown in Figs. 16–18.

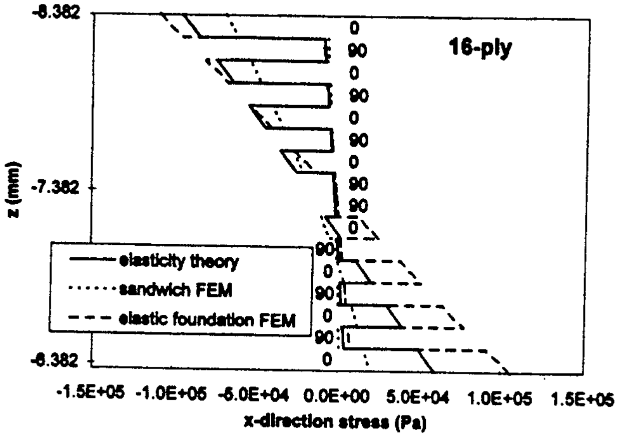

FIG. 16. Comparison of Top Facesheet In-Plane Direct Stress, σ_x, at the Center of the Plate for the Large Contact Radius, Three-Dimensional Case (12.7-cm-Square Sandwich Plate, 16-Ply Facesheets, 1.0-N Load, 12.7-mm Contact Radius)

Fig. 16 shows how the in-plane stresses compare between the finite-element models and the three-dimensional elasticity solution. As expected, the 0° plies, having much greater x-direction stiffness than the 90° plies, are shown to take the majority of the load. Although the primary damage mechanism driven by in-plane stress is fiber failure (in compression near the top surface), depending on the damage criteria chosen, matrix cracking could also be affected. Taking the elasticity solution to be the correct one (within the approximation of the Hertzian load and the assumption that the material behaves elastically), it can be seen that the elastic foundation (local) solution is significantly better than the sandwich (global) solution, particularly near the top surface where fiber failure will presumably begin. An interesting observation that can be made from Fig. 16 is that the elasticity solution shows the stress in the 0° plies to be almost linearly related to z in the top facesheet. The elastic foundation finite-element solution is able to model this feature because the cubic kinematics (Palazotto and Dennis 1992) can represent a linear function and only the top facesheet is in the model. The sandwich finite-element

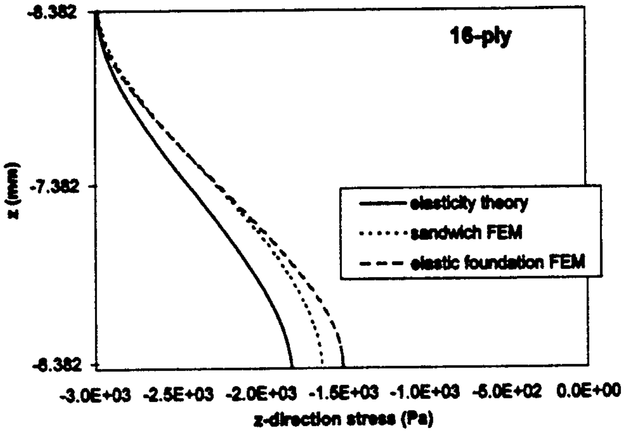

FIG. 17. Comparison of Top Facesheet Transverse Direct Stress, σ_z, at the Center of the Plate for the Large Contact Radius, Three-Dimensional Case (12.7-cm-Square Sandwich Plate, 16-Ply Facesheets, 1.0-N Load, 12.7-mm Contact Radius)

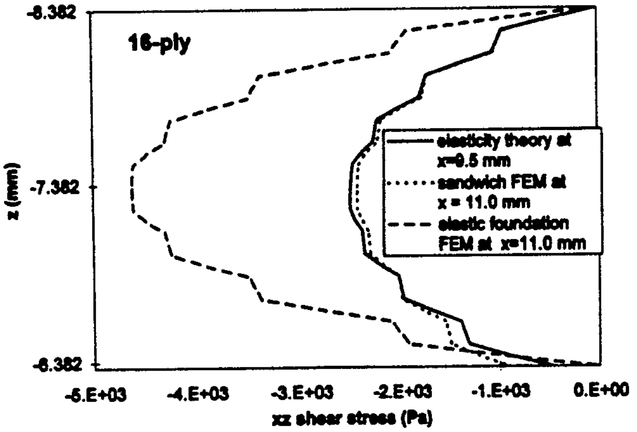

FIG. 18. Comparison of Top Facesheet Transverse Shear Stress, τ_{xz}, at Location of Peak for the Large Contact Radius, Three-Dimensional Case (12.7-cm-Square Sandwich Plate, 16-Ply Facesheets, 1.0-N Load, 12.7-mm Contact Radius)

model is not able to represent a linear function through the thickness of the top facesheet, because the core and bottom facesheet represent significant property variation through the thickness, and thus require the familiar "zig-zag" kinematic relationship, which is not well represented by the cubic kinematics in the model. It is true that the properties vary through the thickness within the facesheets, but since the lamina are thin and many, the error associated with averaging their properties through the facesheet thickness is small. Thus, in a gross sense, the sandwich behaves as a three-ply laminate in which the two facesheets are considered to be represented by two stiff plies and the core is a single flexible ply between them. The in-plane displacement of such a laminate is known to take on a Z shape (Pagano 1969, 1970) which is not well approximated by a cubic. For this reason, it is thought that including zig-zag kinematics could improve the in-plane stresses of the sandwich model, but that the elastic foundation model would be less drastically improved. This is an example of the insight available from the present three-dimensional elasticity solution.

Fig. 17 shows that σ_z for the large contact radius case is marginally well predicted by either the sandwich or the elastic foundation model. It can be observed that the sandwich model does somewhat better than the elastic foundation, but either one will be nonconservative for a stress-based core failure prediction since the σ_z at the bottom of the top facesheet ($z = -6.35$ mm) is identical to the stress at the top of the core. Thus, the low prediction of core stress will presumably result in a high prediction of core crushing load if a stress-based criteria for core failure is used.

For the 16-ply large contact radius case, Fig. 18 shows the transverse shear stress, τ_{xz}, through the thickness at the x-location of the peak transverse shear stress (and $y = 0$). This location is between 9.5 and 11.0 mm away from the plate centerline. As shown for a smaller contact radius in Fig. 11, the transverse shear stress is zero at the plate centerline but grows quickly in the x-direction, attaining a peak near the edge of the applied load (12.7 mm in this case). While the sandwich finite-element model prediction is slightly low, the elastic foundation model prediction is very high. This result, combined with that of Fig. 17, indicates that for the large contact radius case, the sandwich model produces a better three-dimensional stress result that the elastic foundation model, albeit nonconservative for shear. Both models correctly predict that the peak shear is in the middle two 90° plies.

The three-dimensional stresses obtained from the equilibrium equations and the in-plane finite-element stresses compare favorably with the elasticity solution. The sandwich (global) model does reasonably well for the case in which the load is distributed over a large portion of the top surface, but for the small contact radius case, the elastic foundation (local) model does better. Again, this insight is only available because of the existence of the current three-dimensional elasticity solution.

CONCLUSIONS

The elasticity solution is a useful tool for developing a general understanding of the characteristics of the stress field produced in a composite sandwich plate by a contact-type load. While the three-dimensional solution can only be used for unrealistically large contact radii, the cylindrical bending solution can be used for realistic contact dimensions. The cylindrical bending has been shown to provide insight into the experimentally observed phenomena. In particular, the role of facesheet thickness in determining the core failure load was evident. The three-dimensional solution has been shown to be a valuable discriminator between different approximate solution methodologies.

ACKNOWLEDGMENTS

The project was sponsored by William Baron of the Flight Dynamics Directorate of Wright Laboratories.

APPENDIX I. REFERENCES

Bitzer, T. N. (1983). "Honeycomb toughness and proportional limits." *Hexcel Corp. Rep. LSR 932277.*

Greszczuk, L. B. (1982). "Damage in composite materials due to low velocity impact." *Impact dynamics*, Krieger Publishing Co., Malabar, Fla., 55–93.

Hackman, L. E. (1965). "Sandwich construction and design." *Analysis and design of flight vehicle structures*, E. F. Bruhn, ed., Tri-State Offset Co., c12.1–c12.52.

Harrington, T. M. (1994). "An experimental investigation of sandwich panels under low velocity impact," MS thesis, AFIT/GAE/ENY/94D-22, School of Engrg., Air Force Inst. of Technol. (AU), Wright-Patterson AFB, Ohio.

Herup, E. J. (1996). "Low-velocity impact on composite sandwich plates," PhD dissertation, AFIT/DS/ENY/96-11, School of Engrg., Air Force Inst. of Technol. (AU), Wright-Patterson AFB, Ohio.

Pagano, N. J. (1969). "Exact solutions for composite laminates in cylindrical bending." *J. Comp. Mat.*, 3, 398–411.

Pagano, N. J. (1970). "Exact solutions for rectangular bidirectional composites and sandwich plates." *J. Comp. Mat.*, 4, 20–34.

Palazotto, A. N., and Dennis, S. T. (1992). *Nonlinear analysis of shell structures.* Am. Inst. of Aeronautics and Astronautics (AIAA), Washington, D.C., AIAA Education Ser.

Rhodes, M. D. (1975). "Impact fracture of composite sandwich structures." *Proc., 16th Struct., Struct. Dyn., and Mat. Conf., AIAA Paper, No. 75-748*, 1–9.

Rhodes, M. D. (1975). "Impact tests on fibrous composite sandwich structures." *NASA Tech. Memo. 78719*, Nat. Aeronautics and Space Admin. (NASA), Washington, D.C., Scientific and Tech. Information Ofc. Ser.

Schoeppner, G. A. (1994). "Low velocity impact response of tension preload composite laminates." *Proc., 10th DOD/NASA/FAA Conf. on Fibrous Comp. in Struct. Des.*, VIII-47–VIII-61.

APPENDIX II. NOTATION

The following symbols are used in this paper:

$\mathbf{AA}$ = solution vector ($4m \times 1$);
A_{ji} = constants chosen to satisfy the governing equations;
$a_i b_i c_i$ = ith lamina constitutive terms;
$\mathbf{B}$ = matrix used to satisfy boundary and lamina interface continuity conditions ($4m \times 4m$);
$\mathbf{BC}$ = boundary-condition vector ($4m \times 1$);
$\mathbf{E}_i$ = lamina modulus in the i direction;
F_{fail} = load at first major load drop (empirical);
$f_i(z)$ = exponential functions chosen to satisfy the governing equations;
$\mathbf{G}_{ij}$ = lamina shear modulii;
h = monolithic plate thickness;
h_i = ith lamina thickness;
h_{core} = sandwich plate core thickness;
h_{ply} = sandwich plate face-sheet lamina thickness;
L = plate width;
m = number of orthotropic layers in the laminate;
m_{ji} = ith lamina constitutive term;
p = π divided by plate width;
$q(x)$ = applied normal traction;
q_0 = amplitude of applied normal traction;
R_{ij} = reduced compliance coefficients for plane strain;
R_{contact} = contact radius at first major load drop (empirical);
S_{ij} = lamina shear strengths;
S_{ij} = compliances with respect to the axes of material symmetry;
thk = sandwich plate thickness;
u = displacement in the x-direction;
w = displacement in the z-direction;
$\mathbf{X}$ = lamina strength in the longitudinal (fiber) direction;
x, y = plate in-plane coordinates (global system);
x_i = ith lamina in-plane coordinate (local system);
$\mathbf{Y}$ = lamina strength in the lateral direction;
$\mathbf{Z}$ = lamina strength in the transverse (z) direction;
z = plate transverse coordinate measured from the neutral axis;
z_i = ith lamina transverse coordinate measured from the center of the lamina (local system);
ε_x = in-plane direct strain;
ε_z = transverse direct strain;
γ_{xz} = transverse shear engineering strain;
ν_{ij} = lamina Poisson ratios;
σ_x = in-plane direct stress;
σ_z = transverse direct stress;
$\bar{\sigma}_z$ = normalized transverse direct stress at top of core (from elasticity solution); and
τ_{xz} = transverse shear stress.

ATTACHMENT V

FINITE ELEMENT ANALYSIS OF LOW VELOCITY IMPACT ON COMPOSITE SANDWICH PLATES

FINITE ELEMENT ANALYSIS OF LOW-VELOCITY IMPACT ON COMPOSITE SANDWICH PLATES

A. N. Palazotto, E.J. Herup and L.N.B. Gummadi
Air Force Institute of Technology, Wright-Patterson AFB, Ohio 45433

Abstract

The response of composite sandwich plates to low-velocity impact is predicted by a displacement based, plate bending, finite element algorithm. 5th order Hermitian interpolation allows three-dimensional equilibrium integration for transverse stress calculations to be carried out symbolically on the interpolation functions so that transverse stresses within the elements are expressed directly in terms of nodal quantities. Nomex honeycomb sandwich core is modeled using an elastic-plastic foundation and contact loading is simulated by Hertzian pressure distribution for which the contact radius is determined iteratively. Damage prediction by failure criteria and damage progression via stiffness reduction are employed. Comparison to experimental low-velocity impact and static indentation data shows the ability to model some of the important features of static indentation of composite sandwich structures. In particular, the slope of the load displacement curve (stiffness), including contact, before damage is well represented. Core failure load is predicted by the analysis within ten percent of the experimental value. Delamination patterns predicted by the analysis are similar in shape to the delaminations observed by C-scans from the experiments, but are smaller for the same load.

Introduction

Sandwich structures have long been recognized as one of the most weight-efficient plate or shell constructions for resisting bending loads[1]. The aerospace industry, with its many bending stiffness dominated structures and its need for low weight, has employed sandwich constructions using aluminum honeycomb cores extensively. The most common currently fielded sandwich constructions suffer from two major maintenance problems: corrosion damage to the core from trapped moisture, and low-velocity impact damage. The core corrosion problem can be greatly reduced by using a non-corrosive core such as Nomex honeycomb. Prediction of low-velocity impact damage to such structures is the subject of the present research. Low-velocity implies that strain rate dependencies of the material properties can be neglected. This assumption is made for the current research.

Closed-form methods for predicting the response of laminated composite plates to mechanical loads are limited to linear solutions (with many simplifying assumptions) for specific geometries, lay-ups, loads, and boundary conditions. Experimental testing can yield response data for a particular plate and load, but it is not generally practicable, in terms of time and monetary expense, to experimentally characterize the effects of a wide range of variables. In contrast to experimental testing, numerical techniques like the finite element method (FEM) have been applied to plates and shells of different shapes, sizes, compositions, loadings and supports without the expense and lead time required for testing. The accuracy and practicality of FEM are dependent on the governing theories, model complexity, mesh refinement, user's skill (in the representation of the geometric structures, material properties, boundary conditions and loads), and a given computer's memory capacity, speed, and precision. The failure modes commonly observed in low-velocity impact to composite sandwich plates (fiber failure, matrix cracking, delamination, core crushing[2]) are driven by three-dimensional stress states. This implies that any model representing low-velocity impact to composite sandwich plates should be capable of accurately predicting three-dimensional stresses. The obvious approach is to employ a three-dimensional FEM, but the detail required in such a model very quickly overwhelms the computational capacity available to the analyst. A two-dimensional FEM that can accurately represent low-velocity impact to composite sandwich structures can dramatically reduce the computational expense. The review papers of Cantwell and Morton[3] and Abrate[4] are excellent starting points for review of the low-velocity impact resistance of monolithic laminates as are the "Previous Work" chapter of Tsang's Ph.D. thesis[5] and the review paper of Noor et al[6] for composite sandwich structures.

The finite element program developed for this research is capable of modeling composite sandwich plates while extracting quasi three-dimensional stress values by employing the differential equations of equilibrium for a deformable continuous body[7]. Geometric nonlinearity and transverse shear effects are modeled. Contact between the plate and the impactor is also modeled. Damage initiation and progression criteria are employed,[8-11] and the code reduces the stiffness of the damaged elements to model the effects of matrix cracking, delamination, fiber failure, and core crushing damage progression.

Approach

The approach for this effort involves a local/global method. The local model represents a single facesheet and its supporting core by plate finite elements (the facesheet) with an elastic foundation (the core). The global model represents the entire sandwich structure by plate finite elements in which the facesheets and the core contribute to the stiffness of each element. In both cases the plate elements incorporate cubic kinematics and in the local model a post-processing algorithm integrates three-dimensional equilibrium equations producing a quasi three-dimensional stress tensor. Contact between the plate and the tup is assumed to produce a Hertzian pressure distribution under the tup. In the local model, the transverse strains (obtained from the three-dimensional stresses) are integrated to establish the contact surface between the plate and the impactor. The contact radius is a product of the local model and is obtained through an iterative algorithm in which the three-dimensional shape of the top surface of the plate under the load is made to conform to the known shape of the tup. In this way, an iterative scheme produces a stress field satisfying compatibility (via the plate finite element model), the contact problem, and the approximately satisfying the three-dimensional differential equations of equilibrium for the plate.

Once this contact radius is known from the local model, it establishes the distribution of load on the global model since the total force is known for the given load increment and the form of the distribution of the force is assumed to be Hertzian. The sandwich plate (global) FEM is then run to obtain the midplane displacement of the sandwich. This is required because the local model includes no sandwich plate midplane displacement and it is desired to compare displacement with the experimental data. In particular, the top surface displacement is taken to be the sum of the top surface displacement in the local model (for which sandwich midplane displacement was zero) and the midplane displacement from the global model.

The six components of stress within the top facesheet resulting from this procedure are used with failure criteria to update the constitutive relationship in the local finite element model. When the transverse load of the plate reaches sufficient magnitude, the failure criteria indicate localized failure of the composite sandwich structure via fiber failure, matrix cracking, and delamination. The displacement from the local finite element model establishes an average core stress by an empirical elastic-plastic relationship between core strain and core stress derived from the core manufacturer's uniaxial compression test data.[10] This core stress provides the foundation pressure distribution that supports the facesheet. The displacement from the local finite element model divided by the core thickness is taken to be the average core strain. The failure of the core is predicted by a simple maximum strain criteria in which the core is assumed to fail (core crushing/crippling) when the strain reaches the magnitude of the failure strain in a uniaxial compression test[10]. In this way, appropriate failure criteria[11] estimate both the modes and extent of the failure at any given load increment. As the individual plies or interfaces fail, a stiffness reduction routine simulates the varying material response, smearing the effect of the damage over the damaged element(s). As the core fails, the foundation stiffness for a given element is reduced to simulate the fact that a crushed/crippled core does not provide transverse support to the facesheet.

Theory

The element-independent portion of the finite element development as well as the geometric nonlinear iteration method applied for this research have been documented previously[12,13]. Only the new developments will be considered in the following paragraphs.

Geometry and coordinate systems

Figure 1 illustrates the geometry and coordinate systems which were used for modeling sandwich plates. The facesheets are composite laminates of arbitrary stacking sequence. The facesheets are perfectly bonded to an assumed homogeneous core of Nomex honeycomb. Both X-Y-Z (X_1-X_2-X_3) and L-T-Z represent orthogonal systems. The longitudinal and lateral directions correspond to the principal material directions of an orthotropic ply. As shown in Fig. 1, a ply's orientation angle θ is the angle from X to L (or from Y to T). All plates analyzed in this research were symmetric about their midplanes (z=0), that is, $\theta(z) = \theta(-z)$. This symmetry was chosen for convenience; it is not required by the theory.

Plate assumptions

Several assumptions are inherent in most plate analyses and are retained or relaxed in the present research. A plate is assumed to be in a state of plane stress at distances from the datum surface. As a result, all transverse normal stresses σ_{zz} are zero, and plate behavior can be described by displacements and rotations at and relative to the midsurface. Transverse normal strains ε_{zz} are nonzero in general, but they are consequences (due to Poisson effects) of the other strains and do not affect the stress state. Transverse shear strains ε_{xz} and ε_{yz} are assumed to have parabolic distributions in the Z-direction. This distribution satisfies the boundary conditions of zero transverse shear on the top and bottom plate surfaces.

Various plate theories are available to describe the through-the-thickness variation of strains. Displacements of the midplane of the plate are used to characterize displacements throughout the plate. Polynomial functions of *z* are most often employed with the order of the theory based on the highest order polynomial present in the kinematics. The order of the transverse shear is typically one less than the order of the displacement function, so for example, a parabolic shear deformation theory will require cubic terms in the in-plane displacements. Parabolic shear deformation theory was used for this research due to its presumed ability to capture the most important features of the transverse shear with relatively few degrees of freedom. Displacement functions used in this research are

$$\begin{aligned} \mathrm{u}(x,y,z) &= u + z\psi_1 + z^3 k(\psi_1 + w_{,1}) \\ \mathrm{v}(x,y,z) &= v + z\psi_2 + z^3 k(\psi_2 + w_{,2}) \\ \mathrm{w}(x,y,z) &= w \\ k &= -4/(3h^2) \end{aligned} \tag{1}$$

where the italic quantities *u, v,* and *w* are the midplane displacements which are independent of *z* so that, for example, $u = u(x,y)$.

Each point within the plate's midsurface has seven displacement components as shown in Fig. 2. Displacements *u, v* and *w* are translations in the X, Y and Z directions. The terms $w_{,1}$ and $w_{,2}$ are physical slopes of the midsurface in the X-Z and Y-Z planes, while ψ_1 and ψ_2 are rotations due to bending alone in those respective planes. Transverse shearing in a single plane is described by the algebraic sum of the two rotations. Translational displacements away from the midsurface are evaluated through the previous plate kinematics.

For this research, von Karman strain-displacement relations are used. Though the plate displacements are expected to be small, the deflections of the top surface of the plate in the contact region are not. In particular, the solution is expected to be improved by inclusion of the slopes of the midplane in the strain-displacement relations. The von Karman-type strain displacement relations are[12]

$$\begin{aligned} \varepsilon_1 &= \mathrm{u}_{,1} + \tfrac{1}{2}\mathrm{w}_{,1}{}^2 \\ \varepsilon_2 &= \mathrm{v}_{,2} + \tfrac{1}{2}\mathrm{w}_{,2}{}^2 \\ \varepsilon_6 &= \mathrm{u}_{,2} + \mathrm{v}_{,1} + \mathrm{w}_{,1}\,\mathrm{w}_{,2} \end{aligned} \tag{2}$$

These can be expressed in terms of the current kinematics as

$$\begin{aligned} \varepsilon_1 &= u_{,1} + z\psi_{1,1} + z^3 k(\psi_{1,1} + w_{,11}) + \tfrac{1}{2} w_{,1}{}^2 \\ \varepsilon_2 &= v_{,2} + z\psi_{2,2} + z^3 k(\psi_{2,2} + w_{,22}) + \tfrac{1}{2} w_{,2}{}^2 \\ \varepsilon_6 &= u_{,2} + v_{,1} + z(\psi_{1,2} + \psi_{2,1}) + z^3 k(\psi_{1,2} + \psi_{2,1} + 2w_{,12}) + w_{,1}\, w_{,2} \end{aligned} \tag{3}$$

It is convenient at this point to rewrite Eq. (2) as an operator on the displacements. This notation will simplify the development of the equilibrium equations later on.

$$\begin{Bmatrix} \varepsilon_1 \\ \varepsilon_2 \\ \varepsilon_6 \end{Bmatrix} = \begin{bmatrix} \partial_1 & & \frac{c\mathrm{w}_{,1}}{2}\partial_1 \\ & \partial_2 & \frac{c\mathrm{w}_{,2}}{2}\partial_2 \\ \partial_2 & \partial_1 & c\mathrm{w}_{,1}\partial_2 \end{bmatrix} \begin{Bmatrix} \mathrm{u} \\ \mathrm{v} \\ \mathrm{w} \end{Bmatrix} \tag{4}$$

where $\partial_\alpha = \partial/\partial x_\alpha$, $c = 1$ for von Karman strain displacement relations or $c = 0$ for linear strain displacement relations.

Constitutive Relations

Before damage, all ply materials are assumed linearly elastic and orthotropic. The three-dimensional kth ply constitutive relations for stress and strain are:

$$\begin{Bmatrix} \sigma_1 \\ \sigma_2 \\ \sigma_3 \\ \hline \sigma_4 \\ \sigma_5 \\ \hline \sigma_6 \end{Bmatrix}^{k} = \left[\begin{array}{ccc|cc|c} \overline{Q}_{11} & \overline{Q}_{12} & \overline{Q}_{13} & & & \overline{Q}_{16} \\ \overline{Q}_{12} & \overline{Q}_{22} & \overline{Q}_{23} & & & \overline{Q}_{26} \\ \overline{Q}_{13} & \overline{Q}_{23} & \overline{Q}_{33} & & & \overline{Q}_{36} \\ \hline & & & \overline{Q}_{44} & \overline{Q}_{45} & \\ & & & \overline{Q}_{45} & \overline{Q}_{55} & \\ \hline \overline{Q}_{16} & \overline{Q}_{26} & \overline{Q}_{36} & & & \overline{Q}_{66} \end{array}\right]^{k} \begin{Bmatrix} \varepsilon_1 \\ \varepsilon_2 \\ \varepsilon_3 \\ \hline \varepsilon_4 \\ \varepsilon_5 \\ \hline \varepsilon_6 \end{Bmatrix}^{k} \tag{5}$$

where the numerical subscripts on the stress and strain represent the following indexing of the stress and strain tensor components:

$$\begin{gathered} [\sigma] = \begin{bmatrix} \sigma_1 & \sigma_6 & \sigma_5 \\ \sigma_6 & \sigma_2 & \sigma_4 \\ \sigma_5 & \sigma_4 & \sigma_3 \end{bmatrix} = \begin{bmatrix} \sigma_{xx} & \sigma_{xy} & \sigma_{zx} \\ \sigma_{xy} & \sigma_{yy} & \sigma_{yz} \\ \sigma_{zx} & \sigma_{yz} & \sigma_{zz} \end{bmatrix} \\ [\varepsilon] = \begin{bmatrix} \varepsilon_1 & \frac{1}{2}\varepsilon_6 & \frac{1}{2}\varepsilon_5 \\ \frac{1}{2}\varepsilon_6 & \varepsilon_2 & \frac{1}{2}\varepsilon_4 \\ \frac{1}{2}\varepsilon_5 & \frac{1}{2}\varepsilon_4 & \varepsilon_3 \end{bmatrix} \equiv \begin{bmatrix} \varepsilon_{xx} & \frac{1}{2}\gamma_{xy} & \frac{1}{2}\gamma_{xz} \\ \frac{1}{2}\gamma_{xy} & \varepsilon_{yy} & \frac{1}{2}\gamma_{yz} \\ \frac{1}{2}\gamma_{xz} & \frac{1}{2}\gamma_{yz} & \varepsilon_{zz} \end{bmatrix} = \begin{bmatrix} \varepsilon_{xx} & \varepsilon_{xy} & \varepsilon_{zx} \\ \varepsilon_{xy} & \varepsilon_{yy} & \varepsilon_{yz} \\ \varepsilon_{zx} & \varepsilon_{yz} & \varepsilon_{zz} \end{bmatrix} \end{gathered} \tag{6}$$

and the kth ply constitutive matrix $[Q]_k$ is transformed to the laminate axis system by the modified direction cosine matrix for the kth ply, $[T]_k$.

$$[\overline{Q}]^{k} = [T]_k [Q]_k [T]_k^{T} \tag{7}$$

The in-plane kth ply constitutive relations for stress and strain for the originally assumed transverse direct stress ($\sigma_3 = 0$) are a simple contraction of the three-dimensional constitutive relations:

$$\begin{Bmatrix}\sigma_1\\ \sigma_2\\ \sigma_6\end{Bmatrix}^k = \begin{bmatrix}\overline{Q}_{11} & \overline{Q}_{12} & \overline{Q}_{16}\\ \overline{Q}_{12} & \overline{Q}_{22} & \overline{Q}_{26}\\ \overline{Q}_{16} & \overline{Q}_{26} & \overline{Q}_{66}\end{bmatrix}^k \begin{Bmatrix}\varepsilon_1\\ \varepsilon_2\\ \varepsilon_6\end{Bmatrix}^k \qquad (8)$$

Transverse stresses

To obtain the transverse stress components this research abandoned the constitutive relations for calculating σ_{zx} and σ_{yz} in favor of satisfying the three-dimensional equilibrium equations with the FEA in-plane stresses as a means of estimating both transverse direct stress σ_z and transverse shear stresses σ_{zx} and σ_{yz}. The stresses thus obtained are an improvement over those obtained from the constitutive equations alone[12]. The three-dimensional equilibrium equations can be expressed in the *x-y-z* coordinate system as

$$\sigma_{xx},_x + \sigma_{xy},_y + \sigma_{zx},_z = 0 \qquad (8a)$$

$$\sigma_{xy},_x + \sigma_{yy},_y + \sigma_{yz},_z = 0 \qquad (8b)$$

$$\sigma_{xz},_x + \sigma_{yz},_y + \sigma_{zz},_z = 0 \qquad (8c)$$

The first two equilibrium equations, (8a) and (8b), each contain a single unknown and can be readily integrated through the thickness with traction free boundaries on the surface of the plate and (potentially) on any delaminated ply interface to obtain σ_{zx} and σ_{yz} through the thickness (h) of the plate. That is, for any given in-plane coordinate (x,y),

$$\begin{aligned}\sigma_{zx}(z) &= \int_{-\frac{h}{2}}^{z}\left(-\sigma_{xx},_x(\zeta) - \sigma_{xy},_y(\zeta)\right)d\zeta\\ \sigma_{yz}(z) &= \int_{-\frac{h}{2}}^{z}\left(-\sigma_{xy},_x(\zeta) - \sigma_{yy},_y(\zeta)\right)d\zeta\end{aligned} \qquad (9)$$

In Eq. (9), the integration must be done on a ply-by-ply basis. With these quantities known, in-plane (and with the von Karman terms, transverse) derivatives can be taken and the third equilibrium equation can be integrated with a traction free boundary on the lower surface to obtain the transverse direct stress, σ_{zz}. The integration involved is:

$$\sigma_{zz}(z) = \int_{-\frac{h}{2}}^{z} \left(-\sigma_{xz},_{x}(\zeta) - \sigma_{yz},_{y}(\zeta)\right) d\zeta \qquad (10)$$

The integration given in Eq. (10) assumes continuity of transverse direct stress across ply interfaces. The integration is carried out ply-by-ply from the bottom surface (zero stress) to the top.

Integration of the three-dimensional equilibrium Eqs. (8) is complicated by the von Karman type strain displacement nonlinearity. The following highlights the complication and the developments needed to handle it. The in-plane stresses are obtained from the FEM displacement solution by applying the constitutive relations and strain displacement relations to the displacement vector, ***q***. In terms of the midplane displacement component vector, ***q***, the assumed displacement field is

$$\begin{Bmatrix} \mathrm{u} \\ \mathrm{v} \\ \mathrm{w} \end{Bmatrix} = \begin{bmatrix} 1 & & & z^3k & & z+z^3k & \\ & 1 & & & z^3k & & z+z^3k \\ & & 1 & & & & \end{bmatrix} \begin{Bmatrix} u \\ v \\ w \\ w,_1 \\ w,_2 \\ \psi_1 \\ \psi_2 \end{Bmatrix}, \qquad (11)$$

$$\equiv \begin{bmatrix} 1 & & & z^3k & & z+z^3k & \\ & 1 & & & z^3k & & z+z^3k \\ & & 1 & & & & \end{bmatrix} \boldsymbol{q}$$

With these kinematics, the von Karman strains Eqs. (4) become

$$\begin{Bmatrix} \varepsilon_1 \\ \varepsilon_2 \\ \varepsilon_6 \end{Bmatrix} = \left[\begin{bmatrix} \partial_1 & 0 & 0 & z^3k\partial_1 & 0 & \left(z+z^3k\right)\partial_1 & 0 \\ 0 & \partial_2 & 0 & 0 & z^3k\partial_2 & 0 & \left(z+z^3k\right)\partial_2 \\ \partial_2 & \partial_1 & 0 & 2z^3k\partial_2 & 0 & \left(z+z^3k\right)\partial_2 & \left(z+z^3k\right)\partial_1 \end{bmatrix} + \begin{bmatrix} 0 & 0 & 0 & \frac{c}{2}w,_1 & 0 & 0 & 0 \\ 0 & 0 & 0 & 0 & \frac{c}{2}w,_2 & 0 & 0 \\ 0 & 0 & 0 & cw,_2 & 0 & 0 & 0 \end{bmatrix} \right] \begin{Bmatrix} u \\ v \\ w \\ w,_1 \\ w,_2 \\ \psi_1 \\ \psi_2 \end{Bmatrix} \qquad (12)$$

where the nonlinear terms have been isolated into a separate matrix in order to provide insight into their role in the development. The in-plane strain derivatives can be written

$$\begin{Bmatrix} \varepsilon_{1,1} \\ \varepsilon_{1,2} \\ \varepsilon_{2,1} \\ \varepsilon_{2,2} \\ \varepsilon_{6,1} \\ \varepsilon_{6,2} \end{Bmatrix} = \left[\begin{bmatrix} \partial_{11} & 0 & 0 & z^3 k \partial_{11} & 0 & \left(z + z^3 k\right)\partial_{11} & 0 \\ \partial_{12} & 0 & 0 & z^3 k \partial_{12} & 0 & \left(z + z^3 k\right)\partial_{12} & 0 \\ 0 & \partial_{12} & 0 & 0 & z^3 k \partial_{12} & 0 & \left(z + z^3 k\right)\partial_{12} \\ 0 & \partial_{22} & 0 & 0 & z^3 k \partial_{22} & 0 & \left(z + z^3 k\right)\partial_{22} \\ \partial_{12} & \partial_{11} & 0 & 2z^3 k \partial_{12} & 0 & \left(z + z^3 k\right)\partial_{12} & \left(z + z^3 k\right)\partial_{11} \\ \partial_{22} & \partial_{12} & 0 & 0 & 2z^3 k \partial_{12} & \left(z + z^3 k\right)\partial_{22} & \left(z + z^3 k\right)\partial_{12} \end{bmatrix} + C \begin{bmatrix} 0 & 0 & 0 & w_{,1}\partial_1 & 0 & 0 & 0 \\ 0 & 0 & 0 & 0 & w_{,1}\partial_1 & 0 & 0 \\ 0 & 0 & 0 & w_{,2}\partial_2 & 0 & 0 & 0 \\ 0 & 0 & 0 & 0 & w_{,2}\partial_2 & 0 & 0 \\ 0 & 0 & 0 & w_{,2}\partial_1 & w_{,1}\partial_1 & 0 & 0 \\ 0 & 0 & 0 & w_{,2}\partial_2 & w_{,1}\partial_2 & 0 & 0 \end{bmatrix} \right] \begin{Bmatrix} u \\ v \\ w \\ w_{,1} \\ w_{,2} \\ \psi_1 \\ \psi_2 \end{Bmatrix}$$

$$\equiv \underset{6x7}{\left[\partial\partial\right]} \underset{7x1}{\boldsymbol{q}} \tag{13}$$

in which the 6x7 operator matrix (including linear and nonlinear portions) has been defined as $[\partial\partial]$. Writing the midplane displacement vector as $\boldsymbol{q}$, and considering the equilibrium equations and the stress-gradient/strain-gradient constitutive relation, the transverse shear stress gradients can be written as

$$\underset{2x1}{\begin{Bmatrix} \sigma_{4,3} \\ \sigma_{5,3} \end{Bmatrix}^k} = \left[- \underset{2x6}{\begin{bmatrix} \overline{Q}_{16} & \overline{Q}_{12} & \overline{Q}_{26} & \overline{Q}_{22} & \overline{Q}_{66} & \overline{Q}_{26} \\ \overline{Q}_{11} & \overline{Q}_{16} & \overline{Q}_{12} & \overline{Q}_{26} & \overline{Q}_{16} & \overline{Q}_{66} \end{bmatrix}^k} \underset{6x7}{\left[\partial\partial\right]} \right] \underset{7x1}{\boldsymbol{q}} \tag{14}$$

In Eq. 14 it can be seen that the whole of the z dependence (for any given ply) is contained in the $[\partial\partial]$ operator. The integration of Eqs (9) is carried out on the nonlinear operator $[\partial\partial]$ symbolically (outside the finite element solution) and the evaluation of transverse shear stress is reduced to algebraic manipulation within the finite element code. In this way, the three-dimensional equilibrium equations have provided an alternative means to obtain the transverse shear stresses without the standard use of the constitutive relations, i.e.,

$$\begin{Bmatrix} \sigma_4 \\ \sigma_5 \end{Bmatrix}^k = - \begin{bmatrix} \overline{Q}_{16} & \overline{Q}_{12} & \overline{Q}_{26} & \overline{Q}_{22} & \overline{Q}_{66} & \overline{Q}_{26} \\ \overline{Q}_{11} & \overline{Q}_{16} & \overline{Q}_{12} & \overline{Q}_{26} & \overline{Q}_{16} & \overline{Q}_{66} \end{bmatrix}^k \int \left[\partial\partial\right] dz \boldsymbol{q} \tag{15}$$

as opposed to[12]

$$\begin{Bmatrix} \sigma_4 \\ \sigma_5 \end{Bmatrix}^k = \begin{bmatrix} \overline{Q}_{44} & \overline{Q}_{45} \\ \overline{Q}_{45} & \overline{Q}_{55} \end{bmatrix}^k \begin{bmatrix} 0 & 0 & 0 & 0 & 1 & 0 & 1 \\ 0 & 0 & 0 & 1 & 0 & 1 & 0 \end{bmatrix} 2(1 + 3kz^2)\boldsymbol{q} \tag{16}$$

It should be observed that the transverse shear stress obtained in this way is forth-order in z as compared to parabolic for the standard constitutive solution. The third equilibrium equation, Eq. (10), requires in-plane derivatives of these stresses. Here the nonlinear portion of the $[\partial\partial]$ operator complicates the situation. Taking derivatives of the integrated [$\partial\partial$] times $\boldsymbol{q}$ expressions of Eq. (15) (in which both the operator and the vector have in-plane coordinate dependencies), the third equilibrium equation solved for the transverse direct stress gradient becomes

$$\sigma_{3,3}{}^{k} = \begin{bmatrix} \bar{Q}_{16} & \bar{Q}_{12} & \bar{Q}_{26} & \bar{Q}_{22} & \bar{Q}_{66} & \bar{Q}_{26} \\ \bar{Q}_{11} & \bar{Q}_{16} & \bar{Q}_{12} & \bar{Q}_{26} & \bar{Q}_{16} & \bar{Q}_{66} \end{bmatrix}^{k} \begin{Bmatrix} \dfrac{\partial\left(\int \left[\partial\partial\right] dz \boldsymbol{q}\right)}{\partial x_2} \\ \dfrac{\partial\left(\int \left[\partial\partial\right] dz \boldsymbol{q}\right)}{\partial x_1} \end{Bmatrix}^{k} \tag{17}$$

and integrating through the thickness once more,

$$\sigma_{3}{}^{k} = \begin{bmatrix} \bar{Q}_{16} & \bar{Q}_{12} & \bar{Q}_{26} & \bar{Q}_{22} & \bar{Q}_{66} & \bar{Q}_{26} \\ \bar{Q}_{11} & \bar{Q}_{16} & \bar{Q}_{12} & \bar{Q}_{26} & \bar{Q}_{16} & \bar{Q}_{66} \end{bmatrix}^{k} \begin{Bmatrix} \dfrac{\partial\left(\int\int \left[\partial\partial\right] d\zeta dz \boldsymbol{q}\right)}{\partial x_2} \\ \dfrac{\partial\left(\int\int \left[\partial\partial\right] d\zeta dz \boldsymbol{q}\right)}{\partial x_1} \end{Bmatrix}^{k} \tag{18}$$

where the integrations are again carried out symbolically, so that transverse direct stress is also a simple algebraic manipulation within the program. It should be observed that the transverse direct stress obtained in this way is fifth-order in z as compared to zero for the standard constitutive solution.

Finite Element Solution

With the assumed kinematics, the only essential active degrees of freedom are those related to the midplane displacements, slopes, and rotations of Eq. (1). The analysis reduces to that of parabolic shear deformation theory, and rectangular plate elements with four nodes and 28 degrees of freedom (seven per node as in figure 2) could be used. The geometry of an individual element and the representation of its global, local and natural coordinates are shown in figure 3.

Displacements within the given element are interpolated from the nodal displacements through appropriate shape functions. The displacement field for w requires C^1 continuity (as defined in the textbook by Cook et al,[14] therefore cubic Hermitian shape functions have been used in previous research for nodal displacements w, $w_{,1}$ and $w_{,2}$. The interpolation can be represented as,

$$w(\xi,\eta) = \begin{bmatrix} H_1 & H_2 & H_3 & H_4 \end{bmatrix} \begin{Bmatrix} q_1 \\ q_2 \\ q_3 \\ q_4 \end{Bmatrix} \tag{19a}$$

$$H_K = \begin{Bmatrix} \frac{1}{8}(1+\xi_K\xi)(1+\eta_K\eta)(2+\xi_K\xi+\eta_K\eta-\xi^2-\eta^2) \\ \frac{1}{8}\Delta x\xi_K(1+\xi_K\xi)^2(\xi_K\xi-1)(1+\eta_K\eta) \\ \frac{1}{8}\Delta y\eta_K(1+\xi_K\xi)(\eta_K\eta-1)(1+\eta_K\eta)^2 \end{Bmatrix}^T \tag{19b}$$

$$q_K = \{w \quad w_{,1} \quad w_{,2}\}_K^T \tag{19c}$$

where K=1 through 4 represent the local node numbers for an element found at global position (x,y). ξ_K and η_K are the values of the natural coordinates at node K. Thus Eq. (19b) represents 12 cubic polynomial interpolation functions. These are determined as follows. Defining a function for each degree of freedom, m (m=1,2,...,12),

$$\begin{aligned} H^m(\xi,\eta) = {} & a_1^m + a_2^m\xi + a_3^m\eta + a_4^m\xi^2 + a_5^m\xi\eta + a_6^m\eta^2 + \\ & a_7^m\xi^3 + a_8^m\xi^2\eta + a_9^m\xi\eta^2 + a_{10}^m\eta^3 + a_{11}^m\xi^3\eta + a_{12}^m\xi\eta^3 \end{aligned} \tag{20}$$

in which the coefficients are different for each degree of freedom, its in-plane derivatives are readily evaluated as,

$$\begin{aligned} H^m{}_{,\xi}(\xi,\eta) &= a_2^m + 2a_4^m\xi + a_5^m\eta + 3a_7^m\xi^2 + 2a_8^m\xi\eta + a_9^m\eta^2 + 3a_{11}^m\xi^2\eta + a_{12}^m\eta^3 \\ H^m{}_{,\eta}(\xi,\eta) &= a_3^m + a_5^m\xi + 2a_6^m\eta + a_8^m\xi^2 + 2a_9^m\xi\eta + 3a_{10}^m\eta^2 + a_{11}^m\xi^3 + 3a_{12}^m\xi\eta^2 \end{aligned}. \tag{21}$$

We define a vector of the coordinates for each degree of freedom, m,

$$AA^m = \{a_1, a_2, a_3, \ldots, a_{12}\}^m \tag{22}$$

And define an 12-dimensional vector function of the coordinates for each degree of freedom, m, containing the interpolation functions and their derivatives evaluated at the nodes,

$$HH_n(AA^m) = \begin{Bmatrix} H^m(\xi_1,\eta_1), H^m{}_{,\xi}(\xi_1,\eta_1), H^m{}_{,\eta}(\xi_1,\eta_1), \ldots, \\ H^m(\xi_4,\eta_4), H^m{}_{,\xi}(\xi_4,\eta_4), H^m{}_{,\eta}(\xi_4,\eta_4) \end{Bmatrix}. \tag{23}$$

We now let that vector function take on values of a unit basis vector for each degree of freedom, m, i.e.,

$$HH_n(AA^m) = \delta_n^m. \tag{24}$$

Which we solve for the coefficients AA^m for each degree of freedom, m. With these then H^m is fully defined and can be placed in the relationship given in Eq. (19b) by separating them out by nodes. The other displacement fields only need C^0 continuity and employ Lagrangian shape functions:

$$\begin{Bmatrix} u(x,y) \\ v(x,y) \\ \psi_1(x,y) \\ \psi_2(x,y) \end{Bmatrix} = \begin{bmatrix} N_1 & 0 & 0 & 0 & \dots & N_4 & 0 & 0 & 0 \\ 0 & N_1 & 0 & 0 & \dots & 0 & N_4 & 0 & 0 \\ 0 & 0 & N_1 & 0 & \dots & 0 & 0 & N_4 & 0 \\ 0 & 0 & 0 & N_1 & \dots & 0 & 0 & 0 & N_4 \end{bmatrix} \begin{Bmatrix} q_1 \\ q_2 \\ q_3 \\ q_4 \end{Bmatrix} \tag{25a}$$

$$N_K = \tfrac{1}{4}(1+\xi_K\xi)(1+\eta_K\eta) \tag{25b}$$

$$q_K = \{u \quad v \quad \psi_1 \quad \psi_2\}_K^T \tag{25c}$$

The formulation of such an element and the solution of the resulting finite element problem for static analysis is fully described in the textbook by Palazotto and Dennis[12].

Higher order element development

The 4-noded, 28 degree-of-freedom element[12], used as the starting point for this research, employs shape functions that are at most cubic polynomials in the in-plane coordinates. In the displacement based, plane stress, finite element formulation, the transverse direct stress is assumed zero and the transverse shear stress is assumed to be related to the transverse shear strains via constitutive relationships. This is to say, the element is two-dimensional, and the assumed kinematics limit the accuracy of the available transverse stresses. To provide better transverse stresses, the current research solved the finite element problem to obtain displacements (and strains), and then used constitutive relationships to obtain in-plane stresses, and finally used three-dimensional equilibrium equations to obtain transverse stresses. Since the three-dimensional equilibrium satisfaction did not affect the finite element solution, it can be considered a post-processing algorithm. The equilibrium post-processing in the present research required third derivatives of the in-plane and shear displacements and fourth derivatives of the transverse displacement. This can be observed in equations 18. Here the interpolation used for the displacement vector becomes important. Clearly, if the displacement vector contains at most cubic polynomials (as it does in the 28 degree of freedom element of [12]) and third and fourth derivatives are taken of it, little will survive and the transverse stresses of equations (15) and (18) have little hope of accurately representing the three-dimensional effects. The approach taken for this research to get higher-order midplane displacement functions for equations (15) and (18) was to increase the order of the polynomial shape functions representing the displacements inside the element. This required a new element with more degrees of freedom at the nodes. The capability to use the 28 degree of freedom element was retained by writing the code to allow the user to select the order of the interpolation polynomials for the w, ψ_1, and ψ_2 displacement functions. In particular, 3rd or 5th order polynomials could be chosen for w, while linear or 3rd order polynomials could be chosen for ψ_1 and ψ_2. Linear interpolation was by Lagrangian functions as described in [12] providing C^0 continuity while Hermitian functions provided C^1 and C^2 for the 3rd and 5th order interpolations respectively. The terms included in the Hermitian interpolation polynomials are illustrated in figure 5.

The 3rd order Hermitian functions are precisely the same as those defined above for w, but for the higher order elements they can be applied to ψ_1 and ψ_2 as well as w. Interpolation using the 5th order Hermitian interpolation functions can be represented as,

$$w(x,y) = \begin{bmatrix} H_1 & H_2 & H_3 & H_4 \end{bmatrix} \begin{Bmatrix} q_1 \\ q_2 \\ q_3 \\ q_4 \end{Bmatrix}, \tag{26}$$

in which each H_K is now a 1x6 row vector rather than the 1x3 vector shown in equation (18) and,

$$q_K = \{w \quad w_{,1} \quad w_{,2} \quad w_{,11} \quad w_{,12} \quad w_{,22}\}_K^T \tag{27}$$

Thus equation 26 represents 24 5th order polynomial interpolation functions. These are determined as follows. Defining a function for each degree of freedom, m (m=1,2,...,24),

$$\begin{aligned} H^m(\xi,\eta) = {} & a_1^m + a_2^m\xi + a_3^m\eta + a_4^m\xi^2 + a_5^m\xi\eta + a_6^m\eta^2 + \\ & a_7^m\xi^3 + a_8^m\xi^2\eta + a_9^m\xi\eta^2 + a_{10}^m\eta^3 + \\ & a_{11}^m\xi^4 + a_{12}^m\xi^3\eta + a_{13}^m\xi^2\eta^2 + a_{14}^m\xi\eta^3 + a_{15}^m\eta^4 + \\ & a_{16}^m\xi^5 + a_{17}^m\xi^4\eta + a_{18}^m\xi^3\eta^2 + a_{19}^m\xi^2\eta^3 + a_{20}^m\xi\eta^4 + a_{21}^m\eta^5 + \\ & a_{22}^m\xi^5\eta + a_{23}^m\xi^3\eta^3 + a_{24}^m\xi\eta^5 \end{aligned} \tag{28}$$

in which, as before, the coefficients are different for each degree of freedom, its in-plane derivatives of concern are now,

$$\begin{array}{l} H^{m}{}_{,\xi} \\ H^{m}{}_{,\eta} \\ H^{m}{}_{,\xi\xi} \\ H^{m}{}_{,\xi\eta} \\ H^{m}{}_{,\eta\eta} \end{array} \qquad (29)$$

We again define a vector of the coordinates for each degree of freedom, *m*,

$$AA^{m} = \{a_1, a_2, a_3, \ldots, a_{24}\}^{m} \qquad (30)$$

and define an 24-dimensional vector function of the coordinates for each degree of freedom, *m*, containing the interpolation functions and their derivatives evaluated at the 4 nodes,

$$HH_n(AA^{m}) = \left\{ \begin{array}{l} H^{m}(\xi_1,\eta_1), H^{m}{}_{,\xi}(\xi_1,\eta_1), H^{m}{}_{,\eta}(\xi_1,\eta_1), \\ H^{m}{}_{,\xi\xi}(\xi_1,\eta_1), H^{m}{}_{,\xi\eta}(\xi_1,\eta_1), H^{m}{}_{,\eta\eta}(\xi_1,\eta_1), \\ \ldots, \\ H^{m}(\xi_4,\eta_4), H^{m}{}_{,\xi}(\xi_4,\eta_4), H^{m}{}_{,\eta}(\xi_4,\eta_4), \\ H^{m}{}_{,\xi\xi}(\xi_4,\eta_4), H^{m}{}_{,\xi\eta}(\xi_4,\eta_4), H^{m}{}_{,\eta\eta}(\xi_4,\eta_4) \end{array} \right\} \qquad (31)$$

We now let that vector function take on values of a unit basis vector for each degree of freedom, *m*, i.e.,

$$HH_n(AA^{m}) = \delta_n^{m} \qquad (32)$$

Which we again solve for the coefficients AA^{m} for each degree of freedom, *m*. With these then, H^{m} is fully defined and can be placed in the relationship given in equation (26) by separating them out by nodes. The 5th order Hermitian shape functions thus derived are,

$$H_1 = \left\{ \begin{array}{c} \tfrac{1}{32}(-1+\xi)(-1+\eta)(8-7\eta-7\eta^2+3\eta^3+3\eta^4-7\xi+2\eta\xi-7\xi^2+2\eta^2\xi+2\eta\xi^2+2\eta^2\xi^2+3\xi^3+3\xi^4) \\ \tfrac{1}{32}(-1+\xi)^2(-1+\eta)(1+\xi)(-5+2\eta+2\eta^2+2\xi+3\xi^2) \\ \tfrac{1}{32}(-1+\eta)^2(-1+\xi)(1+\eta)(-5+2\eta+3\eta^2+2\xi+2\xi^2) \\ \tfrac{1}{32}(-1+\eta)(-1+\xi)^3(1+\xi)^2 \\ \tfrac{1}{16}(-1+\eta)^2(1+\eta)(-1+\xi)^2(1+\xi) \\ \tfrac{1}{32}(-1+\eta)^3(-1+\xi)(1+\eta)^2 \end{array} \right\}^{T} \qquad (33)$$

$$H_2 = \left\{ \begin{matrix} \frac{1}{32}(-1+\eta)(1+\xi)(-8+7\eta+7\eta^2+2\eta\xi+2\eta^2\xi-3\eta^3-3\eta^4-7\xi+7\xi^2-2\eta\xi^2-2\eta^2\xi^2+3\xi^3-3\xi^4) \\ \frac{1}{32}(1+\xi)^2(-1+\eta)(-1+\xi)(-5+2\eta+2\eta^2-2\xi+3\xi^2) \\ \frac{1}{32}(-1+\eta)^2(1+\xi)(1+\eta)(5-2\eta-3\eta^2+2\xi-2\xi^2) \\ \frac{1}{32}(1-\eta)(-1+\xi)^2(1+\xi)^3 \\ \frac{1}{16}(-1+\eta)^2(1+\eta)(-1+\xi)(1+\xi)^2 \\ \frac{1}{32}(1-\eta)^3(1+\xi)(1+\eta)^2 \end{matrix} \right\}^{T} \tag{34}$$

$$H_3 = \left\{ \begin{matrix} \frac{1}{32}(1+\eta)(1+\xi)(8+7\eta-7\eta^2+2\eta\xi-2\eta^2\xi-3\eta^3+3\eta^4+7\xi-7\xi^2-2\eta\xi^2+2\eta^2\xi^2-3\xi^3+3\xi^4) \\ \frac{1}{32}(1+\xi)^2(1+\eta)(-1+\xi)(5+2\eta-2\eta^2+2\xi-3\xi^2) \\ \frac{1}{32}(1+\eta)^2(1+\xi)(-1+\eta)(5+2\eta-3\eta^2+2\xi-2\xi^2) \\ \frac{1}{32}(1+\eta)(-1+\xi)^2(1+\xi)^3 \\ \frac{1}{16}(-1+\eta)(1+\eta)^2(-1+\xi)(1+\xi)^2 \\ \frac{1}{32}(-1+\eta)^2(1+\xi)(1+\eta)^3 \end{matrix} \right\}^{T} \tag{35}$$

$$H_4 = \left\{ \begin{matrix} \frac{1}{32}(1+\eta)(-1+\xi)(-8-7\eta+7\eta^2+2\eta\xi-2\eta^2\xi+3\eta^3-3\eta^4+7\xi+7\xi^2+2\eta\xi^2-2\eta^2\xi^2-3\xi^3+3\xi^4) \\ \frac{1}{32}(-1+\xi)^2(1+\eta)(1+\xi)(5+2\eta-2\eta^2-2\xi-3\xi^2) \\ \frac{1}{32}(1+\eta)^2(-1+\xi)(-1+\eta)(-5-2\eta+3\eta^2+2\xi+2\xi^2) \\ \frac{1}{32}(1+\eta)(1+\xi)^2(1-\xi)^3 \\ \frac{1}{16}(-1+\eta)(1+\eta)^2(-1+\xi)^2(1+\xi) \\ \frac{1}{32}(-1+\eta)^2(1-\xi)(1+\eta)^3 \end{matrix} \right\}^{T} \tag{36}$$

Nodal degrees of freedom for the linear case consisted of the values of displacement functions at the nodes. Nodal degrees of freedom for the 3rd order Hermitian interpolation polynomials consisted of the values of displacement functions as well as the slopes of those functions at the nodes. Nodal degrees of freedom for the 5th order Hermitian interpolation polynomials consisted of the values of displacement function, the slopes of that function, and the second and cross derivatives of the function at the nodes. Allowing the user to select the order of the interpolation polynomials for the w, ψ_1, and ψ_2 independently provided the possibility of using elements having 7, 9, 10, 11, 12, or 14 degrees-of-freedom per node. Though the code is capable of all of these elements, it was only exercised for this research using 7, 11, and 14 degrees-of-freedom per node. After checking out the transverse stress results (via equilibrium) using these, the 14 degrees-of-freedom per node element was settled on for the remainder of the work. The element with 7 degrees-of-freedom per node has nodal degrees-of-freedom u, v, w, $w_{,x}$, $w_{,y}$, ψ_1, and ψ_2. The element with 11 degrees-of-freedom per node has nodal degrees-of-freedom u, v, w, $w_{,x}$, $w_{,y}$, ψ_1, $\psi_{1,x}$, $\psi_{1,y}$, ψ_2, $\psi_{2,x}$, and $\psi_{2,y}$. The element with 14 degrees-of-freedom per node has nodal degrees-of-freedom u, v, w, $w_{,x}$, $w_{,y}$, $w_{,xx}$, $w_{,xy}$, $w_{,yy}$, ψ_1, $\psi_{1,x}$, $\psi_{1,y}$, ψ_2, $\psi_{2,x}$, and $\psi_{2,y}$. All elements used 5x5 point Gauss quadrature. These three elements and their nodal degrees-of-freedom are illustrated in figure 6.

Generalized Newton-Raphson method

For this research, geometric nonlinearity of the response of a sandwich structure to load was allowed by a generalization of the Newton-Raphson method. Letting the displacement be represented by the vector $\mathbf{q}$, the nonlinear stiffness of the structure be represented by the matrix $\mathbf{K(q)}$, and the applied load be represented by the vector $\mathbf{R}$, equilibrium of the structure with the applied load can be represented by the matrix-vector equation,

$$\mathbf{K(q)q} = \mathbf{R}. \tag{37}$$

When material nonlinearities are also present (as in the case of damage in the current research), analysis must proceed in an incremental manner because the solution at any given displacement may depend not only on the current displacement but also on the previous loading history [14]. The problem is linearized over any increment of load by considering two stiffness matrices $\mathbf{K}_T(\mathbf{q})$, and $\mathbf{K}_S(\mathbf{q})$, which represent the tangent and secant stiffnesses. An iterative procedure is employed for each load increment, i, to solve for $\mathbf{q}_i$. Let $\mathbf{q}^0{}_i$ be the converged displacement vector for the $(i\text{-}1)^{\text{th}}$ load increment $\mathbf{R}_{i-1}$. That is,

$$\mathbf{R}_{i-1} - \mathbf{K}_S(\mathbf{q}^0{}_i)\mathbf{q}^0{}_i \approx 0 \tag{38}$$

Then when the load is incremented, the solution is no longer in equilibrium,

$$\mathbf{R}_i - \mathbf{K}_S(\mathbf{q}^0{}_i)\mathbf{q}^0{}_i \equiv \text{residual force} \neq 0 \tag{39}$$

We desire to modify the displacement vector in order to get the structure in equilibrium with the new load. This update is done by solving,

$$\mathbf{K}_T(\mathbf{q}^0{}_i)\Delta\mathbf{q} = \mathbf{R}_i - \mathbf{K}_S(\mathbf{q}^0{}_i)\mathbf{q}^0{}_i, \tag{40}$$

for $\Delta\mathbf{q}$ and updating $\mathbf{q}_i$.

$$\mathbf{q}^1{}_i = \mathbf{q}^0{}_i + \Delta\mathbf{q}. \tag{41}$$

For iteration step j we solve,

$$\mathbf{K_T}(\mathbf{q}^{j-1}{}_i)\Delta\mathbf{q} = \mathbf{R}_i - \mathbf{K_S}(\mathbf{q}^{j-1}{}_i)\mathbf{q}^{j-1}{}_i\,, \tag{42}$$

and update $\mathbf{q}_i$,

$$\mathbf{q}^j{}_i = \mathbf{q}^{j-1}{}_i + \Delta\mathbf{q}\,. \tag{43}$$

We continue this process until,

$$\frac{\sqrt{\sum_n \left(q_n{}^j{}_i\right)^2} - \sqrt{\sum_n \left(q_n{}^{j-1}{}_i\right)^2}}{\sqrt{\sum_n \left(q_n{}^1{}_i\right)^2}} \leq \text{convergence tolerance}\,, \tag{44}$$

in which the summations over n represent summations over each degree-of-freedom in the vector $\mathbf{q}$. So that,

$$\mathbf{R}_i - \mathbf{K_S}(\mathbf{q}^j{}_i)\mathbf{q}^j{}_i \approx 0\,, \tag{45}$$

and then set,

$$\mathbf{q}^0{}_{i+1} = \mathbf{q}^j{}_i\,, \tag{46}$$

and proceed with the next load increment, i+1. Terminate when load increment $\mathbf{R}_i$ is at least equal to the maximum load required for the given analysis.

Every quasi-three-dimensional case study in this research considered a square plate with simply supported edges (u and v translations are free). Since all ply orientations were either 0 or 90 degrees, it was only necessary to generate finite element meshes for a single quadrant of each plate by prescribing bi-axial symmetry. Figure 7 shows the displacement boundary conditions which were applied to each square quarter-plate. In addition to the boundary conditions shown in figure 7, the models using cubic Hermitian shape functions for ψ_1 and ψ_2 (11 DOF and 14 DOF) had $\psi_{1,1}$ and $\psi_{2,2}$ set to zero on the simple support boundaries and $\psi_{1,2}$ and $\psi_{2,1}$ set to zero on the symmetric boundaries. The 14 DOF model used 5th order Hermitian interpolation for w and had the additional boundary conditions of $w_{,11}$ and $w_{,22}$ set to zero on the simple support boundaries and $w_{,12}$ set to zero on the symmetric boundaries.

Failure Criteria

Progressive failure analysis of composite structures with arbitrary lay-ups and loading requires both a laminate stress analysis model and a failure model that can account for general states of stress and modes of damage. After pointwise stresses in each layer of the composite are known from laminate analysis, failure of the composite is predicted either by employing a phenomenological failure criterion at the macromechanical (lamina) level or by relating the lamina stresses to the stresses in each constituent of the composite and employing a failure criterion at the micromechanical level. Micromechanical criteria are not considered in this research. Failure criteria are used for determining the extent of matrix cracking and core damage as well as predicting the onset and progress of delamination. These were compared with one another and with the experimental results in an attempt to determine which are best for the particular mode in question. In this report, Hashin's failure criteria [8] (shown in Appendix) is used.

Matrix cracking and core damage.

With the improved stress values anticipated from the three-dimensional equilibrium integration, stress-based failure criteria looked particularly promising for this research. The progression of matrix cracking and core damage was assumed to be governed by load transfer associated with previous failures, so that the failure criteria combined with a reduced stiffness routine was used to follow the progression of damage

Delamination.

Two classifications of analyses into which the published work can be separated are damage mechanics and fracture mechanics. Damage mechanics, or progressive degradation modeling, describes the damage with damage state variables, cracks are not directly modeled. Stress-based damage evolution laws are typically used to model the progression of damage. The analysis can begin without any damage. Fracture mechanics, on the other hand, follows the growth of a particular crack. No crack initiation is predicted, instead an initial crack is assumed and its progression is sought. A Griffith type energy release rate-based criterion is typically used to predict the growth of the crack. The scales of these two classifications of analyses are typically very different. Fracture mechanics often requires a smaller scale since a particular crack, rather than a multiply cracked lamina for example, must be modeled. The delamination damage progression tool used in this research was of the damage mechanics classification. A stress-based failure criterion indicated delamination and a stiffness reduction was in the lamina adjacent to the indicated delamination was used to model the effect of the delamination on the response of the structure.

Contact Problem

The interaction between the flexible plate and the near-rigid hemispherical tup is a very important facet of the low-velocity impact problem for composite sandwich panels. The force that the tup applies to the plate must be distributed over some area (contact area) so that finite stress is induced in the plate. The induced stresses produce local deformations in the plate that tend to conform the plate surface to the tup surface, changing the contact area. Since the contact area influences the stress and the stress influences the contact area, the contact problem is evidently non-conservative. The non-conservative nature of the contact problem was neglected.

The quasi-static assumption made here simplifies the approach by making the tup force a program input rather than an unknown. The problem is reduced to that of an indentor in static equilibrium (at any given load) with a deformed (and perhaps damaged) plate. In order to load the finite element model simulating this event, a Hertzian contact law was employed to distribute the tup force over the contact area. This contact law is axisymmetric (elliptical or proportional to distance from the axis of symmetry to the 3/2 power). This contact law idea has its roots in isotropic analyses where it has proved valuable. The validity of the assumed axisymmetric pressure response of anisotropic plates to a hemispherical indentor or tup is certainly questionable, since the plate properties are directional. For tup radii that are small compared to the global curvature of the plate under load, the contact radii will be small and the particular form of the contact pressure profile may be less important than the total load and the area over which it acts. These two parameters, load and contact area, can be experimentally correlated to verify that the analysis is distributing the load in a way that simulates the true load distribution of the experiment. It should be kept in mind that the spherical indentor is itself a simulation of the generally-shaped impactor (e.g. stone, dropped wrench, or other hard object) that these structures will encounter in service.

The following describes the impact event which is of interest, and the static contact algorithm employed for this research.

A moving rigid mass (the tup) makes contact with a simply-supported, stationary, laminated composite plate at time $t = 0$. The progress of the tup is impeded by the presence of the plate. For the tup to continue its motion, it must move the plate or deform it. Rigid body motion of the plate is prevented by the supports. The deformation of the plate stores elastic (and possibly, plastic and damage) energy until the kinetic energy of the tup is reduced to zero (the tup does work on the plate). The stored elastic energy then does work on the tup, accelerating it back up. In both cases, the work is done by the force between the two bodies moving through a distance. Force then can be considered the actual load applied to the plate, while the distribution of that force (pressure profile or "footprint") is determined by the radius of the indentor and the local stiffness of the plate. The quasi-static assumption has removed time from the picture.

Let the x-, y-, and z-direction displacements of the plate for a given tup force, F, be $u_1(x,y,z,F)$, $u_2(x,y,z,F)$, and $u_3(x,y,z,F)$ to distinguish them from the midplane displacements $u(x,y,F)$, $v(x,y,F)$, and $w(x,y,F)$. Let the vertical displacement of the center of the contact area (the point (0,0), where the tup and the plate first touch) be,

$$w_{top}(0,0,F) = \mathrm{w}(0,0,-\frac{\mathrm{h}}{2},F) \tag{47}$$

Assume that when F is zero the configuration is that of figure 8 and the plate has just made contact with the tup. The plate deflection is zero when F is zero. Choose some small interval of load, ΔF such that no damage occurs below $F = \Delta F$. The portion of the event between $F = 0$ and $F = \Delta F$ is then of no concern to this analysis. Choose also some small radius of contact, $\mathrm{R}_{contact}$, and assume that the load, ΔF, is distributed over the contact area as,

$$\mathrm{q}(r) = \begin{cases} 0, & r > \mathrm{R}_{contact} \\ q_0\sqrt{1-\dfrac{r^2}{\mathrm{R}_{contact}{}^2}}, & r \le \mathrm{R}_{contact} \end{cases}$$

$$q_0 = \frac{3F}{2\pi\,\mathrm{R}_{contact}{}^2} \tag{48}$$

Apply the first ΔF, so that at load $F = \Delta F$ the tup has moved a distance:

$$w_{top}(0,0,\Delta F) = \mathrm{w}(0,0,-\frac{\mathrm{h}}{2},\Delta F) \tag{49}$$

in which $\mathrm{K}_{eff}(F)$ is the nonlinear effective plate stiffness including both the plate bending stiffness and the contact stiffness. Neglecting the transverse strain, of the plate, the two-dimensional finite element solution without the equilibrium integration produces the situation illustrated in figure 9.

Notice that this implies that the top surface and midplane of the plate move together with the tup. This effectively equates the motion of the top of the plate with that of the midplane. Though this assumption is common for plate problems, it is clearly wrong for transverse impact. Equilibrium integration is used to improve on these assumptions.

When the load is applied to the finite element model, the resulting plate displacement produces a response force from the stiffness of the plate (via FEM) as well as a transverse direct strain profile through the thickness under the point of impact (via constitutive relationships and transverse stresses found from the equilibrium equations and the in-plane stresses from the FEA). Call this first iteration value of the force F_1 and strain ε_3. That is, for a compressive strain, the top surface moves toward the midplane (see figure 10). For any given load F, call this relative motion Δh.

$$\Delta h(x,y) = \int_0^{-h/2} \varepsilon_3(x,y,z)dz \tag{50}$$

This integration is carried out for all Gauss points (where stresses are calculated) within the contact area prescribed by the assumed contact radius, $R_{contact}$, and added to the midplane displacements at those points to produce a top surface deflection profile under the tup.

$$w_{top}(x,y) = \Delta h(x,y) + w(x,y) \tag{51}$$

The total displacement of the top surface illustrated in figure 10 does not, in general enforce the condition that the tup is rigid and the plate can not occupy the space occupied by the tup. Assuming the top surface of the center of the plate is in contact with the surface of the tup, this constraint is simply that the top surface must displace at least as much as the surface of the tup. The surface of the tup is illustrated in figure 11. The constraint can be expressed as,

$$w_{top}(x,y,F) \geq w_{top}(0,0,F) - R + \sqrt{R^2 - x^2 - y^2} \tag{52}$$

where R is the tup radius and the inequality in equation (52) implies an iterative approach and enforces the condition that the surface can not move into the space occupied by the tup (rigid spherical contact surface).

Having shown how the top surface displacements are found (equation (52)) and the constraint that must be imposed upon them through the an iterative approach (equation (52), the specific algorithm developed for the present research to enforce the constraint will now be described. For an elastic spherical tup in contact with an elastic half-plane Timoshenko and Goodier [15] give the relationship between contact radius $R_{contact}$, applied load F, tup radius R, and elastic modulus E, as,

$$R_{contact} = 1.109\sqrt[3]{\frac{FR}{E}} \tag{53}$$

This suggests that for a given load and material, a proportionality should exist between the contact radius and the tup radius, i.e.

$$R_{contact} \propto \sqrt[3]{R} \tag{54}$$

This idea was used to iterate the finite element solution for any given load (and damage condition) to obtain the contact radius. In particular, the radius of the top surface under the load was made to be the same (within a specified tolerance) as the tup radius by changing the estimated contact radius. The top surface displacement of all Gauss points within the assumed contact radius were fitted to a sphere of arbitrary radius by a least squares method resulting in a calculated tup radius, R_{top}, (the radius that best fits the top surface displacements) which was in general different from the tup radius, R, which the simulation was intended to model. The contact radius is updated to reflect the fact that it produced the wrong tup radius and another iteration of the solution is performed with this new $R_{contact}$. For iteration i, the estimate of the contact radius was given by,

$$R_{contact_i} = R_{contact_{i-1}}\sqrt[3]{\frac{R}{R_{top}}} \tag{55}$$

and the finite element solution was repeated with the new contact radius (and resulting Hertzian contact pressure profile). This process continued until the calculated tup radius was the same as the required tup radius within some small tolerance. In practice, this convergence took only 3 to 5 iterations. Both top surface radius, R_{top}, and contact radius, $R_{contact}$ are shown as a function of contact iteration number in figure 12.

When the contact solution had converged, the damage algorithm was invoked. At some point, the damage criteria identified a damage. When that happened, the stiffness was modified and the iteration continued with the contact algorithm again. The contact algorithm was iterated within the local model and the resulting contact radius was used in the global model. Further discussion will be subsequently presented to show how the contact algorithm was incorporated into the local and global finite element models.

Adaptive Mesh

As the contact algorithm is invoked, the contact radius changes, so that with a fixed grid, the number of elements over which the contact load is applied may change. In particular, as the load increases, the contact radius does as well. A mesh that is refined enough for one contact radius may not be refined well enough for a different contact radius. To overcome this problem, one could make a single grid which is refined tightly enough in the center for the smallest contact radius anticipated and refined far enough away from the center for the largest contact radius anticipated, but the number of degrees of freedom for such a model would be large compared to that of a mesh refined for a single contact radius. The highly iterative nature of the solution algorithm used in this analysis demanded the number of degrees of freedom be as small as practical. To accomplish this, an adaptive mesh algorithm in which the plate dimensions, initial contact radius, and number of elements was chosen by the user, but the adaptive mesh algorithm set the grid spacing within the computational domain based on the current contact radius. The equation defining the grid spacing was designed to place the majority of the elements within 2.5 contact radii of the center of the plate and provide near unit element aspect ratios in that region. The equation defining the element x-dimension length was,

$$\Delta x_i = a\left\{\left[\left(\frac{si}{n}\right)+\left(\frac{i}{n}-1+(1-s)^{1/power}\right)^{power}\right]-\left[\left(\frac{s(i-1)}{n}\right)+\left(\frac{i-1}{n}-1+(1-s)^{1/power}\right)^{power}\right]\right\}$$

where,

$$\begin{aligned}&a = \text{plate half width (63.5 mm)}\\&power = 16\\&s = \frac{4\mathrm{R}_{contact}}{a}\\&n = \text{number of elements in the x-direction}\\&i = 1,2,\ldots,n\end{aligned}\tag{56}$$

in which the choices of *s* and *power* were made after a parameter study in which the resulting grids were compared graphically and subjectively judged by the author with respect to the degree of refinement near the contact region and the smoothness of the transition. With this choice of parameters,

$$\begin{aligned}&\Delta x_1 \approx \frac{4}{n}\mathrm{R}_{contact}\\&\text{and,}\\&\sum_{i=1}^{n}\Delta x_i = a\end{aligned}\tag{57}$$

Each time the contact algorithm modified the contact radius, the adaptive mesh algorithm redefined the grid spacing, so that the new grid was tailored to the new contact radius. The change in the position of the nodes required the finite element stiffness to be recalculated. It should be observed that moving the nodes implied that the degrees of freedom from one contact iteration to the other were not the same. An implication of the modified degrees of freedom was that the displacements from one load increment to the next load increment may not be based on the same nodal coordinates. The nodal coordinates were made consistent between load increments by starting each load increment with the contact radius (hence nodal coordinates) found from the previous load increment. Nodal displacements could not be compared directly between load increments except at the corners of the model (one of which was at the center of the applied load), because only there were the nodal coordinates fixed. In practice, the contact radius change between load increments was small, and the change in the location of the nodes between load increments was small.

Core Properties

Since the primary functions of the core in a sandwich construction are to resist transverse compression (supporting the facesheets) and transfer shear loads. Although Nomex honeycomb core is known to exhibit nonlinear load deflection relations in both compression and shear before any damage,[10] linear material properties were used in this research up to the point of core damage. A core constitutive model that includes a linear secant modulus for the ratio of transverse direct stress to transverse direct strain before core damage was used. Similarly, the ratio of maximum transverse shear stress to transverse shear strain in each of the in-plane directions will form the constitutive components for the 4 and 5 components. Having no data from which to deduce Q_{45} or Q_{66}, Q_{45} was assumed to be zero and Q_{66} was assumed to have a value of 10% of the average of Q_{44} and Q_{55}. The later was done to avoid problems associated with a zero stiffness in in-plane shear. In particular, the Q_{ij} terms before translation are:

$$Q_{33} = \frac{\sigma_{zz_{crush}}}{\varepsilon_{3_{crush}}}, Q_{44} = \frac{\sigma_{yz_{\max}}}{\varepsilon_{4_{@\sigma_{yz_{\max}}}}}, Q_{55} = \frac{\sigma_{zx_{\max}}}{\varepsilon_{5_{@\sigma_{zx_{\max}}}}}, Q_{66} = \frac{Q_{44}+Q_{55}}{20}, Q_{45} = 0 \qquad (58)$$

Damage progression

Matrix cracking.

Matrix cracking was assumed to be present in a particular lamina when one of the stress-based failure criteria was violated. The damage mode matrix cracking was handled as a constitutive change in which the coefficients Q_{12}, Q_{22}, Q_{23}, Q_{44}, and Q_{66} were reduced by three orders of magnitude. The progression of matrix cracking was based on load transfer within the finite element model. It is assumed that all forms of damage are coupled, so that matrix cracking will affect and be affected by core damage and delamination. Both core damage and delamination were modeled in the local FEM as was matrix cracking. Matrix cracking progression was not included in the global FEM. That is, the stiffness reduction associated with matrix cracking and as well as the load transfer leading to the continuation of matrix cracking was included in the local but not the global finite element model. The approach then, was not complicated. Within the local model, after each FEA step, in-plane stress was calculated. Three-dimensional equilibrium was approximately satisfied, producing transverse stresses and modified in-plane stresses. These stresses are used in the failure criteria to determine if matrix cracking was present in any particular ply at any particular Gaussian point (all integration was done at these points rather than the nodes). If matrix cracking was determined to exist, the constitutive relation for that ply in that element was modified in proportion to the number of Gaussian points that failed. That is, if one fifth of the Gauss points within a given element showed matrix cracking at ply k, the constitutive terms for that ply were reduced by one fifth. The finite element solution was repeated without changing the load. Within the damage algorithm, iteration continued until no additional changes to the constitutive relation ensued.

Core damage.

In the global model, core damage was handled in much the same way as matrix cracking. All the comments concerning the matrix damage apply directly to core damage as well. After damage, the entire core stiffness was effectively removed (it was necessary to leave it nonzero to avoid conditioning problems). In the local model, core damage was modeled by removing the elastic foundation stiffness for elements found to have core damage. In addition to this stiffness change, equilibrium integration for the local model was accomplished with zero stress at the bottom surface of the facesheet (since the core stiffness is zero). This was done by integrating equations (18) through the facesheet and taking the lower boundary condition as zero. In this way, the condition $\sigma_3=\sigma_4=\sigma_5=0$ is enforced for the facesheet locally at the interface between the core and the facesheet. This equilibrium change partially accounts for the fact that when the core is damaged it does not support the facesheet. That is, the motion of the facesheet into the space formerly occupied by the core will not induce any transverse direct or shear stress at the lower surface of the facesheet. The effect was a much higher bending-type load within the top facesheet as the transverse direct stress formerly taken by the core must be transferred by transverse shear within the facesheet to the surrounding supported facesheet. The intact core immediately surrounding the damaged core saw an increased transverse load since it acts as a fulcrum for the bending top facesheet.

The interaction between the tup, the top facesheet, and the core is illustrated schematically in figure 13. In the figure, the core is represented by springs to emphasize its role in providing vertical support for the top facesheet. The leftmost undamaged spring in figure 13 is seeing a greatly increased transverse load as described above.

Delamination.

The effect of delamination on the plate response was considered in the local model through a procedure very similar to that described above for matrix cracking. The only significant differences were that the failure criterion was based on the interface stresses and constitutive terms for both plies adjacent to the failed interface were reduced. In this way, the constitutive terms contributing to transverse shear stiffness were reduced, but the in-plane stiffness of the facesheet was unaffected by the simulated delamination.

Local Model Solution Algorithm

The algorithm developed for this research is local-global in that it incorporates a local model which is solved first and a global model which depends on the local model solution. The local model simulates the sandwich structure by modeling the top facesheet as a plate and the core as a foundation supporting the facesheet. The core stiffness is constant (elastic) until the core stress reaches the yield stress, taken to be the maximum stress attained in uniaxial compression.[10] The strain at which the core first attains the yield stress is the yield strain. Between yield strain and failure strain, the core (secant) stiffness varies to maintain the core yield stress at the lower surface of the top facesheet. Thus the foundation must be called elastic-plastic, even though the finite element does not include plasticity. The principal feature not included in the local model (hence the need for a global model) is midplane displacement of the sandwich. The motion of the top facesheet relative to the sandwich midplane is modeled in the local model and the motion of the sandwich midplane is modeled in the global model (a full sandwich plate). Facesheet damage modes (fiber failure, matrix cracking, and delamination) are assumed to develop in such a way that they can be approximated by a progressive reduction in plate stiffness through the constitutive relations. Core crushing is also treated as a stiffness reduction of sorts, but is included as a reduction in the foundation stiffness rather than a constitutive adjustment. In the global model, facesheet damage made such a small difference to the global stiffness in the early runs, that it was neglected for the later runs. The main features of the local model algorithm are presented in flowchart form in figure 14.

For a given load increment, the solution proceeds as follows. An estimated contact radius (that of the previous load increment, or the user-supplied starting value for the first load increment) determines the mesh and applied pressure profile. The finite element model for these boundary conditions is solved using a modified Newton-Raphson iterative procedure. The displacements from the finite element solution are used to calculate in-plane stresses and the in-plane stresses are used in the three-dimensional equilibrium equations to determine the transverse stresses and the transverse direct strain. The transverse direct strain is integrated through the thickness and added to the midplane displacements to estimate the top surface displacement profile. The top surface displacements within the contact region are fit to a sphere using a lest squares technique and the contact radius is updated based on the resulting surface radius. This is iterated until the tup radius and the top surface radius are in agreement. When the contact radius has thus converged, the core failure algorithm is invoked. The failure criteria are checked to determine if any new core failures are found. If so, the foundation stiffness is modified for the affected elements and contact algorithm is repeated. This iteration of the core failure continues until no additional core failures ensue. At that point, facesheet damage is checked. If new facesheet damage is found, the appropriate ply stiffnesses are reduced and the core failure algorithm is repeated. The facesheet damage algorithm is iterated until no additional facesheet damages are found. At that point, the contact, core, and facesheet algorithms have converged and the global model is run using the present load and contact radius to determine the sandwich plate midplane displacements. The load is then incremented and the process is begun anew.

Global Model Solution Algorithm

As mentioned above, the principal feature not included in the local model is displacement of the sandwich midplane. It is desired to compare load verses displacement curves between the analysis and the experiment. The displacements available from the local model are with respect to the sandwich midplane and thus do not include the overall bending of the sandwich under the applied load. This motivates the need for a global model in order to obtain the displacement of the sandwich midplane. The displacements predicted by the local/global analysis are the sum of the midplane displacement of the global model and the displacement from the local model. The global model uses the same grid, boundary conditions (except it does not include a foundation), contact radius, and load as the local model. Damage is not included in the global model, and contact is not iterated so the global model solution algorithm is much simpler than the local model. The global model solution algorithm is illustrated by a flowchart in figure 15.

Local/Global Interaction

The local model determines the contact radius based on the deformations in the vicinity of the tup. Localized stiffness changes due to core and facesheet damage are included. The only interaction then, between the local model and the global model is the contact radius. For any given load step, the local model is satisfied first. The contact radius determined by the local model is used with the given load (and the assumption of Hertzian distribution) to produce the applied pressure profile for the global model. The global model midplane displacement is added to the local model displacement to obtain the predicted total displacement.

Comparison to Experiment

In the tests to which the finite element analysis will be compared, sandwich plate structures were loaded both statically and dynamically through contact with a 12.7 mm radius spherical indentor located at the center of the plate which moved transverse to the plane of the plate. To model this, sandwich plate plane stress elements are loaded with a Hertzian contact load. Two different models are actually used, a local model and a global model. In the local model, the top facesheet are modeled with plane stress elements while the balance of the plate are modeled by an elastic-plastic foundation supporting the top facesheet. In a second model (the global model) the entire sandwich structure (both facesheets and the core) are modeled using plane stress elements to obtain the gross deformations of the plate. The grids, loads, and edge boundary conditions for the two models were the same. The sum of the displacement of the midplane of the global model and the displacement of the top surface in the local model was taken to be the predicted displacement of the top surface of the sandwich plate. In this way, the global model provides the solution for the sandwich plate bending while the local facesheet bending and the contact between the indentor and the specimen were modeled by the plate on an elastic-plastic foundation in the local model. Stress and failure were evaluated from the results of the local model. Damage was modeled in the local model by constitutive (facesheet) and foundation (core) stiffness reductions in the elements in which damage was indicated by stress and strain based criteria.

A significant difference between the analysis and the experiment must be kept in mind when interpreting these results, namely, the fact that the experiment was conducted using displacement "control" while the analysis used load control. That is, in the experiment, indentor (or impactor) displacement was the controlled parameter (input) while the load developed by the plate was a result (output). In the analysis, the load applied by the indentor was the controlled parameter, and the displacement was a result. Load control in the analysis was needed in order to maintain a Hertzian contact pressure under the indentor, but it lead to the inability of the analysis to directly resolve load drops associated with damage.

It should be emphasized that the grid shown in figure 16 is for the smallest contact radius observed in the experiment, so that the grid distortion shown in that figure (the distortion of the elements from a square shape) is the maximum expected from the simulations of the test data. That is, no actual test runs are expected to have poorer shaped elements, so if a given mesh refinement is sufficient for these test cases, it should be sufficient for all of the actual test runs as well. As can be seen in figure 16, the adaptive mesh algorithm placed the majority of the elements within 2.5 contact radii of the center of the plate, and bilateral symmetry was exploited. Though the adaptive mesh algorithm did maintain square elements in the vicinity of the applied load (where strain gradients are high), the aspect ratio of the elements far from the applied load is seen to be very high. Thus, even the 13x13 mesh must still be considered coarse away from the applied load. The problems associated with high aspect ratio elements were not observed in these tests. This may be due to the fact that the stress in the poorly shaped elements was nearly aligned with the long axis of the elements, and the strain gradients within those elements were relatively small. Results from the 4- and 48-ply test cases with a 1.0 mm contact radius and a unit (1.0 N) load are shown for the various grid sizes in figure 17. This figure shows that the center displacement of the plate increased with grid refinement, but appears to asymptotically approach a limit. This figure indicates that the finite element model was too stiff, as expected, but that the stiffness error is virtually eliminated by refining the mesh to a 9x9 grid. Increasing the grid size above 9x9 did not, in the opinion of the authors, significantly improve of the stiffness of the finite element solution.

Test Cases

For the 16-ply specimens, three test cases were run in order to highlight the roles of the different damage mechanisms. For each cae, the tup radius was 12.7 mm and the load varied in 16 equal increments from 409.1 N to 3477.2 N. The symmetric boundary conditions were those shown in figure 7 in which a/2 took on the value of 63.5 mm so that the entire plate modeled was 127 mm square as was the fixture in which the specimens were tested experimentally[8]. The element employed had 14 degrees of freedom per node and is described earlier. Each case employed a local model in which the facesheet was modeled as a monolithic laminate on an elastic foundation, and a global model on which both facesheets and the core were modeled by a sandwich element. Details peculiar to each test case are described below.

Case 1, no damage.

In the first case, no damage was modeled. For each step in load, the contact problem was solved iteratively with the local model. The core and facesheet material properties in the local model were constant for all loads. The contact radius (as a function of load) obtained from the local model was used in the global model so that the applied load distribution on the global model, for any given load, was determined by the local facesheet bending and core compression effects as modeled in the local model. This case provided a baseline to show the effects of the damage in the other two cases which included damage.

Case 2, core damage only.

In the second case, core damage was modeled, but facesheet damage was not. That is, in the local model, the elastic-plastic foundation stiffness was reduced under each element that showed core failure. This was done via the damage algorithm described. The reduction of the stiffness was constant for the entire element and proportional to the number of Gauss points within the element that failed due to core crushing. Within the local model, and for a given load increment, if the core failed, the contact algorithm was reiterated until a new converged contact radius was obtained. The damage algorithm was then re-invoked to determine if additional damages were brought about by load shedding due to the core stiffness reduction or by load redistribution due to the changed contact radius. This process was repeated for any given load step until the damage did not change further and the contact algorithm indicated that the portion of the top surface of the plate over which the load was applied was conformed to the known spherical tup radius. Contact and damage algorithms were thus nested so that for any given load increment the local model provided a converged damage profile and contact radius. The resulting contact radius (as a function of load) was the same as that of case 1 until the load at which core damage began (core damage initiation load) was reached. Beyond this core damage initiation load, the contact radius for case 2 was generally different from that of case 1. The contact radius output from the local model was used to load the global model with Hertzian contact loads. While the core failure algorithm was employed for this case, the facesheet failure algorithm was not. The material properties of the facesheets were constant for all loads. This case provided a means to understand the role of core damage without facesheet damage.

Case 3, facesheet and core damage.

In the third case, core and facesheet damages (fiber failure, delamination, matrix cracking, and core crushing) were all modeled together. Within the local model, facesheet damages were allowed in the top facesheet only. This restriction was considered due to the fact that damage was not found in the bottom facesheet in the experimental effort. No damages were modeled in the global model. The third case shows the ability of the algorithms developed for this research to model the damage of a composite sandwich structure by transverse Hertzian contact-type loads simulating low-velocity impact.

Metrics for Success of the Analysis

The analysis and the experimental data must be compared in some meaningful way to determine how well the analysis did at predicting the experimental results. The particular measures chosen as the basis for comparison between experimental and analytical results are, contact radius as a function of load, the load verses displacement curves, and delamination patterns. The metrics are here described.

Contact radius.

The first metric is contact radius as a function of load. This metric should indicate how well the contact algorithm in the analysis models the actual event. The experimental data available for contact radius were not measured directly. Separate tests were conducted in which a pressure sensitive paper was placed between the indentor and the specimen. After loading to the prescribed load, the pattern left on the paper was an impression of the "footprint" of the indentor for that load. The widest portion of the footprint was measured with a ruler and taken to be twice the contact radius for that load. The edges of the footprint were not well defined, so the measurements were rather subjective. For this reason, the experimental contact radii should be considered rough estimates. The experimental error was not determined.

Load verses displacement curve.

The static indentation load verses displacement curves provide a stiffness check of the finite element algorithm as well as a check of the load at which core failure begins. The load drops seen in the experiment were not observed in the analysis because the analysis, being load controlled, did not permit load reduction.

Delamination pattern.

The C-scans from the experiments[8] can be compared to the delamination patterns predicted by the analysis. Though the analysis determined the delamination pattern at each interface, the C-scans provide only a single pattern for the whole facesheet. The through the thickness variation of the delamination pattern was provided by Harrington's photomicrographs [5].

Analysis Results

Contact radius.

In the analysis, the inclusion of facesheet damage in the form of reduced constitutive terms in the damaged elements has very little effect on the contact radius. This can be seen in figure 18, in which facesheet damage was present for all loads above 1300 N.

From the experimental data shown in Figure 18, the contact radius in the experiment is very much effected by the presence of localized damage which occurred at 2250 N. The load of 2250 N is the load associated with the first major load drop in the static testing of the 16-ply specimens. The localized damage associated with this load in the experiment was to both the core and the facesheet. Even with the inclusion of both of these damage types, the analysis does not show the experimentally observed jump in the contact radius. The failure of the analysis to predict the jump in contact radius indicates a limitation of this research. The three-dimensional effects of the damage as they "soften" the contact between the tup and the specimen are evidently not well modeled by the algorithm. This is believed to be due to the fact that the algorithm reduces the stiffness of the facesheet in the area of damage, but still models the damaged facesheet as a single element through the thickness. A single element with continuous kinematic relations through the thickness is not able to model the reduction in local bending stiffness which must be present when delaminations exist. Locally, delaminations change a single, relatively thick laminate into multiple, kinematically independent, comparatively thin, sublaminates. The local bending stiffness provided by the sum of all of the sublaminate contributions is much less than the local bending stiffness of the single laminate. The facesheet damage algorithm used in this research reduced the shear stiffnesses of the plies adjacent to the delamination, but did not allow the sublaminates to move independently. A thick laminate with reduced shear stiffnesses is still stiffer in bending than would be the sum of the component sublaminates. The effect of maintaining the single-plate kinematics in the presence of delaminations is that the stiffness reduction in the damage algorithm does not adequately reduce the local bending stiffness of the facesheet. Since the local bending stiffness of the facesheet is too high, the midplane curvature under the load is too low. The top surface displacement is calculated from the sum of the midplane displacement and the through the thickness integral of the transverse direct strain. The low curvature of the midplane thus produces a low curvature of the top surface. The contact algorithm uses the curvature of the top surface to determine what the next estimate of the contact radius should be. In effect, the contact algorithm forces the top surface curvature to conform to the curvature of the tup. If the midplane curvature is low, the contact radius will be artificially small. Thus, the facesheet damage algorithm is believed to be responsible for the inability of the analytical algorithm to model the contact radius jump observed in the experiments. Modeling the delaminated facesheet with multiple independent elements stacked through the thickness may sufficiently model the local bending stiffness loss associated with delamination to allow the contact radius jump to be predicted, but was considered to be beyond the scope of this research. Another approach that may be able to improve the modeling would be to include delamination capable kinematics. It should be observed, however, that the present analysis model allow only a single delamination, whereas the experiments, elasticity solution, and finite element solution all show multiple delaminations. Extension of the delamination capable kinematics to multiple delaminations is considered beyond the scope of this paper. Another simplification in the analysis contributing to the contact radius error is the fact that the contact algorithm is only used in the local model. Thus, sandwich midplane curvature can not effect the contact radius. The authors believes this error to be small, but nothing was done to quantify it.

Load verses displacement.

As for the contact radius, the inclusion of facesheet damage as modeled with reduced constitutive terms in the damaged elements has very little effect on the local stiffness as shown in the load verses displacement curves in figure 18. In that figure, the curves representing load verses displacement including only core damage and that including both core and facesheet damage are so close as to be indistinguishable. It should be noted that facesheet damage was present for all loads above 1300 N.

As seen in the experimental data shown in figure 19[8], it can be observed that the load verses displacement curve is very much effected by the occurrence of localized damage which occurred at 2000 N. The load of 2000 N is the load associated with the first major load drop in the static testing of the 16-ply specimens. The localized damage associated with this load in the experiment was to both the core and the facesheet. Since load control was used in the analysis, it was not possible to predict the load drop associated with damage. To account for this, the load at which the failure occured is held constant and with the reduced stiffness parameters (caused by the failure), another equilibrium state is determined. That is at the same load level, there are two equilibrium configurations, one corresponding to the configuration without failure and the other correspond to the equilbrium configuration with failure. This resulted in a horizontal jump in the load deflection curve as seen in Figure 19. It should be noted that if a displacement control algorithm is used, the same failure would have resulted in two different load levels for the same displacement configuration. That procedure would have resulted in a vertical jump in the load deflecion curve. Since the experiment conducted is a displacement cntrol configuation, such a jump can be seen in the experimental load deflection curve shown in Figure 19. The dotted line in Figure 19 indicate the interpolated load displacement curve if the displacement control algorithm was used instead of load control. That is under load control at 2000 N, the displacement jumps from 0.7 mm to just over

0.8 mm If a displacement control algorithm is used, at 0.7 mm displacement, the load would have dropped to 1800 N before increasing again to 2000 N at a displacement of 0.8 mm. With this interpolation, a very close agreement can be seen between both the analytical and experimental load deflection curves. The load associated with the beginning of this new equilibrium curve is the load at which core damage begins. The progress of core damage under a given (constant) load is illustrated in figure 20.

When core damage is present in some localized area of the sandwich, the only resistance to motion of the top surface toward the midplane (or vice versa in the static experiment) within the damaged area is the local bending stiffness of the top facesheet. In the experiment core damage leads to large movement of midplane of the specimen toward the top surface due to the flexibility of the delaminated facesheet. This flexibility also is thought to lead to rotation of the facesheet at the edge of the core damage region, so that the entire transverse load is reacted by a relatively thin ring of the core surrounding the damaged core. This situation is illustrated as the "initial position" in figure 20. The innermost portion of this thin ring of core experiences high stresses (ultimate) and core failure continues, expanding the ring. The expanded ring, having more area due to a greater radius, reacts to the transverse load with a lower average stress. This situation is illustrated as the "intermediate position" in figure 20. When the stress in the undamaged core at the edge of the damage is above (less negative than) the compressive ultimate stress of the core, the core failure is halted ("final position" in figure 20).

Delamination patterns.

Delamination can significantly reduce the residual compressive strength of a composite. It is therefore important to determine the delaminations produced by a given impact event. For this reason, delamination patterns were chosen as a metric to judge the analysis. The delaminations predicted by the finite element analysis can be compared with the C-scans shown in figure 21[8]. The physical dimensions are not given in figure 21, but the scans are magnified by 150% so that the maximum width of the 16-ply static case is 12 mm. Figure 22 shows the delamination patterns produced by the analysis for the same load. The shapes of the delaminations predicted by the analysis appear to be very good, while the size of the delaminations are too small by a factor of 2.0. The patterns shown in figure 22 are surprisingly close to those seen in the C-scan in figure 21 when one considers that the analysis based delamination on stress alone and did not include a singularity (crack tip) or even a physical discontinuity as was present in the experiment.

Conclusions

The analysis shows the ability to model some of the important features of static indentation of composite sandwich structures. In particular, the slope of the load displacement curve (stiffness), including contact, before damage is well represented. Perhaps the most important feature, core failure load, is predicted by the analysis within ten percent of the experimental value. Damage progression is under predicted by the analysis. This is believed to be attributable to the facesheet damage algorithm which evidently does not adequately reduce the local bending stiffness of the top facesheet when delamination occurs. Delamination patterns predicted by the analysis bear a striking resemblance to the C-scans from the experiments, but are smaller in size. A more accurate model for the local bending stiffness in the delaminated region should produce better damage progression results. Possible ways to do this without resorting to a full three-dimensional finite element model are by modeling the delaminated facesheet as a stack of independent sublaminates, or, including delamination capable kinematics.

References

[1] Hackman, L. E., "Sandwich construction and design," in Analysis and design of flight vehicle structures. Ed. E.F. Bruhn. Tri-State Offset Company, 1965, pp. c12.1-c12.52.

[2] Harrington, T.M. An Experimental Investigation of Sandwich Panels Under Low Velocity Impact, MS thesis, AFIT/GAE/ENY/94D-22. School of Engineering, Air Force Institute of Technology (AU), Wright-Patterson AFB OH, December 1994.

[3] Cantwell, W.J., and Morton, J. "The impact resistance of composite materials - A review," Composites, Vol. 22, 1991, pp. 347-362.

[4] Abrate, S. "Impact on laminated composite materials," Applied Mechanics Reviews, Vol. 44, No. 4, 1991, pp. 155-190.

[5] Tsang, P.H.W. Impact resistance and damage tolerance of composite sandwich panels, PhD dissertation, MIT. 1994.

[6] Noor, A.K. Burton, W.S. "Computational models for sandwich panels and shells," *Applied Mechanics Reviews*, Vol 49, No 3, 1996, pp. 155-199.

[7] Washizu, K., *Varitaional methods in elasticity and plasticity, 3rd Edition*, Oxford: Pergamon Press, 1982.

[8] Herup, E. J., *Low-Velocity Impact on Composite Sandwich Plates*, Ph.D. dissertation, AFIT/DS/ENY/96-11. School of Engineering, Air Force Institute of Technology (AU), Wright-Patterson AFB OH, 1996.

[9] Nahas, M.N. "Survey of failure and post-failure theories of laminated fiber-reinforced composites," *Journal of Composites Technology & Research*, Vol. 8, No. 4, 1986, pp. 138-153.

[10] Bitzer, T.N. *Honeycomb toughness and proportional limits*, Hexcel Corporation Report LSR 932277. 1983.

[11] Hashin, Z-.H. Failure criteria for unidirectional fiber composites," *Journal of Applied Mechanics,* Vol 47, 1980, pp: 329-334.

[12] Palazotto, A.N., and Dennis, S.T. *Nonlinear analysis of shell structures, AIAA Education Series.* Washington DC: AIAA, 1992.

[13] Tsai, C.T., and Palazotto, A.N. "On the finite element analysis of non-linear vibration for cylindrical shells with high-order shear deformation theory," *International Journal of Non-Linear Mechanics*, Vol. 26, pp: 379-388.

[14] Cook, R.D., Malkus, D.S., and Plesha, M.E. *Concepts and applications of the finite element method*," third edition, John Wiley & Sons, 1989.

[15] Timoshenko, S. and Goodier, J.N., *Theory of Elasticity*, New York: McGraw-Hill, 1951

APPENDIX

Hashin's Failure Criteria

Fiber Failure

Tensile:

$$\left(\frac{\sigma_1}{X_T}\right)^2+\frac{\sigma_5^2+\sigma_6^2}{T^2}\geq 1$$

Compressive:

$$\sigma_1\geq\frac{G_r}{1-k}$$

Matrix Failure

Tensile

$$\frac{\sigma_2^2+\sigma_3^2}{R^2}+\frac{\sigma_4^2+\sigma_5^2+\sigma_6^2-\sigma_2\sigma_3}{R^2}\geq 1$$

Compressive

$$\frac{1}{Y_c}\left[\left(\frac{Y_c}{2T}\right)^2-1\right](\sigma_2+\sigma_3)+\frac{(\sigma_2+\sigma_3)^2}{4T^2}+\frac{\sigma_4^2+\sigma_5^2+\sigma_6^2-\sigma_2\sigma_3}{T^2}\geq 1$$

Delamination

$$\left(\frac{\sigma_3}{Z_T}\right)^2+\frac{\sigma_5^2+\sigma_6^2}{R^2}\geq 1$$

Here $\sigma_1,\sigma_2,\sigma_3$ are the normal stress components, $\sigma_4,\sigma_5,\sigma_6$ are the shear stress components, X_T,Y_T,Z_T,X_C,Y_C,Z_C are the lamina normal strengths in tension and compression along 1,2,3 directions, R,S,T are the shear strengths in the 23,13 and 12 planes.

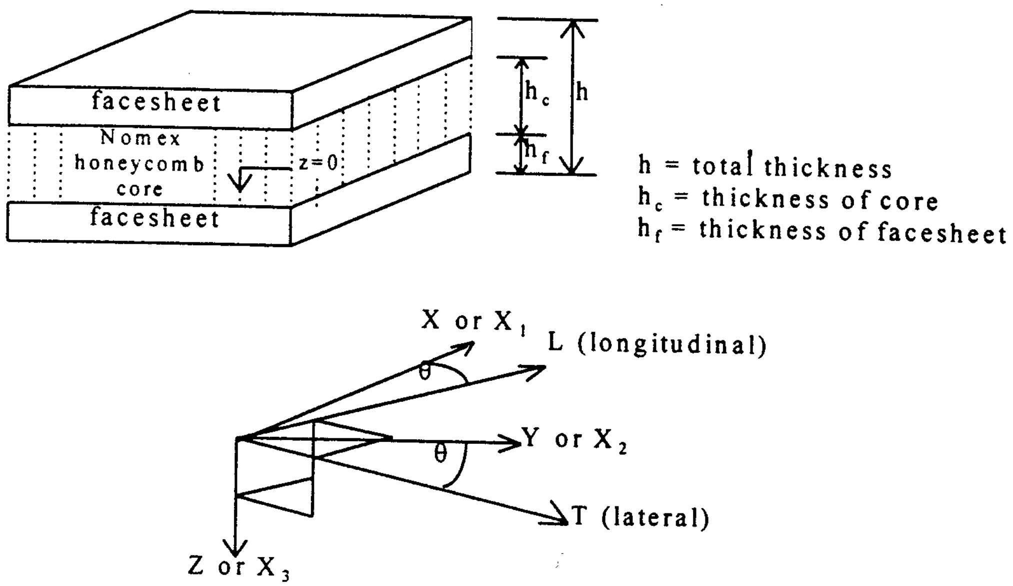
facesheet
Nomex
honeycomb
core
z=0
facesheet
h_c
h
h_f
h = total thickness
h_c = thickness of core
h_f = thickness of facesheet
X or X_1
L (longitudinal)
θ
Y or X_2
θ
T (lateral)
Z or X_3

Fig. 1 Sandwich plate geometry and coordinate systems.

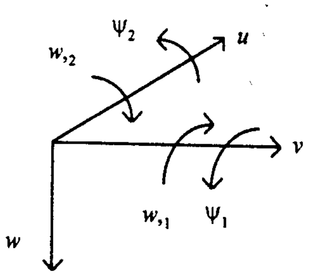
Ψ_2
u
$w,_2$
v
$w,_1$
Ψ_1
w

Fig. 2 Plate displacement vector components.

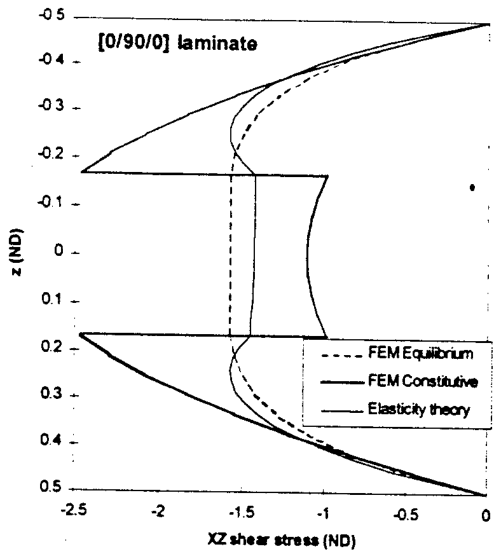

Fig. 3 Transverse shear as calculated by elasticity theory, constitutive relations, and equilibrium equations for sinusoidally loaded plate in cylindrical bending. Dimensions, material properties, and scaling from Pagano [236].

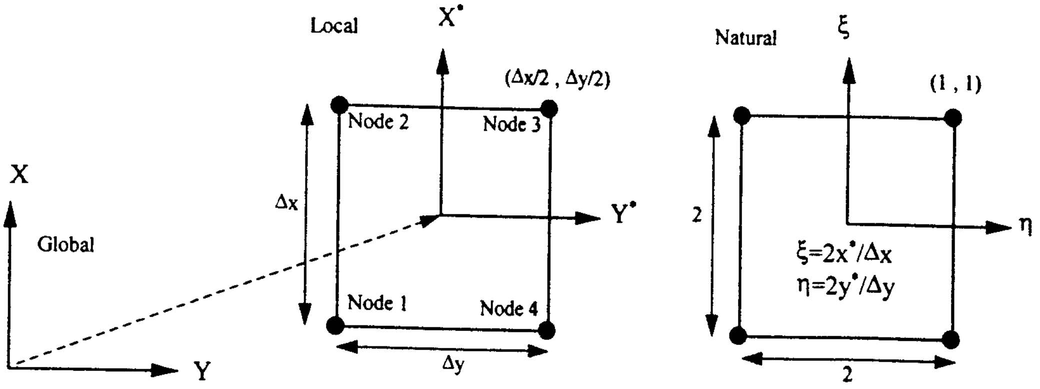
Local
X*
(Δx/2 , Δy/2)
Node 2
Node 3
Δx
Y*
X
Global
Node 1
Node 4
Δy
Y
Natural
ξ
(1 , 1)
2
η
ξ=2x*/Δx
η=2y*/Δy
2

Fig. 4 Four-node plate element geometry and coordinate systems.

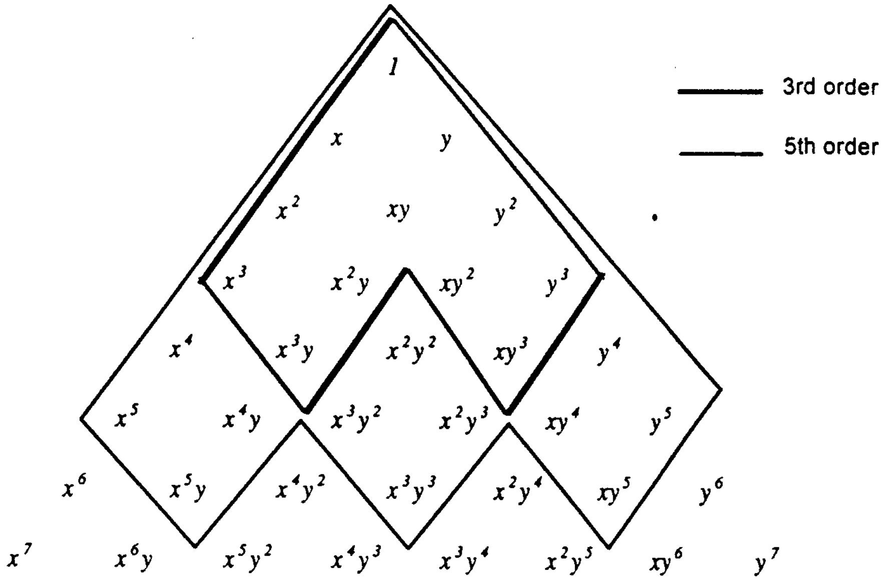
3rd order
5th order
1
x
y
x²
xy
y²
x³
x²y
xy²
y³
x⁴
x³y
x²y²
xy³
y⁴
x⁵
x⁴y
x³y²
x²y³
xy⁴
y⁵
x⁶
x⁵y
x⁴y²
x³y³
x²y⁴
xy⁵
y⁶
x⁷
x⁶y
x⁵y²
x⁴y³
x³y⁴
x²y⁵
xy⁶
y⁷

Fig. 5 Pascal's triangle showing interpolation polynomials for 3rd and 5th order shape functions. Note, polynomials are complete to 3rd and 5th order, respectively.

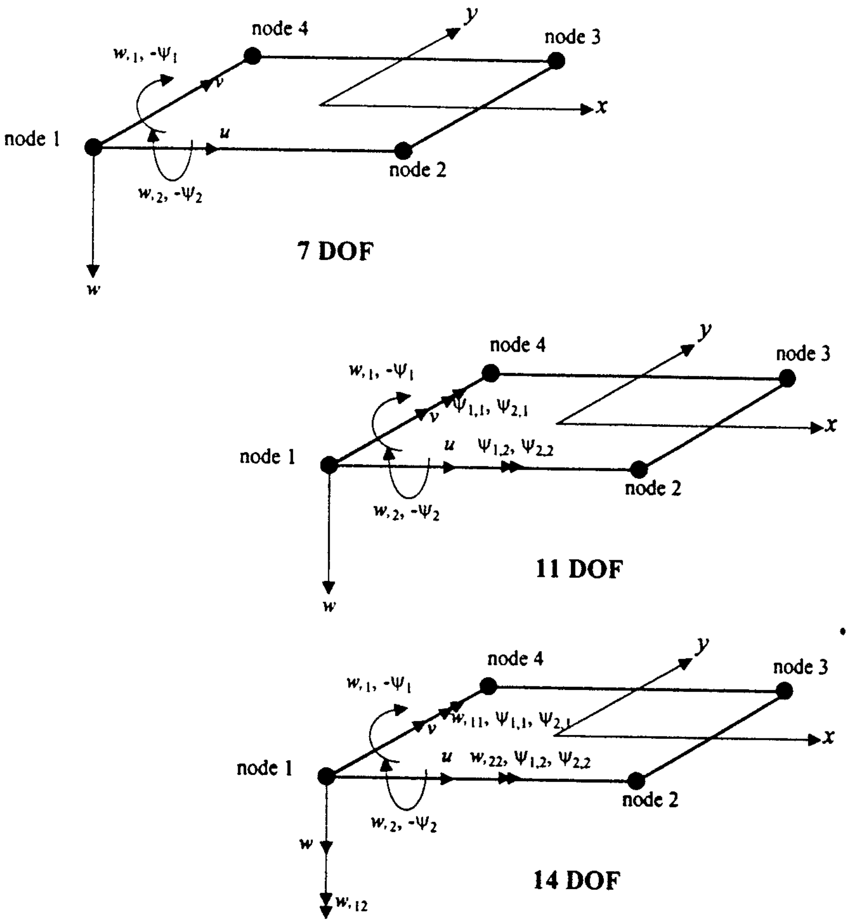
node 1
node 2
node 3
node 4
x
y
u
v
w
w,1, -Ψ1
w,2, -Ψ2
Ψ1,1, Ψ2,1
Ψ1,2, Ψ2,2
w,11, Ψ1,1, Ψ2,1
w,22, Ψ1,2, Ψ2,2
w,12

7 DOF

11 DOF

14 DOF

Fig. 6 Four-node plate elements with 7, 11, and 14 degrees of freedom per node.

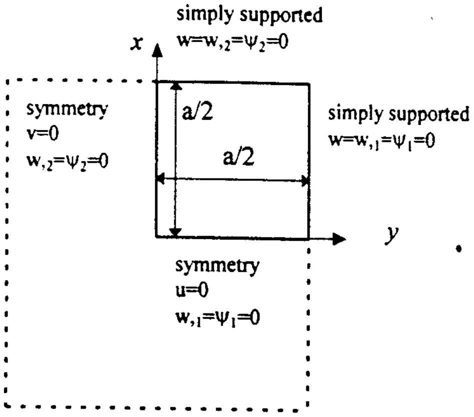
simply supported
w=w,₂=ψ₂=0
x
symmetry
v=0
w,₂=ψ₂=0
a/2
a/2
simply supported
w=w,₁=ψ₁=0
y
symmetry
u=0
w,₁=ψ₁=0

Fig.7 Boundary conditions common to each square quarter plate.

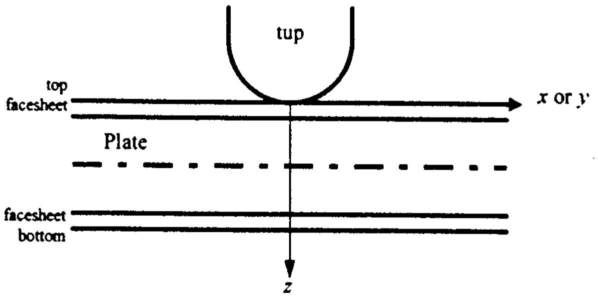
tup
top
facesheet
x or y
Plate
facesheet
bottom
z

Fig. 8 Contact problem geometry and coordinate system.

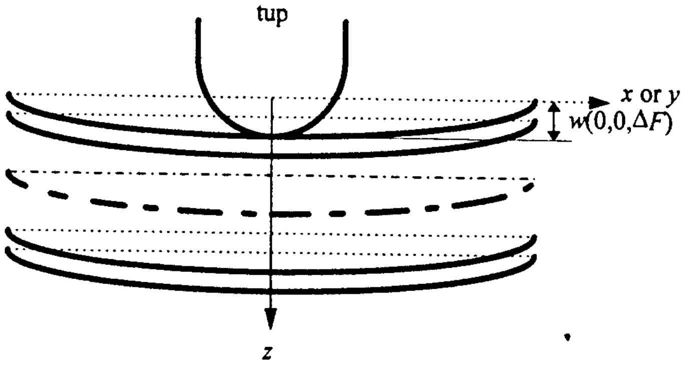
tup
x or y
w(0,0,ΔF)
z

Fig. 9 Finite element displacements for initial small load.

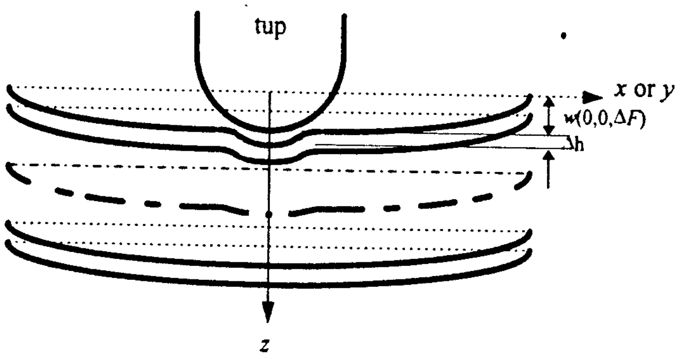
tup
x or y
$w(0,0,\Delta F)$
h
z

Fig. 10 After first step of FEM/3D-equations of motion.

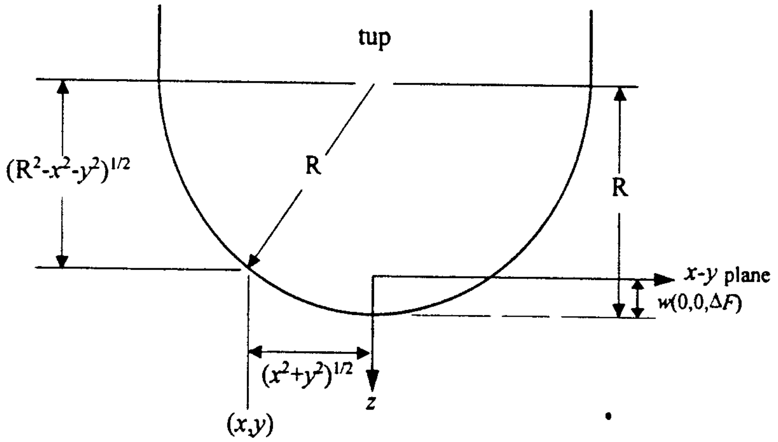
tup
$(R^2-x^2-y^2)^{1/2}$
R
R
x-y plane
$w(0,0,\Delta F)$
$(x^2+y^2)^{1/2}$
z
(x,y)

Fig. 11 Tup surface as a constraint on the plate top surface displacement.

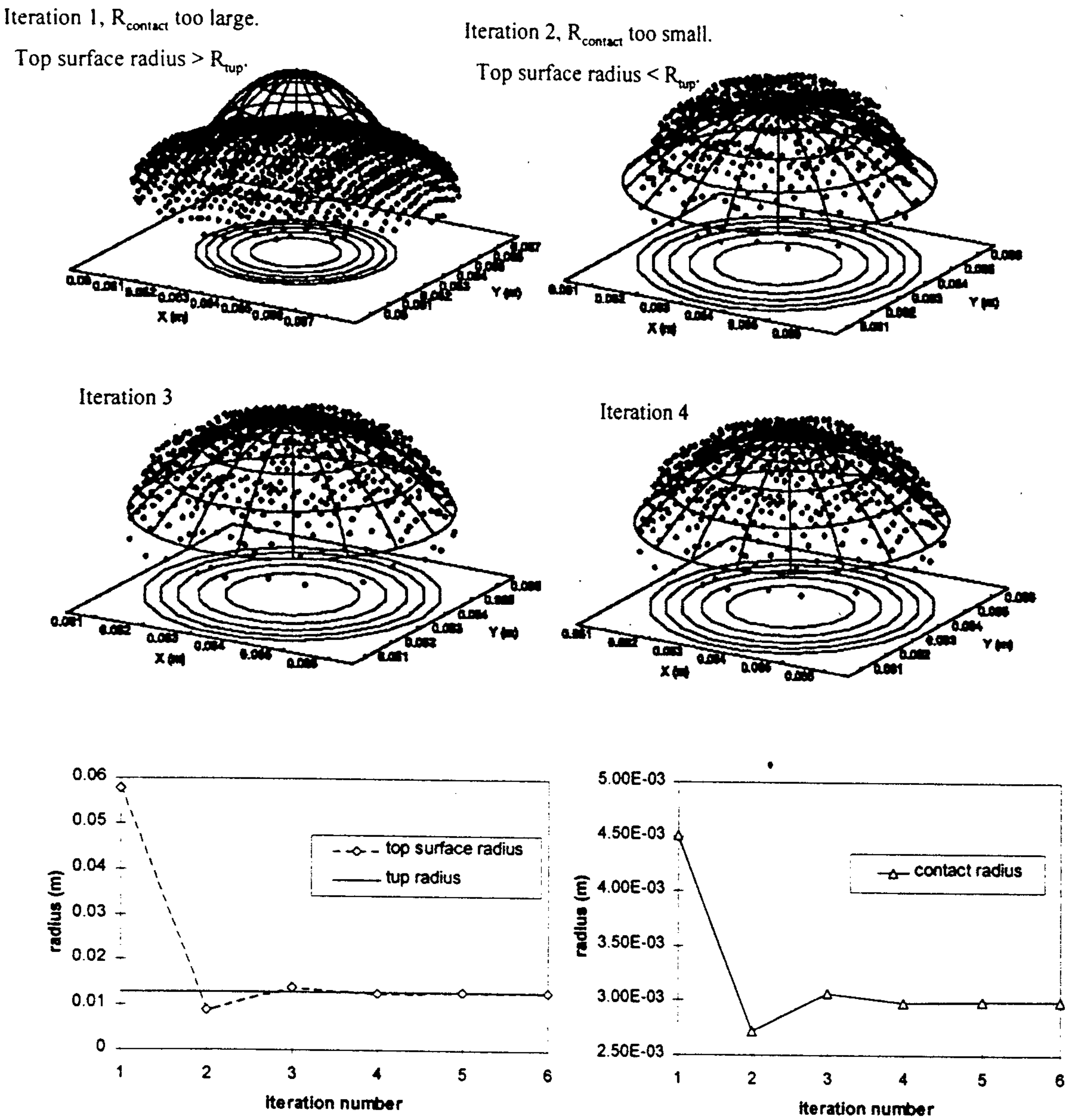

Iteration 1, $R_{contact}$ too large.

Top surface radius > R_{tup}.

Iteration 2, $R_{contact}$ too small.

Top surface radius < R_{tup}.

Iteration 3

Iteration 4

Fig. 12 Typical convergence of tup surface radius and contact radius with contact iteration.

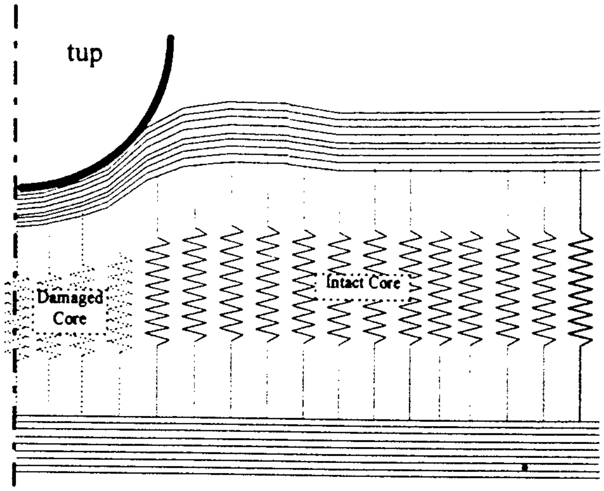
tup
Damaged Core
Intact Core

Fig. 13 Schematic of core failure

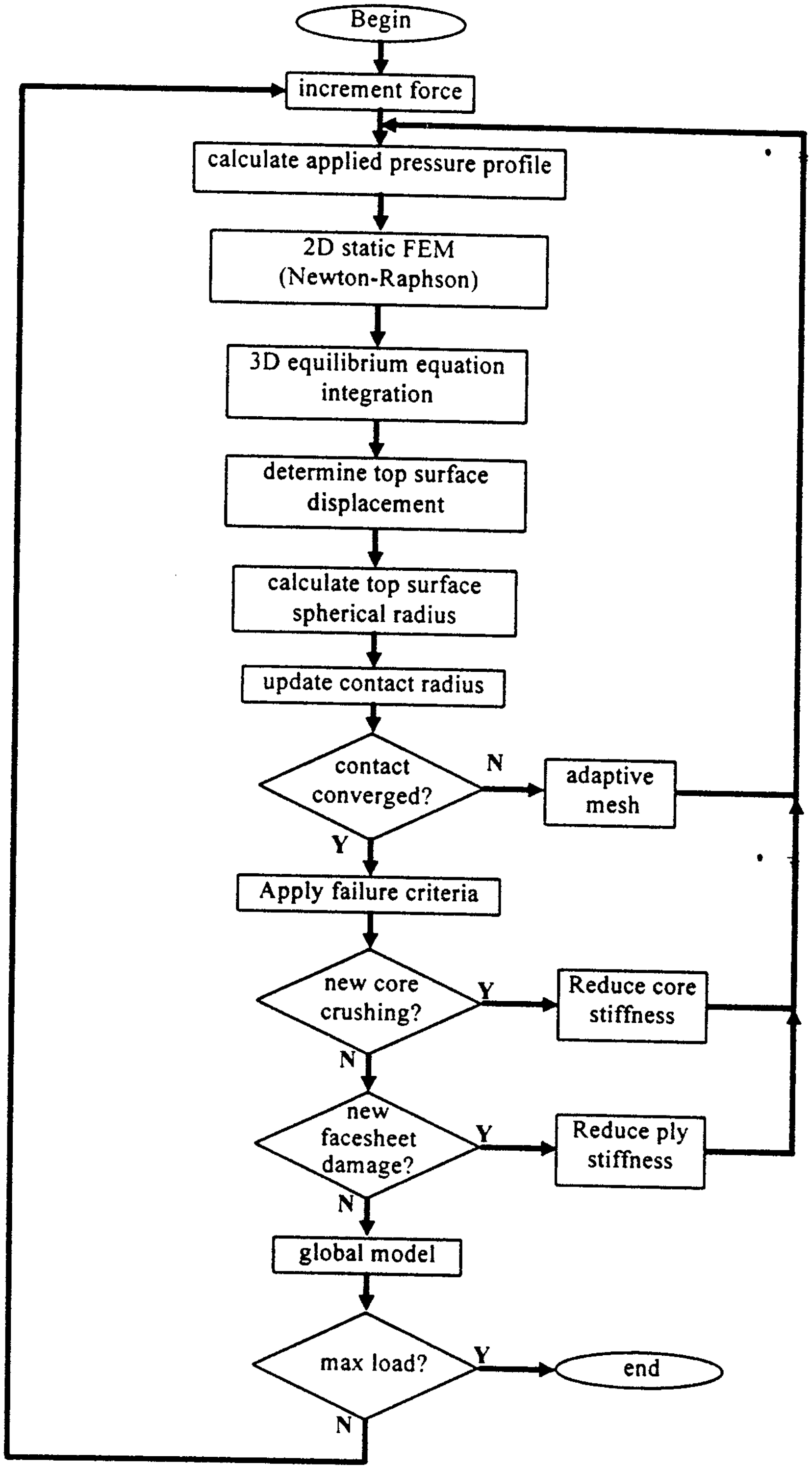
Begin
increment force
calculate applied pressure profile
2D static FEM (Newton-Raphson)
3D equilibrium equation integration
determine top surface displacement
calculate top surface spherical radius
update contact radius
contact converged?
N
adaptive mesh
Y
Apply failure criteria
new core crushing?
Y
Reduce core stiffness
N
new facesheet damage?
Y
Reduce ply stiffness
N
global model
max load?
Y
end
N

Fig. 14 Local-global solution algorithm flowchart.

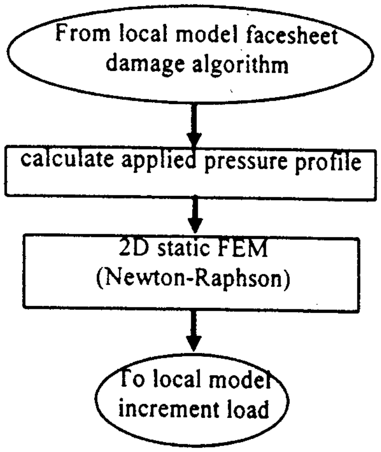
From local model facesheet damage algorithm
calculate applied pressure profile
2D static FEM (Newton-Raphson)
To local model increment load

Fig. 15 Global solution algorithm flowchart.

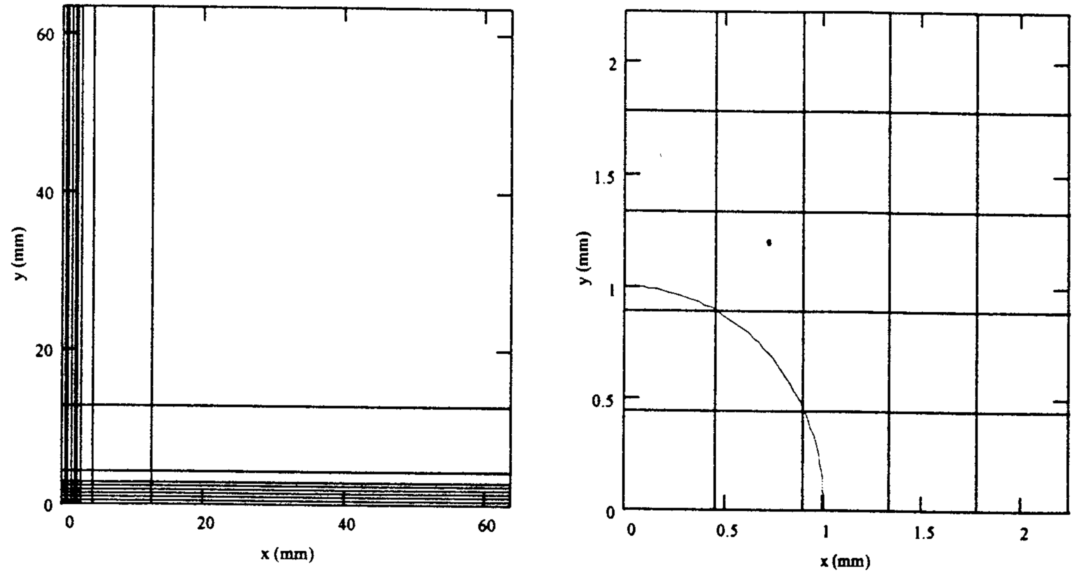

(see detail a)

(detail a)

Figure 16 9x9 grid for contact radius = 1.0 mm. Maximum aspect ratio = 115.

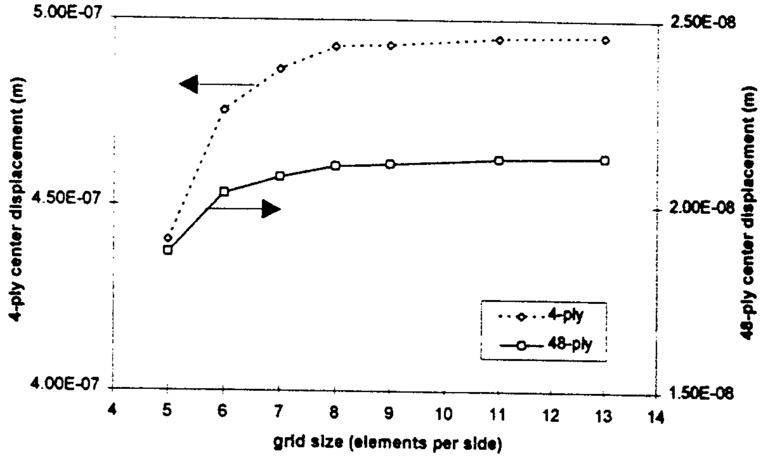

Figure 17 Plate center displacement verses grid size (4- and 48-ply sandwich plate, 1.0 N load, contact radius = 1.0 mm), showing that above 9 elements per side, the solution does not significantly change.

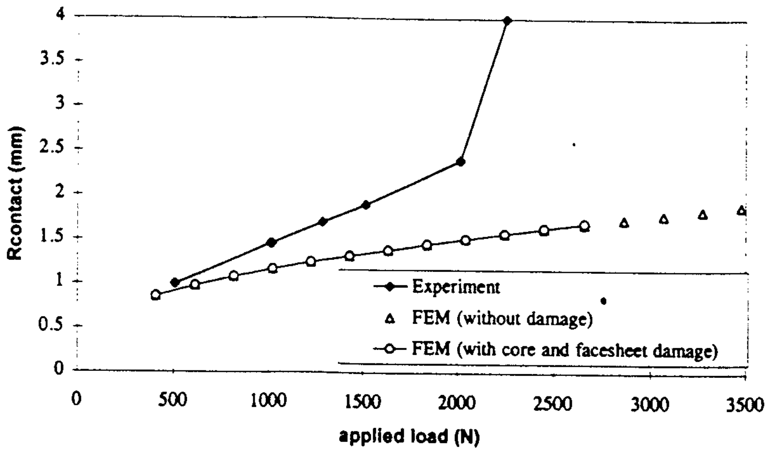

Figure 18 Contact radius predicted by local finite element model with facesheet and core damage considered (16-ply).

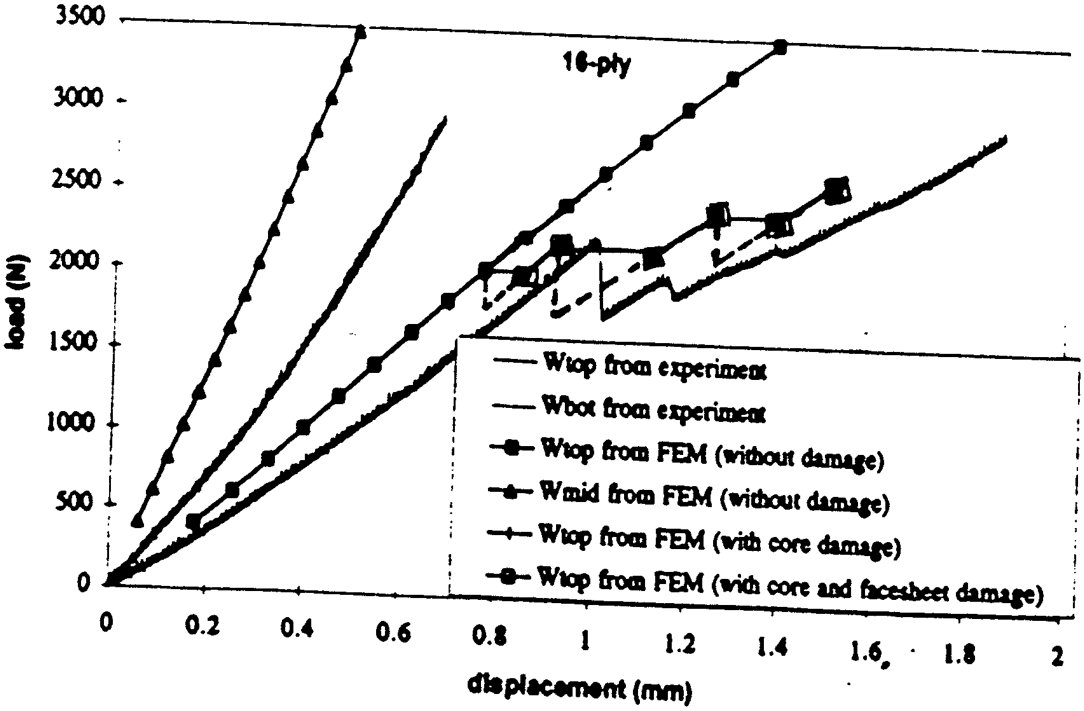

Figure 19 **Load verses displacement predicted by local finite element model with and without considering facesheet and core damage (16-ply).**

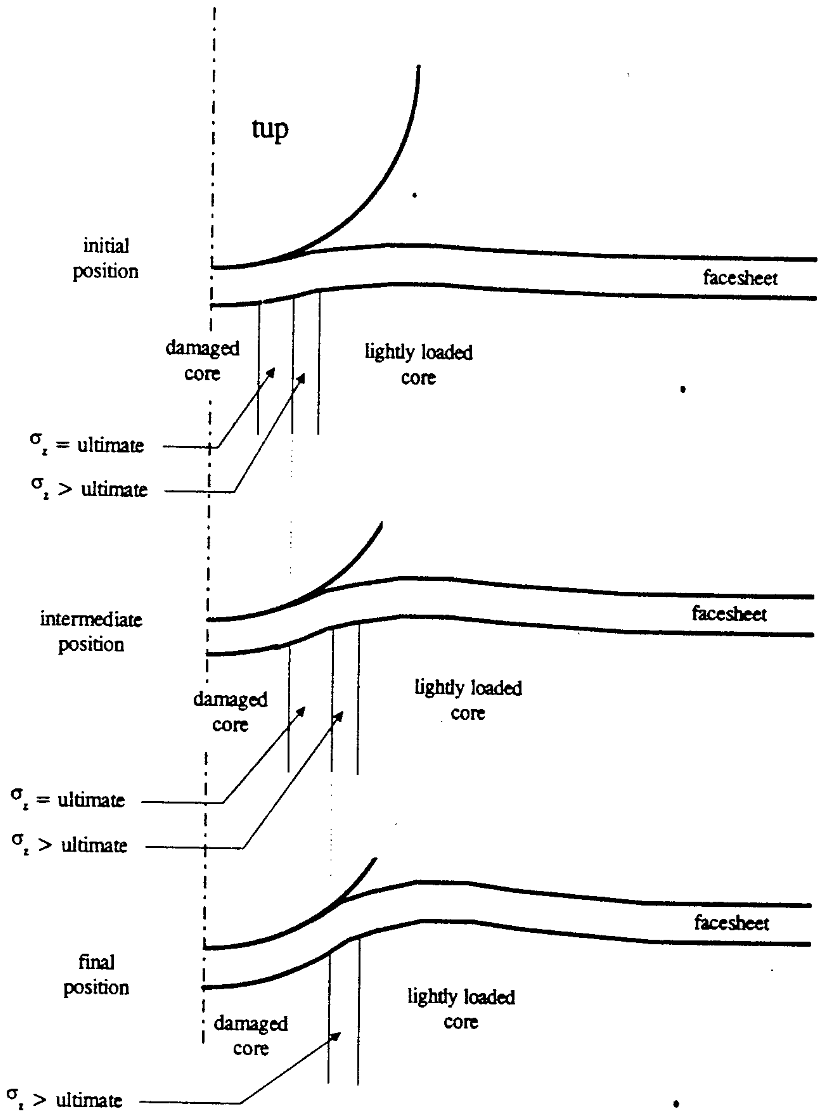
tup
initial position
facesheet
damaged core
lightly loaded core
σ_z = ultimate
σ_z > ultimate
intermediate position
facesheet
damaged core
lightly loaded core
σ_z = ultimate
σ_z > ultimate
facesheet
final position
damaged core
lightly loaded core
σ_z > ultimate

Figure 20 Illustration of the progress of core damage under a constant applied force.

	4-ply	8-ply	16-ply	32-ply	48-ply
Static		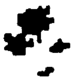	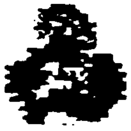	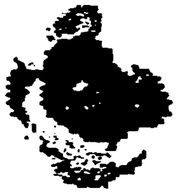	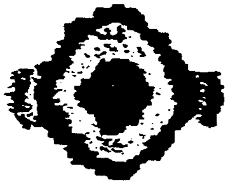

Figure 21 C Scans under static loading for different ply lay ups

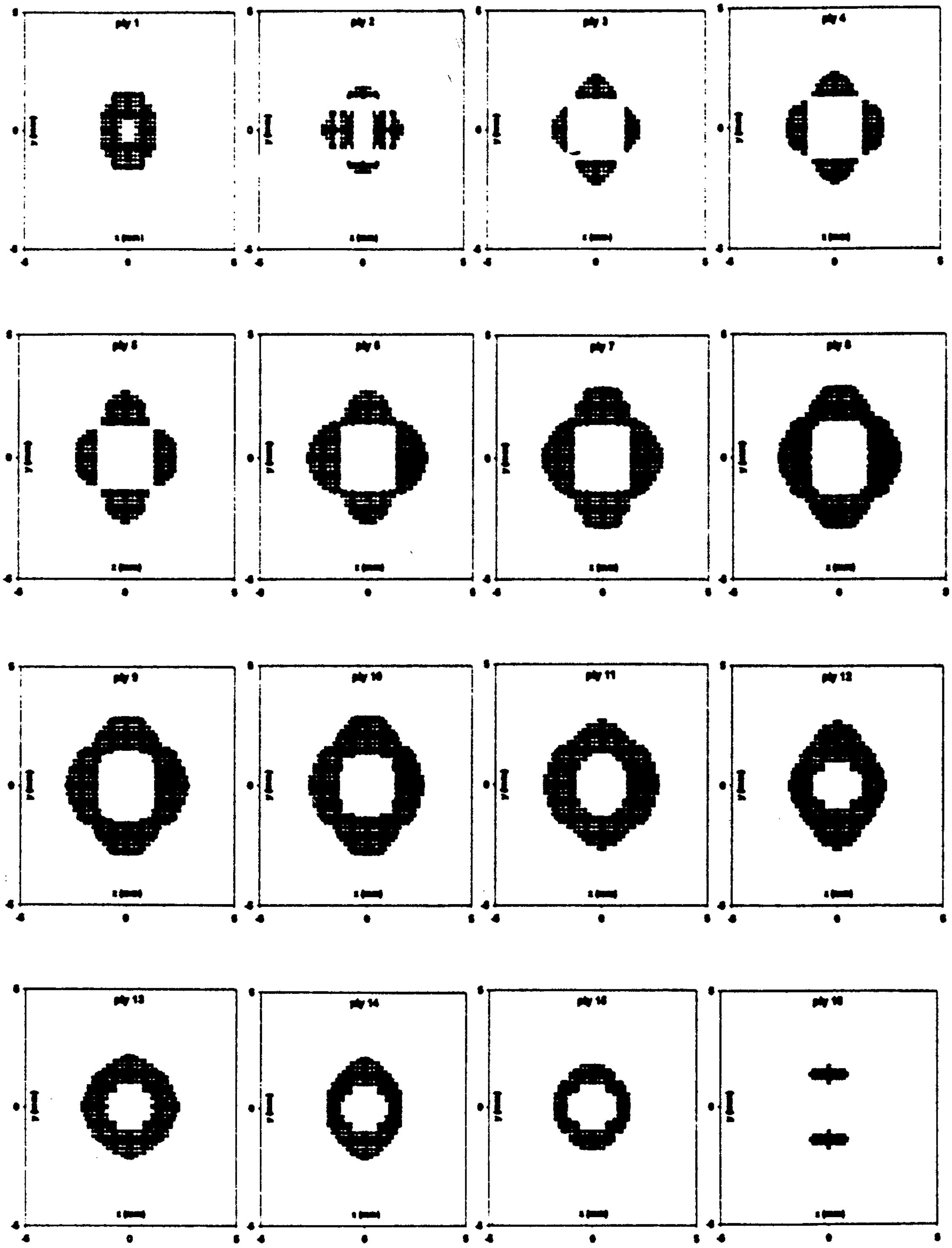

Figure 22 Delamination patterns predicted by the analysis for 2250N load (16 ply)

ATTACHMENT VI

ANALYTICAL MODELING OF SANDWICH PLATE DYNAMICS UNDER LOW VELOCITY IMPACT

ANALYTICAL MODELLING OF SANDWICH-PLATE DYNAMICS UNDER LOW-VELOCITY IMPACT

Introduction

The dynamics of a homogeneous and isotropic elastic plate due to low velocity impact has been examined for many years. Expermental evidence seems to support the theory reasonably well. On the other hand, nonhomogeneous anisotropic materials, such as composite sandwich-plates are not as easily modelled. Here we analyze the sandwich-plate dynamics under low velocity impact by considering the global behavior under a dynamic load distribution while incorporating the local effects of the impacting object (figure 1). A tractable model for the global sandwich-plate will depend on impact energy and stiffness of the upper face plate. Observations of experimental data suggest that the loading dynamics should be modelled by a power law (non-Hertzian) which depends on the ply lay-up and thickness[5,8]. In this paper we summarize some analysis of a sandwich-plate model with a general power law for impact pressure.

The Sandwich-Plate

The sandwich-plate consists of two orthotropic composite face sheets of constant thickness h_f separated by a core material of constant thickness h_c (figure 2). The core material functions to stabilize the face sheets and is assumed to be of low density. Following the development of Whitney[10], these assumptions are made.

1. The core material is transversely isotropic and is much thicker than the face sheets ($h_f \ll h_c$).
2. The inplane stresses of the core, σ_x, σ_y and σ_{xy}, are negligible while the inplane core displacements are assumed to be linear in the transverse coordinate (z).
3. In the face sheets, the inplane displacements are uniform through the thickness of the face sheets and transverse shear stresses σ_{xz} and σ_{yz} are negligible.
4. The sandwich-plate's transverse displacement is small compared to the thickness.
5. The inplane strains are small compared to unity.
6. The transverse displacement is independent of the transverse coordinate, that is, ϵ_z is negligible.
7. The core and each ply of the face sheet obeys Hooke's law.

Under these assumptions, a simply supported rectangular sandwich-plate with a dynamic load distribution $P(x, y, t)$ is modelled by a system of partial differential equations given by

Whitney in reference 10. This set of equations along with its boundary conditions is reduced, using a modal expansion.

$$w(x,y,t) = \sum_{m,n=1}^{\infty} W_{m,n}(t)\sin(m\pi x/a)\sin(n\pi y/b) \tag{1}$$

and forms the uncoupled ordinary differential equations of the form

$$\rho A\ddot{W}_{m,n}(t) + Q_{m,n}W_{m,n}(t) = p_{m,n}(t) \quad \text{with } W_{m,n}(0) = \dot{W}_{m,n}(0) = 0. \tag{2}$$

Here ρA is the density times the plate area, $p_{m,n}(t)$ is found from the Fourier sine series of the load $P(x,y,t)$, and $Q_{m,n}$ is a stiffness coefficient which accounts for the material properties, geometry and boundary conditions.

As the thickness of the face sheets increases, assumptions 1, 3 and 6 may no longer apply. A new model consisting of the top face sheet on an elastic foundation was considered. This model resulted in a similar set of equations as Whitney[9] with an additional term to account for the stiffness associated with the elastic foundation. Again the equations are reduced using modal expansions and produce the same equation as 2 above however, now the stiffness coefficient is changed. This equation has the well known solution

$$W_{m,n}(t) = \frac{1}{\sqrt{\rho A Q_{m,n}}}\int_0^t p_{m,n}(\tau)\sin\sqrt{\frac{Q_{m,n}}{\rho A}}(t-\tau)d\tau \tag{3}$$

It can be shown that if $P(x,y,t)$ is bounded then the solution for each mode is bounded by a constant which vanishes as the mode numbers increase. We therefore only consider the first mode.

The Load Distribution

Historically the load distribution for the impact of a perfectly elastic spherical object on an infinite half space satisfies the Hertzian contact law[11], that is, the pressure is proportional to the impact penetration depth raised to the 1.5 power. This contact law and a modified form proposed by Yang and Sun has been used for loading composite plates of finite thickness by many authors[1,2,3,4,6,12]. Recently, some authors have suggest an alternate power law may be more appropriate. Liou[5] examined load vs indentation data for various laminations and thicknesses and found that a power of less than 1.5 better fit the data. Kim and Goo[7,8] used a penalty finite element method to analyze a two dimensional contact dynamics problem and concluded the Hertz law consistantly underestimated the contact force.

In our work, we examine a general contact power law

$$P = k\alpha^{\nu}. \tag{4}$$

Using the statically determined load vs indentation data and a nonlinear least squares fit, the constants k and ν were estimated for a 4, 16, and 48 ply sandwich-plate. The results can be seen in Table 1 as well as figure 3,4, and 5.

Table 1: Proportionality constant and power for various ply

Ply	k	ν
4	2046	1.052
16	5342	1.136
48	15250	1.290

Notice as the number of plys decreases the thickness of the face sheet decreases and the value of ν approaches one. Further, as the thickness of the face sheet increases, ν could be expected to approach 1.5, the Hertzian law. This is of course a conjecture, and can only be supported by more careful experiments and analysis. A comment about units is approprate at this point. Since P has units of pressure and α has units of length, it stands to reason that if ν changes with thickness then k must necessarily change as a function of thickness. With this general power law for determining the load distibution, we can describe the dynamics of the impactor.

Indentation equations

Following the development of Greszczuk[13], the impactor displacement, $w_I(t)$, is related to the indentation depth, α, and the plate displacement, $w_p(x_0, y_0, t)$ by $w_I(t) = \alpha(t) + w_p(x_0, y_0, t)$. Because the impactor produces the loading pressure, its dynamics are given by $m_I \ddot{w}_I = -P$. Combining these two equations and using equation 4 produces the governing equation for indentation depth as

$$m_I \ddot{\alpha} + k\alpha^{\nu} = -m_I \ddot{w}_p. \tag{5}$$

Further, if the plate is at rest upon inital impact and impact energy, E_0, is known, then the velocity of the impactor is found to be $v_0 = \sqrt{2E_0/m_I}$. This leads to initial conditions

$$\alpha(0) = 0 \text{ and } \dot{\alpha}(0) = v_0. \tag{6}$$

Coupling equations 5 and 6 with equation 2, where w_p is the first mode and the pressure is governed according to equation 4, produces

$$\rho A \ddot{w}_p(t) + Q w_p(t) = k\alpha^{\nu} \text{ with } w_p(0) = \dot{w}_p(0) = 0. \tag{7}$$

Under the assumption of no plate movement, equation 5 is implicitly solvable in terms of incomplete Beta functions, $B[z; a, b]$ i.e

$$t = \begin{cases} q(\alpha), & 0 < t \le t_m \\ 2t_m - q(\alpha), & t_m < t < 2t_m \end{cases} \tag{8}$$

where

$$q(\alpha) = \frac{\alpha_m}{v_0(\nu + 1)} B\left[\left(\frac{\alpha}{\alpha_m}\right)^{\nu+1} ; \frac{1}{\nu+1}, \frac{1}{2}\right], \tag{9}$$

with

$$\alpha_m = \left[\frac{\nu+1}{k} E_0\right]^{\frac{1}{\nu+1}} \quad \text{and } t_m = \frac{\alpha_m}{v_0} \sqrt{\pi} \frac{\Gamma(\frac{1}{\nu+1} + 1)}{\Gamma(\frac{1}{\nu+1} + \frac{1}{2})}. \tag{10}$$

Here α_m is the maximum indentation depth and t_m is the time at which this depth is achieved. An approximate inversion of equation 8 is given by

$$\alpha(t) \approx \alpha_m \sin \frac{\pi t}{2t_m}$$

which becomes exact when $\nu = 1$. Since this solution is for no plate movement, all of the impact energy goes into indentation. Thus α_m is an upper bound on the solution for $\alpha(t)$ with plate movement. Additionally, we expect the plate movement to be small, by assumption 4 above. Thus α_m becomes a natural length scale and t_m a natural time scale for the coupled equations. Introducing dimensionless variables $\tau = t/2t_m$, $\beta(\tau) = \alpha(t)/\alpha_m$ and $v(\tau) = w_p(t)s/\alpha_m$ along with dimensionless mass ratio $m = m_I/\rho A$ and dimensionless stiffness ratio $s = Q/k\alpha_m^{\nu-1}$, equations 2, 5 and 6 are reduced to

$$\ddot{\beta} + 2(1+m)\beta^\nu = 2mv, \quad \beta(0) = 0, \quad \dot{\beta}(0) = 2, \tag{11}$$

$$\ddot{v} + 2msv = 2ms\beta^\nu, \quad v(0) = 0, \quad \dot{v}(0) = 0. \tag{12}$$

At this point it is possible to make a few qualitative observations. First we observe that the mass ratio m is simply the ratio of the impactor mass to the plate mass. However, the stiffness ratio s is a ratio of Q, which captures material properties as well as geometry and boundary conditions for the plate, to $k\alpha_m^{\nu-1}$. From the definition of α_m, this term is characterized by the impact energy, E_0, as well as k and ν. Thus, increasing the impact energy will necessarily decrease the stiffness ratio. From equation 12, we see the natural frequency of the plate is $\omega = \sqrt{2ms}$. Thus, if the impact energy is doubled, the stiffness ratio, s, is decreased by a factor of $2^{\frac{1-\nu}{1+\nu}}$. This leads to a decrease in the oscillation frequency of the plate. In this dimensionless form, the duration of impact, T, is scaled to one as $s \to \infty$. From some parameter studies with $\nu = 1.5$, the impact duration appears to have the asymptotic behavior $T \sim 1 + c/s$ for some constant c and is relatively insensitive to changes in mass ratio m. The number of oscillations during the impact duration can now be approximated by $\omega T/2\pi$. These oscillations can be seen in the load-time plot of the data (figure 6) for a 16 ply sandwich-plate. Returning to equation 12 we observe that if the product ms is large the acceleration term, $\ddot{v}$, will be dominated by the last two terms. This leads to an approximation that $v(\tau) \approx \beta^\nu(\tau)$. With this approximation, equation 11 is reduced to the homogeneous problem which has the solution given in equations 8 and 9 for dimensioned variables. Figures 7 and 8 illustrate the results of a numerical solution to equations 11 and 12 where the stiffness ratio $s = 10$, the mass ratio $m = 39.6$ and $\nu = 1.5$. Figure 7 is a plot of dimensionless indentation depth, β, versus dimensionless time, τ. The plot has a near smooth half-sinusoid behavior as expected in the approximation. Figure 8 is a plot of dimensionless plate displacement scaled by s, w_p/α_m, versus dimensionless time. We see the peak displacement is approximately $1/s$ of the indentation depth and the plot is close to a $\beta^{3/2}$ with the addition of a few ripples. These ripples are due to lower order behaviors which correct for the acceleration term, $\ddot{v}$, in equation 12. Figures 9 and 10 are similar to 7 and 8 except now the stiffness ratio is reduced to one. In Figure 9 we see greater deviation from the near half-sinusoid as the plate movement becomes more pronounced as it is now on the same order as the indentation depth. Figure 10 show that the plate displacement is on the order of the indentation depth.

Summary

We have taken a brief look at a sandwich-plate model and shown through modal expansion the differential equations can be reduced to a simple harmonic oscillator given by equation 2. Exploring measured data, we found the impact pressure might be better described by a general power law as apposed to the Hertzian contact model. Using this general power law we were able to examine some general features of the plate dynamics under low velocity impact.

References

1. CT Sun and S Chattopadhyay. "Dynamic Response of Anisotropic Laminated Plates Under Initial Stress to Impact of a Mass", Journal of Applied Mechanics, Vol. 42, Sept. 1975, pp 693-698.

2. AL Dobyns, "Analysis of Simply-Supported Orthotropic Plates Subject to Static and Dynamic Loads", AIAA Journal, Vol 19 No.5, 1980.

3. CT Sun and JK Chen , "On the Impact of Initially Stressed Composite Laminates", Journal of Composite Materials, Vol 19, Nov 1985.

4. T Schroeder and K Chandrashekhara, "Nonlinear Impact Response of Laminated Plates Using a Higher Order Theory". European Journal of Mechanics, A/Solids, Vol 13 No. 6, 1994, pp 833-855.

5. WJ Liou, "Impact Analysis of Laminated Composite Plates with Stactical Indentation Laws", Computers and Structures, Vol 62, No. 5, 1997, pp 817-829.

6. SJ Kim, NS Goo. and TW Kim, "The Effect of Curvature on the Dynamic Response and Impact-Induced Dammage in Composite Laminates", Composites Science and Technology, Vol 57, 1997, pp 763-773.

7. SJ Kim and NS Goo. "Dynamic Contact Responses of Laminated Composite Plates According to the Impactor's Shapes". Computers and Structures, Vol 65,No. 1, 1997, pp 83-90.

8. NS Goo and SJ Kim. "Dynamic Contact Analysis of Laminated Composite Plates Under Low-Velocity Impact". AIAA Journal, Vol 35, No. 9, Sept 1997, pp 1518-1521.

9. JM Whitney and NJ Pagano. "Shear Defformatrion in Heterogeneous Anisotropic Plates", Journal of Applied Mechanics. Vol 37, 1970, pp 1031-1036.

10. JM Whitney. " Stress Analysis of Thick Laminated Composite ans Sandwich Plates", Journal of Composit Materials, Vol 6. 1972. pp 426-440.

11. AEH Love, *A Treatise on the Mathematical Theory of Elasticity*, Dover Publications, 1944, pp 198-199.

12. KN Shivakumar. W Elber. and W Illg. "Prediction of Impact Force and Duration Due to Low-Velocity Impact on Circular Composite Laminates", Journal of Applied Mechanics, Vol 52, Sep 1985. pp 674-680.

13. LB Greszczuk. "Damage in Composite Materials Due to Low Velicity Impact". in *Impact Dynamics*, Editors J.A. Zukas. T. Nicholas. H.F. Swift L.B. Greszczuk and D.R. Curran. John Wiley and Sons. 1982 pp 55-93.

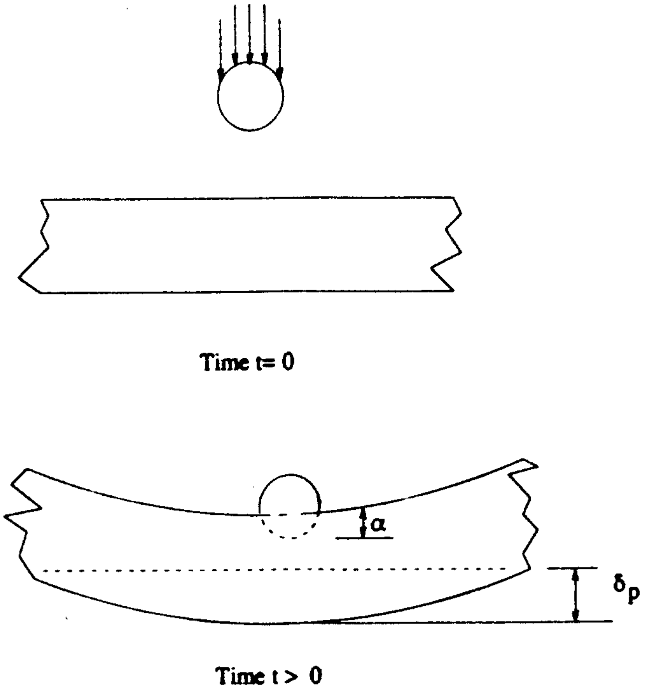
Time t= 0
α
δ_p
Time t > 0

Figure 1: Local and global deformation of a flexible target.

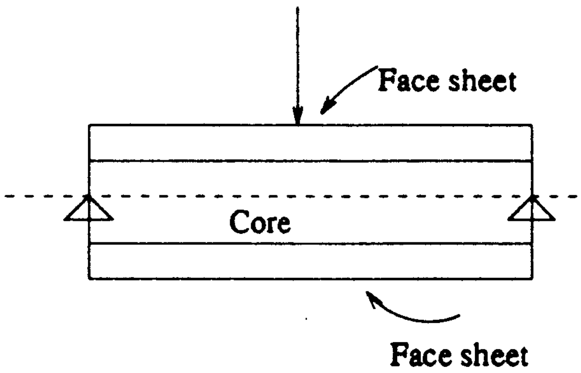
Face sheet
Core
Face sheet

Figure 2: Sandwich-plate construction.

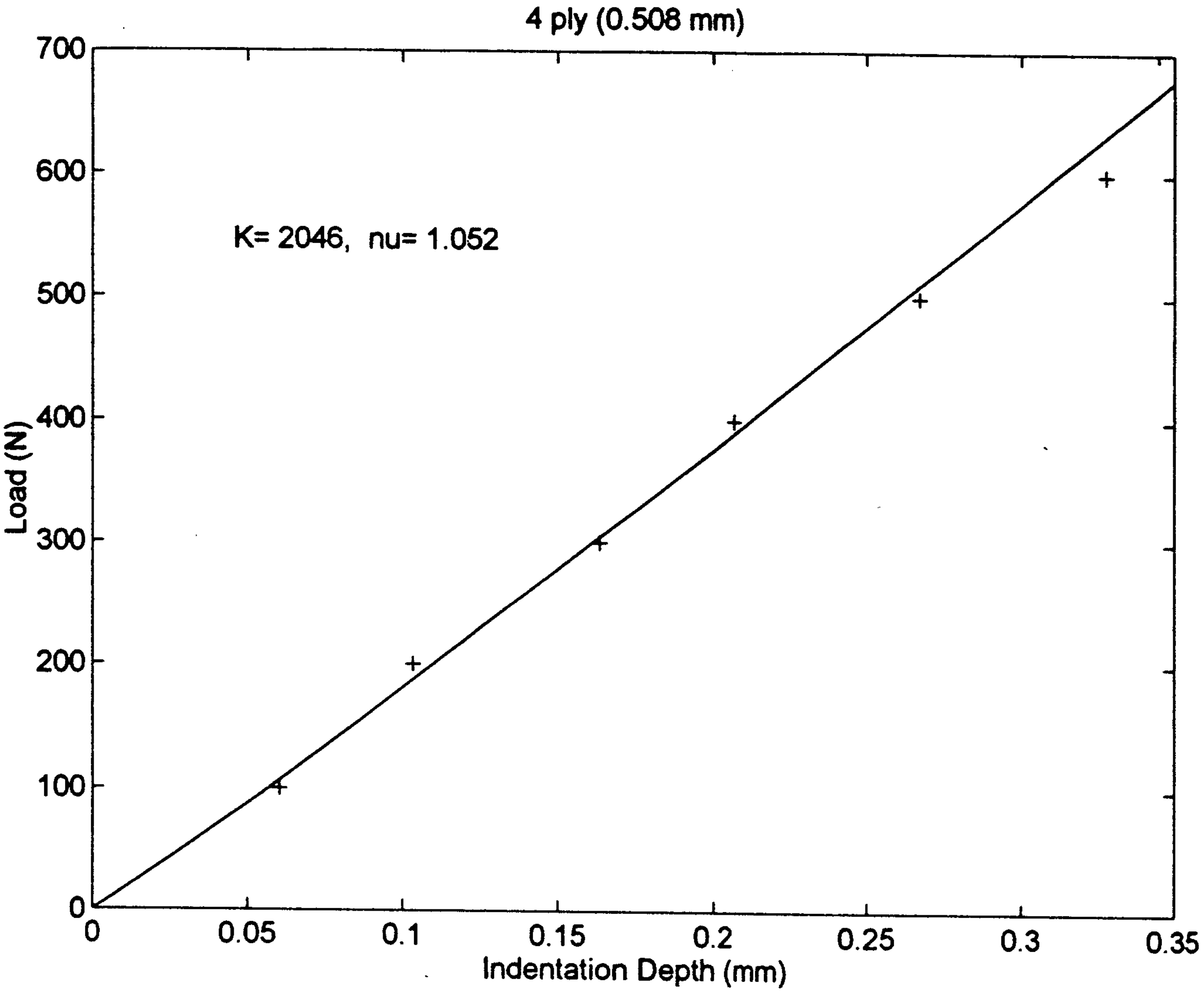

Figure 3: Indentation vs load data and fit for a 4 ply face sheet with a honeycomb core.

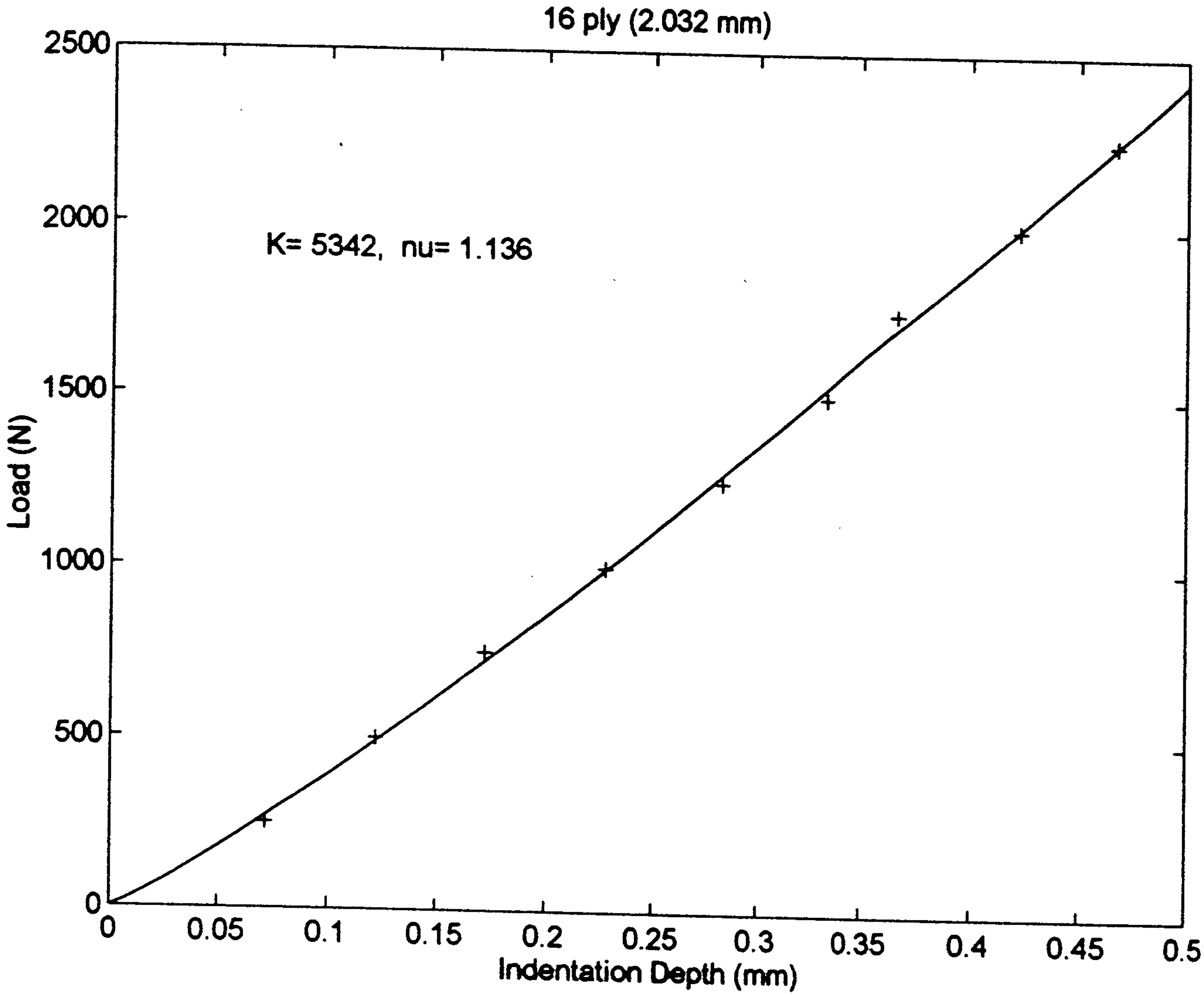

Figure 4: Indentation vs load data and fit for a 16 ply face sheet with a honeycomb core.

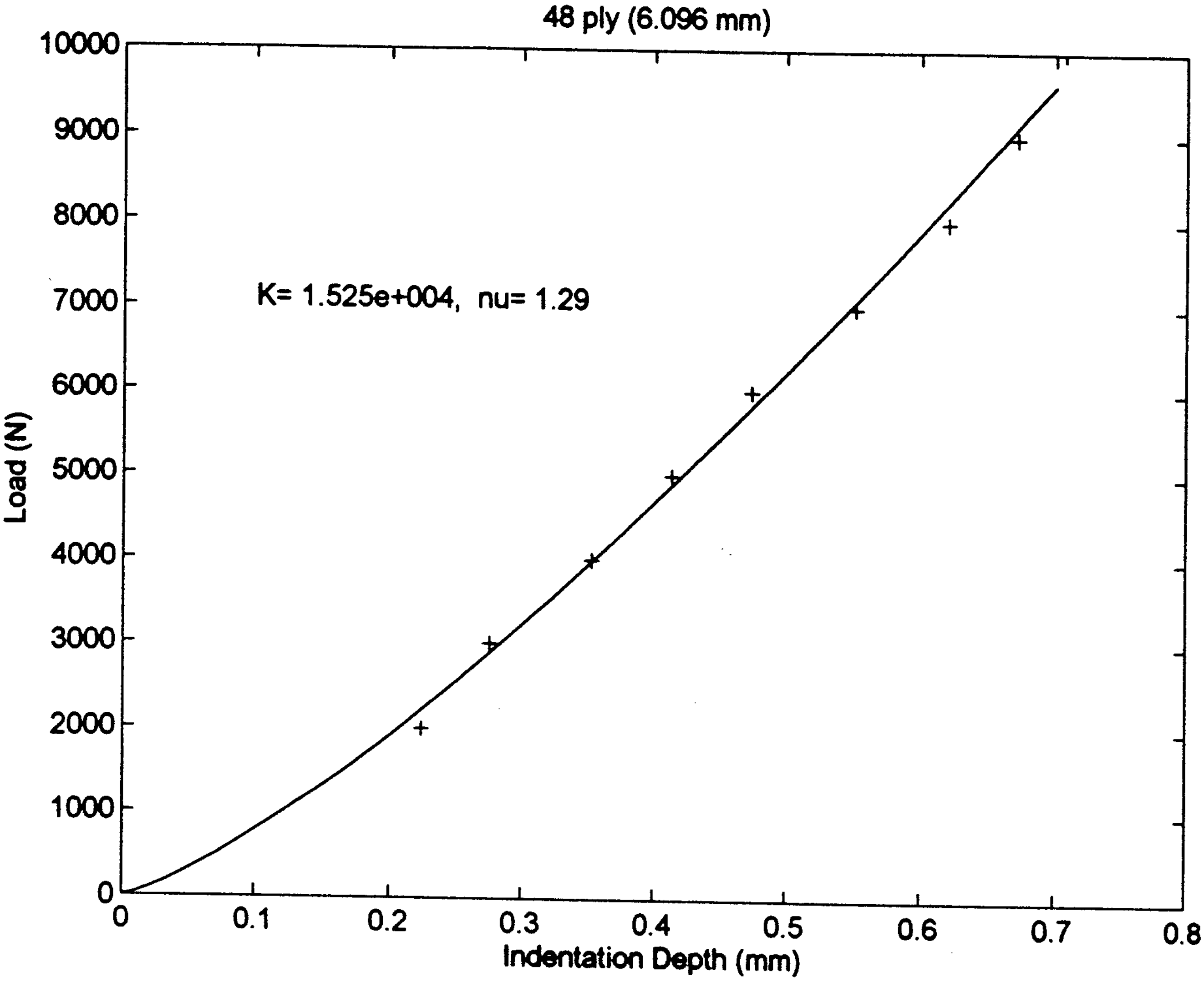

Figure 5: Indentation vs load data and fit for a 48 ply face sheet with a honeycomb core.

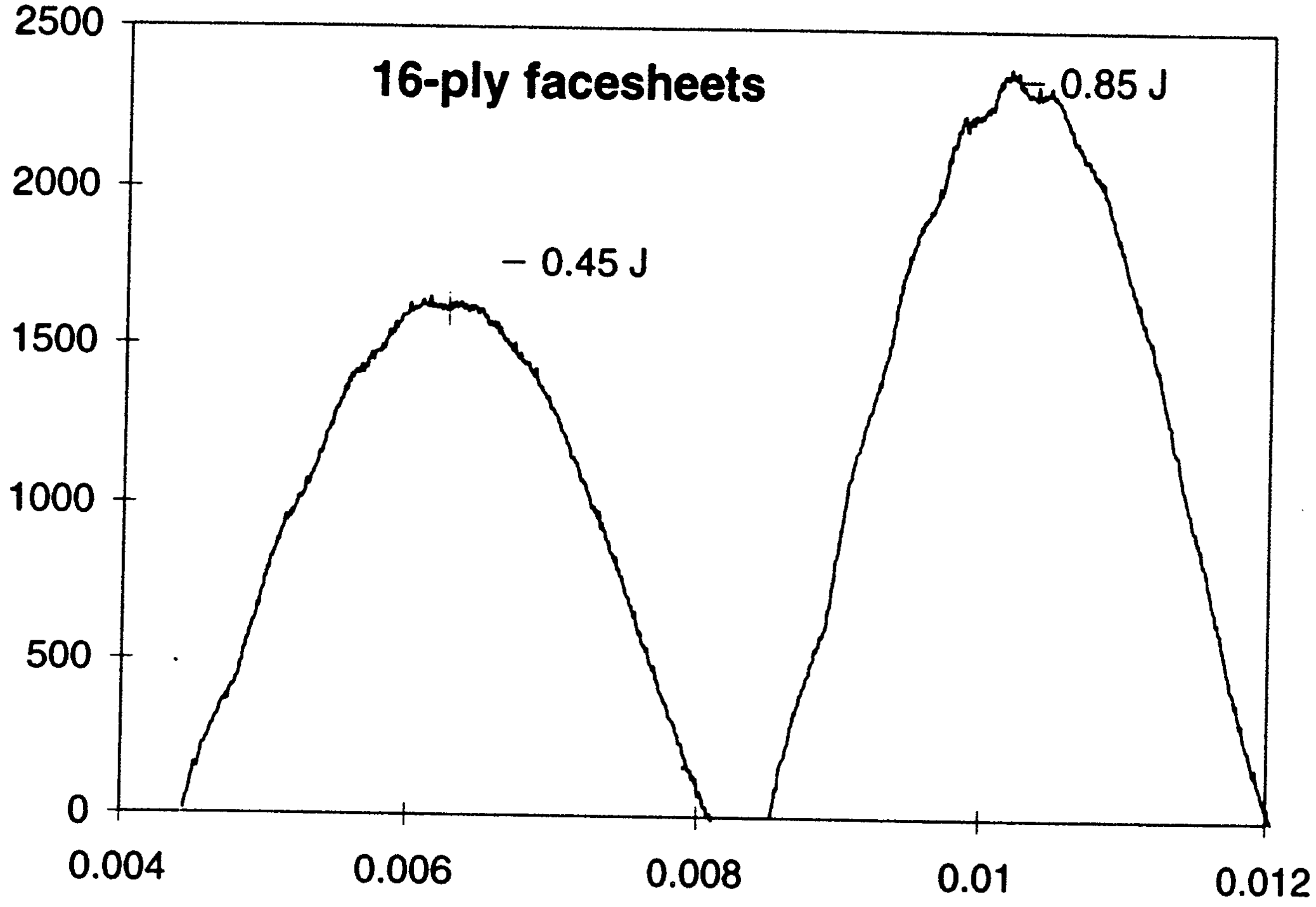

Figure 6: Load vs time plot for a 16 ply sandwich with impact energies of .45 Joules and .85 Joules.

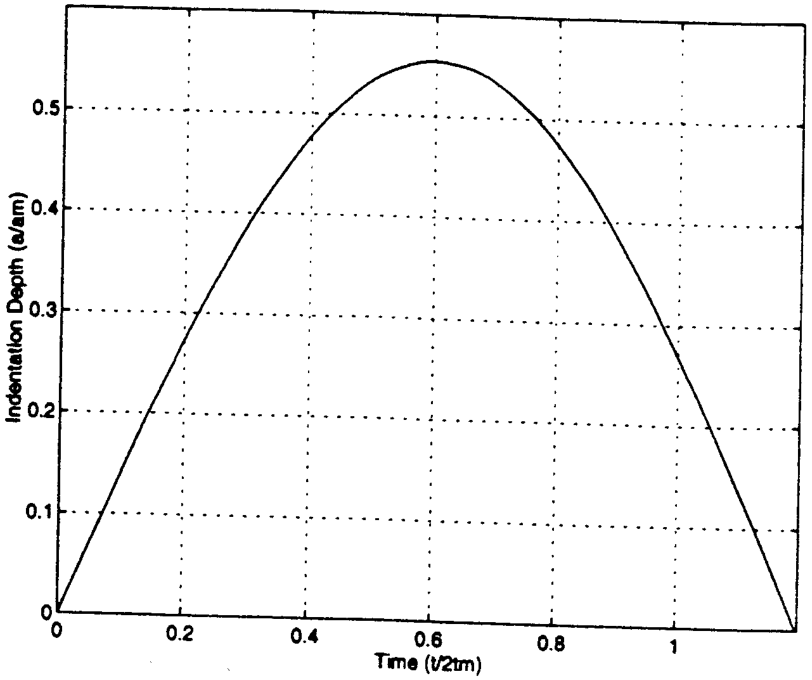

Figure 7: Indentation depth vs time for $m = 39.6$, $s = 10$, and $\nu = 1.5$.

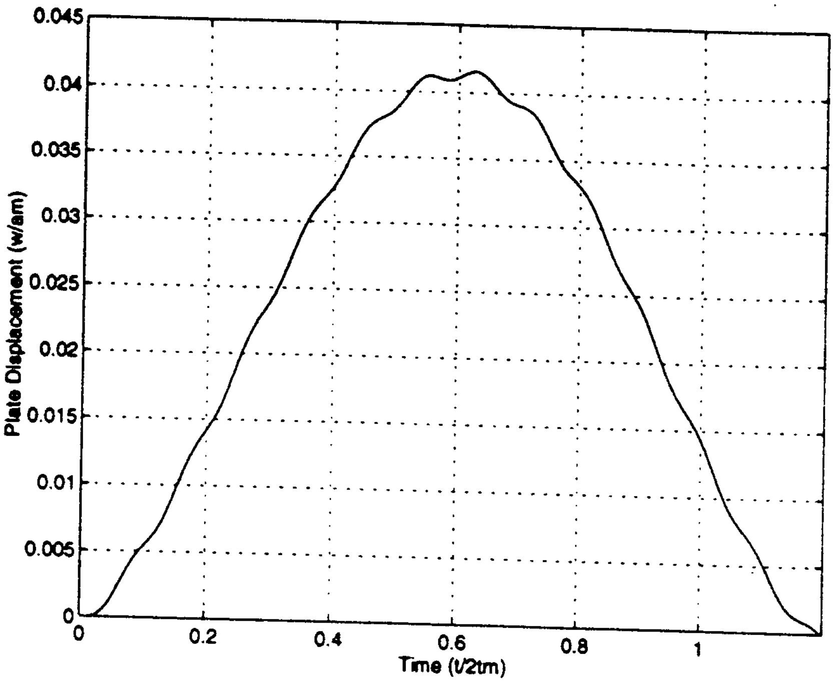

Figure 8: Plate displacement vs time for $m = 39.6$, $s = 10$, and $\nu = 1.5$.

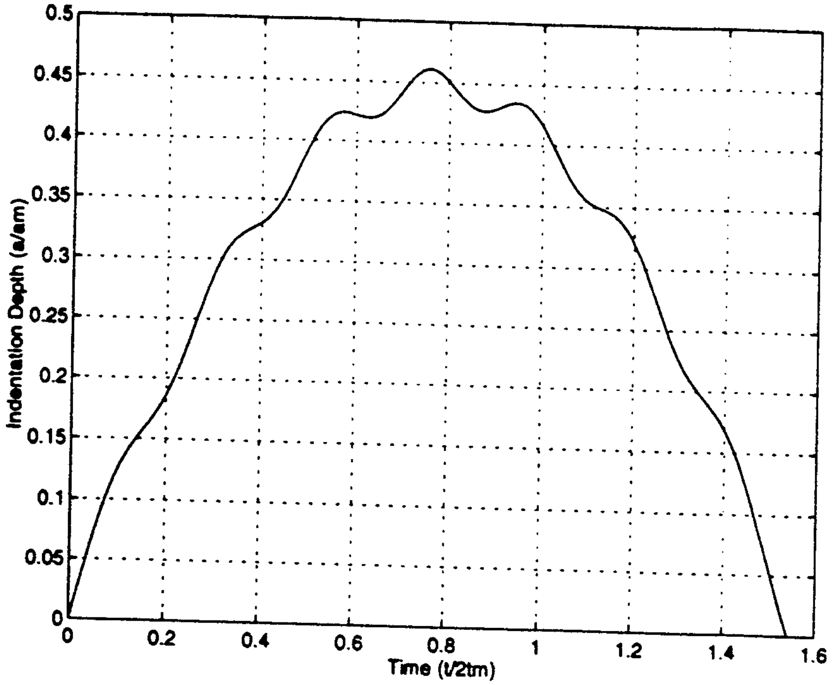

Figure 9: Indentation depth vs time for $m = 39.6$, $s = 1$, and $\nu = 1.5$.

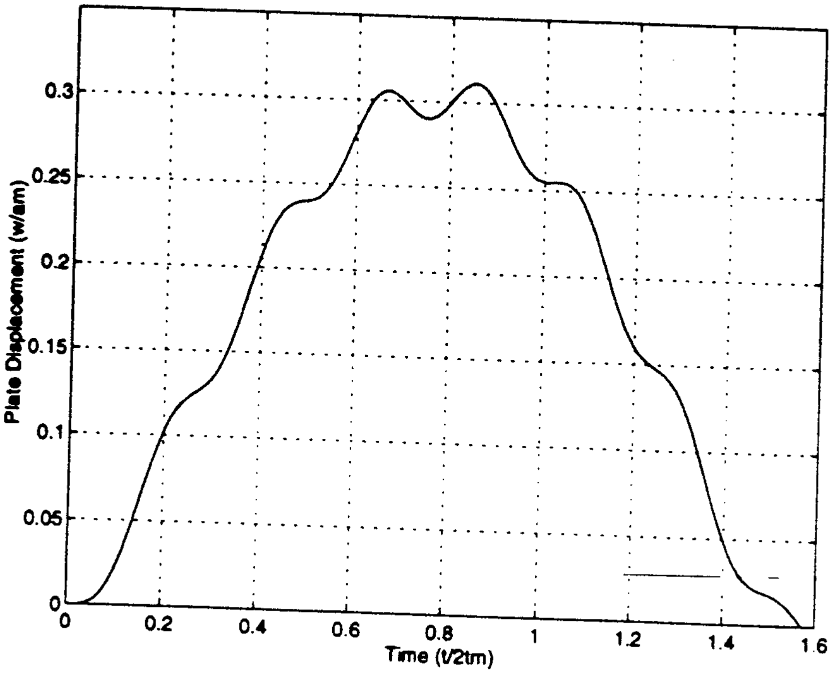

Figure 10: Plate displacement vs time for $m = 39.6$, $s = 1$, and $\nu = 1.5$.

ATTACHMENT VII

FINITE ELEMENT ANALYSIS OF SANDWICH COMPOSITE PLATES UNDER LOW VELOCITY IMPACT

FINITE ELEMENT ANALYSIS OF SANDWICH COMPOSITE PLATES UNDER LOW-VELOCITY IMPACT

Introduction

The goal of this work was to study stress distribution in sandwich composite plates, with pins as a core, under low velocity impact, and predict their possible modes of failure. For this purpose, 6 models were constructed and solutions obtained using I-DEAS as preprocessor, postprocessor and for analysis and NASTRAN for analysis. The models (described in detail below) were: a two-dimensional local model, a three-dimensional global model with rod (truss) and plate elements, a three-dimensional global model with beam and plate elements, a three-dimensional global model with brick elements, and a three-dimensional local model with brick elements. In the two-dimensional model and the three-dimensional models with plate elements in the face sheets the purpose was to study face sheet stresses and forces in the pins, making up the core. The face sheets were considered homogeneous, values of the elastic constants were taken as effective values, corresponding to the given ply properties, number of plies and fiber orientations (calculations of effective constants are shown below). In the three-dimensional local model with brick elements, the purpose was to study stress distribution through the thickness of the face sheets. Each face sheet ply was represented with a layer of elements with its own (in the global coordinate system) elastic constants, depending on the fiber orientation. Calculations of the constants are shown in the description of the model.

Calculation of effective elastic constants $E_x, E_y, \nu_{xy}, G_{xy}$ of graphite-epoxy face sheets with [0/90/+45/-45/0/90/+45/-45/0/90]s lay-up and thickness t=0.085 in neeed for the NASTRAN run. (These are values in the global coordinate system)

Elastic properties of a ply:

$$E_1 = 20 \times 10^6 \, psi, E_2 = 2.1 \times 10^6 \, psi, \nu_{12} = 0.21, G_{12} = 0.95 \times 10^6 \, psi \,. \tag{1}$$

Stiffness coefficients of a ply in the principal material coordinate system (figure 1) are:

$$Q_{11} = \frac{E_1}{1 - \nu_{12}^2 \dfrac{E_2}{E_1}} = 0.2009 \times 10^8 \, psi \,, \quad Q_{22} = \frac{E_2}{1 - \nu_{12}^2 \dfrac{E_2}{E_1}} = 0.2110 \times 10^7 \, psi \,,$$

$$Q_{12} = \nu_{12} Q_{22} = 0.4431 \times 10^6 \, psi \,, \; Q_{66} = G_{12} = 0.95 \times 10^6 \, psi \,. \tag{2}$$

Stiffness coefficients of plies in the global coordinate system (figure 1), the axes of which coincide with the sides of the face sheets, were calculated by the formulas:

$$\overline{Q_{11}} = Q_{11} \cos^4\theta + 2(Q_{12} + 2Q_{66}) \sin^2\theta \cos^2\theta + Q_{22} \sin^4\theta \,,$$

$$\overline{Q_{12}} = (Q_{11} + Q_{22} - 4Q_{66}) \sin^2\theta \cos^2\theta + Q_{12}(\sin^4\theta + \cos^4\theta)$$

$$\overline{Q_{22}} = Q_{11} \sin^4\theta + 2(Q_{12} + 2Q_{66}) \sin^2\theta \cos^2\theta + Q_{22} \cos^4\theta \,,$$

$$\overline{Q_{66}} = (Q_{11} + Q_{22} - 2Q_{12} - 2Q_{66}) \sin^2\theta \cos^2\theta + Q_{66} \sin^4\theta \cos^4\theta \tag{3}$$

For ply $\theta = 90^0$

$$\overline{Q_{11}} = Q_{22} = 0.2110 \times 10^7 \, psi, \overline{Q_{22}} = Q_{11} = 0.2009 \times 10^8 \, psi,$$

$$\overline{Q_{12}} = Q_{12} = 0.4431\times 10^6\,psi, \overline{Q_{66}} = Q_{66} = 0.95\times 10^6\,psi. \tag{4}$$

For plies $\theta = 45^0$ and $\theta = -45^0$

$$\overline{Q_{11}} = \overline{Q_{22}} = 0.6723\times 10^7\,psi, \overline{Q_{12}} = 0.4823\times 10^7\,psi, \overline{Q_{66}} = 0.5329\times 10^7\,psi. \tag{5}$$

Laminate stiffness coefficients A_{ij} are

$$A_{ij} = h\sum_{k=1}^{n}(\overline{Q_{ij}})_k, \tag{6}$$

where $n = 20$ is the number of plies, $h = \frac{t}{n}$ is thickness of each ply of a face sheet, $t = 0.085 in$ is thickness of a face sheet. So,

$$h = \frac{t}{20} = \frac{0.085}{20} = 4.25\times 10^{-3} in, \tag{7}$$

$$A_{ij} = 2h[3\overline{Q_{ij}}(0^o) + 3\overline{Q_{ij}}(90^o) + 2\overline{Q_{ij}}(45^o) + 2\overline{Q_{ij}}(-45^o)], \tag{8}$$

$$A_{11} = A_{22} = 7.9468\times 10^5\,\frac{lb}{in}, A_{12} = 1.8658\times 10^5\,\frac{lb}{in}, A_{66} = 2.2964\times 10^5\,\frac{lb}{in}. \tag{9}$$

Effective elastic constants are

$$\begin{gathered} E_x = \frac{A_{11}A_{22} - A_{12}^2}{tA_{22}} = 8.8339\times 10^6\,psi, \\ E_y = \frac{A_{11}A_{22} - A_{12}^2}{tA_{11}} = 8.8339\times 10^6\,psi, \\ G_{xy} = \frac{A_{66}}{t} = 2.7016\times 10^6\,psi\ ,\ \ v_{xy} = \frac{A_{12}}{A_{22}} = 0.2348. \end{gathered} \tag{10}$$

Assuming that the material of the face sheets is transversely isotropic in the plane y-z and , in addition, assuming $V_{yz} = V_{xy}$,we find

$$\begin{gathered} E_z = E_y = 8.8339\times 10^6\,psi, \\ G_{xz} = G_{xy} = 2.7016\times 10^6\,psi, \ v_{yz} = v_{xz} = v_{xy} = 0.2348\ , \\ G_{yz} = \frac{E_y}{2(1+v_{yz})} = 3.577\times 10^6\,psi. \end{gathered} \tag{11}$$

Two-dimensional Model (for representing pin response)

This is a local model (figure 2), the purpose of which is to estimate the bending moment in pins under the effect of a force applied to a face sheet, and thus to decide what load to apply to the pin in subsequent local three-dimensional analysis, what elements will best represent pins in a global three dimensional model, and to see if bending of the pins plays a substantial role in their failure. Face sheets were modeled with plane strain elements, pins were modeled with plane stress elements. The model is simply supported in the lower and upper corners. The face sheets are taken to be homogeneous with the effective elastic properties calculated above. Pins are made of titanium with the following properties:

$$E_{pins} = 16.82 \times 10^6\, psi\ , \nu_{pins} = 0.32\ ,\ G_{pins} = \frac{E_{pins}}{2(1+\nu_{pins})} = 6.3712 \times 10^6\, psi. \tag{12}$$

Elastic properties of the material of the face sheets (calculated in the previous part) are

$$E_{facesheets} = 8.8339 \times 10^6\, psi\ , \nu_{facesheets} = 0.2348. \tag{13}$$

Ratio of area of horizontal section of a pin to area of region 1 in figure 3, which represents the plan view of the typical area of a face sheet is

$$A_{pins} = \frac{\pi \times (0.023)^2}{4 \times 0.35 \times 0.023} = 5.1612 \times 10^{-2}. \tag{14}$$

Material properties of the parts of the pins inserted into the face sheets (region 1 in figure 2), are taken to be the average of the properties of the pin and the face sheet. In averaging account is taken of the area fraction A_{pins} of pins' horizontal sections in the plan view of the face sheets (figure 3), that was done by using the rule of mixtures:

$$E = E_{pins} A_{pins} + E_{facesheets}(1 - A_{pins}) = 9.246 \times 10^6\, psi, \tag{15}$$

$$\nu = \nu_{pins} A_{pins} + \nu_{facesheets}(1 - A_{pins}) = 0.2392\ , \tag{16}$$

$$G = \frac{E}{2(1+\nu)} = 3.731 \times 10^6\, psi. \tag{17}$$

Using the results from the FE analysis, bending moment acting on the horizontal sections of the pin, at the interface with the lower face sheet is calculated to be $2.5 \times 10^{-4}\, lb \times in$; at the interface with the upper face sheet is $1.9 \times 10^{-3}\, lb \times in$; in the middle of the pin is $-1.2 \times 10^{-3}\, lb \times in$. Since these values are small, we conclude, that in the three-dimensional model bending of the pins can be neglected, and they can be modeled with truss elements. The fact that the bending moments, transmitted from the face sheets to the pins, are small, are also apparent from the color plot of stress σ_{yy} distribution at a joint of pin and face sheet (figures 4 and 5) - the variation of this stress along the thickness of the pin is very small.

Three-dimensional Models

1) Face sheets modeled with plate elements, pins modeled with truss elements (figure 6).

The purpose of this model, shown in figure 6, is to find the forces in the pins, under a load applied to the sandwich plate, to find out which pins undergo compression and tension in a test specimen; to define the force, under which buckling of the pins begins, and the distribution of stresses in the face sheets (in the planes of the face sheets, but not across the thickness of the face sheets). Material properties were taken to be the same as in the two-dimensional model, i.e. material of the face sheets is taken to be homogeneous with effective (average) elastic constants. The model corresponds to the actual testing conditions reported by the Foster-Miller company: the specimen is 8 inches long and 3 inches wide, tested with a three point bend fixture (figure 6). Figure 7 shows one quarter of the specimen with symmetry boundary conditions. The external force, applied to the specimen, was taken to be *100 lb*, and this force is distributed over the area of $3in^2$. So the distributed load per unit area is $-33.33psi$. The element size was chosen by doing convergence studies. Figure 8, generated by the IDEAS, demonstrates absolute values of axial forces in the pins. The directions of these forces (tensile or compressive) were obtained by running analysis in NASTRAN and making use of IDEAS postprocessing capabilities.

Distribution of stresses $\sigma_{xx}, \sigma_{yy}, \sigma_{zz}$ is shown in figures 9,10 and 11. We see that the highest bending stresses $(\sigma_{xx}, \sigma_{yy})$ occur, as it was expected, in the center of the plate, where the curvature of the plate is the largest, and along the line, where the plate rests on the block (where the nodal restraints are imposed). The highest compressive stresses in the direction perpendicular to the plate (negative values of the stress σ_{zz}) occur at the points, where the pins enter the face sheets. The highest tensile stresses in the direction perpendicular to the plate (positive values of the stress σ_{zz}) occur along the lines which connect these points. Table 1 shows the maximum values of stresses, obtained from this model. From this table we see, in particular, that the maximum values of stresses σ_{xz} and σ_{yz} are correspondingly $1.608 \times 10^{-3} psi$ and $6.465 \times 10^{-4} psi$. These values are very small, and therefore we conclude that delamination of the face sheets due to global bending of the sandwich plate can not happen. Delamination due to stress concentration near connections of the pins and the face sheets can not be captured by this model and will be discussed later.

2) Face sheets modeled with plate elements, pins modeled with beam elements.

This model is identical to the previous one in all respects with the exception that the pins are modeled with beam elements (each pin is modeled with one beam element). This model was run to check the validity of the conclusion made from the two-dimensional model, that bending of pins is small and truss (rod) elements can be used for pins in the three dimensional model. In the following table, some of the results obtained from the 3-D truss and beam models are compared.

	truss elements	beam elements
maximum displacement in z-direction (in)	5.413×10^{-4}	5.34×10^{-4}
maximum energy in pins (lb × in)	1.431×10^{-3}	1.428×10^{-3}
maximum forces in pins (lb)	5.32	5.3

We see that changing truss elements with beam elements does not alter results significantly. The slight difference in the results was attributed to the presence of very little rotation and moment at the ends of the beams. Effects of these moments and rotations on the critical buckling load is determined using a Modified Euler equation[1]. If M is the moment and β is the rotation at both the ends of the pins, two parameters α, Λ can be defined as $\alpha = M/\beta$; $\Lambda = EI/\alpha\, l$. Then the critical buckling load can be written as $F_c = [(\Lambda+0.4)/(\Lambda+0.2)]^2 \pi^2 EI/l^2$. Using the data from the analysis, the critical buckling load can be modified as $F_c = 1.2\, \pi^2 EI/l^2$. For the given geometry of the pin, the critical buckling load can be determined as

$$F_c = 1.2\frac{\pi^2 EI}{l^2} = 1.2\frac{\pi^2 E}{l^2}\frac{\pi r^4}{4} = 1.2\frac{16.82X10^6}{(0.5/\cos(30^0))^2}\frac{\pi^3 X 0.01^4}{4} = 4.69lb \qquad (18)$$

However, when a load of 100 lb is applied, it can seen that the maximum compressive force in the pins is 4.69 *lb,* and the maximum tensile force is 5.32 *lb.*

So, failure of the plate due to buckling of the pins begins at an applied force equal to 100 *lb*.

3) Global 3-dimensional model with brick elements.

The model represents one fourth of the 3-point bending test specimen with symmetry boundary conditions (figure 12) and has the same dimensions as the 3-dimensional model with the plate and truss elements. In this model, eight noded three dimensional brick elements are used. Material of the face sheets is taken to be homogeneous with effective elastic properties. The purpose of this model was to obtain an approximate stress distribution in the test specimen and to make a judgment about possible boundary conditions for a local, more refined model. To achieve sufficiently accurate results the number of elements in this model was set equal to atleast the number of elements in the 3-dimensional model with the plate and truss elements. But in fact this number was taken even larger because the pins in this model were represented by the three-dimensional elements (unlike the two previous models, where the pins were represented by the one-dimensional truss or beam elements). The diagrams of stress distribution are shown in figures 13, 14, 15, 16, the diagram of strain energy - in figure 17. We see that

I) maximum stresses in face sheets occur in the same places as in 3D-model #1;
II) the same pins are under tensile and compressive forces in both models;
III) maximum tensile, compressive forces and strain energies occur in the same pins in both models.

Thus, we conclude that the results obtained from this model are approximately identical to the results of the 3-D model #1 (though numerical values of stresses from the two models are not exactly equal), and therefore the global model with brick elements can be used for approximate estimation of displacements on boundaries of small volumes surrounding the pins. This information can be used for deciding on boundary conditions for the next, local three-dimensional model for studying stress distribution in a small volume of face sheet around a pin.

4) Local three-dimensional model with brick elements and with elastic properties of each ply depending on fiber orientation

The purpose of this model is to study the stress distribution in a small volume of the face sheet surrounding the pin. The model represents one pin penetrating into the face sheet (figure 18). The block of material of the face sheet surrounding the pin was taken to be symmetric with dimensions such that the distances from the axis of the pin to the edges of the block are equal to the half of the smallest distances between the pins.

In the previous models it was shown that the bending moments in the pins of the sandwich plate, under effect of a force applied in the center of the plate, are negligibly small. Therefore in the present model the pin was loaded only by the axial force but not by the bending moment.

Displacement boundary conditions (figure 18) were chosen by considering displacements of the boundary points of the same block of material singled out (in postprocessing) from the global 3-D model with the brick elements. Boundary conditions in figure 18 correspond to the case, when the load, applied to the pin, is the buckling load.

Each ply of the face sheet has one element in its thickness, so, in total, there are twenty elements in the thickness of the face sheet.

Each ply of the face sheet in the model was given its own elastic constants in the global coordinate system, depending on orientation of the fibers in the ply. The elastic constants of graphite-epoxy plies in the material coordinate system are:

$$\begin{aligned} &E_1 = 20\times10^6\,psi, E_2 = E_3 = 2.1\times10^6\,psi, G_{12} = G_{13} = 0.95\times10^6\,psi, \\ &G_{23} = 0.7\times10^5\,psi, \nu_{12} = \nu_{13} = 0.21, \nu_{23} = 0.49 \end{aligned} \tag{19}$$

The compliance matrix of a ply in the material coordinate system is

[S]=

$$
\begin{bmatrix}
1/E_1 & -\nu_{12}/E_1 & -\nu_{13}/E_1 & 0 & 0 & 0 \\
-\nu_{12}/E_1 & 1/E_2 & -\nu_{23}/E_2 & 0 & 0 & 0 \\
-\nu_{13}/E_1 & -\nu_{23}/E_2 & 1/E_3 & 0 & 0 & 0 \\
0 & 0 & 0 & 1/G_{23} & 0 & 0 \\
0 & 0 & 0 & 0 & 1/G_{13} & 0 \\
0 & 0 & 0 & 0 & 0 & 1/G_{12}
\end{bmatrix} =
$$

$$
\begin{bmatrix}
5\times10^{-8} & -1.5\times10^{-8} & -1.5\times10^{-8} & 0 & 0 & 0 \\
-1.5\times10^{-8} & 47.6\times10^{-8} & -23.3\times10^{-8} & 0 & 0 & 0 \\
-1.5\times10^{-8} & -23.3\times10^{-8} & 47.6\times10^{-8} & 0 & 0 & 0 \\
0 & 0 & 0 & 1428.6\times10^{-8} & 0 & 0 \\
0 & 0 & 0 & 0 & 105.3\times10^{-8} & 0 \\
0 & 0 & 0 & 0 & 0 & 105.3\times10^{-8}
\end{bmatrix}
$$

The compliance matrix of a ply in the coordinate system, the axes of which are aligned with the sides of the face sheets, is

$$[S'] = [T_\varepsilon][S][T_\sigma]^{-1}, \tag{21}$$

where $[T_\sigma]$ is matrix of coefficients in transformation formula for stresses, $\{\sigma'\} = [T_\sigma]\{\sigma\}$; $[T_\varepsilon]$ is matrix of coefficients in transformation formula for engineering strains, $\{\varepsilon'\} = [T_\varepsilon]\{\varepsilon\}$.

$[T_\sigma] =$

$$
\begin{bmatrix}
m^2 & n^2 & 0 & 0 & 0 & 2mn \\
n^2 & m^2 & 0 & 0 & 0 & -2mn \\
0 & 0 & 1 & 0 & 0 & 0 \\
0 & 0 & 0 & m & -n & 0 \\
0 & 0 & 0 & n & m & 0 \\
-mn & mn & 0 & 0 & 0 & m^2-n^2
\end{bmatrix}
$$

$$[T_\varepsilon] = \begin{bmatrix} m^2 & n^2 & 0 & 0 & 0 & mn \\ n^2 & m^2 & 0 & 0 & 0 & -mn \\ 0 & 0 & 1 & 0 & 0 & 0 \\ 0 & 0 & 0 & m & -n & 0 \\ 0 & 0 & 0 & n & m & 0 \\ -2mn & 2mn & 0 & 0 & 0 & m^2 - n^2 \end{bmatrix}$$

where $m = \cos\alpha$, $n = \sin\alpha$, α is angle of fiber orientation in a ply. The stiffness matrix $[C']$ is the inverse of the compliance matrix $[S']$.

To choose the size (and therefore the number) of elements which can correctly represent the stress field, the two following models were developed:

1) A local three-dimensional brick element model was used to represent homogeneous isotropic face sheet (3-D model #5).

2) An analytical model of shear stress distribution along the joint of the pin and the isotropic homogeneous face sheet. The number of elements in the 3-D FE model #5 was chosen to achieve closeness of values of the interfacial shear stress obtained from this model and the analytical model. After that was accomplished, the same number of elements were used in the local 3-D model with brick elements and laminated face sheets (3-D model #4).

The stresses, obtained from this model, will be discussed later, after the description of the analytical model.

Analytical Model of Interfacial Shear Stress Distribution

The purpose of the analytical model is to determine shear stress distribution at an interface of a pin and a face sheet, considering the face sheets to be isotropic and homogeneous, and to compare this stress with the shear stress obtained from the 3-D model #5. The comparison will show us if the number of elements in the 3-D model #5 (and therefore in the 3-D model #4) is sufficient for accurate evaluation of the stresses.

Let F be the external force acting on the pin in the axial direction (it can be either tensile or compressive), t is interfacial shear force per unit length, τ is interfacial shear force per unit area ($\tau = \frac{t}{a}$, dimension a is shown in fig. 19). The pin and the material of the face sheet are connected with adhesive with a shear modulus G (figure 20). Thickness of layer of the adhesive is denoted by η. Let us introduce subscripts l, r, f and b which denote left, right, front and back joints (figure 19) and let us consider the left joint. From Hook's law for shear deformation, we have

$$\tau_l = G\gamma_l = G\frac{u_l - u}{\eta}, \tag{24}$$

where u_l is displacement along the pin of the face sheet's line segments adjacent to the left layer of adhesive between the pin and the face sheet, u is displacement of the pin's segments, adjacent to the left layer of the adhesive (figure 20, reference [1]). But

$$\tau_l = \frac{t_l}{a}, \tag{25}$$

so

$$t_l = \frac{Ga}{\eta}(u_l - u) \cdot \tag{26}$$

$$\begin{gathered}F = 4lb, A_p = 3.4641 \times 10^{-4} in^2, A_l = (-0.0713x + 0.0082) in^2,\\ A_r = (0.0713x + 0.0022) in^2, A_b = A_f = 0.0063 in^2, E_p = 16.82 \times 10^6 psi,\\ E_l = E_r = E_f = 7.26 \times 10^6 psi, G = 3 \times 10^6 psi, a = 2 \times 10^{-2} in,\\ \eta = 3 \times 10^{-3} in, \frac{Ga}{\eta} = 2 \times 10^7 psi.\end{gathered} \tag{38}$$

Substituting these values into the differential equations (34), (35) and (36), we receive:

$$-\frac{T_l}{5.2 \times 10^5 x - 5.95 \times 10^4} - \frac{4 - T_l - T_r - 2T_f}{5.8 \times 10^3} = 5 \times 10^{-8} T_l'', \tag{39}$$

$$-\frac{T_r}{5.2 \times 10^5 x + 1.6 \times 10^4} - \frac{4 - T_l - T_r - 2T_f}{5.8 \times 10^3} = 5 \times 10^{-8} T_r'', \tag{40}$$

$$-\frac{T_f}{4.5 \times 10^4} - \frac{4 - T_l - T_r - 2T_f}{5.8 \times 10^3} = 5 \times 10^{-8} T_f''. \tag{41}$$

To solve these equations by the Runge-Kutta method (of solution of systems of first-order differential equations), we reduce them to 6 first-order equations by introducing new variables:

Old variable	New variable	Differential equation
T_l	y_1	$y_1' = y2$
T_l'	y_2	$y_2' = 2\times10^7(\frac{y_1}{5.2\times10^5 x - 5.95\times10^4} - \frac{4 - y_1 - y_3 - 2y_5}{5.8\times10^3})$
T_r	y_3	$y_3' = y_4$
T_r'	y_4	$y_4' = 2\times10^7(-\frac{y_3}{5.2\times10^5 x + 1.6\times10^4} - \frac{4 - y_1 - y_3 - 2y_5}{5.8\times10^3})$
T_f	y_5	$y_5' = y_6$
T_f'	y_6	$y_6' = 2\times10^7(-\frac{y_5}{4.5\times10^4} - \frac{4 - y_1 - y_3 - 2y_5}{5.8\times10^3})$

The boundary conditions are (reference [2]):

$$y_1(0) = y_3(0) = y_5(0) = 0, \tag{43}$$

$$y_1(l) = y_3(l) = y_5(l) = 0. \tag{44}$$

To solve these equations by the Runge-Kutta method, we need initial values of the variables $y_2 = T_l', y_4 = T_r', y_6 = T_f'$, since Runge-Kutta method works with initial conditions, but not with boundary conditions. These initial values can be found such that the solution of the differential equations comes out to be satisfying conditions (44).

Part of the output of a computer program, which solves these equations, is shown below.

Part of numerical solution of differential equations (42) with boundary conditions (43) and (44)

```
                         integrating from  .0980 to  .0000,  printing every  10 steps

j     x     h -step of integr.  y1 = T_l         y2 = T_l'       y3 = T_r          y4 = T_r'        y5 = T_f          y6= T_f'
0    .0980 -.1000000E+00  .0000000E+00  .0000000E+00  .0000000E+00  .0000000E+00  .0000000E+00  .0000000E+00
10   .0947 -.2691254E-03 -.7622472E-01  .4659644E+02 -.7634816E-01  .4674134E+02 -.7633841E-01  .4672963E+02
20   .0918 -.2917319E-03 -.2745825E+00  .9209458E+02 -.2759612E+00  .9294297E+02 -.2758437E+00  .9286771E+02
30   .0895 -.1537361E-03 -.5350708E+00  .1351001E+03 -.5396465E+00  .1371296E+03 -.5392343E+00  .1369373E+03
40   .0883 -.1009320E-03 -.7181460E+00  .1616897E+03 -.7257701E+00  .1646288E+03 -.7250640E+00  .1643412E+03
50   .0878 -.2781189E-04 -.8030892E+00  .1734788E+03 -.8123122E+00  .1768529E+03 -.8114486E+00  .1765184E+03
60   .0876 -.1651931E-04 -.8358908E+00  .1779609E+03 -.8457594E+00  .1815046E+03 -.8448317E+00  .1811517E+03
70   .0874 -.1877064E-04 -.8667758E+00  .1821495E+03 -.8772659E+00  .1858536E+03 -.8762762E+00  .1854832E+03
80   .0872 -.1716804E-04 -.8987339E+00  .1864535E+03 -.9098808E+00  .1903244E+03 -.9088252E+00  .1899356E+03
90   .0870 -.1848563E-04 -.9326460E+00  .1909897E+03 -.9445043E+00  .1950382E+03 -.9433771E+00  .1946298E+03
100   .0868 -.1440521E-04 -.9877183E+00  .1982940E+03 -.1000763E+01  .2026322E+03 -.9995157E+00  .2021916E+03
110   .0867 -.7306520E-05 -.1008796E+01  .2010707E+03 -.1022305E+01  .2055202E+03 -.1021010E+01  .2050672E+03
```

We see that

I) $t_l \approx t_r \approx t_f$,

II) at each step of the integration $\frac{T_l}{5.2\times10^5 x - 5.95\times10^4} << \frac{4-T_l-T_r-2T_f}{5.8\times10^3}$,

$\frac{T_l}{5.2\times10^5 x + 1.6\times10^4} << \frac{4-T_l-T_r-2T_f}{5.8\times10^3}$, $\frac{T_f}{4.5\times10^4} << \frac{4-T_l-T_r-2T_f}{5.8\times10^3}$.

So , the first terms in the differential equations (39), (40) and (41) can be neglected, and we can set $T_l = T_r = T_f = T$.

Now, we have one differential equation

$$-\frac{4(1-T)}{5.8\times10^3} = 5\times10^{-8}T'' \tag{45}$$

with boundary conditions

$$T(0) = 0, T(l) = \frac{F}{4} = 1 \tag{46}$$

(in this model applied load F was taken to be equal 1 lb).

Besides, we have the relation

$$\tau = \frac{T'}{a} = 50T'. \tag{47}$$

So, the solution for the shear stress $\tau(x)$ is

$$\tau = 5.908\times10^{-7}\exp(117.4x) + 5874\exp(117.4x) . \tag{48}$$

Plot of the function $\tau(x)$, equation (48), together with the corresponding plot, obtained from the 3-D finite element model #5 with the homogeneous face sheets (solid line), is shown in figure 21. The two plots are close enough so that we can conclude that the number of elements in the 3-D finite element model #5 with homogeneous isotropic face sheets and, therefore in the 3-D finite element model #4 with laminated face sheets (the number of elements in the both models are the same) is sufficient to determine stresses accurately.

Now we can proceed to the analysis of stresses in the face sheets using results obtained from the 3-D finite element model with brick elements and laminated face sheets (3-D finite element model #4).
The maximum allowable stresses in the face sheets for the graphite-epoxy composite material are (reference [3]) :

Tensile strength in 1 direction	$219.5 \times 10^3\ psi$
Tensile strength in 2 and 3 directions	$6.35 \times 10^3\ psi$
Compressive strength in 1 direction	$246 \times 10^3\ psi$
Compressive strength in 2 and 3 directions	$6.35 \times 10^3\ psi$
Shear strength in 2-3 plane	$9.8 \times 10^3\ psi$
Shear strength in 1-3 and 1-2 planes	$12.6 \times 10^3\ psi$

where direction 1 is along the fibers, direction 2 is perpendicular to the fibers in the plane of a ply, and direction 3 is perpendicular to the ply.
Stress distribution in the face sheets was studied under different tensile and compressive loads. The resulting plots and numerical data are shown in figures 22-28. We see that:
1) Variations of stresses in the face sheets, in their planes (in xy- planes) are such that the stresses reach their maximum values near the pins and decrease very rapidly away from the pin. This is seen in figures 22, 23, 24, which show the variations of stresses σ_{xz}, σ_z, σ_x in the y-direction in the middle ply of the face sheet. From this we conclude that the damage of the face sheets, if it occurs, can be localized only in a small vicinity around the pins (within a distance of 0.02 inches from the pins).
Maximum values of stresses σ_{xz} and σ_{yz} in the face sheet, occurring in the elements adjacent to the pin and in the upper plies (Table 2), are $1.8 \times 10^3\ psi$ and $-1.8 \times 10^3\ psi$. These values do not exceed the corresponding maximum allowable values: $2.6 \times 10^3\ psi$ and $9.8 \times 10^3\ psi$ .In addition, from Table 1, (which shows the maximum values of stresses obtained from the 3-D model with the pin and truss elements) one can observe that the maximum values of stresses σ_{xz} and σ_{yz}, due to the global bending of the plate, are very small. Therefore, the FE models allow us to conclude that delamination of the face sheets, which can be caused by these shear stresses, probably will not occur before buckling of the pins. However, if the pins are shorter(i. e. the buckling strength is higher than 4.65 lb, the delaminations are more likely to occur before buckling). This conclusion is confirmed by experiments.

2) Stresses in the face sheets decrease from the upper to lower plies (figures 25-28).
The values of the stresses under the buckling load of the pin (F=4.69 lb) in the first four plies of the face sheet adjacent to the pin, where the stresses are the highest, transformed to the material coordinate systems of each ply, are shown in Table 2. Comparing stresses from Table 2 with the maximum allowable stresses (page 16) one can observe that, before buckling of the pins, the following modes of failure can occur:
a) failure of the adhesive, connecting the pins and the face sheets, in the first ply, due to the shear stress in the adhesive (maximum shear stress is approximately 3000 psi (figures 25, 26), the corresponding strength is 2600 psi);
b) breakage of the adhesive connecting the pins and the face sheet in the first ply by the tensile stress normal to the surface of the pin (the maximum stress normal to the surface of the pin is approximately 3500 psi (figure 28), the corresponding strength is 2600 psi);

c) stresses σ_{yy} and σ_{zz} in the first ply (Table 2) exceed their maximum allowable values (6350 psi). Since these high stresses are localized only in the first ply and in the small vicinity around the pins, and since experimental data did not show damage of the face sheets due to these stresses, this mode of failure is ignored.

REFERENCES

1. Brush, D. & Almroth B. " *Buckling of Bars, Plates and Shells*" , McGraw-Hill, New York, 1975
2. Rzhanitsyn, A. R. "*Built-up bars and plates*" Moscow: Stroiisdat, 1986
3. Reddy, Y. S. N. & Reddy J. N. "*Linear and non-linear failure analysis of composite laminates with transverse shear.*" Composites Science and Technology, Vol. 44, pp. 227-255 (1992)

Figure 1
Global (X,Y) and Material (X',Y') Coordinate Systems

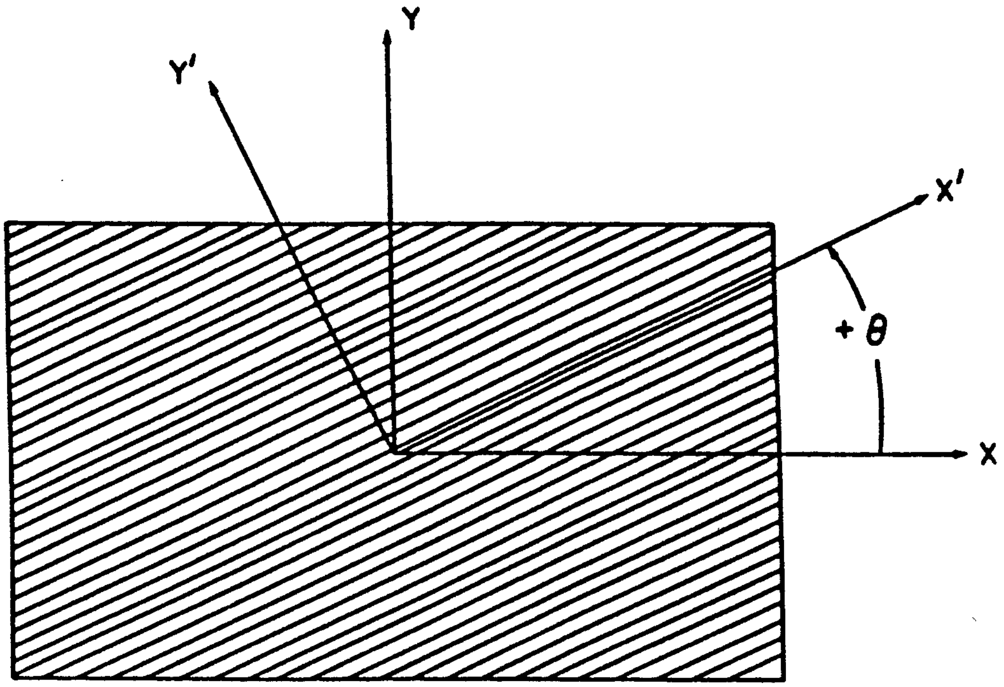

Figure 1

Figure 2

The two-dimensional model

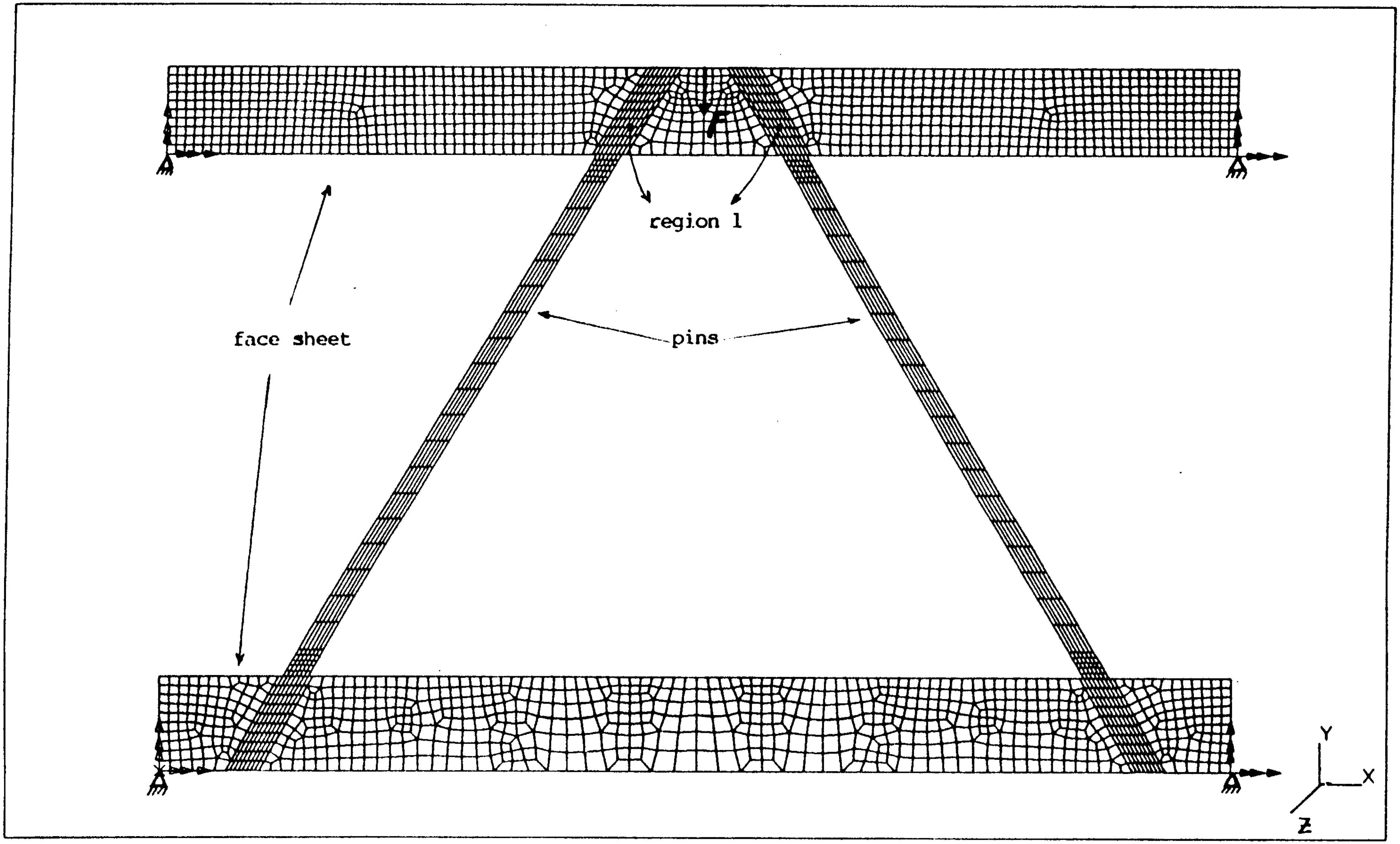
F
region 1
face sheet
pins
Y
X
Z

Figure 3

Plan View of the Typical Area of a Face Sheet

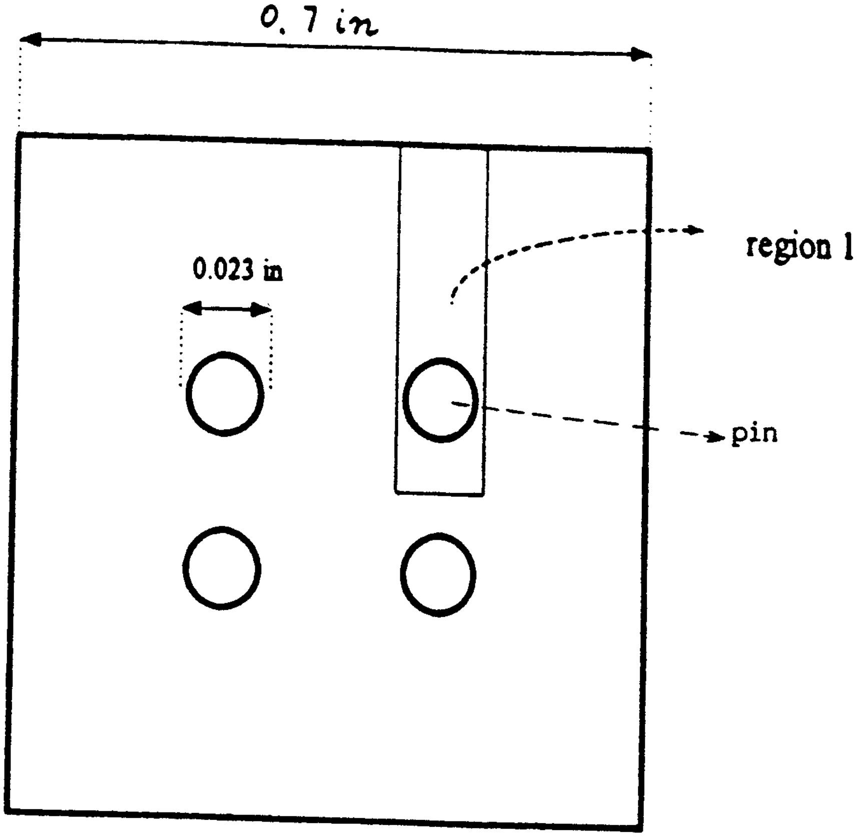
0.7 in
0.023 in
region 1
pin

Figure 4

stress-yy in the lower face sheet

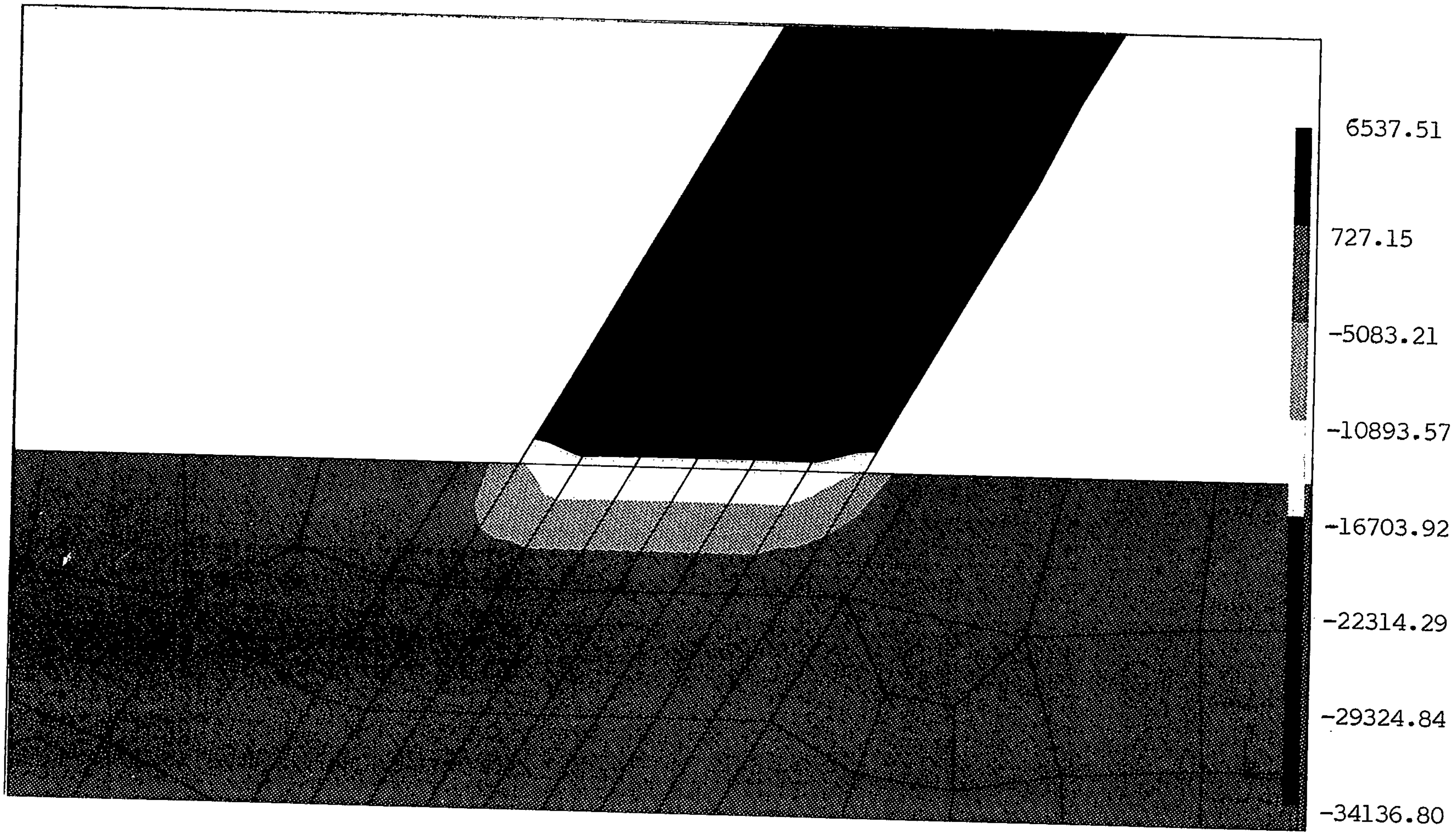

Figure 5

Stress-yy in the upper face sheet

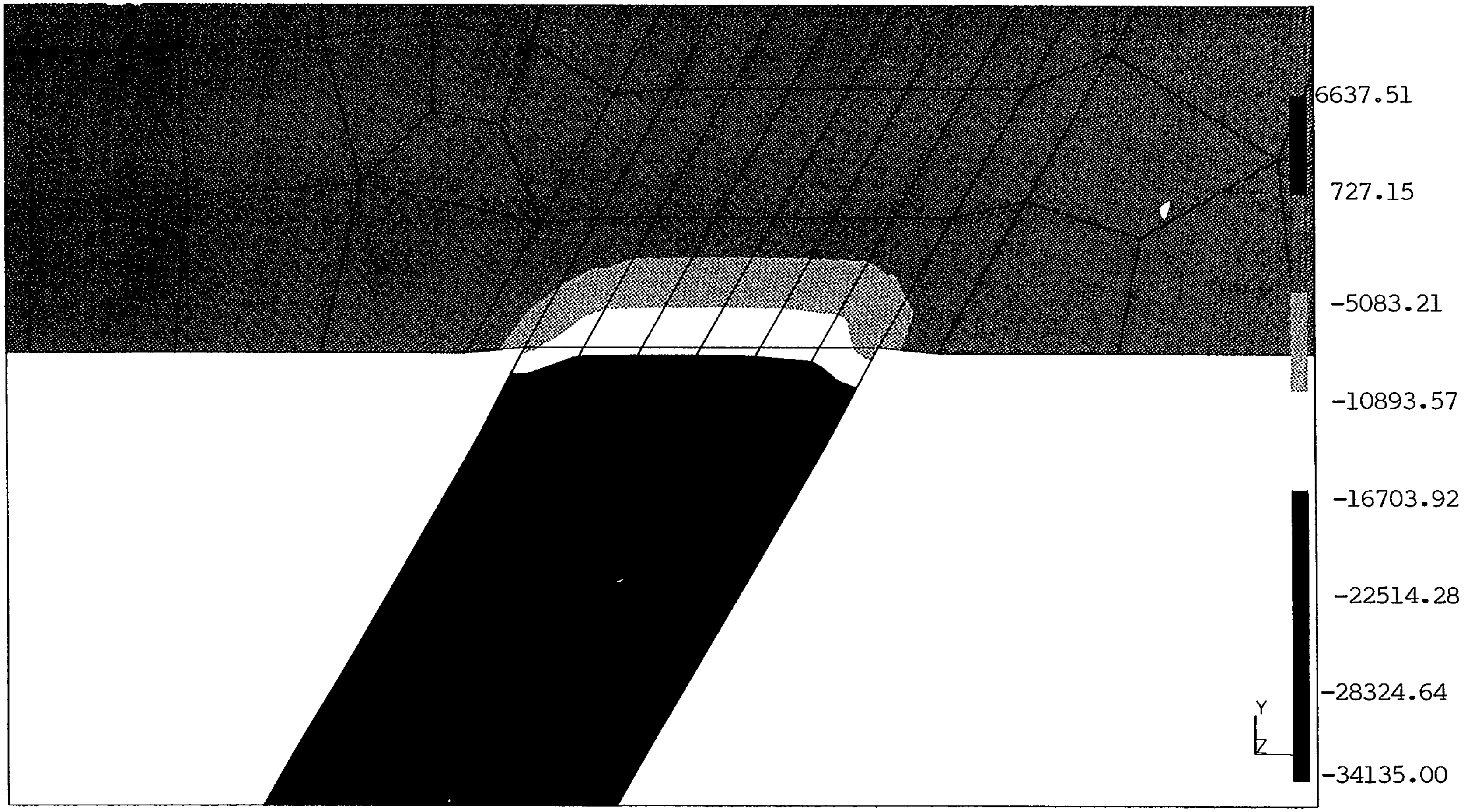

Figure 6

The Lateral View of the Modeled Test Specimen with Load and Supports

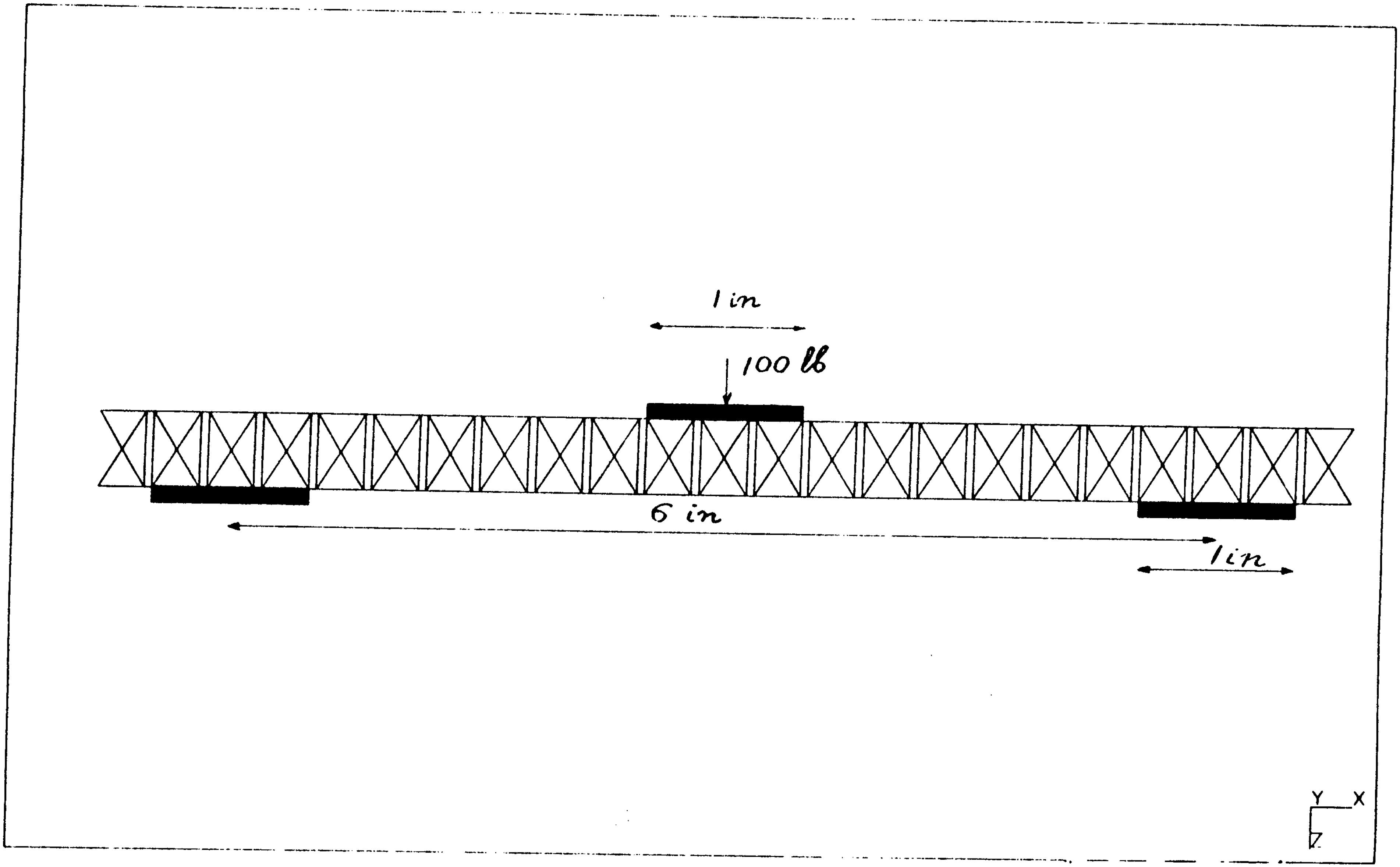
1 in
100 lb
6 in
1 in
Y
X
Z

Figure 7
Finite Element Model with Plate and truss Elements,
One Fourth of the Specimen with Boundary Conditions and Load
u_x, u_y, u_z are displacements, ψ_x and ψ_y are angles of rotation about axes x and y

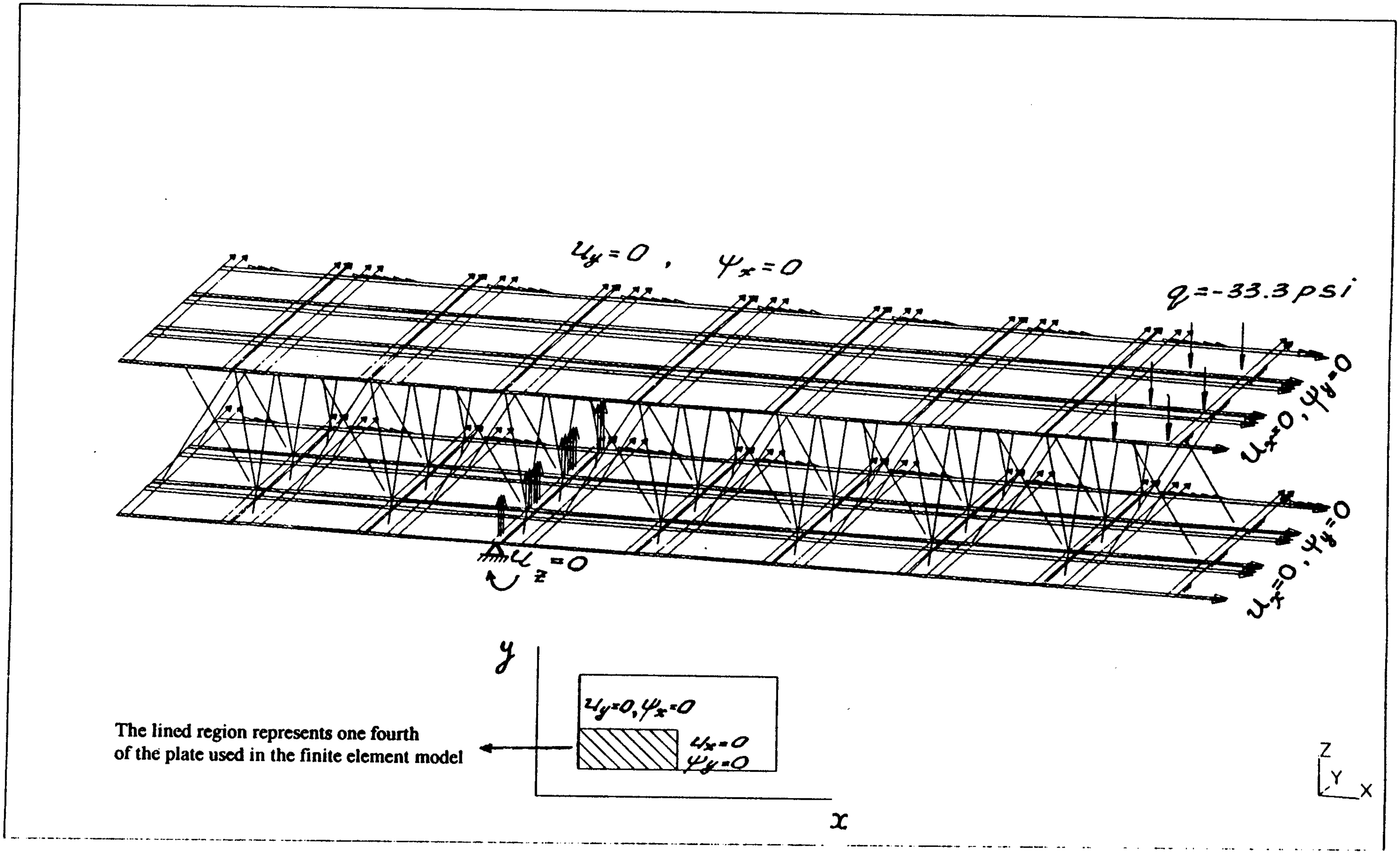
$u_y = 0$, $\psi_x = 0$
$q = -33.3$ psi
$u_x = 0, \psi_y = 0$
$u_x = 0, \psi_y = 0$
$u_z = 0$
y
$u_y = 0, \psi_x = 0$
$u_x = 0$
$\psi_y = 0$
x
Z
Y
X

The lined region represents one fourth of the plate used in the finite element model

Figure 8
Pins making up the core (face sheets not shown) and forces in them under effect of the load 100 lb applied as shown in figures 6 and 7. This is one fourth of the plate as shown in figure 7.

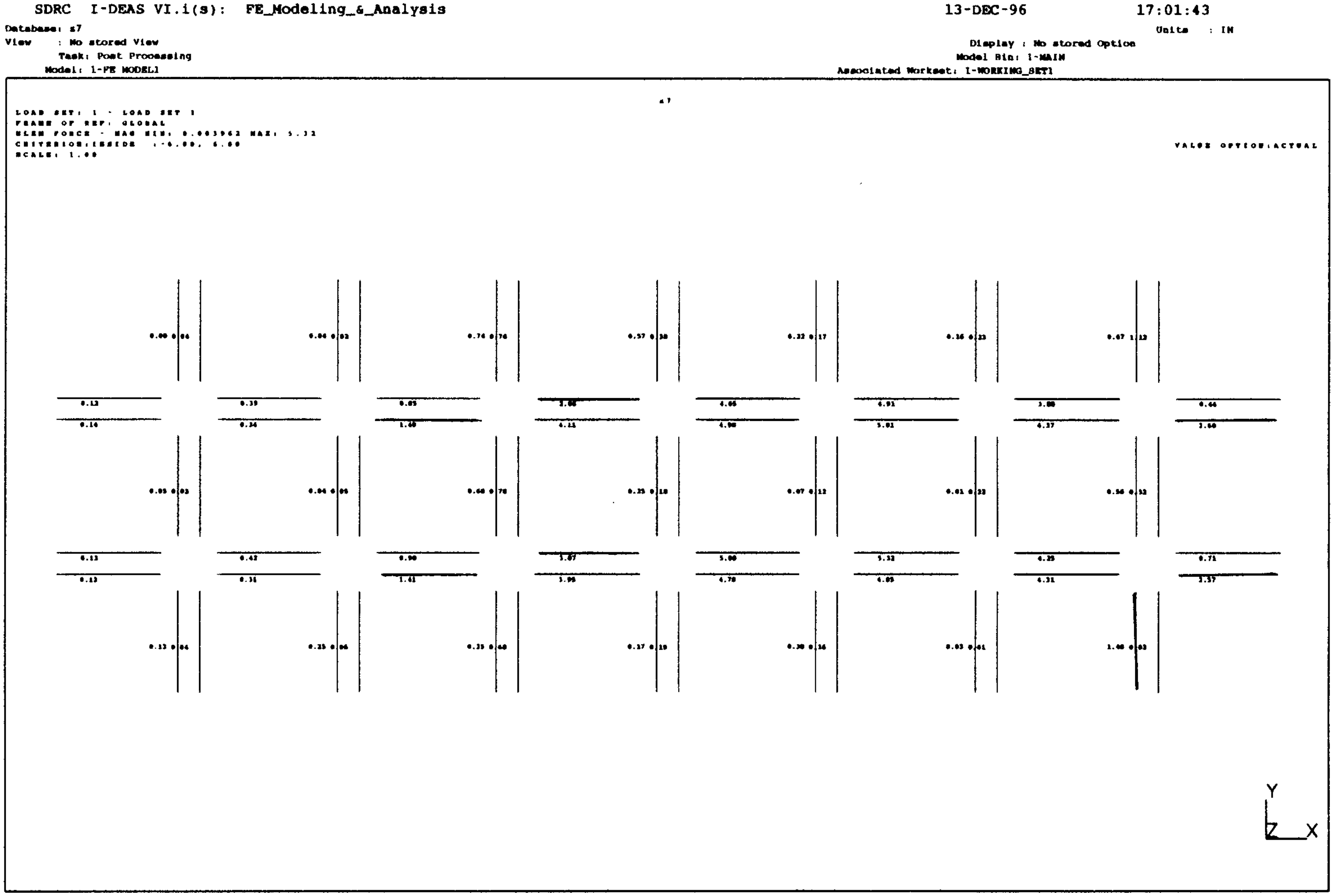

SDRC I-DEAS VI.i(s): FE_Modeling_&_Analysis
Database: s7
View : No stored View
Task: Post Processing
Model: 1-FE MODEL1

13-DEC-96 17:01:43
Units : IN
Display : No stored Option
Model Bin: 1-MAIN
Associated Workset: 1-WORKING_SET1

LOAD SET: 1 - LOAD SET 1
FRAME OF REF: GLOBAL
ELEM FORCE - MAG MIN: 0.003962 MAX: 5.32
CRITERION:INSIDE :-6.00, 6.00
SCALE: 1.00

VALUE OPTION:ACTUAL

s7
0.00 0.04
0.04 0.02
0.74 0.76
0.57 0.38
0.22 0.17
0.16 0.23
0.67 1.12
0.12
0.14
0.39
0.34
0.85
1.60
3.88
4.11
4.66
4.90
4.91
5.01
3.80
4.37
0.44
3.60
0.05 0.03
0.04 0.06
0.60 0.70
0.25 0.18
0.07 0.12
0.01 0.23
0.56 0.12
0.13
0.13
0.42
0.31
0.90
1.41
3.87
3.96
5.00
4.70
5.32
4.85
4.25
4.31
0.71
3.37
0.13 0.04
0.25 0.06
0.35 0.40
0.17 0.19
0.30 0.16
0.03 0.01
1.00 0.03
Y
Z
X

Figure 9

Stress-xx (psi)

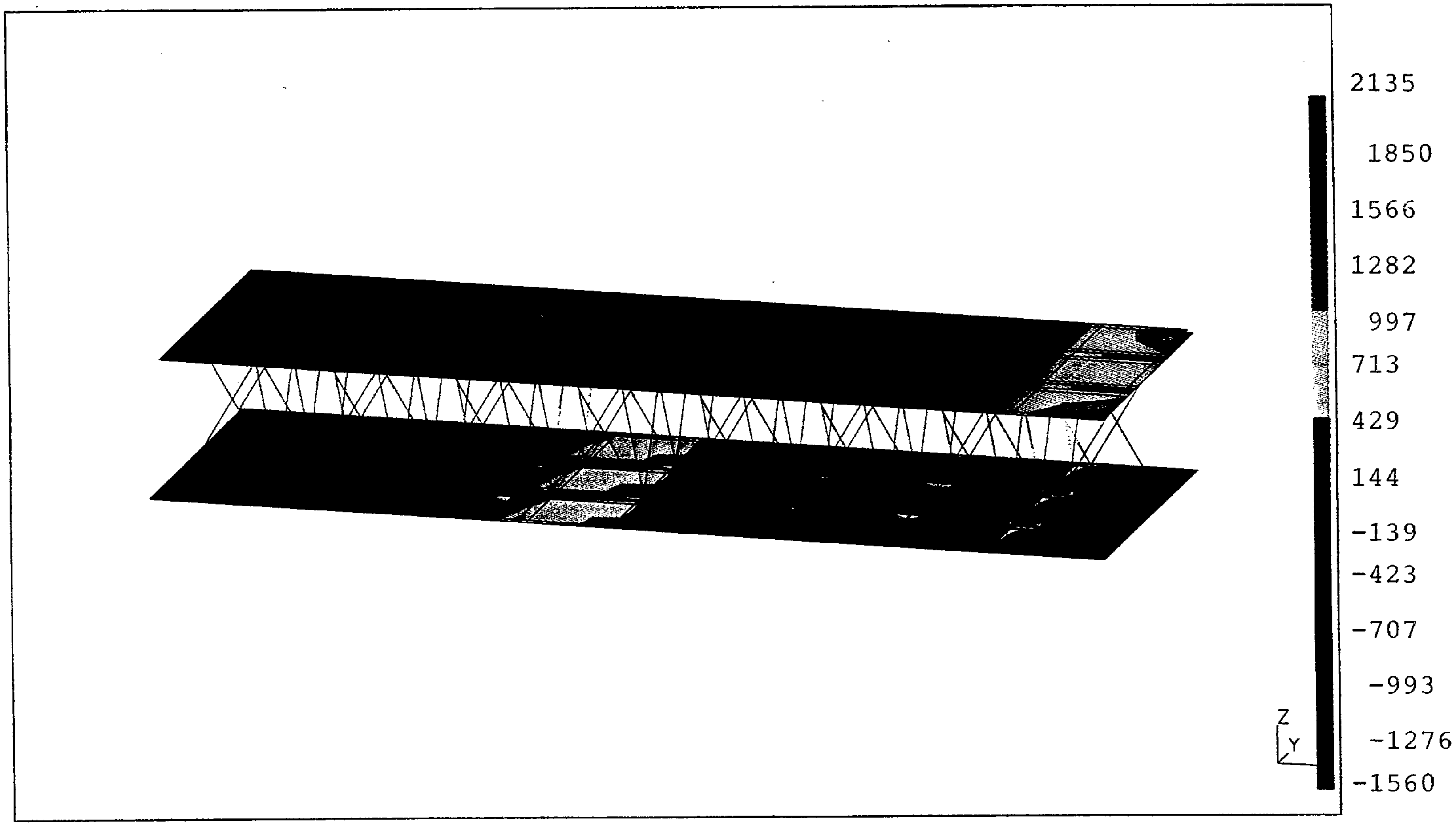

Figure 10

Stress-yy (psi)

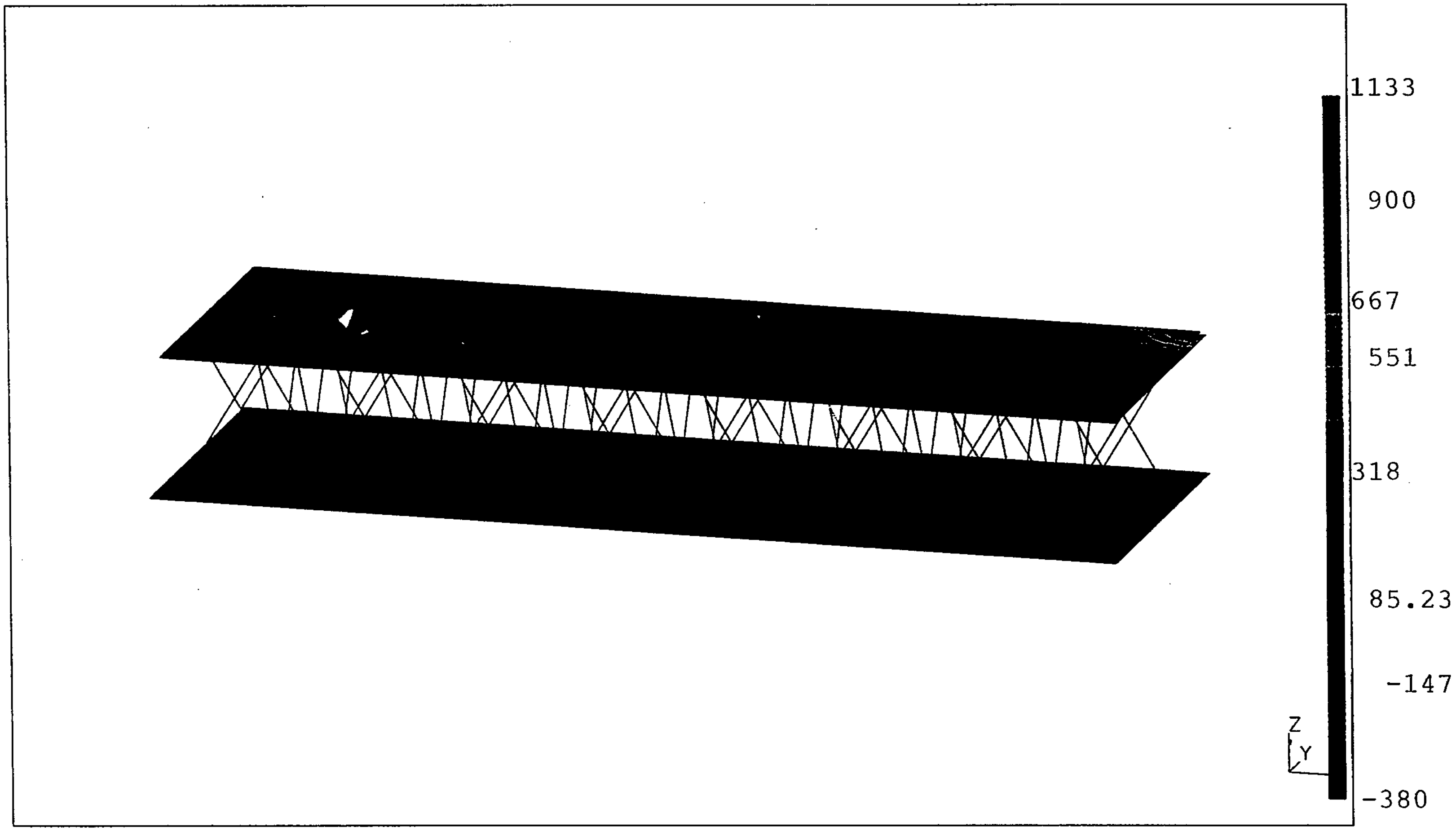
1133
900
667
551
318
85.23
-147
-380
Z
Y

Figure 11

Stress-zz (psi)

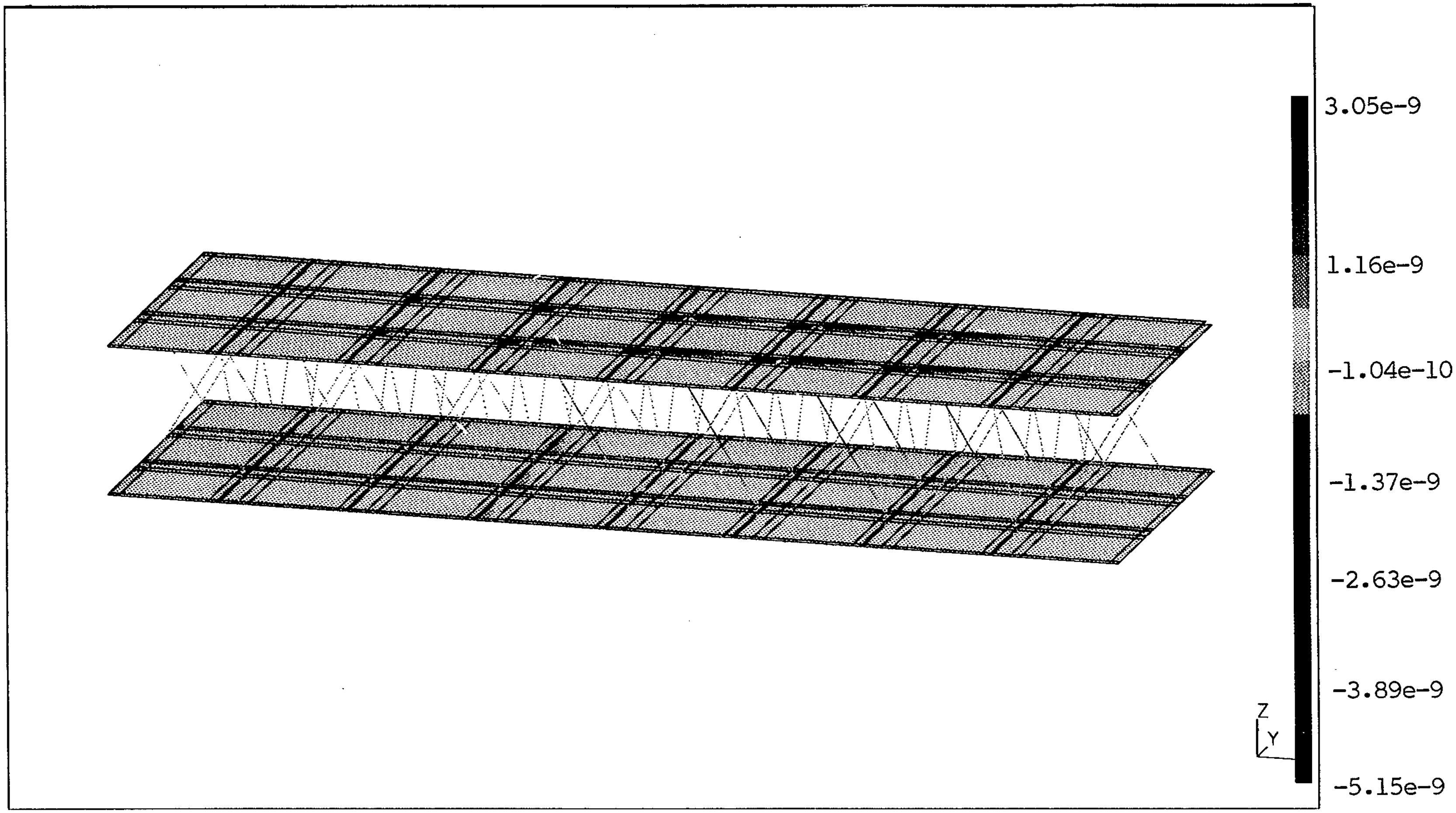
3.05e-9
1.16e-9
-1.04e-10
-1.37e-9
-2.63e-9
-3.89e-9
-5.15e-9
Z
Y

Figure 12
Three-Dimensional Global Model with Brick Elements,
One Forth of the Specimen with Boundary Conditions and Load.

u_x, u_y, u_z are dispacements, ψ_x and ψ_y are angles of rotation about x and y axes

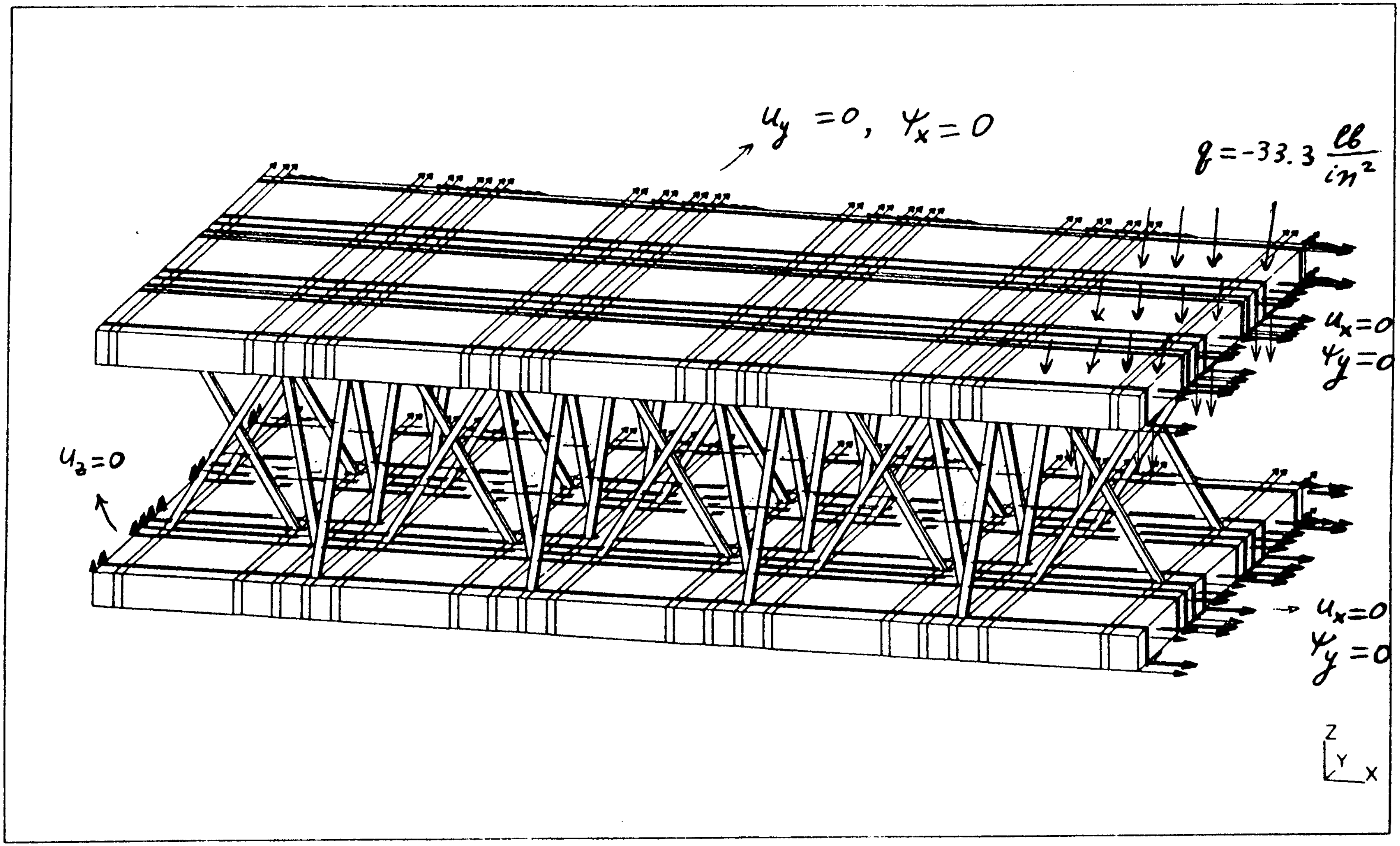

$u_y = 0, \ \psi_x = 0$
$q = -33.3 \frac{lb}{in^2}$
$u_x = 0$
$\psi_y = 0$
$u_z = 0$
$u_x = 0$
$\psi_y = 0$
Z
Y
X

Figure 13
Stress-xx (psi)

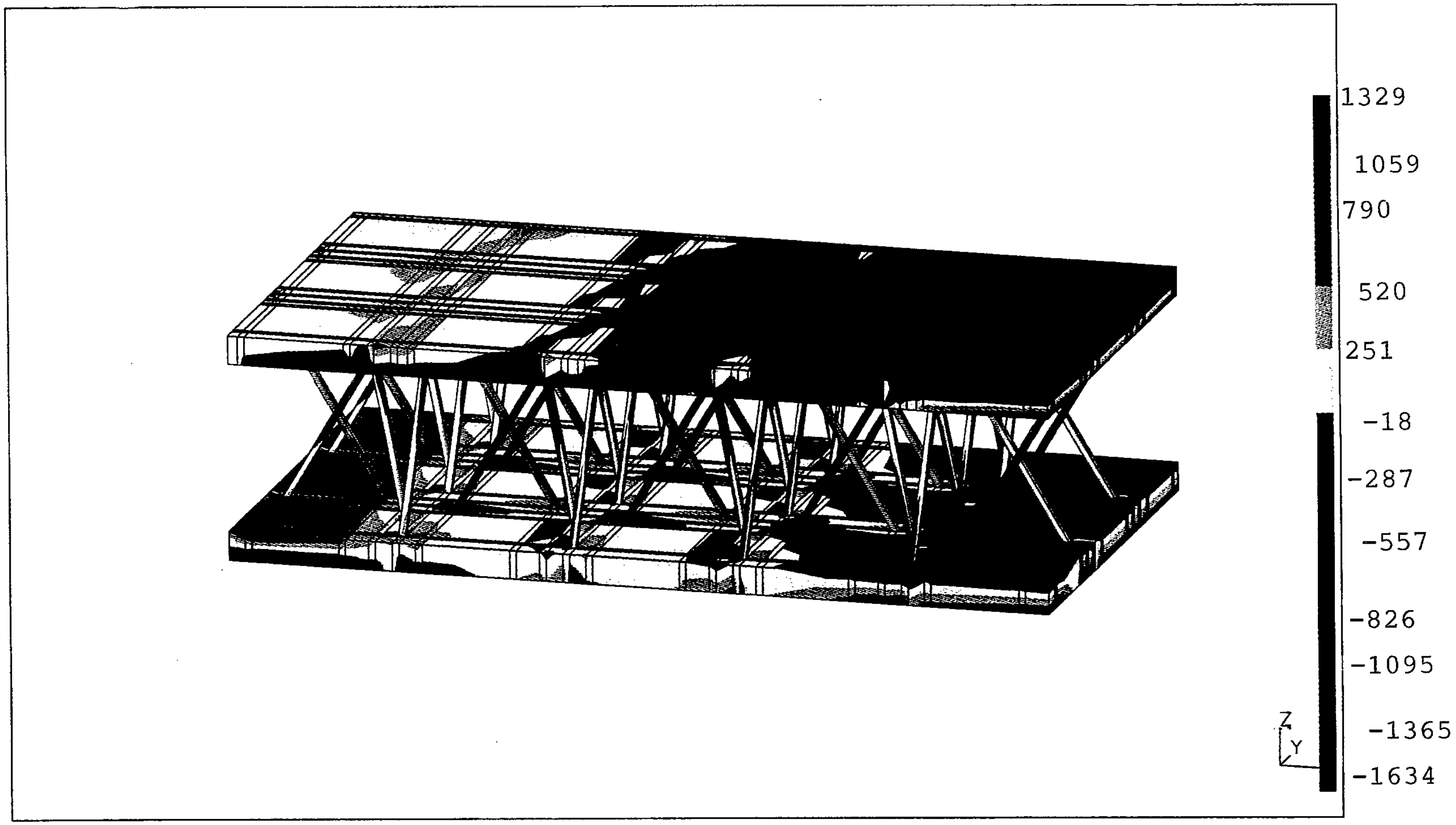
1329
1059
790
520
251
-18
-287
-557
-826
-1095
-1365
-1634
Z
Y

Figure 14
Stress-yy (psi)

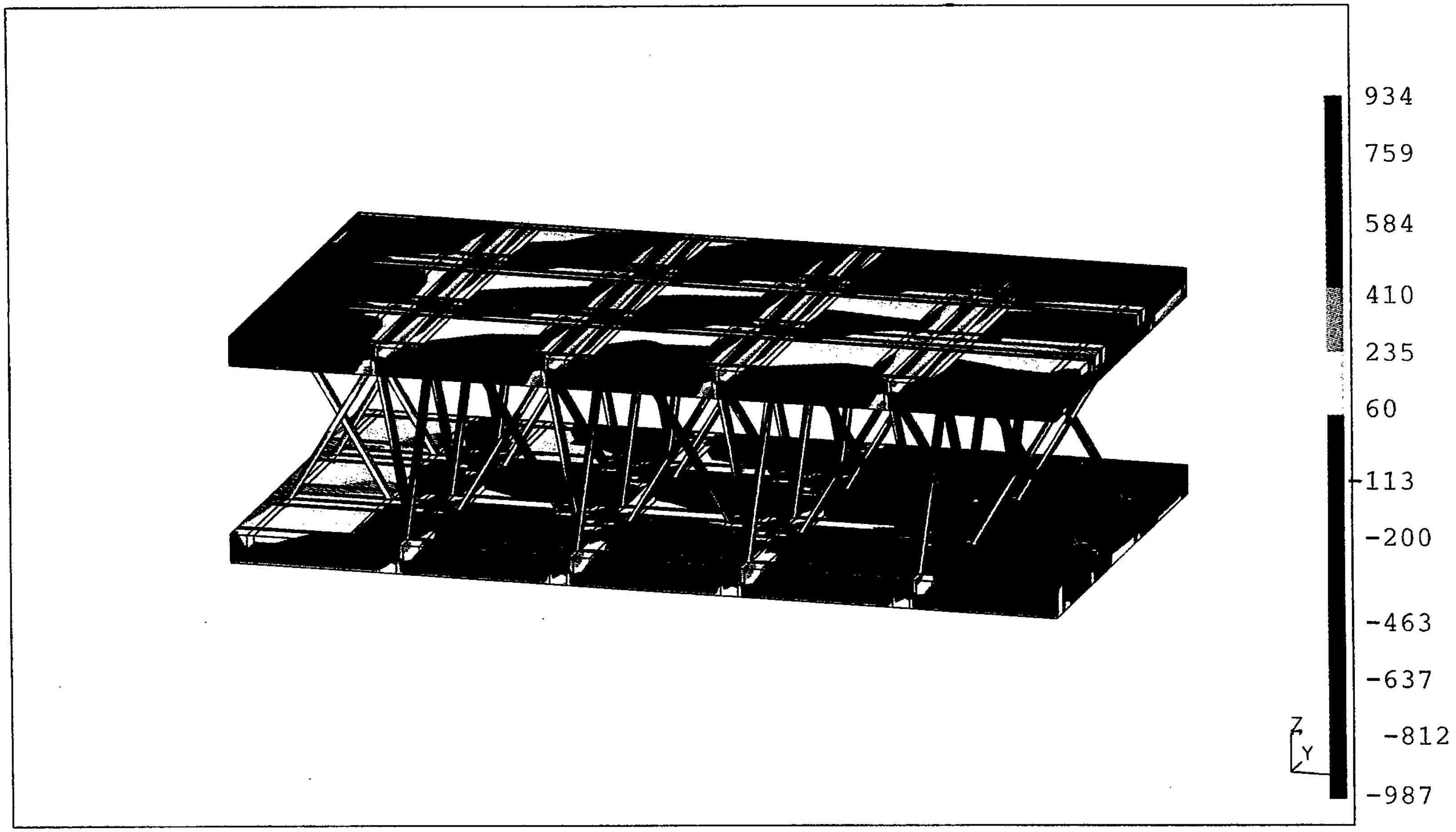
934
759
584
410
235
60
-113
-200
-463
-637
-812
-987
Z
Y

Figure 15

Stress-zz (psi)

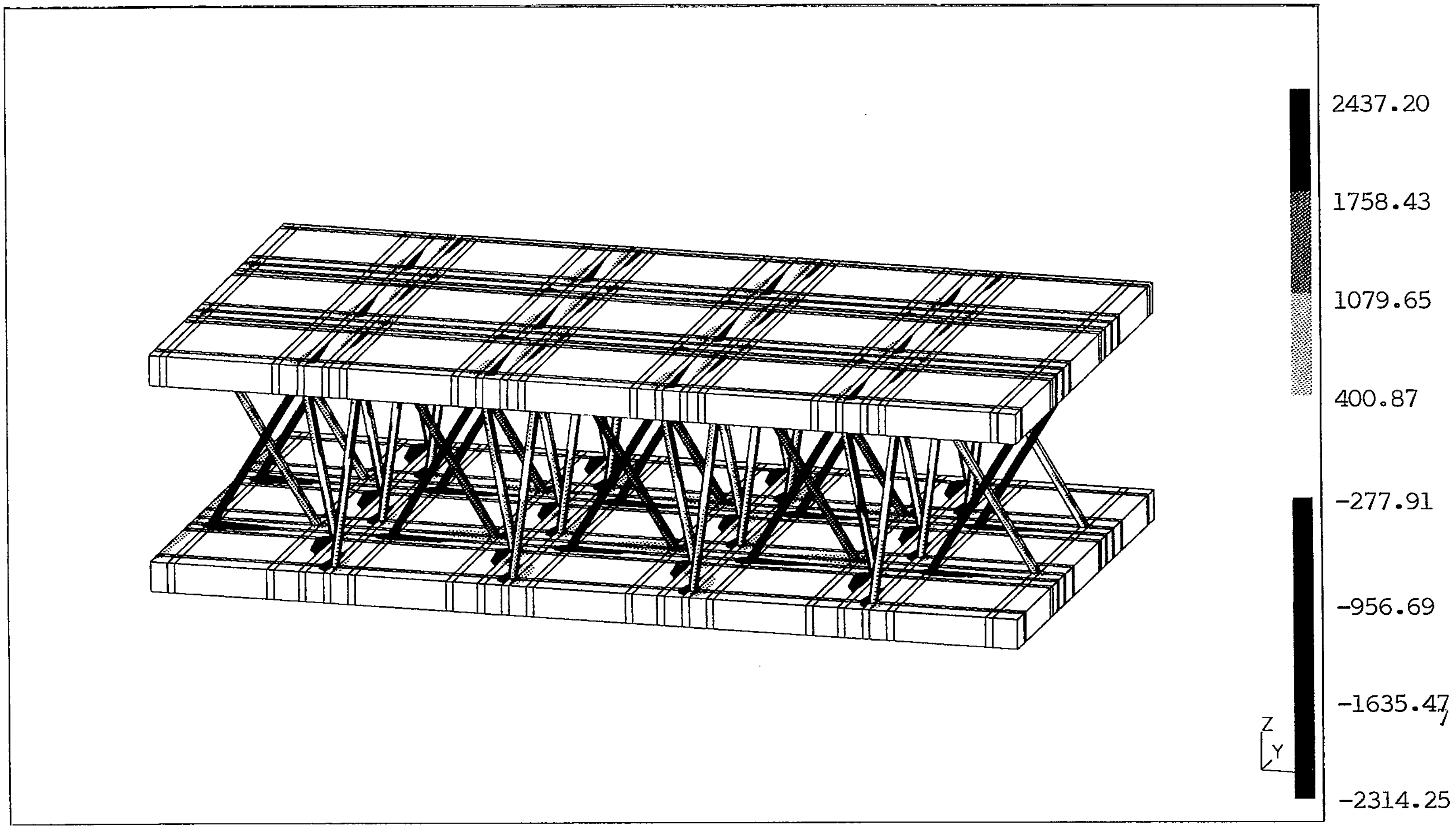
2437.20
1758.43
1079.65
400.87
-277.91
-956.69
-1635.47
-2314.25
Z
Y

Figure 16
Stress-xy (psi)

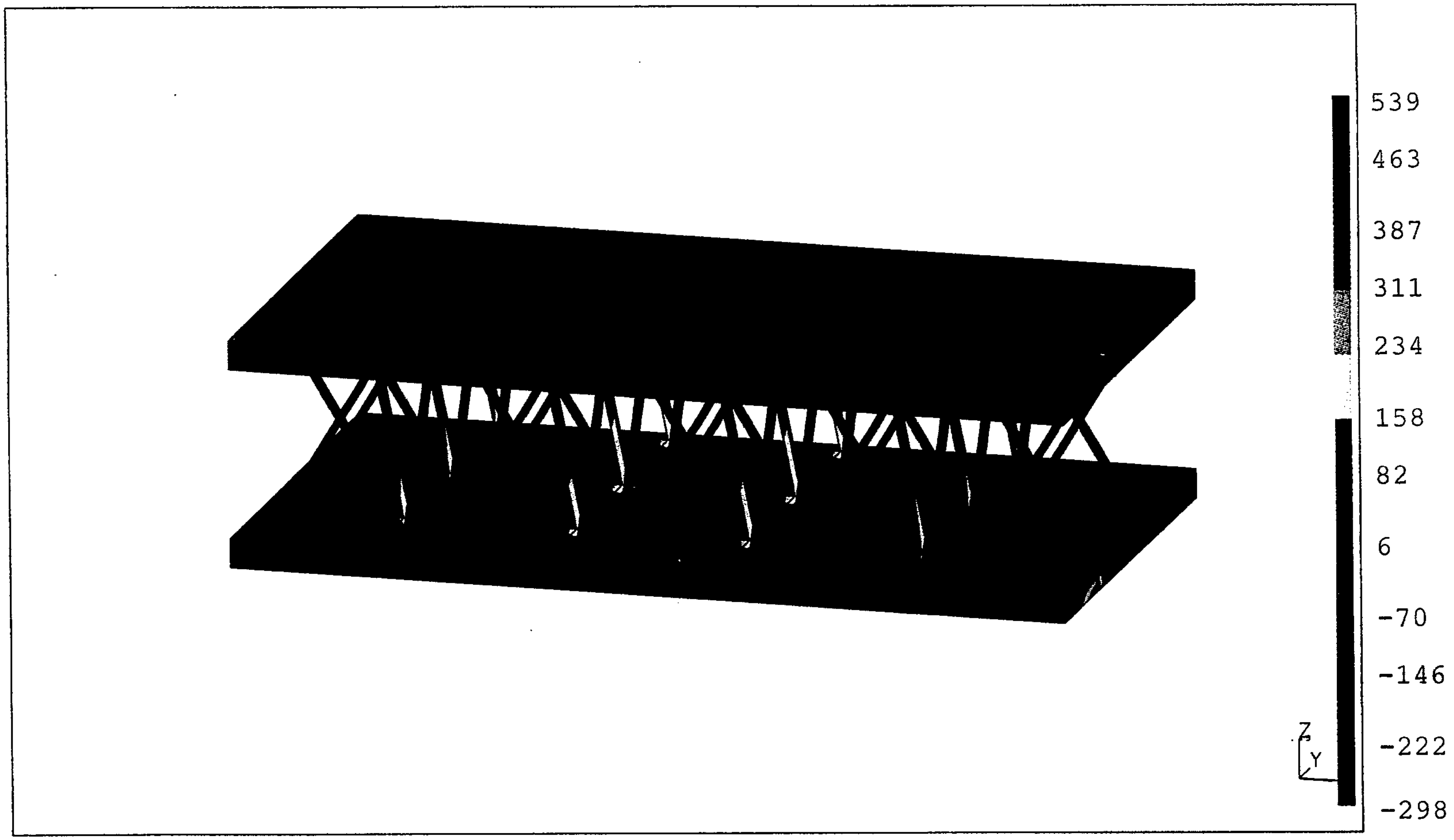
539
463
387
311
234
158
82
6
-70
-146
-222
-298
Z
Y

Figure 17

Strain Energy (lb.in)

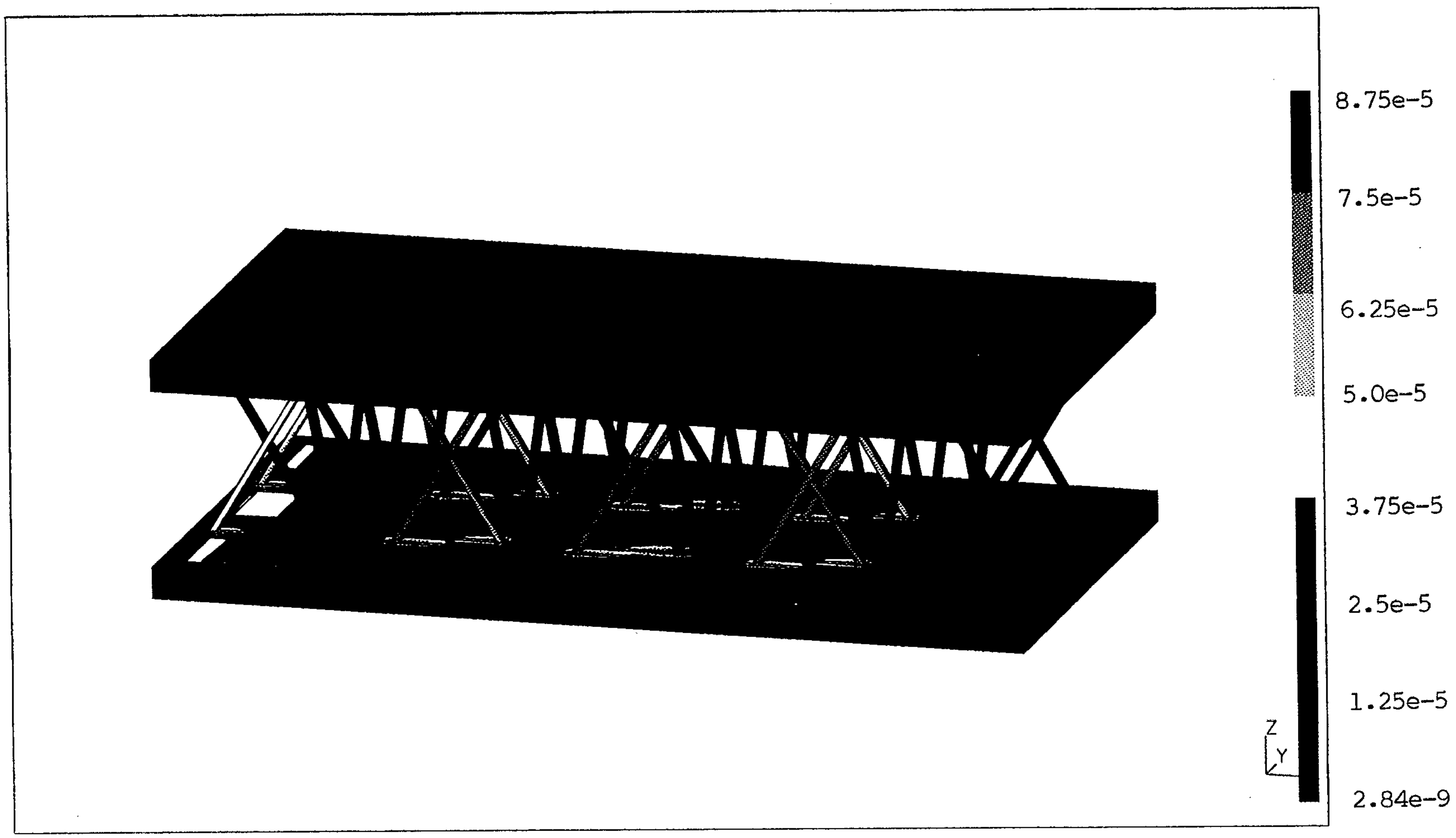
8.75e-5
7.5e-5
6.25e-5
5.0e-5
3.75e-5
2.5e-5
1.25e-5
2.84e-9
Z
Y

Figure 18
Three-dimensional local model with brick elements,
applied load and boundary conditions

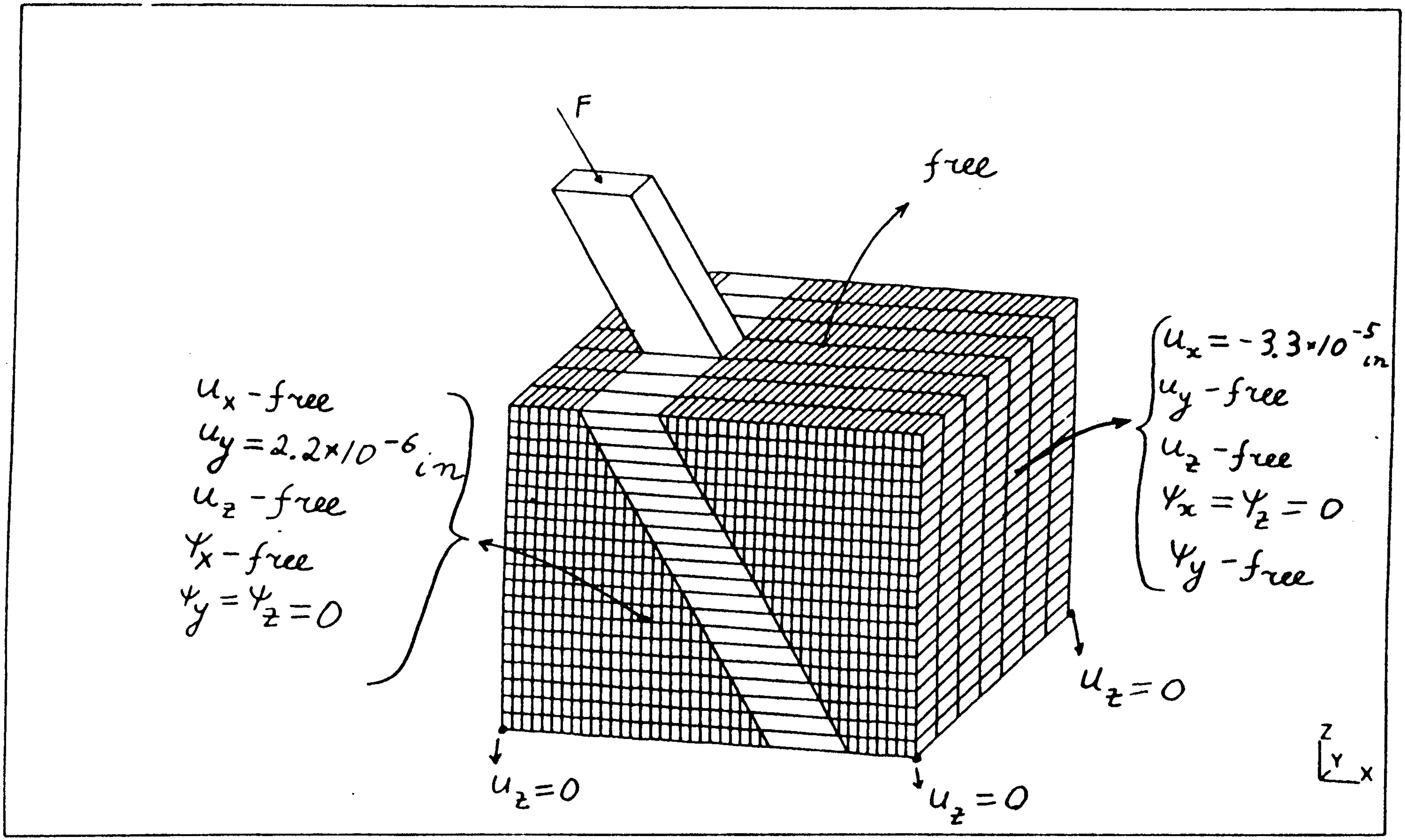
F
free
u_x - free
$u_y = 2.2 \times 10^{-6}$ in
u_z - free
ψ_x - free
$\psi_y = \psi_z = 0$
$u_x = -3.3 \times 10^{-5}$ in
u_y - free
u_z - free
$\psi_x = \psi_z = 0$
ψ_y - free
$u_z = 0$
$u_z = 0$
$u_z = 0$
Z
Y
X

Figure 19

Diagram for Analytical Calculation of Shear Stress on the Surface of the Pin in the Face Sheet

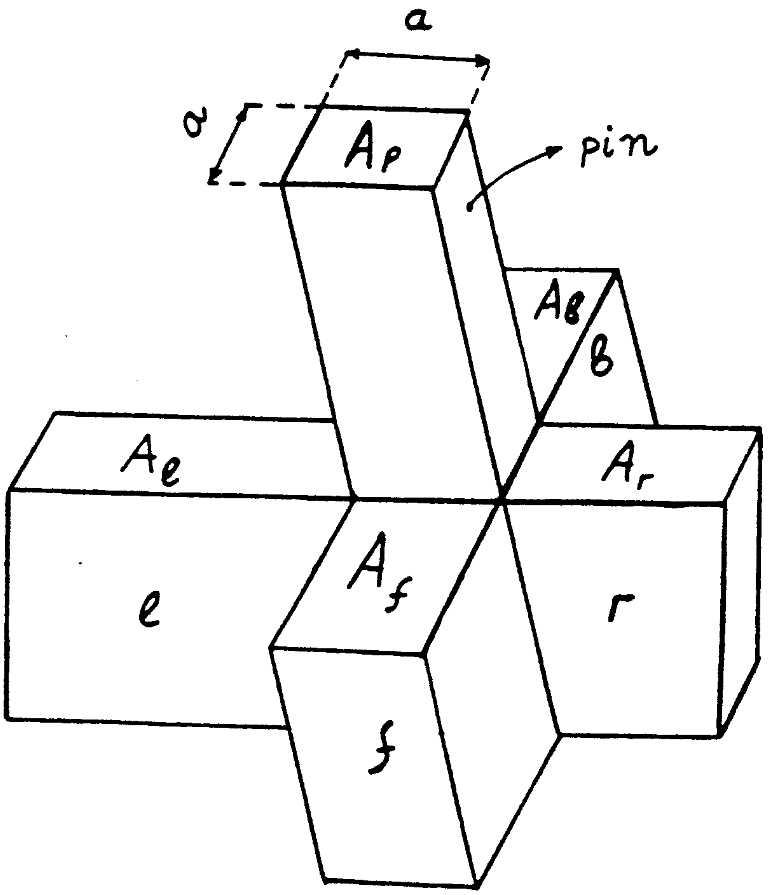
a
a
A_p
pin
A_b
b
A_l
A_r
A_f
l
r
f

Figure 20

Analytical model

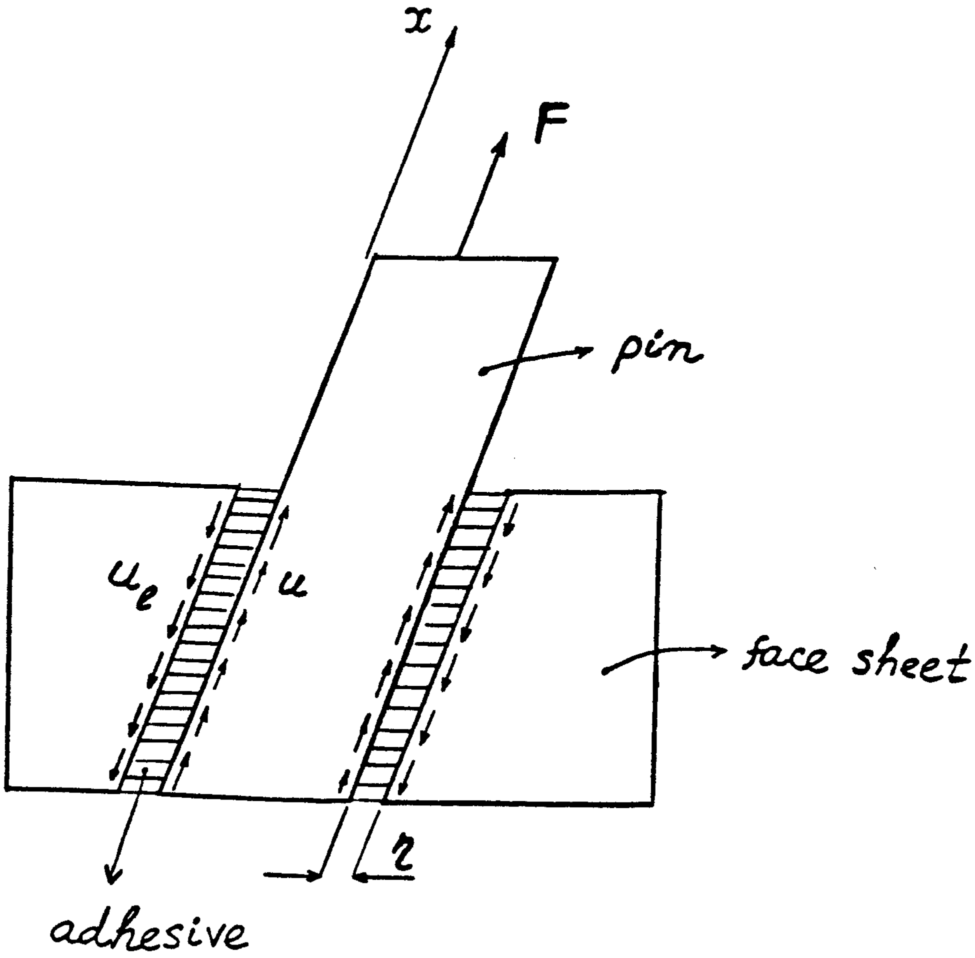

x
F
pin
u_e
u
face sheet
η
adhesive

Figure 21

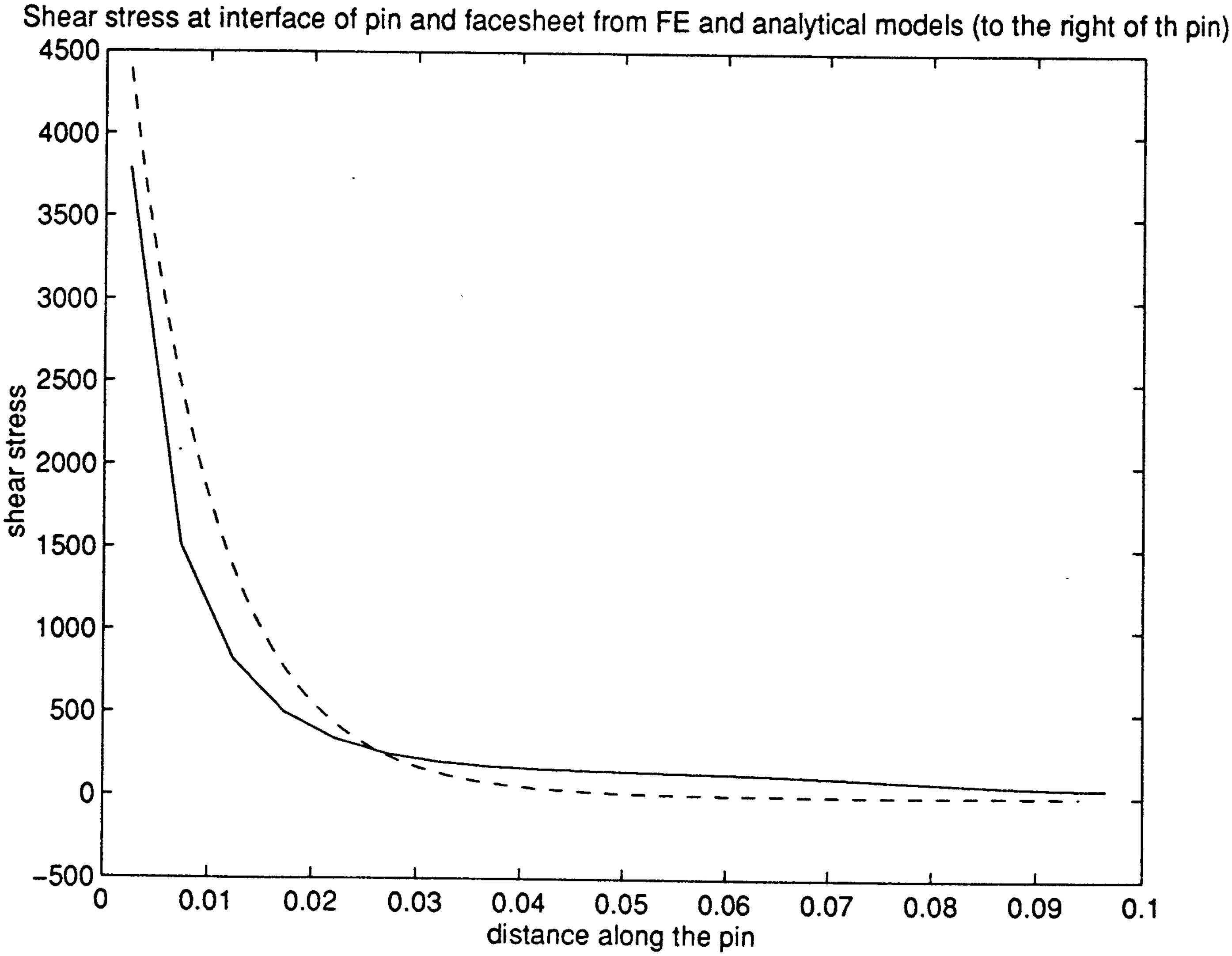
Shear stress at interface of pin and facesheet from FE and analytical models (to the right of th pin)
4500
4000
3500
3000
2500
2000
1500
1000
500
0
−500
shear stress
0
0.01
0.02
0.03
0.04
0.05
0.06
0.07
0.08
0.09
0.1
distance along the pin

Figure 22
Variation of Stress σ_{xz} in the Y-direction in the Middle Ply

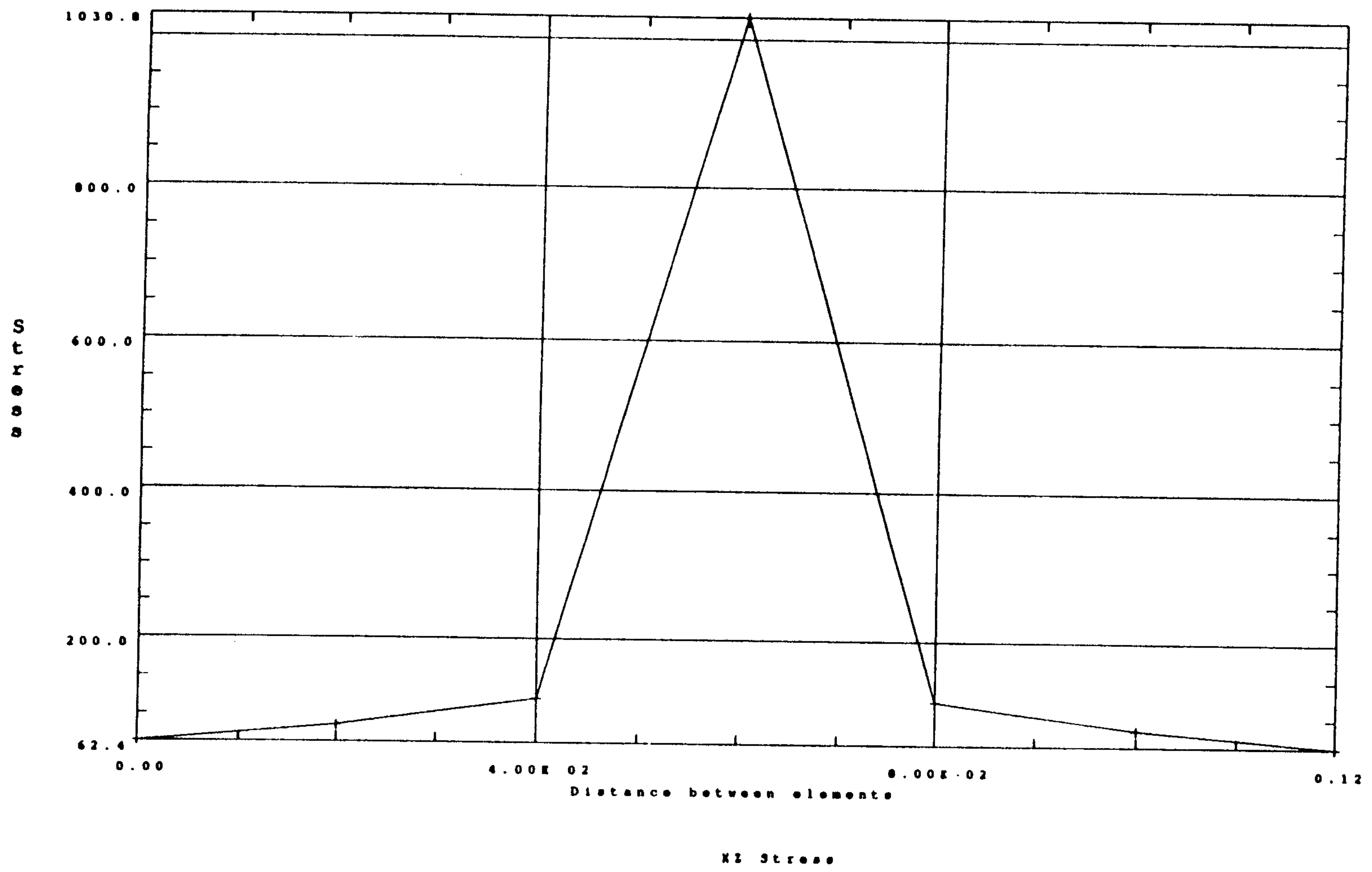

Figure 23

Variation of Stress σ_{zz} in the Y-direction in the Middle Ply

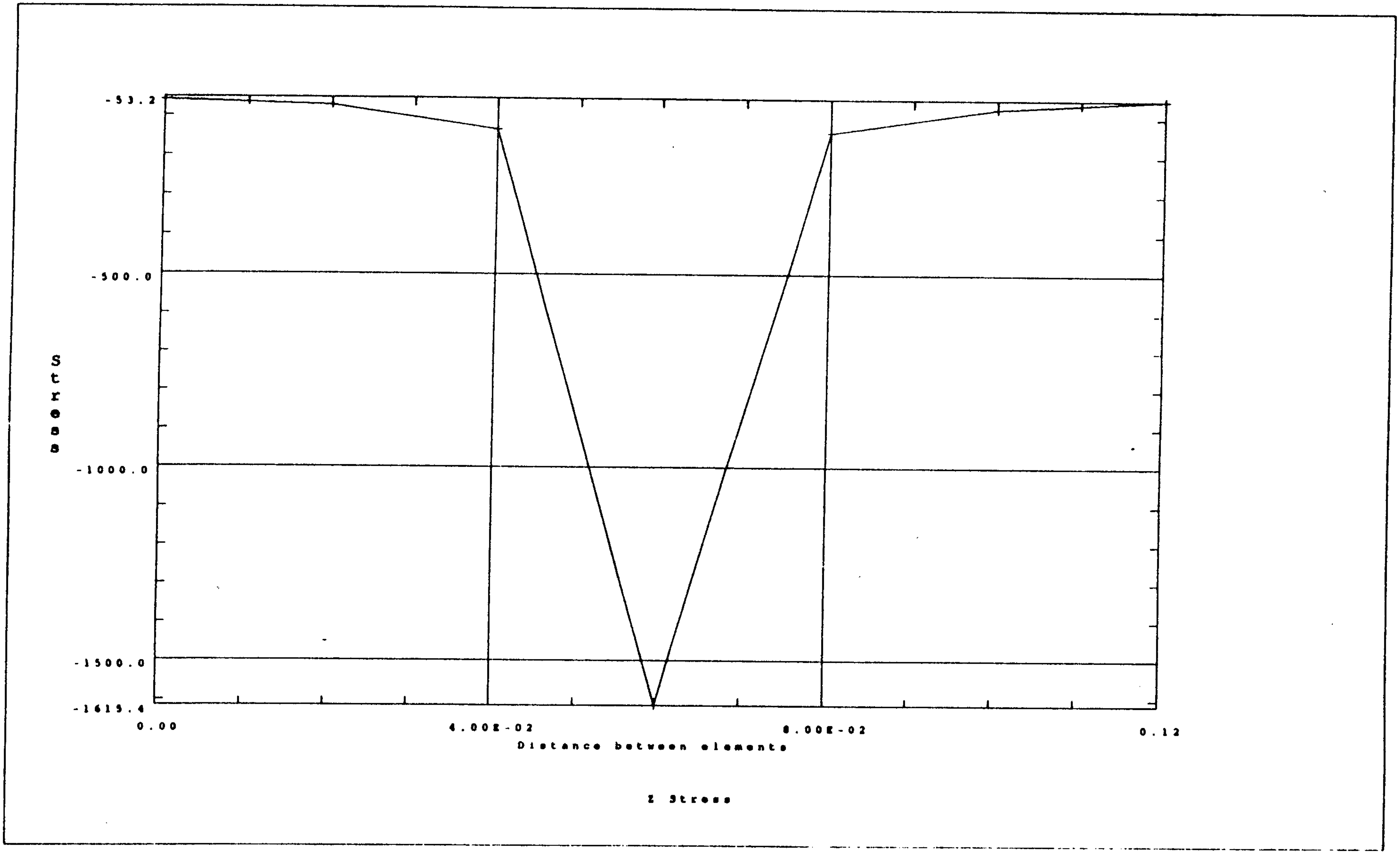

Figure 24

Variation of Stress σ_{xx} in the Y-direction in the Middle Ply

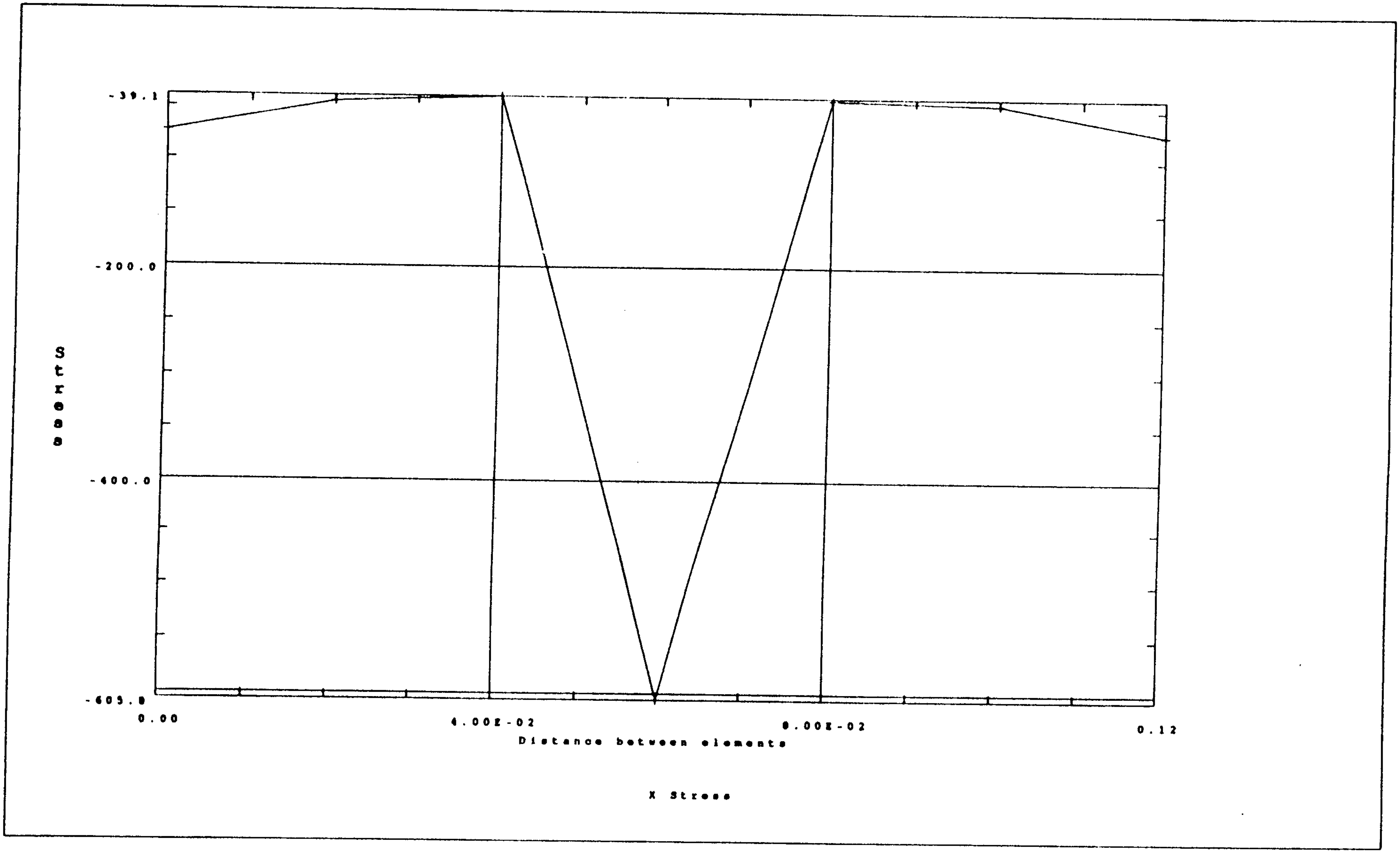

Figure 25

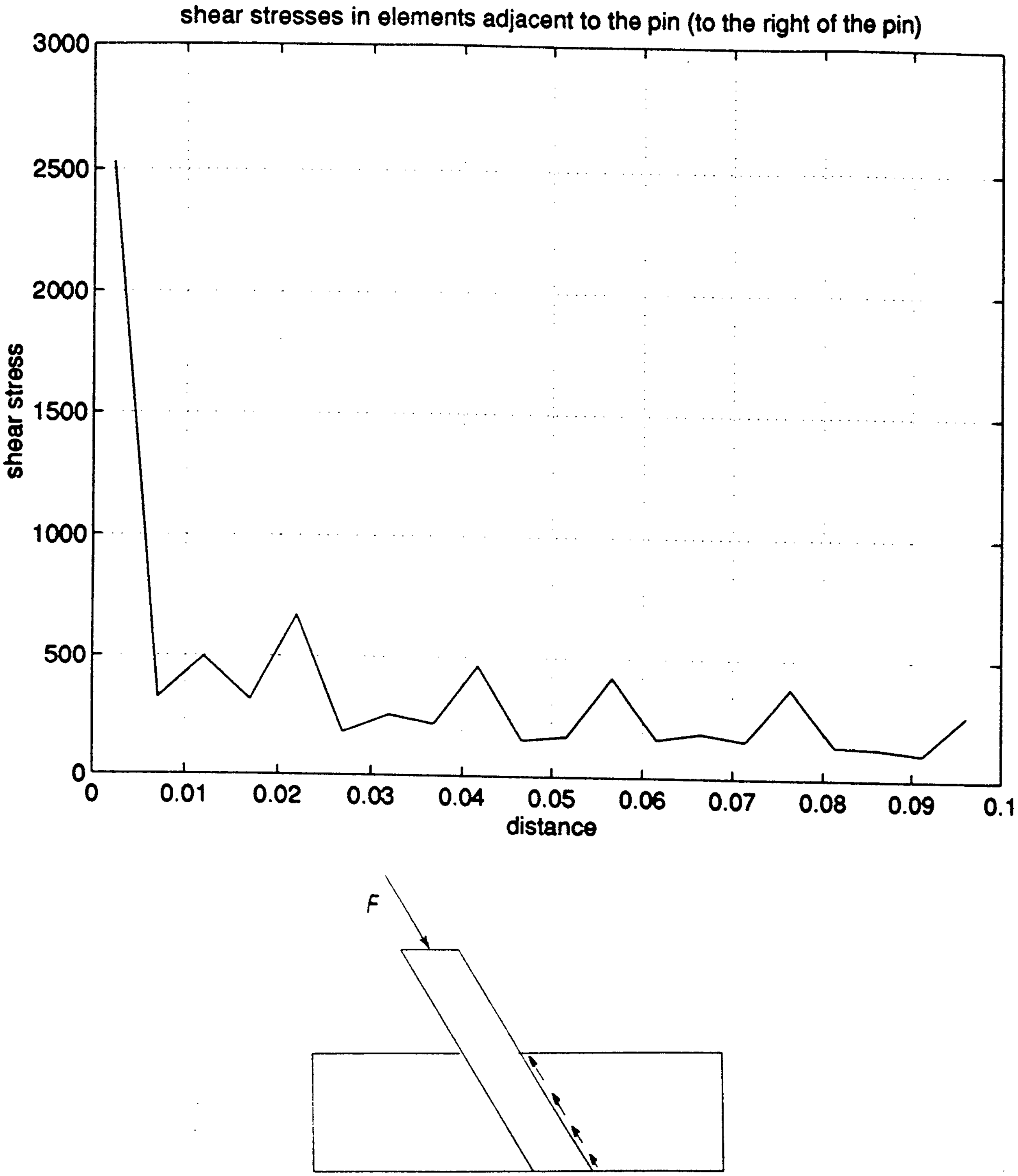
shear stresses in elements adjacent to the pin (to the right of the pin)
shear stress
3000
2500
2000
1500
1000
500
0
0
0.01
0.02
0.03
0.04
0.05
0.06
0.07
0.08
0.09
0.1
distance
F

Figure 26

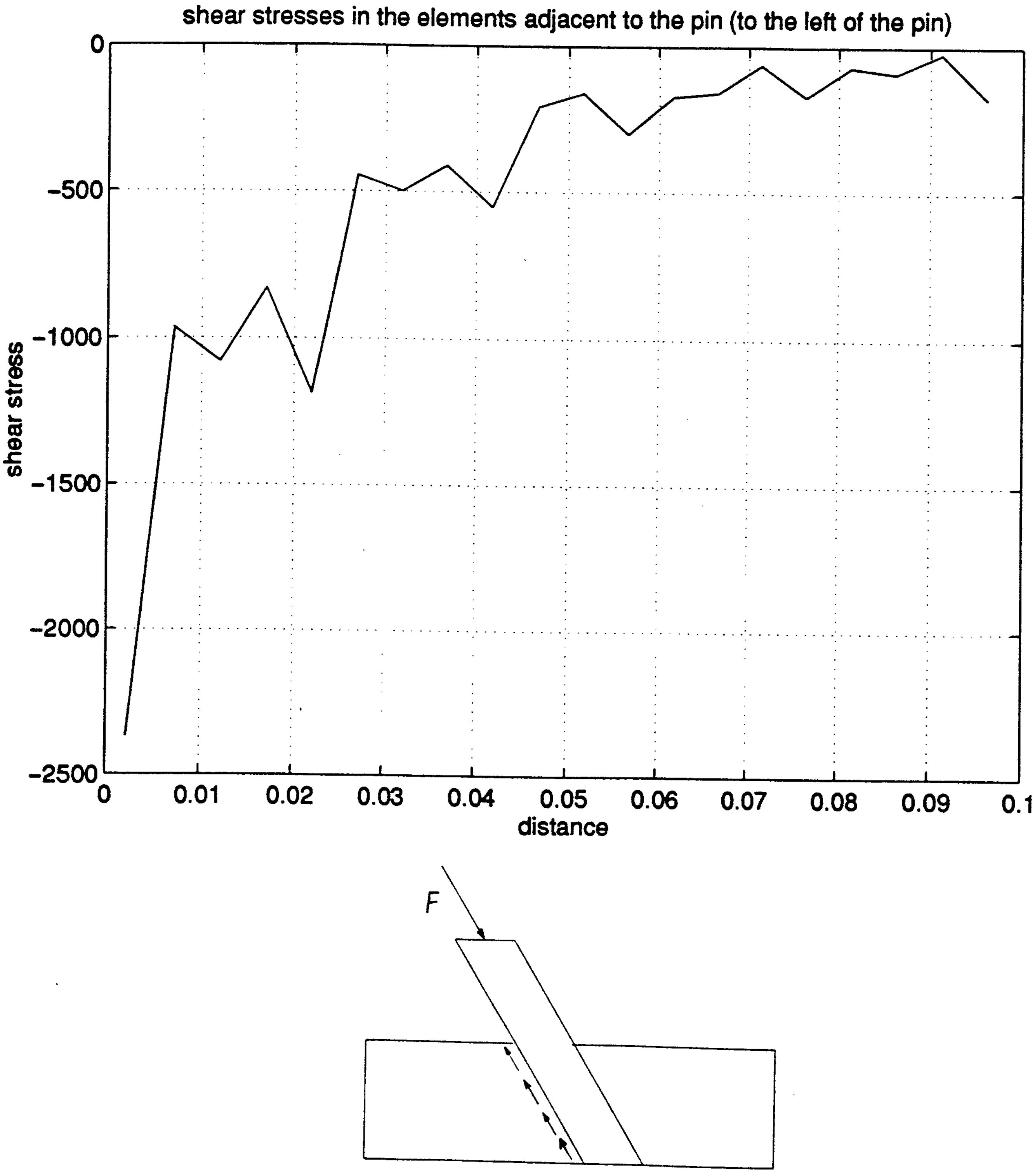
shear stresses in the elements adjacent to the pin (to the left of the pin)
shear stress
0
-500
-1000
-1500
-2000
-2500
distance
0
0.01
0.02
0.03
0.04
0.05
0.06
0.07
0.08
0.09
0.1
F

Figure 27

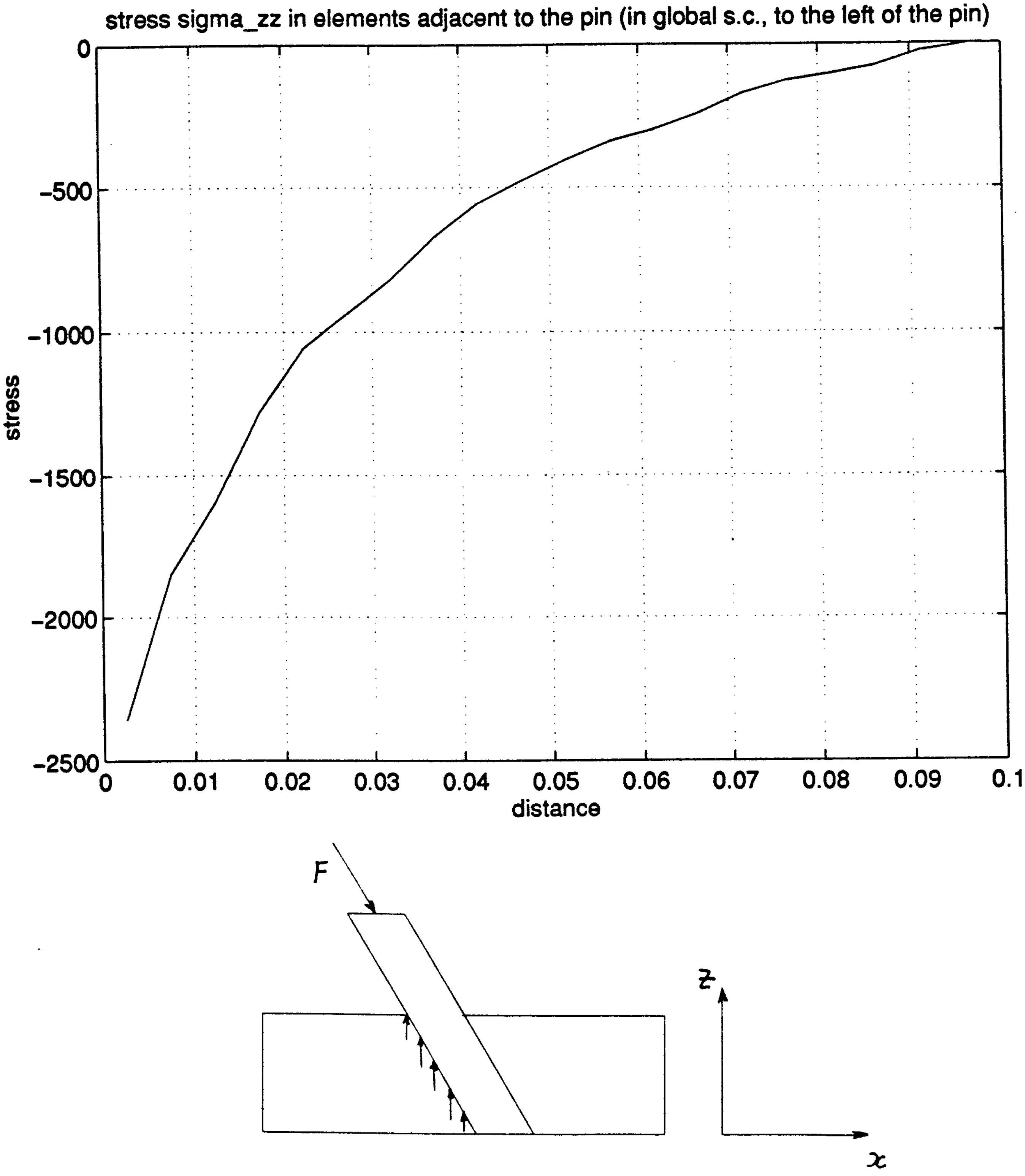
stress sigma_zz in elements adjacent to the pin (in global s.c., to the left of the pin)

Figure 28

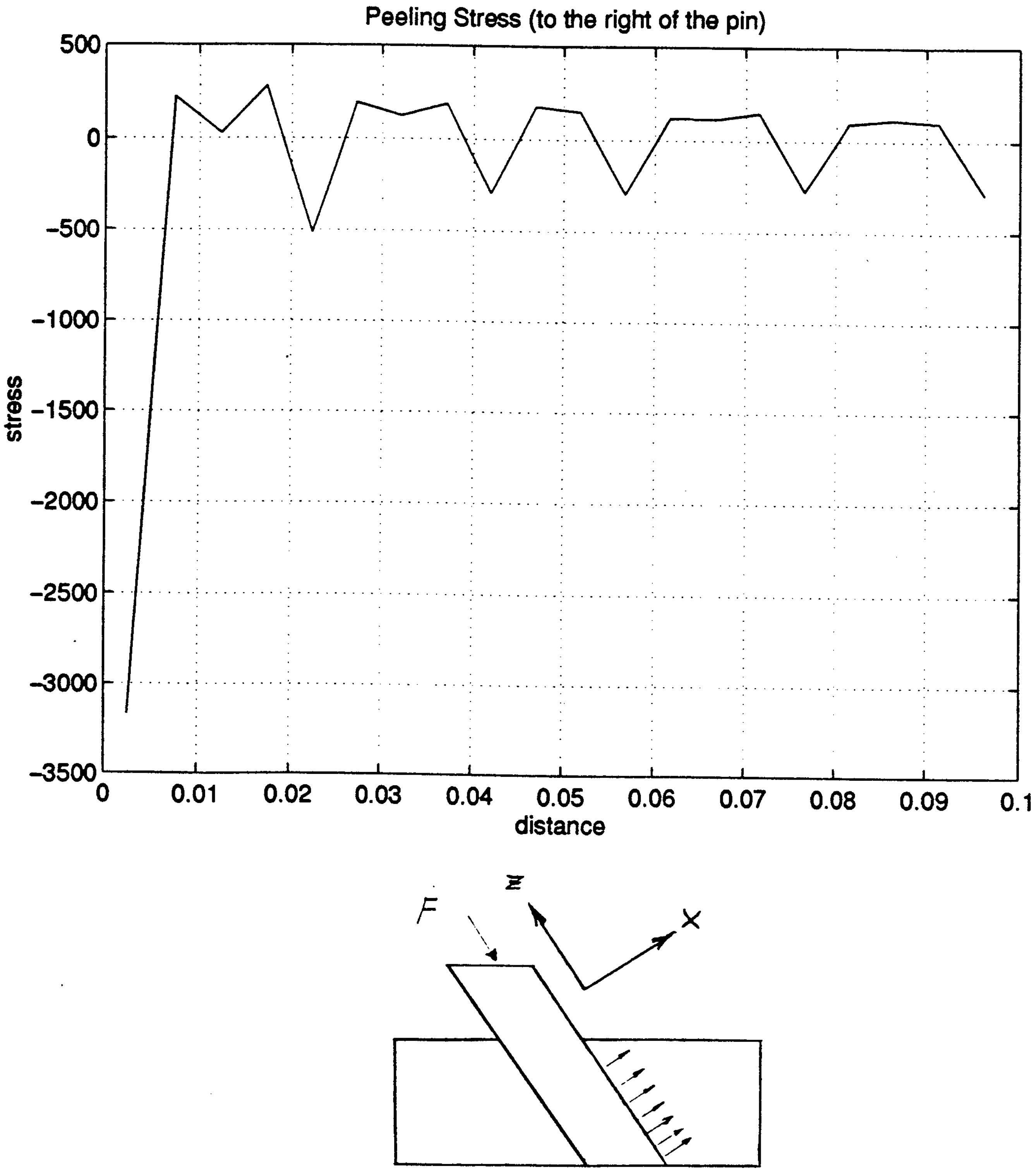
Peeling Stress (to the right of the pin)
stress
distance
500
0
-500
-1000
-1500
-2000
-2500
-3000
-3500
0
0.01
0.02
0.03
0.04
0.05
0.06
0.07
0.08
0.09
0.1
F
z
X

Table 1

Summary of Stresses in 3-D model with Plate and Rod Elements

	Stress-XX	Stress-XY	Stress-YY	Stress-XZ	Stress-YZ	Stress-ZZ
	996	1843	969	1467	1852	1327
Maximum	2.133E+03	1.975E+02	1.132E+03	1.608E-03	6.465E-04	3.053E-09
	1467	969	767	1841	1737	1660
Minimum	-1.552E+03	-2.902E+02	-3.786E+02	-1.799E-03	-1.015E-03	-5.142E-09
Average	-1.238E+01	3.961E+00	-3.374E+00	-3.056E-05	-1.203E-06	-1.104E-10

Table 2

Stresses in plies of face sheets in material coordinate systems of each ply

First Ply (0 degrees)

	Left	Right	Front	Behind
Sigma_xx	9.4E+03	-2.0E+04	-2.6E+03	-2.6E+03
Sigma_yy	-9.4E+03	-3.5E+02	-2.3E+03	-2.3E+03
Sigma_zz	-8.3E+03	-8.6E+02	-1.5E+03	-1.5E+03
Sigma_yz	-2.8E+01	2.3E+01	-1.3E+03	1.3E+03
Sigma_xz	-1.5E+03	3.4E+03	8.2E+02	8.2E+02
Sigma_xy	-5.3E+01	1.7E+01	9.0E+02	-9.0E+02

Second Ply (90 degrees)

	Left	Right	Front	Behind
Sigma_xx	-1.4E+03	-2.3E+02	-5.9E+03	5.9E+03
Sigma_yy	1.5E+02	-1.2E+03	-2.3E+03	-2.3E+03
Sigma_zz	-7.0E+03	-8.8E+02	-1.3E+03	-1.3E+03
Sigma_yz	-1.2E+03	2.4E+03	6.5E+02	6.5E+02
Sigma_xz	1.8E+03	-3.3E+01	2.2E+03	-2.2E+03
Sigma_xy	1.4E+03	-2.3E+01	-7.5E+02	7.5E+02

Third PLy (+45 degrees)

	Left	Right	Front	Behind
Sigma_xx	1.4E+03	-1.4E+03	2.4E+03	-2.4E+03
Sigma_yy	2.8E+03	-2.0E+03	3.4E+03	-3.4E+03
Sigma_zz	-6.2E+03	-5.5E+02	-1.3E+03	-1.3E+03
Sigma_yz	-1.8E+03	2.1E+03	-1.9E+03	3.0E+03
Sigma_xz	3.9E+02	1.3E+03	3.0E+03	-1.9E+03
Sigma_xy	3.5E+02	-7.3E+02	1.0E+02	-1.0E+02

Fourth Ply (-45 degrees)

	Left	Right	Front	Behind
Sigma_xx	2.9E+03	-3.3E+02	-3.4E+03	3.4E+03
Sigma_yy	1.6E+03	9.0E+01	-2.1E+03	2.1E+03
Sigma_zz	-5.0E+03	-4.9E+01	-1.4E+03	-1.4E+03
Sigma_yz	6.5E+02	1.6E+03	2.9E+03	2.9E+03
Sigma_xz	-1.3E+03	1.5E+03	-1.7E+03	-1.7E+03
Sigma_xy	-3.0E+02	-7.1E+02	1.0E+02	-1.0E+02

ATTACHMENT VIII

FINITE ELEMENT ANALYSIS OF Z-PIN SANDWICH PANELS AND COMPARISON TO FAILURE MODES FOUND IN THE EXPERIMENTAL PHASE

FINITE ELEMENT ANALYSIS OF Z-PIN SANDWICH PANELS AND COMPARISON TO FAILURE MODES FOUND IN THE EXPERIMENTAL PHASE

1. INTRODUCTION

In this section, a quasi- nonlinear procedure is developed to analyze the progression of failure under static loading conditions. From the experimental observations (attachment II and III), the failure scenario is very complex in these sandwich panels. Yet, a simple technique has been developed that uses the NASTRAN program. The main feature of this technique is to impose all of the failure phenomena to the pins themselves. The authors do recognize the fact that the failure modes are inherent to the global sandwich construction. This means that the face sheet must be an integral part of the failure process. Thus, to determine the failure loads, some of the experimental observations and the analytical results developed in attachments IV-VII are incorporated. However, these features are included in-conjuction with the failure of the pins in a method based entirely upon the pin's stiffness and resistance. Therefore, two pin force functions are used in representing two types of failure modes. These modes have been developed and incorporated in the determination of the load deflection characteristics. The first failure mode considered is pin buckling, and the second mode of failure is pin push through. Results are compared with those obtained from the experiment.

2. SANDWICH PANEL SPECIFICATIONS

2.3 Dimensions (Fig. 1)

3.00 in x 3.00 in x 0.500in

The panel consists of two face sheets and pins. There are six input parameters which determine the stiffness and geometry of the panel. They are:

1. Face Sheet thickness, (0.087 in)
2. Total Panel Height, (0.500 in)
3. Panel length(note that panel specimen is a square)

4. Pin diameter, (0.020 in)
5. Pin orientation angle(with vertical axis), (20°)
6. Pin separation distance, (0.100 in)
7. The load position is shown

2.2 Face Sheet Construction

16-ply Carbon fiber/ graphite epoxy resin

Approx. ply thickness, 0.005in

Face Sheet thickness, 0.087in

$[0/\pm45/90]_{2S}$ ply orientation

2.3 Pin/Truss Geometry

Pins are fabricated from stainless steel. Pin angle orientation for this analysis was 20 degrees from the vertical axis. The diameter of the pin is d=0.020in. Therefore, the cross-sectional area and moment of inertia of the pin can be determined:

$$A_{pin} = \frac{\pi d^2}{4} \Rightarrow \frac{\pi (0.020\text{in})^2}{4} = 0.000314\text{in}^2 \tag{2.1}$$

$$I = \frac{\pi}{4} r^4 \Rightarrow \frac{\pi (0.010\,\text{in})^4}{4} = 7.85 x 10^{-9}\,\text{in}^4 \tag{2.2}$$

$$J = \frac{\pi}{32} d^4 \Rightarrow \frac{\pi (0.020\,\text{in})^4}{32} = 1.57 x 10^{-8}\,\text{in}^4 \tag{2.3}$$

For plain carbon steel, the following material property values were used:

$E = 3.0 \text{x} 10^7 \frac{\text{lbs}}{\text{in}^2}$ (Modulus of Elasticity)

$G = 11.5 \text{x} 10^6 \frac{\text{lbs}}{\text{in}^2}$ (Shear Modulus)

$\nu = 0.292$ (Poissons' Ratio)

3. FINITE ELEMENT MODEL SPECIFICATIONS

3.1 Finite Element Software/Hardware

The finite element software used is MSC/NASTRAN (V68.2) and the results are verified by using ASTROS. This research was completed using a UNIX Main Frame and a SUN Sparc 10 Workstation.

3.2 Elements Used

The upper and lower face sheets are modeled using CQUAD4 shell elements. Plate input parameters for the CQUAD4 elements include element identification number, property identification number and grid point identification numbers of four connecting grid points, where G1, G2, G3 and G4 are identified sequentially around the circumference of the element as shown in Figure 2. Here MCID denotes a material coordinate identification system. Geometric dimensions of the face sheet are provided by using the PSHELL card, and the material properties are specified using a MAT8 card. MAT8 defines the material property of an orthotropic material for shell elements. Since the face sheet is made up of laminated materials, equivalent material properties are determined. The method of calculating the equivalent orthotropic material properties is discussed in detail in Attachment VII.

The "truss" pins are modeled as CROD pin elements. The CROD element defines a tension-compression element. Input parameters for the CROD elements include element identification number, property identification number and grid point identification numbers of 2 connecting grid points, G1 and G2 as shown in Figure 3. Again, geometric and material properties for the rod elements are provided through PROD and MAT1 cards. MAT1 defines the material property for linear, temperature-independent, isotropic materials.

3.3 Mesh

The mesh of the upper and lower face sheets is geometry dependent. The pin orientation angle and pin separation distance or space between the pins determine the number of pins in a given geometrical square. The pin orientation (of 20 ^{o})created "groups" of four pins. These groups created three different sized meshes, the first being 0.090 x 0.090 (based on the pin angle), in the second 0.090 x 0.163in (based on the pin angle and the space between the pins) and the third being 0.163 x 0.163in (based on the space between the pins). Figure 4 depicts the respective QUAD4 element sizes. Convergence studies concluded that decreasing the mesh size(refining model) showed no enhancement or benefit to the analysis, but substantially increased the CPU analysis time.

3.4 Finite Element Model

The finite element model was created by developing a FORTRAN pre-processor to create all the QUAD4 shell and CROD pin elements. The description and usage of this specific preprocessor for Z-pin sandwich is discussed in detail in attachment IX. The developed finite element model consist of 1058 QUAD4 elements and 528 rod elements with 1152 node points.

3.5 Boundary Conditions

The FEA model analyses the panel using simple supports on all four sides. All transverse displacements are set to zero at the neutral axis.

4. FAILURE MODES

In this section, a detailed discussion about the failure modes is provided. As mentioned earlier in the introduction, the development of these failure modes is phenomenological and is based on the experimental and analytical observations. Two different failure modes (both are pin oriented) are considered. Pin buckling is the first failure mode while the pin piercing the face sheet or pin push through is the second failure mode.

4.1 Pin Buckling

Buckling is a failure mode in which a pin has its equilibrium disturbed. The pins will return to their original equilibrium(position) as long as P(applied axial load) does not exceed a pre-determined value P_{cr}, which is defined as the "critical load". However, if $P>P_{cr}$, the pin will move away from its original position. The system is "stable" if its original equilibrium is maintained, if $P>P_{cr}$, the system is "unstable" and buckling occurs. The pin buckling analysis consisted of the following:

4.1.1 Critical buckling load

The critical buckling load was determined using a modified Euler equation. The modified equation was required to account for the end moments and rotations (a detailed discussion is provided in attachment VII):

$$\begin{aligned} P_{cr} &= \frac{(\Delta+0.4)^2}{(\Delta+0.2)^2}\frac{\pi^2 EI}{l^2} \\ P_{cr} &= \frac{(1.8909+0.4)^2}{(1.8909+0.2)^2}\frac{\pi^2}{1}\frac{3.0\text{x}10^7\,\text{lbs}}{\text{in}^2}\frac{7.85\text{x}10^{-9}\,\text{in}^4}{1}\left(\frac{1}{0.476\text{in}}\right)^2 \qquad (4.1) \\ P_{cr} &= 10.46\text{lbs} \end{aligned}$$

where E = Youngs' Modulus
I = Moment of Inertia
l = length of pin

It is assumed that the phenomena of pin buckling is an isolated phenomena and does not interact with any other failure. But in reality, this may not be true. Some delaminations may result in the face sheet because of the buckling of the pin. Also, it is assumed that the pin will not carry any load once it buckled. This also may not be true as the pin may be able to carry some post buckling load. That is, once the axial load in any pin exceeds the critical buckling load, it is assumed that the pin is buckled and that the pin no longer is a load carrying structural member. Using this assumption, a quasi- nonlinear procedure is developed and is discussed in the next section.

4.2 Pin Push Through

The second failure mode considered is the pin push through. In this failure mode, the portion of the pin that is inside the face sheet will try to pierce through the face sheet. In principle, the phenomena of pin-push through is due to the shear stress and peeling stress distribution across the thickness of the face sheets and along the length of the pin as shown in Figure 25-28 of attachment VII. This phenomena is characterized by the initiation of the breaking of the bond (debonding) between the pin and the face sheet due to the shear and peeling stresses in the face sheet. When the stresses in the face sheet exceeds the allowable (shear stress of the adhesive that is bonding the pin and the face sheet), then the phenomena of push through results. That is, an accurate estimation of the stress distribution along the embedded pin within the face sheets is required to determine the initiation and progression of the pin debonding phenomena. This debonding development also leads to ply delamination. This requires a nonlinear modeling of the face sheets using very expensive three dimensional brick elements (like in attachment VII).

However, a reasonable estimate of the load at which the pin push through phenomena will occur can be determined using the current finite element model (two dimensional shell and rod elements) itself. This is possible if a relationship between the load in the pin and the stress distribution in the face sheet can be determined. If this relationship is established, the analysis can be performed in the same manner as the pin buckling, that is determining a critical axial load in the pin which will produce pin-push through of the face sheet. The relationship between the allowable axial load in the pin, pin geometry and face sheet thickness can be formulated as below. Referring to Figure 5, the pin surface area can be calculated as $2\pi r$ with r being the radius of the pin. The bonded length of the pin and face sheet can be determined as $R = \frac{L}{\cos\theta}$, where L is the thickness of the face sheet and θ is the pin orientation angle. Multiplying by an allowable shear stress, the critical load can then be determined by

$$P_{\text{critical}} = 2\pi r\left(\frac{L}{\cos\theta}\right)\tau_{\text{allowable}} \tag{4.2}$$

Results shown (figures 25-28)in attachment VII using three dimensional brick elements indicate the generic force intensities along the length of the pin within the face sheet when an axial load is applied to the pin. These studies show that the stress distribution is not uniformly distributed, but rather a very small length of face will have a large stress. Also, it can be seen that the development of maximum peeling stress is on the opposite end to the maximum shear stress. This peel stress (which could just as well show up as a crushing stress on the opposite side of the inclined pin), the authors feel, leads to the true representation of the failure in the face sheets based on experimental observations. From the microscopic photographs of the specimens just prior to failure(attachment II and III), delaminations and cracks parallel to the pin can be observed. Also, a certain amount of debonding of the pin can be noticed. From attachment IV, where analytical solutions to the three dimensional stress distribution are provided, in-plane stress is observed to be developing due to a boundary transverse load intensity; which is a similar scenario to the loading brought about by the crushing stress; which is ten times larger than the applied transverse (peeling) stress at a point in the sandwich plate (figure 9 of attachment IV). This in-plane normal (crushing stress) is responsible for the delaminations and cracks parallel to the pins without a total pin push through. This failure mode is truly three dimensional and will not be developed further, but can be used to intimate the features of delamination, debonding of the pin and localized intraply failure. As a simple attempt, the authors have developed a debonding failure mode.

The debonding process was attributed to the shear and peeling stresses. Complete debonding of the pin from the face sheet lead to the push through phenomena. That is the process of the pin push through is characterized as a series of adhesive debondings due to shear and peeling stresses, and when all the adhesive along the length of the pin is debonded, the pin will start pushing through the face sheet. Thus, the axial load in the pin that can cause all the adhesive to break can be termed the pin push through load. In addition, the region at which the maximum bonding shear stress is present also lead to delaminations. From the generic shear stress and peeling stress distribution and the experimentation, it is assumed that at each adhesive break, the pin will be debonded from the layers of the face sheet along with creating a delamination and a free surface . This delamination appears to occur at intervals of two plies. An equivalent stress distribution is assumed along the pin based on the generic stress distribution curves as shown in Figure 6. It consists of two triangles on either end of the pin, one representing the shear stress distribution and the other, peeling stress distribution. Also, the load in the pin is determined by modifying equation (4.2) as

$$P = 2 \pi r A / \cos \theta \qquad (4.3)$$

A is the area under the shear stress curve. The allowable strengths of the adhesive in tension and in shear are 6500 psi and 9800 psi (attachment VII) respectively. Figure 6 shows the starting stress magnitudes from attachment VII which are then used for proportioning. By using linear proportions, from the magnitudes of peeling stress and the shearing stress, it appears that the first debond is due to the peeling stress. That is, when the maximum peeling stress becomes 6500 psi (maximum shearing stress becomes 4500 psi), first debond or pulling away of the adhesive from the pin occurs within the top two layers of the face sheet. Then the overall length of the pin bonded to the face sheet becomes equal to $L_1 = L - 2$ layer thickness. Here L is the original length of the pin and L_1 is the length of the pin after first adhesive debond. At the free surface, peeling stress is again developed. The next debond occurs when this peeling surface in the pin length of L_1 reaches 6500 psi. By then, the maximum shearing stress on the other end of the pin reaches a magnitude of 9000 psi. At this second peeling stress level, the adhesive debonds further(2 more layers). The third breakage is due to the shearing stress since it reaches the allowable stress of 9800 psi before the peeling stress develops to its critical value of 6500 psi. This third stage causes further debonding of 2 more layers of face sheet. This process is continued until the pin is totally debonded. Then the phenomena of push through occurs. The various steps of debond can be described in the following Table

Stage	No of layers of pin bonding	failure mode	Area under the shear triangle	Pin load based on the shear debonding stress(lb)
1	18	peeling	39.15	2.618
2	16	peeling	36.0	2.407
3	14	shear	5.6	0.374
4	12	peeling	27.0	1.805
5	10	peeling	22.5	1.504
6	8	shear	3.2	0.214
7	6	peeling	13.5	0.903
8	4	peeling (final)	9.0	0.602
				10.427 lb

The pin push through phenomena can be characterized by 8 steps in this 16 layer face sheet. In the first load step, the bond up to 2 ply layers is broken away from the pin, and a delamination resulted in the 2 nd layer (figure 7). In the second step, the breakage progressed to the 4 th ply and a delamination results. In the third step, the debonding is up to the 6 th ply layer and again a delamination results. This activity continues through eighth step and the adhesive is completely broken. At each stage, the load in the pin at which the debonding occurred was determined using equation (4.3). The pin will be completely pushed out of the face sheet when the axial load in the pin is equal to 10.427 lb. The push through phenomena occurs at a slightly lower load (in the pin) than the pin buckling. In theory, if the pin does not push through, due to some manufacturing anomaly, it will buckle.

5. QUASI-NONLINEAR PROCEDURE

To determine the load deflection characteristics as the failures progresses, a quasi-nonlinear procedure is developed. In this procedure, only the material nonlinearity is considered without considering the resulting geometric nonlinearity(that is the reason why this procedure is termed quasi-nonlinear). This results in an error because changes in the geometry associated with failure are not taken into consideration. That is, when a pin fails, there will be changes in both the geometrical and material properties corresponding to that fail. In this analysis, the change in material properties is accounted for by changing the material property card while the change in the geometry is not accounted. The outline of the procedure is as below:

(1) Initially, a load is applied to the plate of given geometry and boundary conditions. This load application results in the development of forces in the pin (CROD) elements and the face sheet (CQUAD4) elements.

(2) Increase the load in magnitude until the force in any one of the pins is equal to the failure load of any of the pin. The failure load can be either a buckling or push through load. Since it was established that the pin push through occurs ahead of the pin buckling, for all practical purposes, the failure load refers to the pin push through load. Since we are using linear analysis, the load to be increased can be estimated fairly accurately from the results of step 1.

(3) Identify the pin that failed. In fact due to the symmetry of the loading and geometry of the plate, instead of one pin, a group (4) of pins will fail at the same time. Reduce the stiffness of the pins that failed. This can be achieved by changing the

material properties of the pins that failed. In all the work that is carried out in this report, the Young's modulus of the pins were reduced to 0.01 percent of the original Young's modulus whenever they failed. That is, this pin is physically present to retain the shape of the plate but it can not carry any load.

(4) Apply the next increment or step of load (size of which is based on the next failure load and is determined by trial and error). The stiffness of the plate is different from that of the earlier load due to the failed pins. Also, it should be remembered that all the pins are preloaded (because of the application of earlier load) before determining the next failure load. That is, in this case only the incremental load is applied and a resultant incremental displacement has to be determined. Again, pins will fail in a cluster similar to the earlier case because of the same reasons. Graphically, the procedure can be described as in Figure 8 while in mathematical form, this incremental approach can be described as

$$[K]_i \Delta Q_i = F_i - [K]_{i-1} Q_{i-1} \tag{5.1}$$

$$Q_i = Q_{i-1} + \Delta Q_i$$

where *i* is the load increment number and Q is the displacement, K is the stiffness and F is the resultant force, ΔQ is the incremental displacement. Based on this equation, this procedure can be explained as follows.

To start with, the load increment *i* is equal to 1, applied load is equal to F_1 and K_{i-1} is equal to zero. Initial increment of displacement can be obtained as

$$[K]_1 \Delta Q_1 = F_1 \tag{5.2}$$

$$Q_1 = \Delta Q_1$$

In the next step, an increment of load ΔF_1 is applied. Then the new total load applied is equal to $F_2 = F_1 + \Delta F_1$. Then the incremental displacement can be obtained from

$$[K]_2 \Delta Q_2 = F_2 - [K]_1 Q_1 = \Delta F_1 \tag{5.3}$$

$$Q_2 = Q_1 + \Delta Q_2$$

This process is continued until a significant number of pins failed. Thus, by using this procedure, the progression of failure can be determined.

6. RESULTS

The focus of this research is to develop analytical tools to analyze Z-pin sandwich panels. Hence, initially, it was attempted to see whether any similarities can be observed that are similar to the Nomax sandwich panels which are modeled as plate elements. The basic assumption in that modeling was that there is no significant through the thickness direct strain. To check whether such an assumption is valid, a load deflection curve was generated for the top and bottom face sheets.. The load vs displacement plots for the finite element model of the upper and lower face sheets are shown in Figure 9. This plot shows that the lower and upper face sheets have different load displacement characteristics i.e. there is a significant through the thickness strain between the face sheets. Thus, it would be erroneous to model the Z-pin panel as a plate. It has to be modeled as a three dimensional structure.

Next, the progression of failure in the pins is determined through a number of NASTRAN iterations using the quasi-nonlinear approach. The approximate run time for each iteration of the model was approximately two hours. The actual central processing unit(CPU) time was 22 minutes. After each iteration, the NASTRAN output file was read by a developed FORTRAN batch post processor program which searched for the axial load in each of the 528 CROD elements and saved this information. The information saved included the CROD element number and the axial load in each element. The load in each iteration was then added by the FORTRAN program and the cumulative axial load in each member in each pin is determined. At this point, the number of pins which failed could be determined by comparison with the critical failure load(in this case it happens to be the pin push through load). The finite element model was then modified by reducing the stiffness. Stiffness was reduced by adding a new material property with the same moment of inertia and Poisson's' ratio(v) but changing the Youngs' Modulus(E) and Shear Modulus(G) of each failed pin. These values where changed from 3.0×10^7 psi and 1.15×10^7 psi to 10.0 psi respectively. Essentially this changed the pin from a "load" bearing member into a "non-load" bearing member.

The finite Element results using the quasi-nonlinear approach is shown in Figure 10. Also shown are the experimental results. This load vs displacement plot shows the displacements of the lower face sheets. The finite element model results match reasonably well with the experimental results.

7. CONCLUSIONS

The following conclusions can be drawn from the work presented in this section. It should be emphasized here that these conclusions are valid only for this face sheet and pin combination. Changing the orientation of the pin may lead to different conclusions. This is due to the fact that the core (pins) is discrete and the results depend on this discreteness.

(1) A plate approximation is not valid in modeling Z-pin sandwich panels

(2) A quasi-nonlinear approach can be used to determine the load deflection characteristics considering the progression of failure

(3) Pin push through produces a failure load less than a pin buckling scenario. It appears from all the evidence that another mode of failure exists that is more complex than push through or buckling. This was alluded to in the previous discussion and requires a complete three dimensional face sheet consideration.

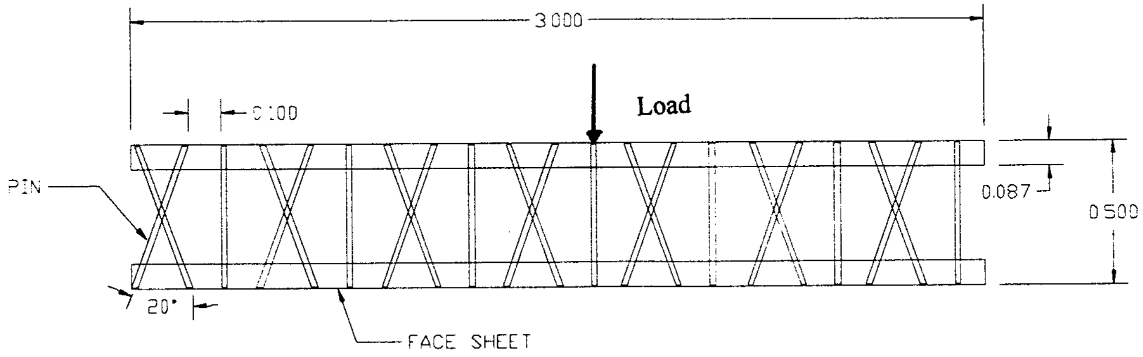
3.000
0.100
Load
PIN
0.087
0.500
20°
FACE SHEET

Figure 1: Geometry of the Z- pin sandwich

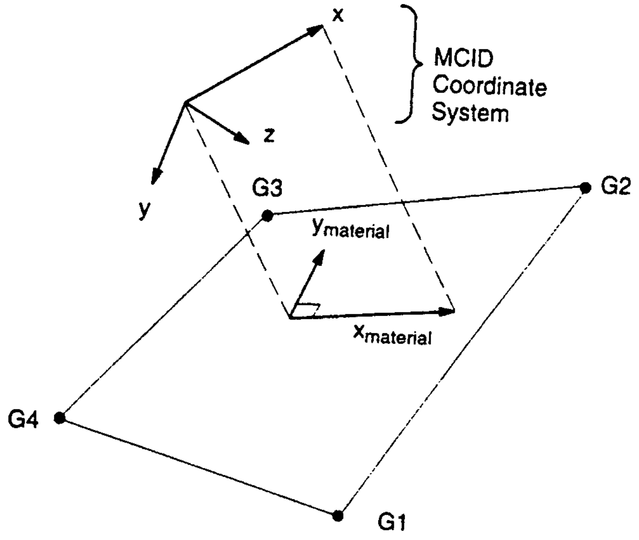
x
MCID
Coordinate
System
z
y
G3
G2
$y_{material}$
$x_{material}$
G4
G1

Figure 2: Description of the CQUAD4 element of NASTRAN

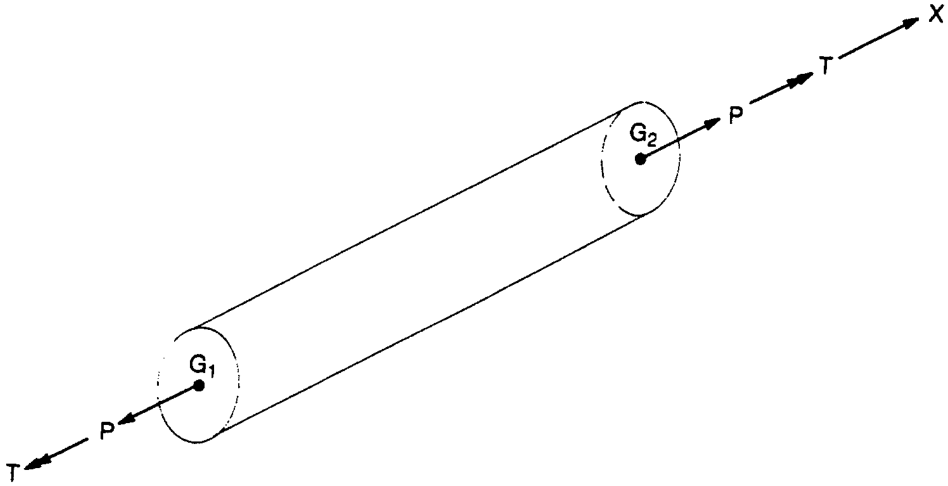

Figure 3: Description of the CROD element

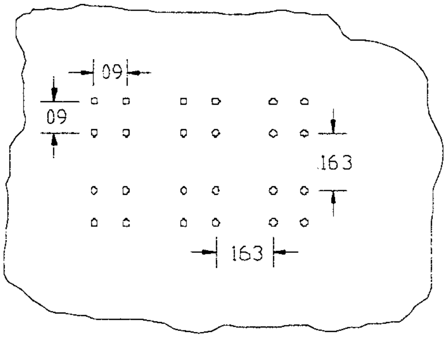
09
09
.163
163

Figure 4: Element sizes of the QUAD4 elements

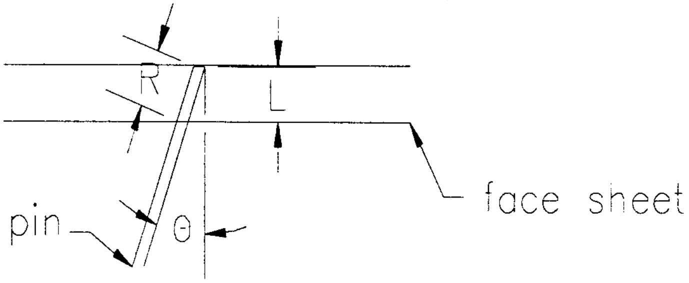
R
L
pin
θ
face sheet

Figure 5: Pin orientation with respect to the face sheet

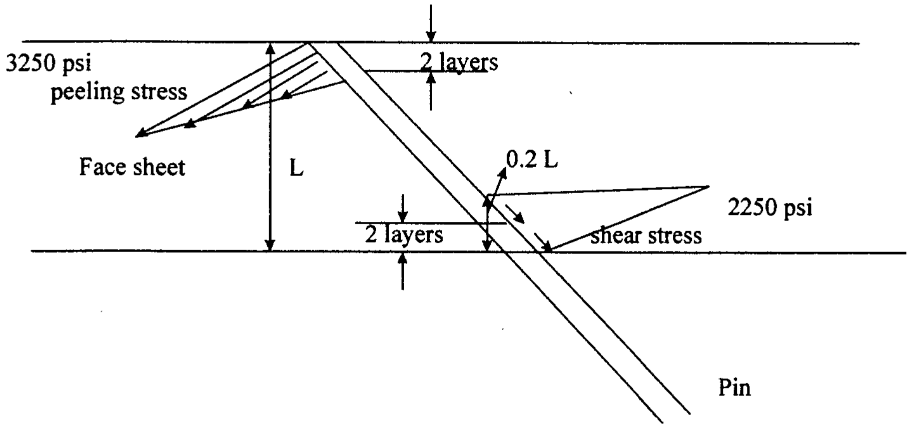
3250 psi
peeling stress
Face sheet
L
2 layers
0.2 L
2250 psi
2 layers
shear stress
Pin

Figure 6: Equivalent load distribution along the pin

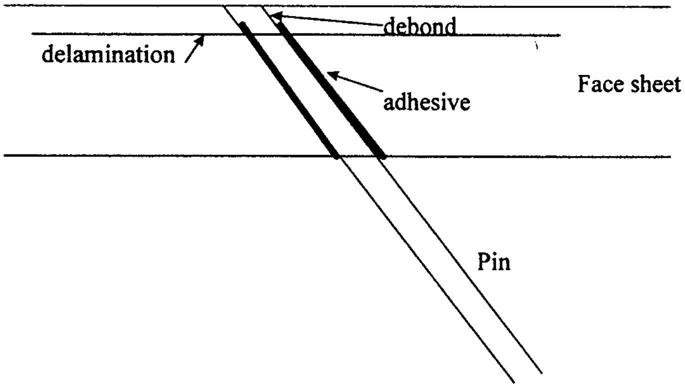
debond
delamination
adhesive
Face sheet
Pin

Figure 7: Mechanism of pin debond (push through)

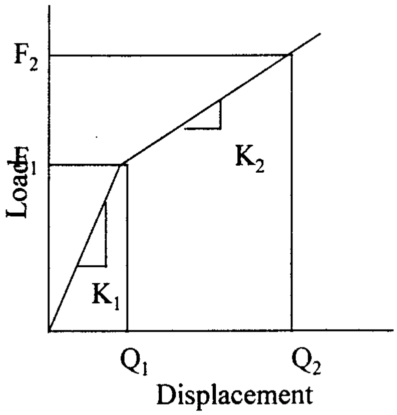
F$_2$
F$_1$
Load
K$_2$
K$_1$
Q$_1$
Q$_2$
Displacement

Figure 8: Schematic of the quasi-nonlinear approach

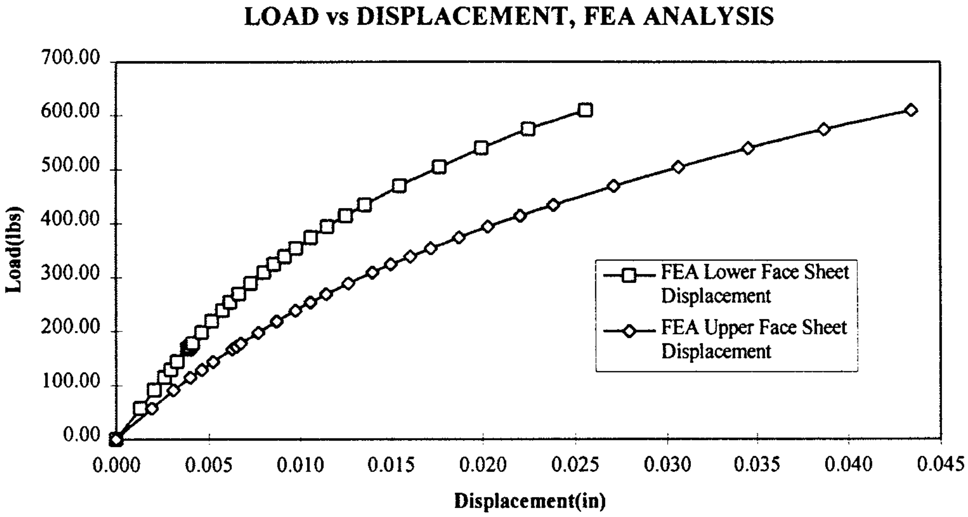

Figure 9: Load deflection curves of the top and bottom face sheets

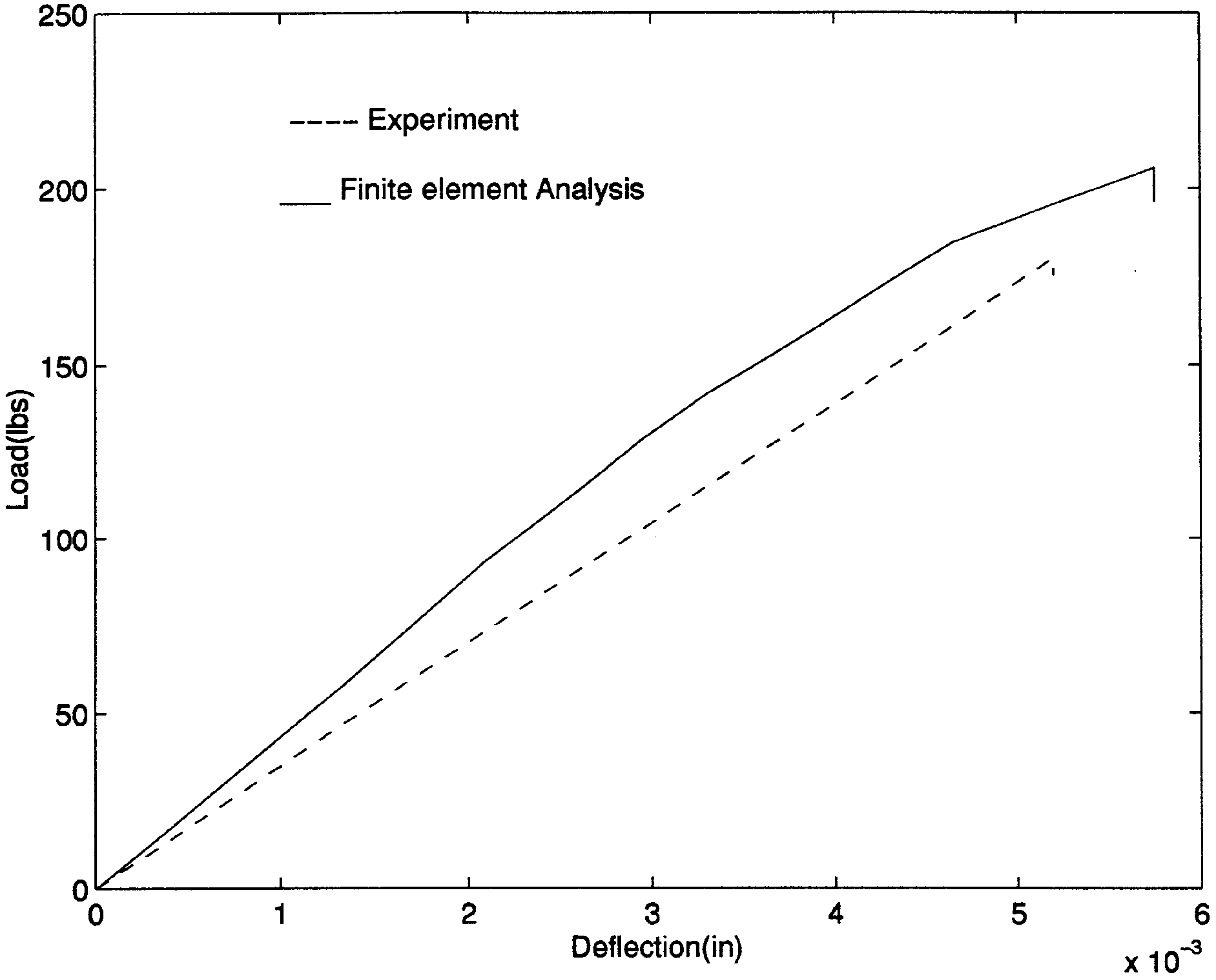

Figure 10: Comparison of load deflection curves for Z pin panel

ATTACHMENT IX

OPTIMIZATION OF Z-PIN COMPOSITE SANDWICH PLATES

OPTIMIZATION OF Z-PIN COMPOSITE SANDWICH PLATES

1. Introduction

In this section, an effort was made to determine the optimal pin angle for the z-pin sandwich plates using the Wright Lab developed commercial software, ASTROS. ASTROS's internal optimization capabilities are size, not shape based. Thus, it's unable to directly determine the optimal pin angle for a given Z- pin configuration. Rather, for a particular pin angle, it can determine the minimum weight through a minimum necessary cross sectional area. However, by repeated weight optimizations using ASTROS, the pin angle can be optimized. This is achieved by considering a series of possible pin angles (as the design space) and optimizing for the minimum weight under given constraints at each of the angles. The angle at which the weight is the lowest with all the constraints satisfied, is the optimum pin angle. The constraints include the compressive strength of the pin, pull out strength of the pin and the buckling strength of the pin. That is, for determining the optimum pin angle dozens of ASTROS runs are required. Developing an ASTROS model using conventional preprocessors like I-DEAS is time consuming for each angle of the pin. It was clear from the outset that hand generation of the ASTROS data decks was completely impractical for the number of configurations that are required to be looked at. That led to the development of a preprocessor program that can generate the ASTROS output instantaneously once the pin angle is specified. The initial portion of this section is dedicated to the description of the preprocessor that is developed for generating the ASTROS input deck. For the reader interested in the optimization studies, this section can be skipped completely. In the next section, results obtained from the number of ASTROS runs are discussed. Each set of runs produced interesting results leading to further analysis. The base configuration used, problems associated with accurate analysis, and the solutions to these problems are discussed.

2. Development of the Preprocessor

A custom pre-processor was designed to build the necessary Bulk Data cards for modeling the Z-pin composite plates. The program was designed to be generic and produces output that works equally well in NASTRAN, ABAQUS and ASTROS.

Below is an example input file for the preprocessor "Build". Build looks for a file "zconfig.dat" containing the information below.

```
4.00                    blength = Sandwich plate length (x)
4.00                    bwidth  = Sandwich plate width  (y)
0.5                     bthick  = Sandwich plate thickness (z)
21.006784215383         α  = pin angle (0=vertical)
0.166667                ratb    = ratio of empty space to pin coverage
1                       NA      = number of elements in pin covered area
1                       NB      = number of elements in empty space
0                       iconst  = constant pin spacing flag
0                       ibuck   = buckling constraint bulk flag
0                       ibeam   = replace rods with beams flag
0                       idistrib= distributed load flag
```

Each term has a short explanation beside it. It is not necessary that this text be in the file; the program does not read or do anything with it. It's there to help the program user. Each term will be explained in further detail during the discussion of the program operation that follows.

The first three terms in the data file are ***blength***, ***bwidth***, and ***bthick***. These are the dimensions of the sandwich plate in consistent units. The pin angle, α, is the alignment, measured from vertical, of each pin. It is given in degrees. These four pieces of data are enough to start the program. Referring to figure 1, the horizontal distance covered by a single pin, a is

$$a = bthick \tan(\alpha)$$

The next item in the configuration file is called ***ratb***. This controls the amount of space between one pin and the next pin in the same direction. If we define b as the empty space between pins then

$$b = ratb * a$$

or if you prefer, the distance between the base of one pin and the next is $a+b$. For all of the analysis done to date the value of ***ratb*** was set to ***1/6***. That is, the space between the pins is dependent on the orientation of the pin. This ratio of 1/6 value was chosen based on the design supplied by the Foster -Miller Inc. Instead, if a constant spacing (independent of pin angle) is used between the pins, the optimization becomes trivial. By choosing the ***iconst*** option, this preprocessor can develop bulk data deck for this arrangement of pins also. Further examination of this parameter might be fruitful.

At this point, **Build** is able to break the plate into unit cells. A top or plan view of a generic unit cell is shown in Figure 2. The large square has dimension ***a*** by ***a***. A pin runs diagonally along each edge of this square. The other three rectangles are the space between pins. This generic cell is modified depending on where in the structure the cell is. No "space" cells are used at the outside edges of the full structure. Also, no pins run along the actual edge of the structure. Figures 3 & 4 show a square plate broken into 4 and 9 unit cells. These two figures correspond to the configurations when the total number of unit cells are even or odd. Significance of this is described later. Typically, these unit cells are quite large for the plate dimensions studied. Thus, an integer number of cells will not, in general, be an exact match for the desired length and width dimensions. Thus, **Build** picks an integer number of cells that comes closest to the desired dimensions. Figure 5 illustrates the result of this compromise fit.

The next two parameters, ***NA*** and ***NB***, allow the user to break the face sheet elements into sub elements. Use of ***NA*** and ***NB*** facilitate the development of finer mesh for the face sheet. ***NA*** controls how many elements make up each distance ***a***. ***NB*** breaks each distance ***b*** into that many elements. Figure 6 illustrates how a ***2x2*** cell bar is broken up for ***NA=2*** and ***NB=1***. Note that not only are the large ***a*** by ***a*** squares broken into 4 **QUAD4**'s, but also the long, thin ***a*** by ***b*** rectangular sections are broken into 2 **QUAD4**'s.

The last four entries in the data file are flags for various program options. Their values should either be 0, meaning off, or 1, meaning on. The flag "***iconst***" is used to keep the unit cells a constant size. If this flag is on, **Build** will change the empty space between pins, ***b***, so that the unit cells for the configuration have the same dimensions as that of the angle configured within the FORTRAN program. This basis angle is currently set to 50 degrees. Another way of looking at this flag is that it keeps the number of pins in the structure constant. If it is desired to change this setting, the variable in question is "α ". The flag "***ibuck***" is used to generate ASTROS buckling constraint cards. This adds a DCONBKE card for each pin to the bulk data. Thus far, we have been unable to get ASTROS to deal with this constraint reliably. No results will be presented for this case. The "***ibeam***" flag controls the modeling of the pins. If the flag is off, the pins are modeled as rods. If the flag is on, the pins are modeled as beams. The "***idistrib***" flag is used to generate FORCE cards. If it is on, it will divide the internal variable "totalload" by the number of pins whose top end does not lie on an edge. It will then generate appropriate FORCE cards to apply that portion of the load to each such pin.

Finally, **Build** will generate boundary condition cards for all the edge nodes. These nodes are constrained against translation, but allowed to rotate freely. There are a number of things that **Build** does not do. It does not generate property or material cards. Nor does it generate the header cards that control the solution. In general, these cards are few in number and do not vary from analysis to analysis. Thus, files are created by hand that are to go before and after the program generated bulk data. A script is used to run **Build** and then combine the header file, **Build**'s output, and the tail file. In our case we have two scripts: one builds an ASTROS input deck, and the other, a NASTRAN deck.

3. Plate Optimization

After the generation of the code, a test case of a 4" square plate with a 1/2" thickness was chosen. The plate was loaded with a concentrated 100 pound center load. As there is never a node at the center of the plate, this was modeled as four 25 pound loads at the nodes surrounding the center.

ASTROS was used to determine the minimum necessary pin cross sectional area subject to one of three different constraints. The first constraint used was termed the "compression" constraint. Each pin was restricted to have no more than a fixed stress in compression. (The stress chosen was 130,000 psi, a typical value for titanium.)

The second constraint was designed to vary with critical stress with the value of the length of the pin. In a very loose sense, this models the variation in the contact length between the pin and the face plate. Thus, this constraint is termed the "pullout" constraint. In our earlier back of the envelop studies and in Attachment VIII, it was shown that the force responsible for the pull out is the shear stress along the length of the pin and can be written as $P_{cr,pull} = 2 \pi r h / \cos(\alpha) \tau_{allo}$.

Here, r is the radius of the pin and h is the thickness of the face plate and τ_{allo} is the allowable shearing strength. When the pin is vertical, $\alpha = 0$ and the pull out strength $P_{cr,0} = 2 \pi r h \tau_{allo}$. That is, for any arbitray pin angle, the critical value varies inversely with the cosine of the pin angle: $P_{cr,pull} = P_{cr,0} / \cos(\alpha)$.

The third constraint varies inversely with the square of the length of the pin. It is intended to roughly model the buckling behavior of the pin and is thus called the "buckling" constraint. Similar to the pull out constraint, the force responsible for the buckling of the pin can be written as $P_{cr,buck} = \pi^2 EI \cos^2(\alpha) / h^2$. Here, EI is the bending stiffness of the pin. When the pin is vertical, $\alpha = 0$ and the buckling strength $P_{cr,0} = \pi^2 EI / h^2$. For any arbitrary orientation of the pin, the critical load is $P_{cr,buck} = P_{cr,0} \cos^2(\alpha)$.

It must be acknowledged that both of the latter constraints are no more than back of the envelope approximations to the actual behavior they are named for. Nevertheless, they allow one to look for general trends and gain understanding of the behavior of the structure.

After performing its optimization, ASTROS outputs one value, the optimal fraction or multiple of the original area, i.e. A / A_0. Thus, if n is the number of pins, and t is the bar thickness (***bthick*** to the **Build** program), the total mass of the pins is:

$$m = \rho \, n \, (A / A_0) \, A_0 \, (t / \cos \alpha)$$

If we note that a number of these values do not vary during a study of the effects of pin angle, we can remove the pin density and initial cross sectional area, as well as the bar thickness. This leaves just the terms that vary from one design to the next. The remaining terms show the behavior of interest and form a relative measure of pin volume. Thus,

$$V = (n / \cos \alpha) \, (A / A_0)$$

is called the relative volume. This will be the parameter plotted on the results to come. If desired, the mass of the pins may be obtained by a simple scaling:

$$m = \rho A_0 t \; V$$

Figures 7, 8, and 9 show the variation in optimal relative volume with respect to pin angle for the compression, pullout, and buckling constraint respectively. It can be seen that on each plot two smooth curves and a wildly zigzagging line exist.

The zigzag lines connect the optimal relative volumes for about twenty values of pin angle. The inexact approximation of the bar dimensions as shown in figure 5 was attributed to this behavior. It was decided to rerun the analysis, but only with pin angles that produce an exact fit of the dimension. Some geometry and algebra leads to the following equation:

$$\alpha_n = tan^{-1} [l / \{t (n \{r+1\} - r)\}]$$

where l is the length desired, t is the bar thickness (***bthick***), r is the spacing ratio (***ratb***), and n is the number of cells. For the test case being modeled, the value of n that was of interest varied between 6 and 19.

These new results, unfortunately, are included in the zigzagged portion of the plot. However, if the new results are broken into two parts based on if n is even or odd, the two smooth curves will appear on each plot.

The reason for this is related to the loading placed on the plate. It can be recalled that four 25 pound loads at the four center most-top nodes are applied. Intuitively, one understands that the pins closest to the loads will absorb most of the load and, thus, will be the ones important to the optimization.

In figure 3, and in any other case with an even number of cells, the four center nodes are isolated. Thus, the four pins that connect to these nodes get little help from their neighbors. Therefore, these four pins support most of the applied load, and thus require a large cross-sectional area. In figure 4, which represents plates with an odd number of unit cells, the four center nodes have neighboring nodes that are very close. Thus, the pins that are loaded are very close to neighboring pins who can help out. Thus, a much lower cross-sectional area is required.

This analysis of the even-odd dependency of the results is born out by the results in figures 7-9. The lower smooth curve on each plot is the results for the cases with a pin angle chosen for an exact fit and with an odd number of cells. The upper smooth curve on each plot connects the exact fitting angle data for even cell counts. These two curves mostly bound the intervening data. The small divergence in the zigzagged data are apparently due to the inexact fit problems discussed earlier.

4. Results

There are a number of factors that compete to form the trends that appear in the results presented previously. Among these are the exponential growth in pin counts and the ability of angled pins to support vertical loads.

In this study, space between the clusters of unit cells is set to 1/6 th size of the unit cell. That is, the number of pins in a given sandwich plate are dependent on the pin orientation angle. Figure 10 shows the variation in the number of pins with pin angle. This growth had a large impact on the pseudo-point-load results (figures 7-9). In this loading configuration, load is applied at only four pints and the pins that are most influenced are the pins close to the application of the load. But while doing the optimization, all of the pins were constrained to have the same area. This means, pins that do not contribute to the load sharing also are constrained to be of same cross section as those that bear the load. That is, the larger the number of pins, the larger the amount of excess, unused volume in the pins away from the load. This leads to the conclusion that the local loading effects are significantly dominating the process of optimization. To eliminate this local loading effect, two more optimization studies are carried out. In the first optimization study, the pin number was set constant by keeping the space between the pins constant. This eliminated the effect of number of pins but resulted in a configuration which may not be practical. For one thing, with this constant pin spacing arrangement, the required pin density at a given pin angle may not be possible. As a second optimization study, a uniform loading distribution is assumed. This eliminated the effect of local loading effects. The optimization obtained is for a unit cell since all the unit cells are exposed to similar loading conditions. As an aside, the growth in pin numbers lead to computational difficulties; angles much smaller than 20 degrees required more resources in terms of memory than were easily available.

In the first optimization study, the spacing of the pins was set at that for the 50 degree case and fixed. As the angle decreased, the space between pins was increased. Figure 11 shows the results for the constant pin spacing analysis. As expected, Pins that are nearly vertical are better able to support a nearly vertical load. It is likely that the more angled pin cases would perform better under other load conditions. In the second optimization study, the four loads were replaced by loads distributed across the entire top face of the plate (other than on edge nodes.) Figure 12 plot the variation in relative volume with pin angle for this load case, for each of the three constraint types. From this figure, it can be seen that **between 20 and 33 degrees, the weight of the sandwich panel is lowest and will satisfy all the constraints.**

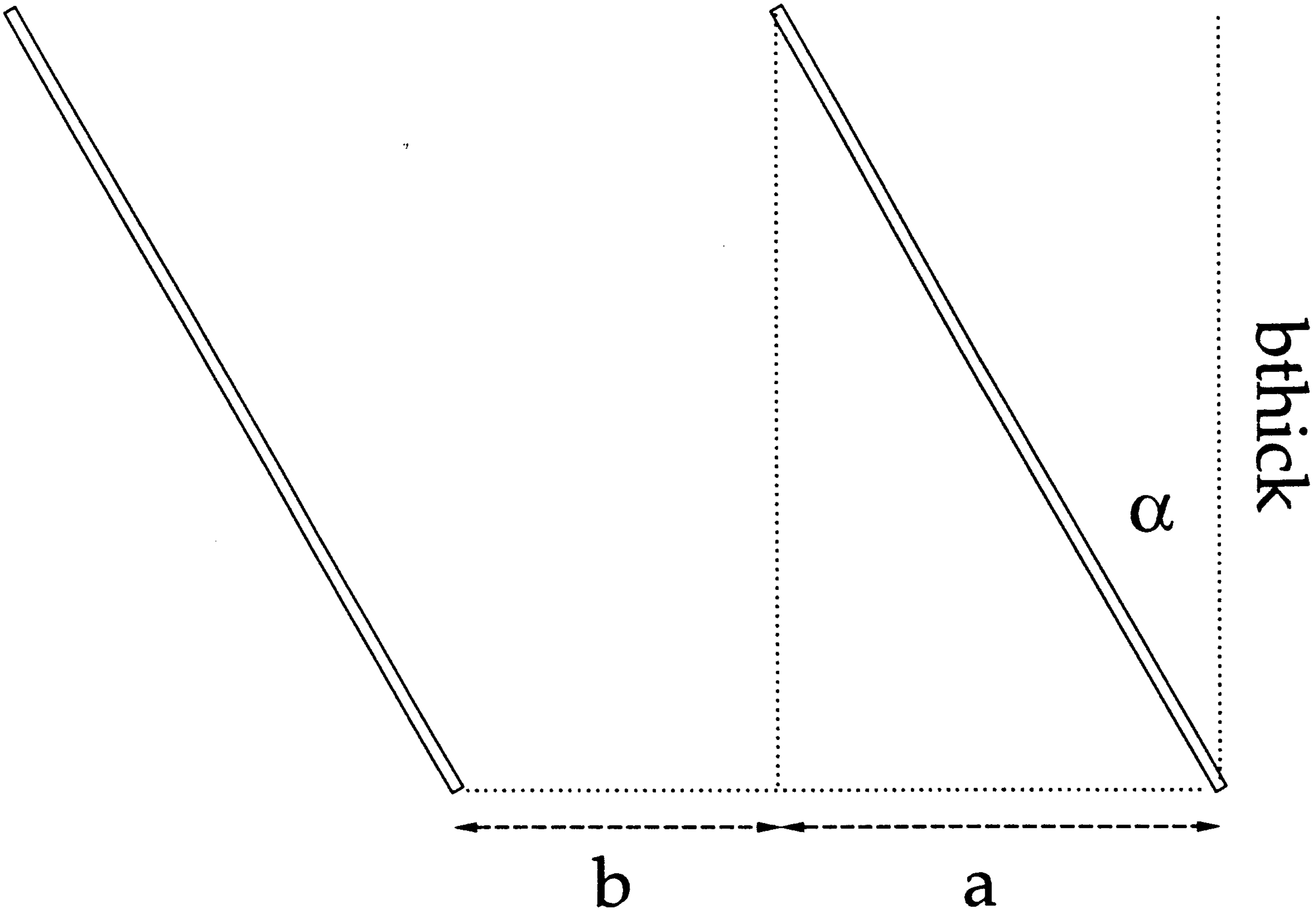

Figure 1: Orientation of the Pin

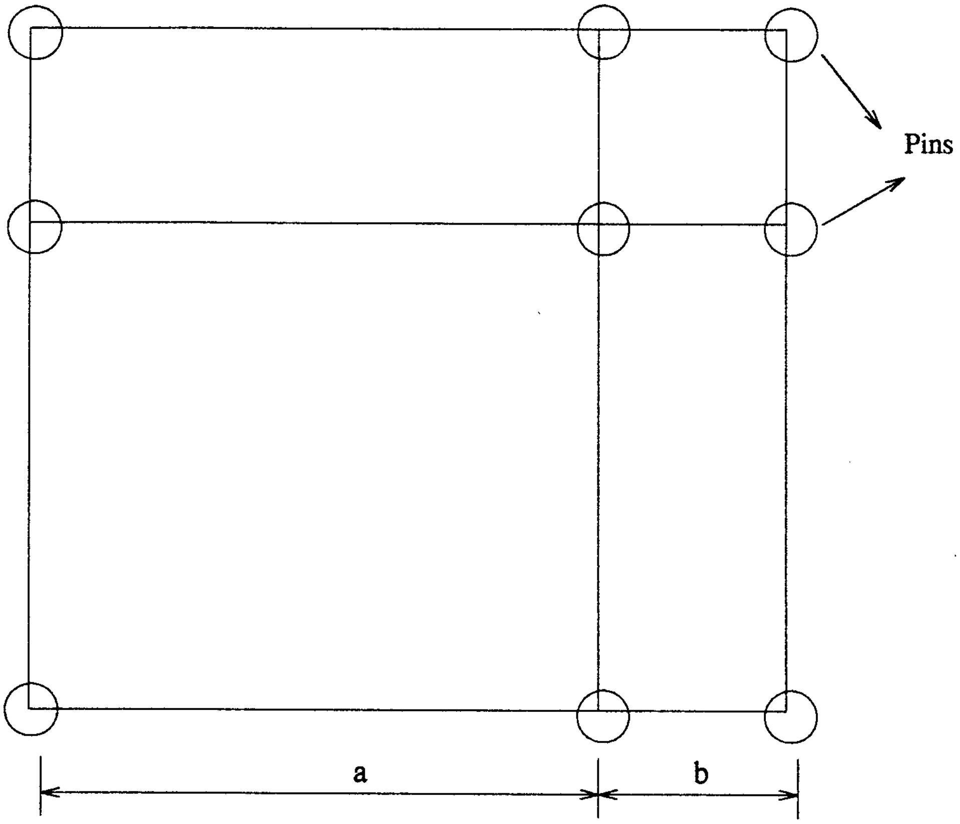

Figure 2: A Generic Unit Cell

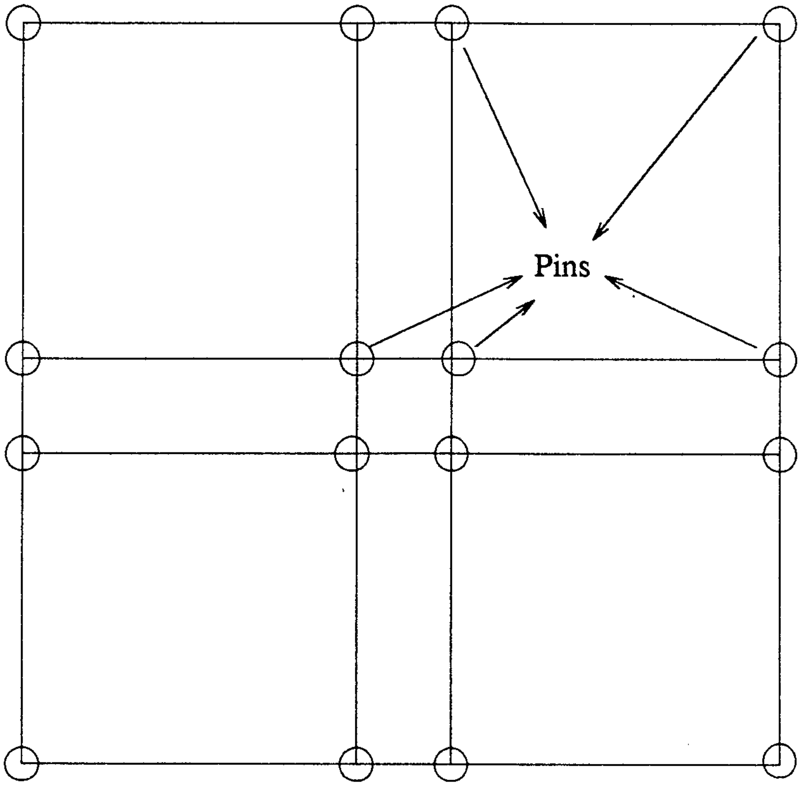

Figure 3: 2X2 Unit Cell

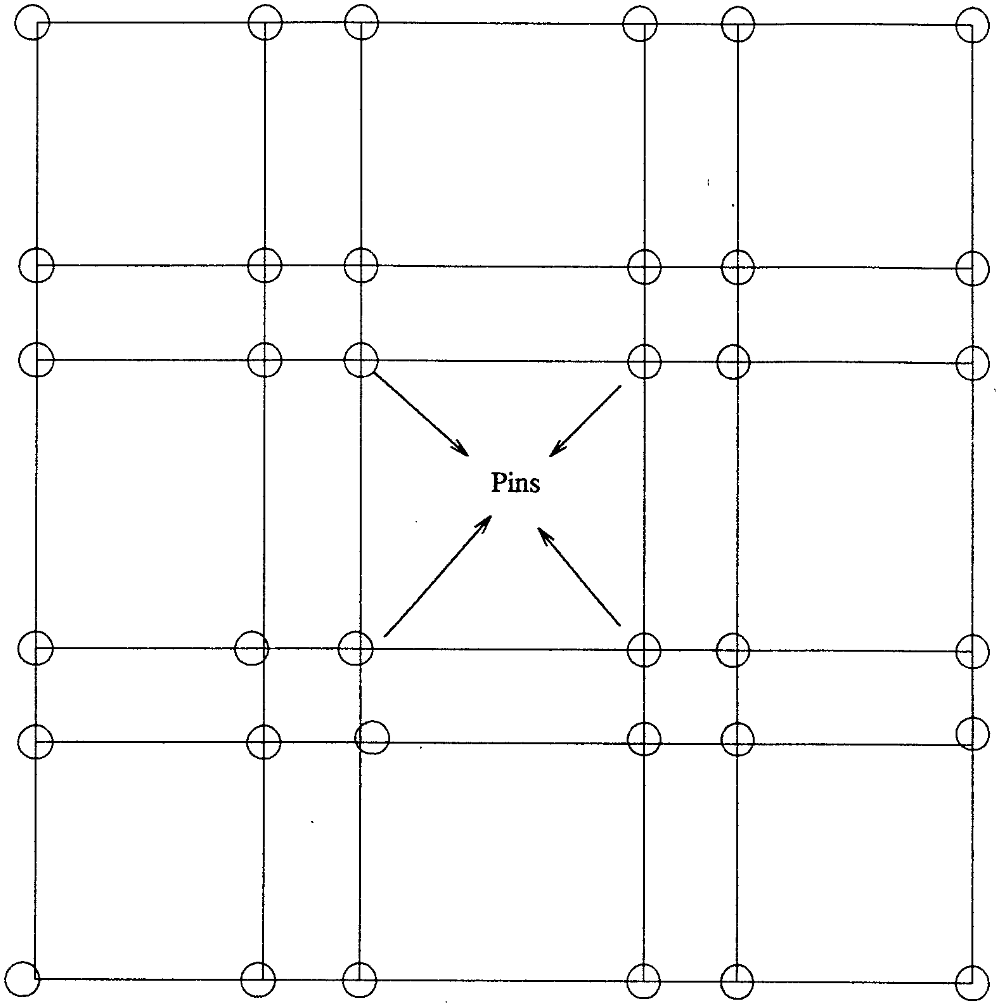

Figure 4: 3X3 Unit Cell

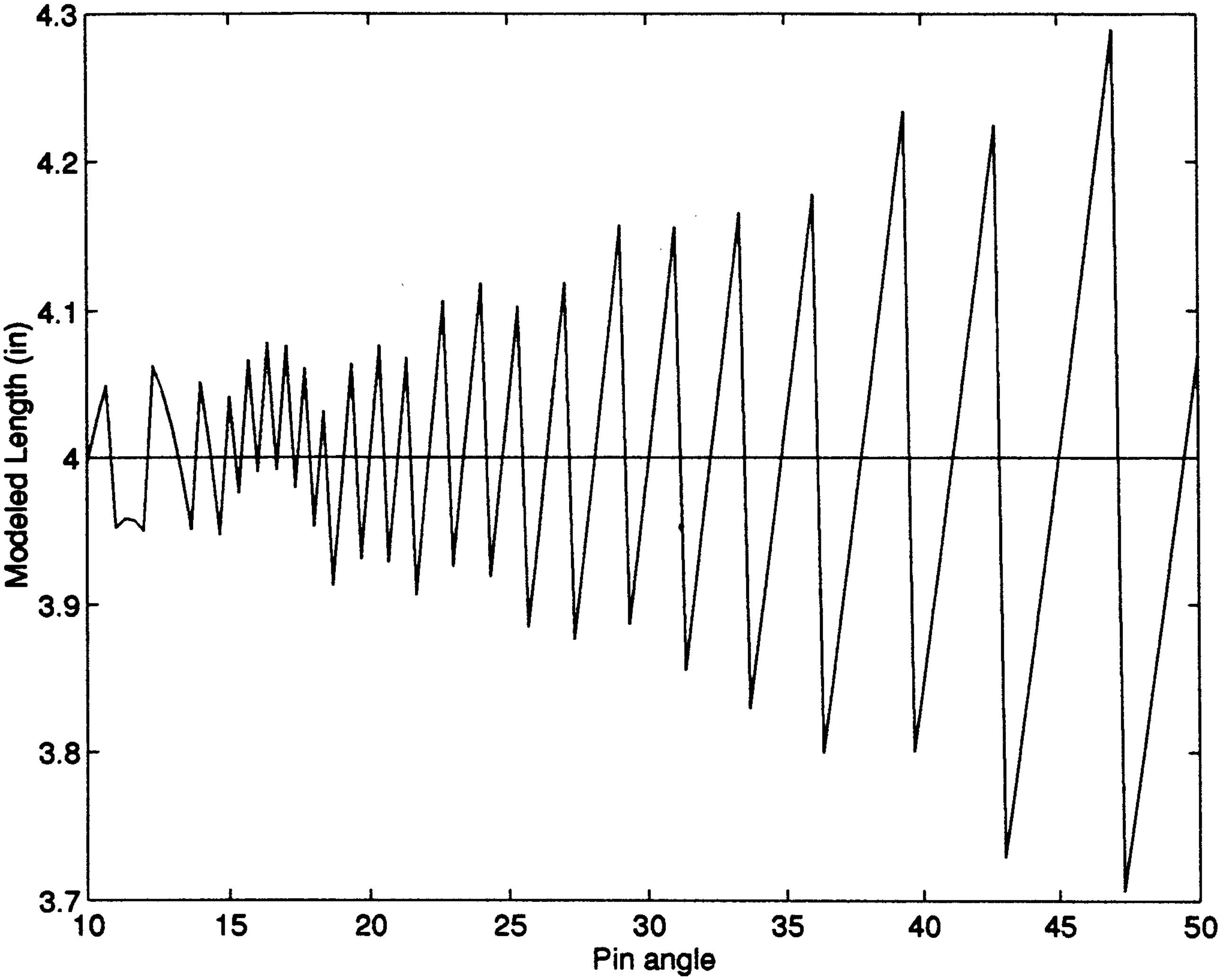

Figure 5: Error in plate length associated with pin angle

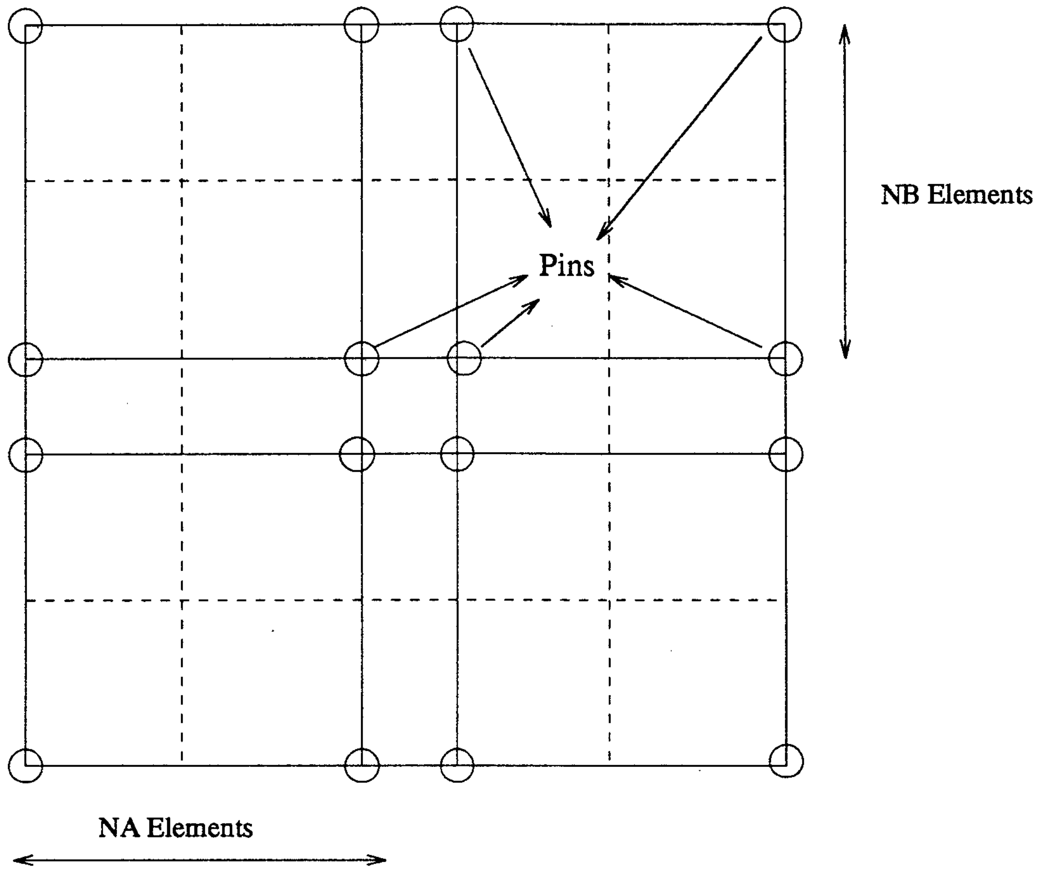
NB Elements
Pins
NA Elements

Figure 6: Breaking Face Sheet into Multiple Elements

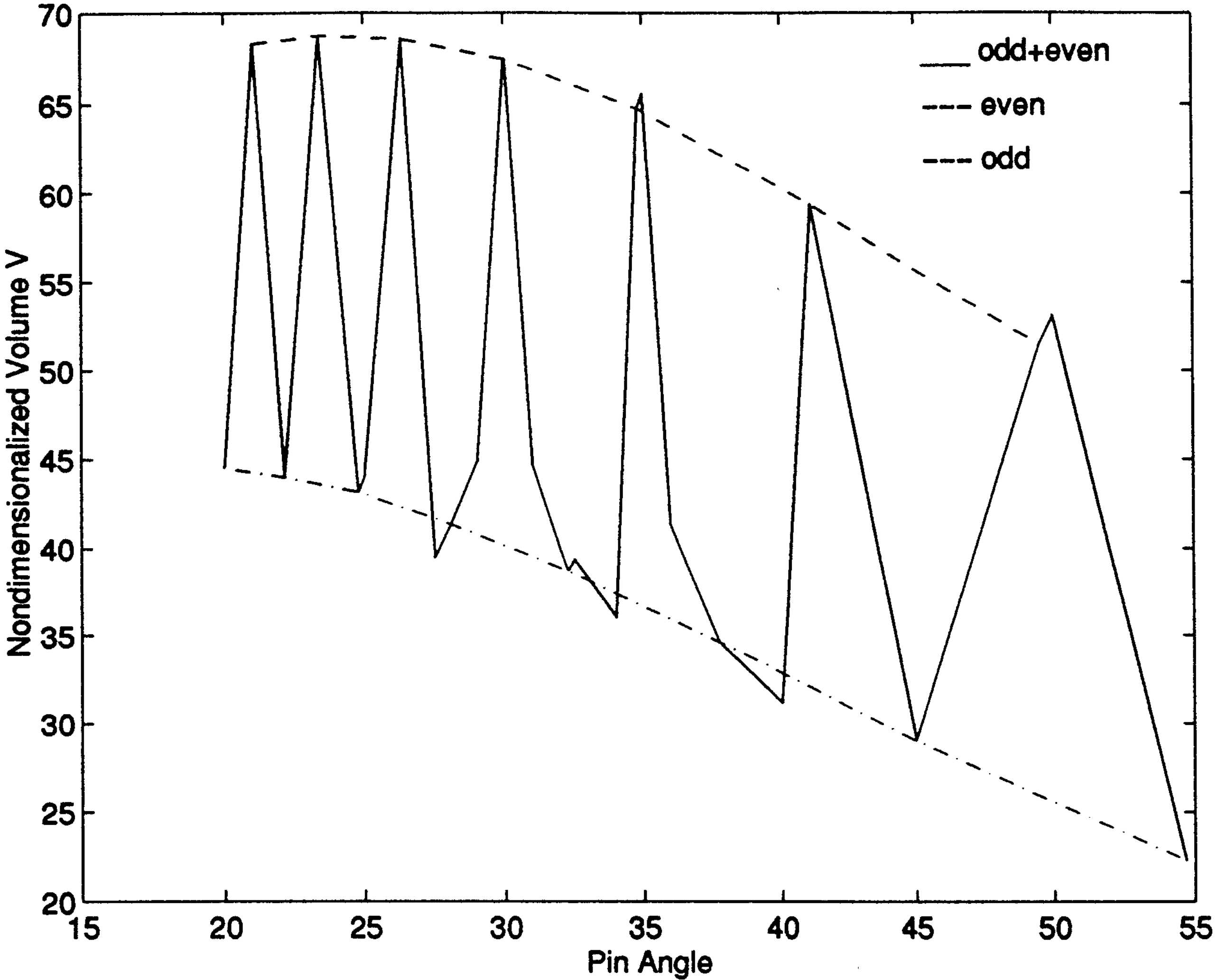

Figure 7: Optimization of pin angles with compressive strength as constraint

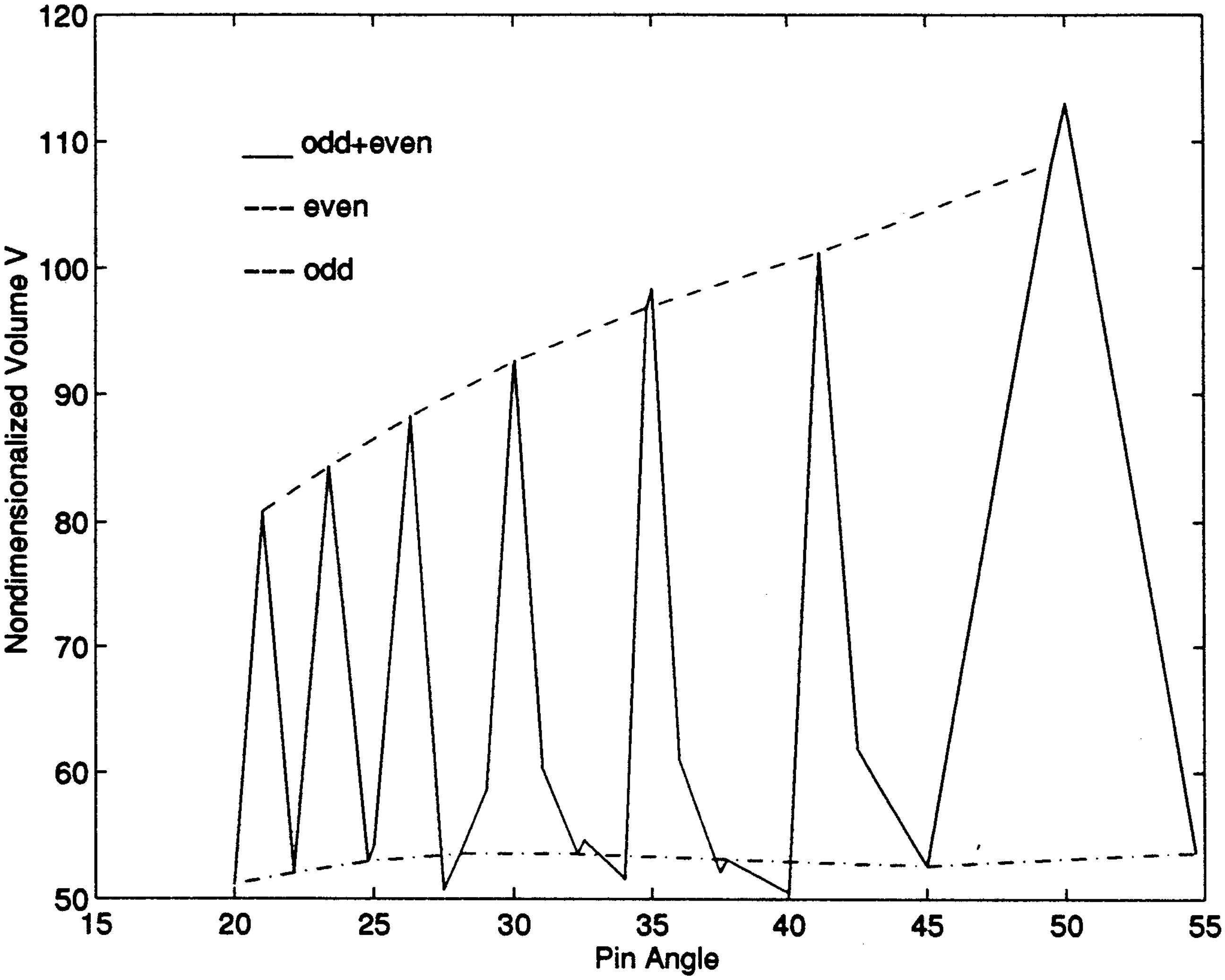

Figure 8: Optimization of pin angles with pullout strength as constraint

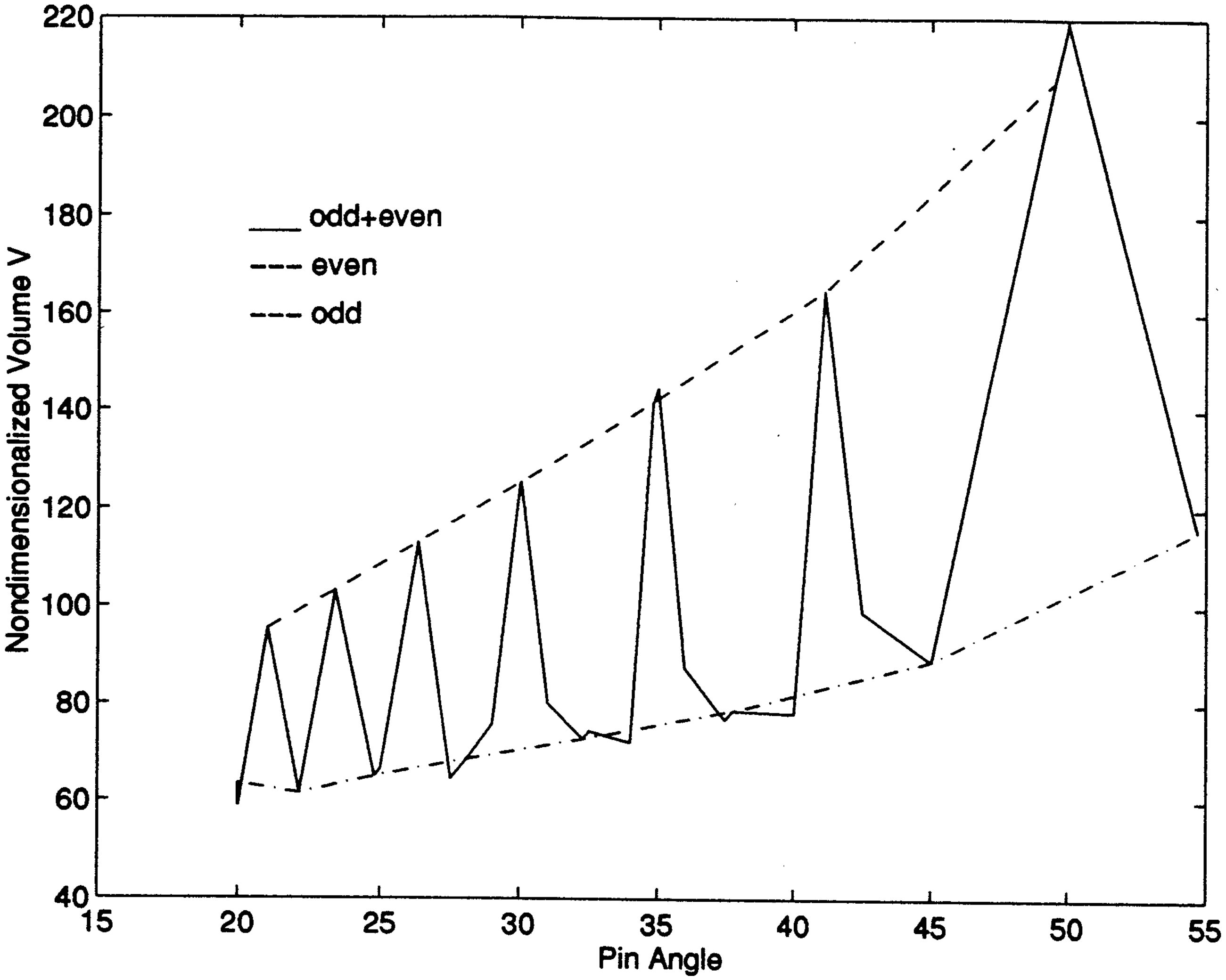

Figure 9: Optimization of pin angles with buckling strength as constraint

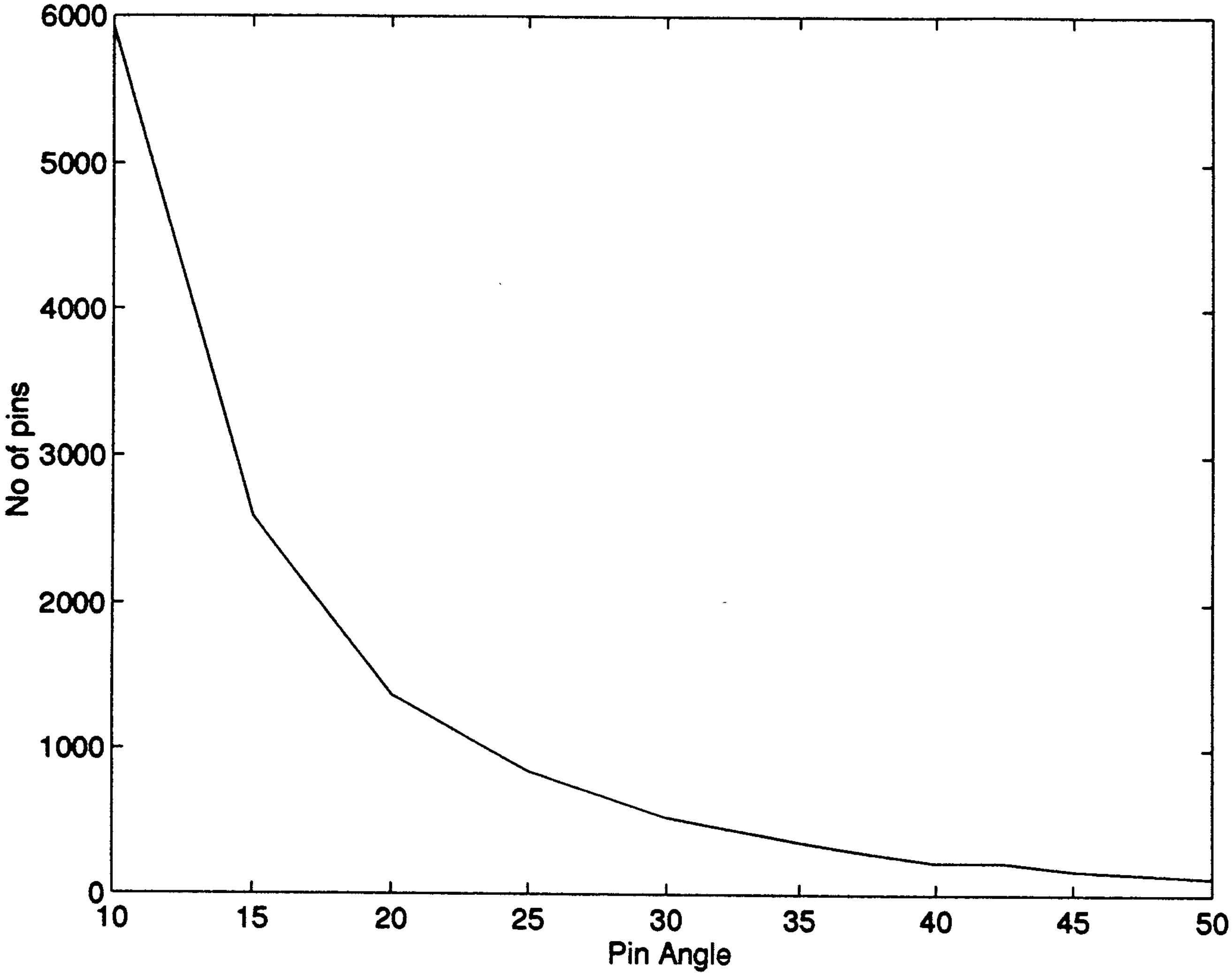

Figure 10: Number of Pins as a function of pin angle

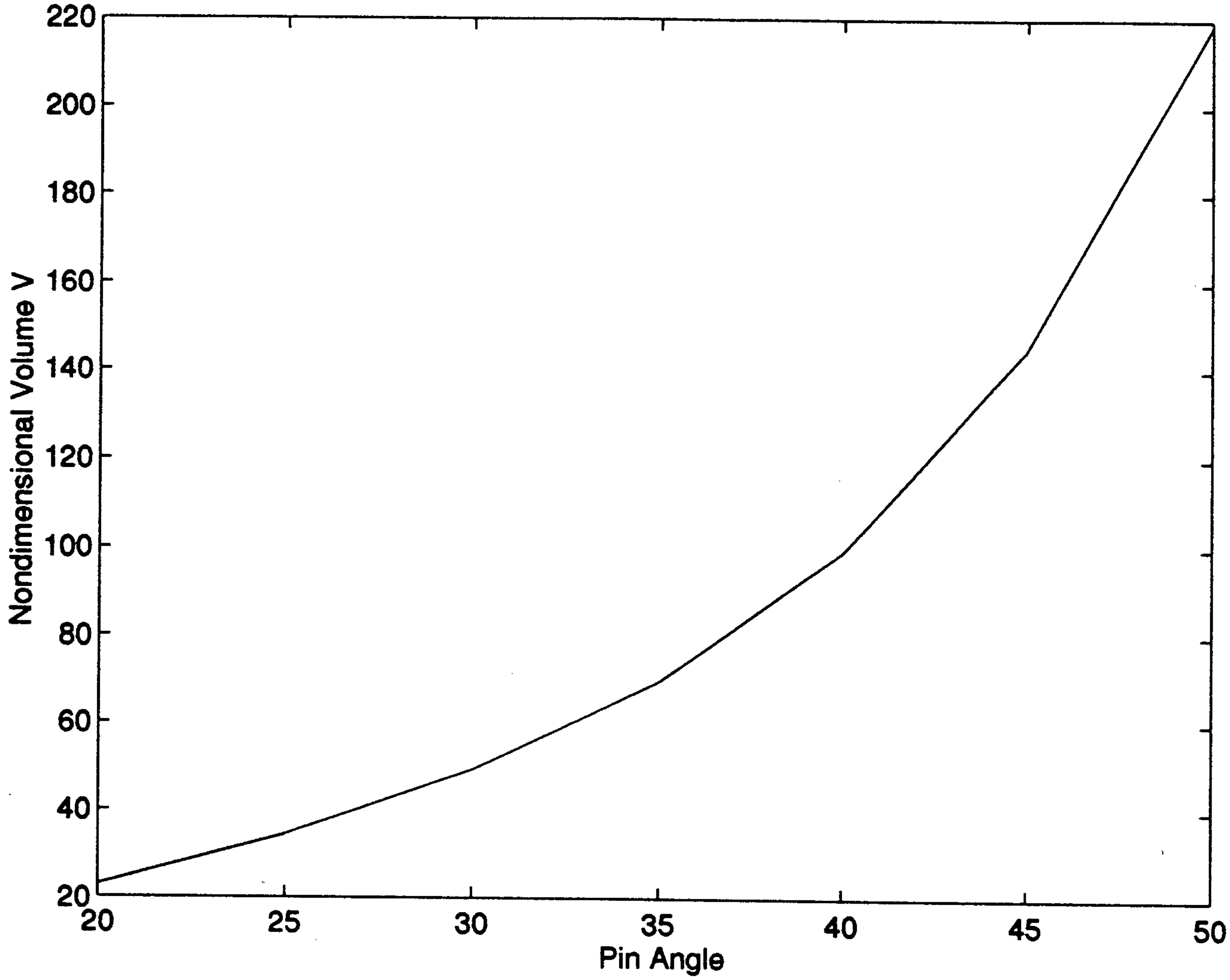

Figure 11: Optimum Weights for various pin angles (Constant spacing)

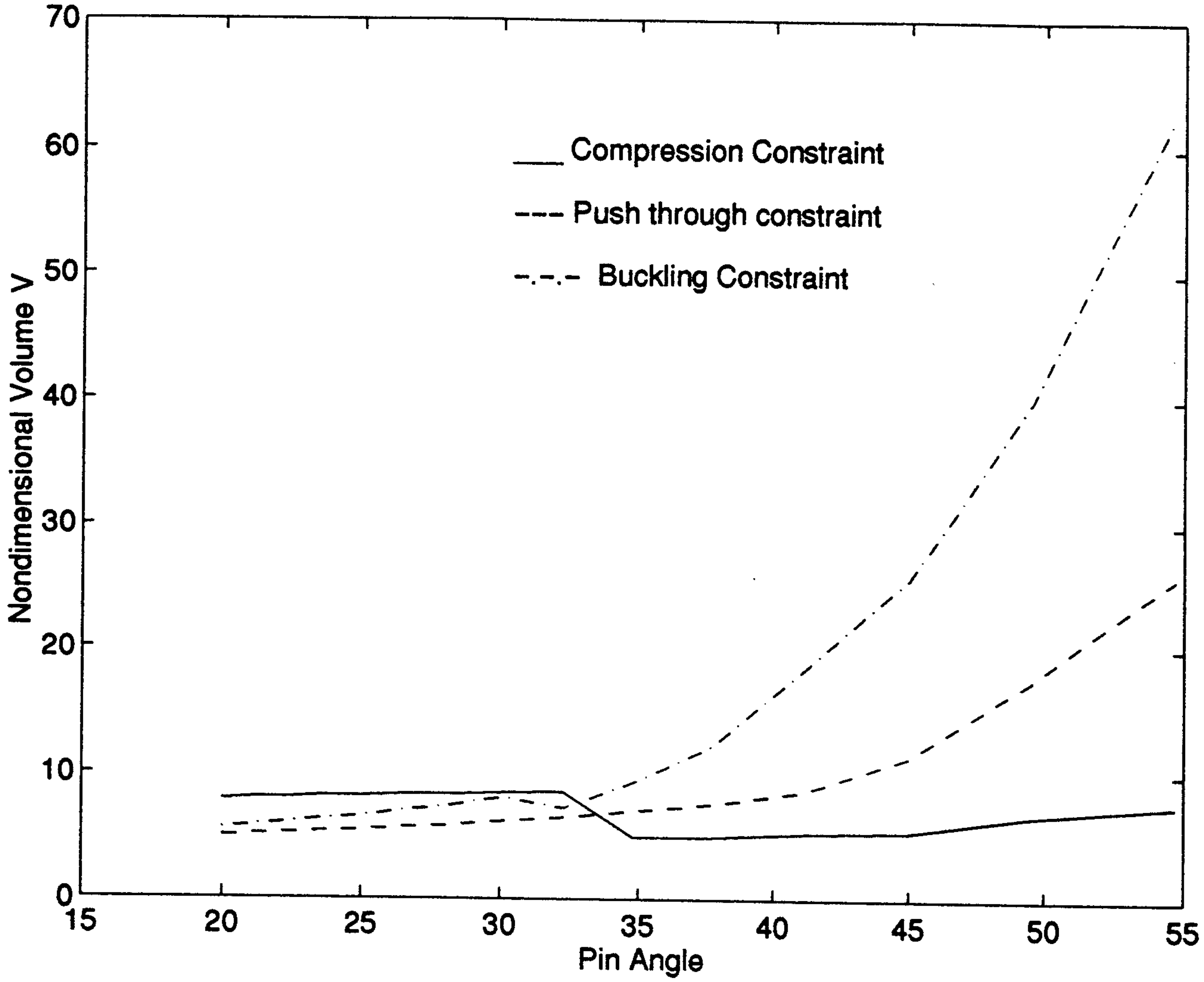

Figure 12: Optimum Weights for various pin angles

REPORT DOCUMENTATION PAGE

Form Approved
OMB No 0704-0188

Public reporting burden for this collection of information is estimated to average 1 hour per response, including the time for reviewing instructions, searching existing data sources, gathering and maintaining the data needed, and completing and reviewing the collection of information. Send comments regarding this burden estimate or any other aspect of this collection of information, including suggestions for reducing this burden, to Washington Headquarters Services, Directorate for Information Operations and Reports, 1215 Jefferson Davis Highway, Suite 1204, Arlington, VA 22202-4302, and to the Office of Management and Budget, Paperwork Reduction Project (0704-0188), Washington, DC 20503

1. AGENCY USE ONLY *(Leave blank)*

2. REPORT DATE
October, 1997

3. REPORT TYPE AND DATES COVERED
Technical report

4. TITLE AND SUBTITLE
FAILURE CHARACTERISTICS OF SANDWICH PLATES
UNDER STATIC AND DYNAMIC LOADING

5. FUNDING NUMBERS

6. AUTHOR(S)
Dr. A.N. Palazotto
Dr. L.N.B. Gummadi

7. PERFORMING ORGANIZATION NAME(S) AND ADDRESS(ES)

Air Force Institute of Technology
WPAFB, OH-45433-6583

8. PERFORMING ORGANIZATION REPORT NUMBER

AFIT/ENY/TR-97-03

9. SPONSORING/MONITORING AGENCY NAME(S) AND ADDRESS(ES)
Mr. W. Baron and T. Holcomb of
Flight Dynamics Directorate
Wright Patterson Air Force Base
OH-45433

10. SPONSORING/MONITORING AGENCY REPORT NUMBER

11. SUPPLEMENTARY NOTES

12a. DISTRIBUTION/AVAILABILITY STATEMENT

Approved for public release; distribution unlimited

12b. DISTRIBUTION CODE

13. ABSTRACT *(Maximum 200 words)*

Laminated sandwich plate constructions are extensively used in various aerospace and industrial applications. However, these plates are prone to many defects. Specifically, their resistance to impact is a major concern. Impact can significantly reduec the strength and stiffness of the structure. Studying various aspects that can be used to improve the impact resistance of sandwich plates is the objective of this report. Two different sandwich models are studied. First, the sandwich plate is made of conventional honeycomb construction while the second plate is made of Z-pins. Experiments are conducted and based on the experimental observations, a phenomenological analytical approach is developed. Issues studied include the determination of impact induced damage initiation, types of damage modes, propagation of damage modes, and the effect of damage on the overall performance of the sandwich plates.

14. SUBJECT TERMS
sandwich plates, low velocity impact, honeycomb z-pins, failure characteristics, finite element methods.

15. NUMBER OF PAGES
252

16. PRICE CODE

17. SECURITY CLASSIFICATION OF REPORT
Unclassified

18. SECURITY CLASSIFICATION OF THIS PAGE
Unclassified

19. SECURITY CLASSIFICATION OF ABSTRACT
Unclassified

20. LIMITATION OF ABSTRACT
Unlimited